

Determination of interval velocities
by inversion of kinematic
3D wavefield attributes

Bestimmung von Intervallgeschwindigkeiten
durch Inversion kinematischer
3D Wellenfeldattribute

Zur Erlangung des akademischen Grades eines
DOKTORS DER NATURWISSENSCHAFTEN

von der Fakultät für Physik der
Universität Karlsruhe (TH)
genehmigte

DISSERTATION

von

Dipl.-Geophys. Nils-Alexander Müller

aus

Groß-Gerau

Tag der mündlichen Prüfung:

1. Juni 2007

Referent:

Prof. Dr. Peter Hubral

Korreferent:

Prof. Dr. Dirk Gajewski

Abstract

In seismic data processing the knowledge of the wave propagation velocities in the subsurface is of fundamental importance. Primarily, these velocities are required for the determination of structural images of the subsurface but in conjunction with additional information they can also be used for various lithological purposes, e. g., the detection of overpressure zones.

In this thesis, a method for the determination of structural velocity models is presented, i. e., models that consist of constant velocity layers separated by smoothly curved interfaces. The data required for this task is provided by the common-reflection-surface (CRS) stack method in terms of kinematic wavefield attributes and traveltimes of primary reflection events. Mathematically, the wavefield attributes represent first and second order derivatives of the traveltimes of the reflection events. Physically, they are related to the curvatures and the propagation direction of two hypothetical wavefronts, the normal-incidence-point (NIP) wave and the normal wave. In context with velocity models the NIP wavefront is of special importance. As it stems from a point source on the reflecting interface in depth a velocity model can be found by requiring all the back-propagated NIP wavefronts to focus at zero traveltime. This imaging condition can be used in different inversion techniques for the evaluation of velocity models.

In this thesis, two opposed methods are combined. The NIP wave tomography, which represents a global inversion algorithm, yields smooth velocity models. Such models do not contain detailed structural information but, if consistency with the input data is achieved, provide a smooth macro-velocity model which can be used to calculate the locations of interfaces by means of kinematic ray tracing. In contrast to the tomographic method, a generalised Dix-type or layer-stripping algorithm for models with smoothly curved interfaces iteratively constructs a structural model starting from the measurement surface and ending with the deepest available layer. If a sufficient amount of structural data can be extracted from the measured seismic data these models provide detailed information on the velocity distribution in the subsurface. A drawback of the Dix-type inversion method is the error accumulation which is due to the fact that each layer is constructed under consideration of the previously determined layers. Therefore, a new method is proposed which combines the advantages of both approaches: the velocity model obtained from NIP wave tomography is used to construct the interfaces in depth by ray tracing. This step does not suffer from error accumulation as the interfaces are treated independently and, thus, provides an accurate structural skeleton which has to be filled with layer velocities in a second step. The latter task is achieved by means of the Dix-type inversion algorithm but instead of the iterative determination of velocities and interfaces only the velocities are calculated. As a consequence, error accumulation due to mispositioned interfaces can be avoided. The improvement of this combined inversion compared to the pure Dix-type inversion is shown by means of a synthetic data example.

In practice, several problems arise which are related to the determination and structural extraction

of the input data for the inversion methods. A precise determination of the velocity model requires accurate parameters. Due to the extremely high computational cost of the CRS stack, this prerequisite is difficult to achieve. Therefore, emphasis is also placed on an effective and accurate implementation of the CRS stack. This includes the determination of the wavefield attributes as well as the treatment of search aperture dependent effects, i. e., the spread-length bias. Furthermore, a technique for the automatic extraction of continuous reflection events from CRS stacked volumes is presented. The algorithm provides the input data required for Dix-type inversion (and also NIP wave tomography) without further human interaction.

The complete workflow, as described in this thesis, is finally applied to a real 3D land dataset. Although the results could not be verified quantitatively due to the lack of a prestack depth migration, the application shows the feasibility of the proposed method.

Zusammenfassung

Vorbemerkung: Die vorliegende Dissertation ist bis auf diese Zusammenfassung in englischer Sprache geschrieben. Da auch in der deutschen Sprache einige englische Fachausdrücke gebräuchlich sind, wurde bei diesen Ausdrücken auf eine Übersetzung verzichtet. Sie werden, mit Ausnahme ihrer groß geschriebenen Abkürzungen, *kursiv* dargestellt.

Einführung

Eine häufig angewandte Methode zur Untersuchung geologischer Strukturen des Erduntergrundes ist die Reflexionsseismik. Hierbei wird der Erde durch künstliche Quellen Energie zugeführt, die in Form elastischer oder akustischer Wellen propagiert. An Diskontinuitäten der elastischen Parameter des Mediums werden diese Wellen gebrochen, gestreut oder reflektiert. Das an der Erdoberfläche als Partikelauslenkung registrierte Wellenfeld wird in Form einer Zeitreihe aufgezeichnet und kann daher genutzt werden, um Rückschlüsse auf den Aufbau des Untergrundes zu ziehen. In dieser Arbeit werden die seismischen Daten eingesetzt, um ein Modell der Ausbreitungsgeschwindigkeiten der seismischen Wellen im Untergrund zu bestimmen. Dazu wird eine Modellbeschreibung zugrunde gelegt, in der beliebig gekrümmte Reflektoren Schichten konstanter Geschwindigkeit trennen. Das erhaltene Modell liefert sowohl strukturelle als auch, in Verbindung mit zusätzlichen Daten, lithologische Informationen über das Medium.

Von besonderer Bedeutung für die vorgestellte Methode ist die Mehrfachüberdeckung der seismischen Daten. Durch eine ganze Reihe sich überlappenden seismischer Einzelexperimente werden die Strukturen des Untergrundes für jeweils verschiedene Quell- und Empfängerpositionen abgebildet. Diese Datenredundanz wird im Verlauf der Auswertung genutzt um sogenannte kinematische Wellenfeldattribute zu bestimmen, die in die Berechnung des Geschwindigkeitsmodells einfließen.

Strahlentheorie

Die hier vorgestellte Methode zur Bestimmung von Geschwindigkeitsmodellen macht ausführlichen Gebrauch von der seismischen Strahlentheorie, die zur Beschreibung hochfrequenter seismischer Wellen in inhomogenen isotropen Medien dient. Im Zusammenhang mit dieser Arbeit ist die Eikonalgleichung, welche sich über eine Hochfrequenzapproximation der Wellengleichung gewinnen lässt, von besonderer Bedeutung. Diese Gleichung beschreibt die Kinematik der Wellenausbreitung und wird über die Methode der Charakteristiken gelöst. Physikalisch können die Charakteristiken als Strahlen interpretiert werden, weswegen das zugehörige Gleichungssystem auch *ray tracing* System genannt

wird. Eng verwandt mit dem *ray tracing* System ist das paraxiale *ray tracing* System, welches Strahlen in der Umgebung eines Referenzstrahls approximiert indem die Wellengeschwindigkeit über eine Reihenentwicklung zweiter Ordnung genähert wird. Das formal mit dem paraxialen *ray tracing* System identische dynamische *ray tracing* System erlaubt es schließlich, Laufzeitapproximationen bis zur zweiten Ordnung für beliebige Wellentypen in der Umgebung des Referenzstrahls zu berechnen. Weiterhin lässt sich aufgrund der Linearität der paraxialen und dynamischen *ray tracing* Systeme eine allgemeine Lösung über die Propagator- bzw. Fundamentalmatrix berechnen.

Die common-reflection-surface Stapelung

Die Laufzeitapproximation, die das dynamische *ray tracing* System liefert, wird benutzt, um Reflexionsereignisse in den aufgezeichneten Daten lokal zu nähern und zu stapeln. Dadurch werden drei Ziele erreicht: durch die Summation beim Stapeln wird das Signal-zu-Rauschen Verhältnis verbessert, eine Messgeometrie mit koinzidenten Quell- und Empfängerpositionen wird simuliert, und die automatisch bestimmten Parameter der Laufzeitapproximation liefern zusätzliche, integrale Informationen über die Strukturen im Untergrund.

In dieser Arbeit wird die *common-reflection-surface* (CRS) Technik zur Stapelung der Daten benutzt. Die acht Parameter der zugehörigen Laufzeitapproximation werden als kinematische Wellenfeldattribute interpretiert, also als Krümmung und Propagationsrichtung zweier verschiedener Wellenfronten an der Messoberfläche. Besonders interessant ist hierbei die sogenannte NIP-Welle, die mit einem hypothetischen Experiment assoziiert wird, bei dem eine Wellenfront, welche von einer Punktquelle im Reflexionspunkt des Referenzstrahls ausgeht, betrachtet wird. Daher werden in einem Geschwindigkeitsmodell, das konsistent mit den Daten ist, die rückpropagierten NIP-Wellen nach der dazugehörigen Laufzeit im Tiefenpunkt fokussieren. Diese *imaging condition* stellt die Grundlage für die zwei benutzten Methoden zur Geschwindigkeitsinversion dar. Der zweite Wellentyp, die sogenannte Normal-Welle, liefert Informationen über die lokale Struktur eines Reflektors und wird genutzt, um die primären Reflexionsereignisse und die zugehörigen Wellenfeldattribute strukturell aus den gestapelten Daten zu extrahieren.

Im Hinblick auf die Geschwindigkeitsinversion ist es nötig, dass die Wellenfeldattribute mit großer Genauigkeit bestimmt werden. Insbesondere für den hier behandelten Fall von 3D akquirierten Daten stellt dies aufgrund der großen Datenmenge ein Problem dar. Weiterhin sind die ermittelten Wellenfeldattribute und Laufzeiten durch aperturabhängige Effekte (*spread-length bias*) verfälscht. Daher wird sowohl eine schnelle und effiziente Implementierung der CRS Stapelung vorgestellt als auch ein Ansatz zur Behandlung des *spread-length bias*. Da letztere Methode sehr rechenintensiv ist, wird sie in der vorliegenden Arbeit allerdings nur zur Behandlung 2D akquirierter Daten diskutiert.

Geschwindigkeitsinversion

Die hier vorgestellte Methode zur Bestimmung struktureller Geschwindigkeitsmodelle besteht aus einer Kombination zweier Ansätze, die auf verschiedenen Modellbeschreibungen basieren: der generalisierten Dix-Inversion und der NIP-Wellen Tomographie. Die Dix-Inversion liefert ein strukturelles Geschwindigkeitsmodell, leidet jedoch unter der Fehlerakkumulierung und dem Auftreten systematischer Fehler, die durch das iteratives Erstellen des Geschwindigkeitsmodells bedingt sind.

Die Schichtgeschwindigkeiten und die dazugehörigen gekrümmten Grenzflächen werden, von der Meso­berfläche beginnend, Schritt für Schritt für größere Tiefen berechnet. Dabei werden jeweils die Ergebnisse der darüber liegenden Schichten benötigt, d. h., dortige Fehler setzen sich in die folgenden Schichten fort. Im Gegensatz zur Dix-Inversion liefert die NIP-Wellen Tomographie ein glattes Geschwindigkeitsmodell, welches über B-Splines parametrisiert ist. Dieses Modell enthält zwar keine strukturellen Informationen in Form von Schichtgrenzen, zeigt dafür aber auch keine systematische Fehlerfortpflanzung.

In der Kombination beider Methoden werden die Ergebnisse der NIP-Wellen Tomographie dazu verwendet, die Lage der Schichtgrenzen in der Tiefe mittels *ray tracings* zu bestimmen. Die Bestimmung der zugehörigen Schichtgeschwindigkeiten geschieht mittels der generalisierten Dix-Inversion. Da diese jetzt allerdings nicht mehr zur Bestimmung der Schichtgrenzen herangezogen wird, betrifft die Fehlerfortpflanzung nur noch die Geschwindigkeiten, und auch diese ist signifikant reduziert. Wie anhand eines synthetischen Datenbeispiels gezeigt wird, liefert diese kombinierte Inversion tatsächlich bessere Ergebnisse als eine alleinige Dix-Inversion.

Anwendung an einem Realdatensatz

Die vorgestellte Methodik wurde an einem Realdatensatz getestet, der im Rahmen des Projektes *High-resolution images of subsurface CO₂ storage sites in time and depth by the CRS methodology (CO₂CRS)* (Trappe et al., 2005) zur Verfügung stand. Im Detail betraf dies die Anwendung der Software zur CRS Stapelung, die strukturelle Extraktion von primären Reflexionsereignissen und die Anwendung der kombinierten Inversion. Eine quantitative Überprüfung der Ergebnisse ist nur mittels einer *prestack* Tiefenmigration möglich, welche im Rahmen dieser Arbeit jedoch nicht durchführbar war. Dennoch bestätigen die Resultate qualitativ das erwartete Verhalten, unter anderem eine Zunahme der Fehler im Geschwindigkeitsmodell mit der Tiefe und eine nahezu horizontale Schichtung der Reflektoren. Weiterhin wurde damit die Anwendbarkeit der Methode auf Realdaten demonstriert.

Schlussfolgerungen

In dieser Arbeit wurde eine Methode vorgestellt, die es ermöglicht, strukturelle Geschwindigkeitsmodelle des Erduntergrundes zu erstellen. Die Methode basiert auf den kinematischen Wellenfeldattributen der CRS Stapelung und wird als eine Kombination zweier gegensätzlicher Ansätze ausgeführt. Eine NIP-Wellen Tomographie erzeugt zunächst ein glattes Geschwindigkeitsmodell. Mittels *ray tracings* in diesem Modell werden Schichtgrenzen erstellt, die anschließend in einer Dix-Inversion zur Berechnung der konstanten Schichtgeschwindigkeiten eingehen. Die Verbesserungen, die mit dieser Kombination erreicht werden, wurden an einem synthetischen Datenbeispiel gezeigt, ein Realdatenbeispiel demonstrierte schließlich die generelle Anwendbarkeit.

Zukünftige Forschungen sollten eine Erweiterung auf inhomogene Schichtgeschwindigkeiten beinhalten, sowie eine Basis für eine lokal beschränkte Durchführung von Geschwindigkeitsinversionen schaffen. Weiterhin ist es notwendig, die Extraktion der benötigten primären Reflexionsereignissen zu vereinfachen, z. B. durch automatische Unterdrückung von multiplen Reflexionen.

Contents

Abstract	i
Zusammenfassung	iii
1 Introduction	1
1.1 Reflection seismics	1
1.2 Data acquisition	1
1.3 Seismic data processing	2
1.4 Determination of velocity models from kinematic wavefield attributes	6
1.5 Outline of the thesis	7
1.6 Notation	8
2 Ray theory	9
2.1 From the elastodynamic wave equation to the eikonal equation	9
2.2 The ray tracing system as solution of the eikonal equation	12
2.3 Paraxial and dynamic ray tracing	13
2.4 Paraxial traveltimes	18
2.5 Ray tracing in media with structural interfaces	19
2.6 The two-point eikonal	25
2.7 Wavefront curvatures	27
3 The common-reflection-surface stack	29
3.1 Midpoint and half-offset coordinates	30
3.2 The surface-to-surface two-point eikonal in midpoint and half-offset coordinates	30
3.3 The surface-to-surface two-point eikonal for normal rays	31
3.4 The common-reflection-surface stacking operator	32
3.5 Implementation of the CRS stack method	37
3.6 Further aspects	46

4	Spread-length bias	47
4.1	Spread-length bias	47
4.2	Correction of the spread-length bias	52
4.3	Implementation of the CRS stack for the treatment of the spread-length bias	55
4.4	Synthetic data example	56
4.5	Further aspects	60
5	Automatic picking of reflection events	65
5.1	Event tracking in ZO volumes with the CRS operator	65
5.2	Navigation in ZO volumes	67
5.3	Automatic picking of a reflection event in real data	68
5.4	Further aspects	69
6	NIP wave tomography	73
6.1	Formulation of the tomographic inverse problem	73
6.2	The inversion algorithm	77
7	Dix-type inversion	79
7.1	Ray tracing in layered media	79
7.2	Dix-type inversion with kinematic wavefield attributes	84
7.3	Synthetic data example	88
7.4	Combined Dix-type inversion	89
7.5	Further aspects	91
8	Application to real data	93
8.1	Prestack data	93
8.2	3D CRS processing	94
8.3	Automatic picking of reflection events	96
8.4	NIP wave tomography	105
8.5	Combined Dix-type inversion	107
9	Summary and outlook	115
A	Coordinate transformations	117

B Properties of ray propagator matrices	121
C The interface curvature matrix	123
List of Figures	125
List of Tables	129
References	131
Danksagung	137
Lebenslauf	139

Chapter 1

Introduction

In this thesis techniques for the determination of layered velocity models of the subsurface by means of kinematic wavefield attributes are presented. Besides the discussion of the inversion methods this also includes a description of the techniques for the preparation and extraction of the required wavefield attributes from the 3D common-reflection-surface (CRS) stack.

The present chapter gives a brief introduction in the subject of reflection seismics and seismic imaging and motivates the use of kinematic wavefield attributes for the purpose of travelt ime inversion.

1.1 Reflection seismics

A widely used method for the collection of information on the Earth's interior is the seismic reflection experiment. For this purpose, elastic energy is generated by artificial sources and emanated into the subsurface. This energy propagation is described in term of elastic or acoustic waves and is affected (e. g., reflected, diffracted, or refracted) by discontinuities of the elastic properties in the medium. Thus, by recording the wavefield with receivers on the Earth's surface or in boreholes information about the subsurface properties can be deduced. In the recorded data, spatially continuous events are recognised as wavefronts. They are kinematically described by means of their travelt ime and emergence location. In reflection seismics, basically so-called primary reflection events (i.e., recorded wavefronts which are reflected only once at inhomogeneities) are utilised for this objective. Depending on the type of the source the area of investigation may have a length scale from a few tens up to hundred thousands of meters.

Although not being restricted to a specific purpose, reflection seismic is mainly used in the oil and gas industry for the exploration of hydrocarbon reservoirs. The reason for this is that resolution and penetration depth covers the range required to detect the geological structures associated with oil and gas reservoirs.

1.2 Data acquisition

Seismic data acquisition can be carried out both on land and on sea and with different source and receiver configurations. In the following, only surface seismic is considered, i. e., sources and receivers

are deployed on the Earth's surface. For land data, the seismic sources are usually explosives, vibrators, or drop weights. The corresponding receivers (geophones) measure one to three components of the particle motion (or a derivative) as a function of the time since excitation of the source (traveltime t). For marine acquisition airguns are commonly used as sources and the receivers (hydrophones) measure the variation of the water pressure as a function of the traveltime. For seismic processing the recorded data is digitised and stored in traces, i. e., in form of discrete time series containing the recorded signal for a specific source-receiver combination. In general, seismic data can be acquired in 2D or 3D surveys. If sources and receivers are deployed along an almost straight line on the measurement surface a 2D dataset is acquired. Such a dataset is characterised by one-dimensional shot and receiver coordinates (s, g) . Thus the data forms a 3D volume $D = (s, g, t)$. Processing schemes that make use of this data assume that the elastic properties of the subsurface do not vary laterally in the direction perpendicular to the acquisition line. Obviously, this assumption may lead to misleading results when not fulfilled. In contrast to 2D surveys, 3D surveys allow arbitrary source-receiver locations on the measurement surface. As a consequence, the source and receiver locations are described by the vectors $\mathbf{s} = (s_x, s_y)$ and $\mathbf{g} = (g_x, g_y)$. Thus, a 3D data acquisition yields a 5D hypervolume $D = (s_x, s_y, g_x, g_y, t)$. The processing of such an amount of data requires significantly more computational power than for a 2D acquired dataset. However, in many cases the processing of 3D data yields better results compared to a 2D survey (see, e. g., [Biondi, 2003](#)) and, therefore, replaces them more and more.

The geometry of the shot and receiver locations plays an important role in 2D and 3D survey design as it defines the spatial resolution and the area that can be investigated (see, e. g. [Vermeer, 2001](#)). Common to most survey designs is that the wavefield generated by the activation of one source is recorded at a multitude of receivers. The ensemble of many of these so-called common-shot (CS) gathers (in 2D acquisition) or volumes (in 3D acquisition) forms a multi-coverage dataset which introduces an inherent redundancy as the same depth point is illuminated by different sources. This redundancy of particular interest in the context of seismic data processing as it is required for the determination of additional medium parameters in many steps of the processing scheme.

1.3 Seismic data processing

Raw seismic data provides information about the subsurface which suffers from several distorting effects as well as from low signal-to-noise (S/N) ratio and unwanted signals (e. g., from multiple reflections). Seismic data processing aims at increasing the S/N ratio and at removing the distortions and unwanted signals, thus providing a structural image of the subsurface. For this purpose redundant information (usually from primary reflection events) has to be identified and transformed into additional parameters describing the kinematic aspects (i. e., traveltimes and locations) of the recorded data. In addition, the consideration of dynamic aspects (i. e., the amplitudes) allows to extract further elastic properties of the subsurface.

The complete processing sequence for seismic data consists of numerous steps. This include preprocessing based on signal theory as well as the actual seismic imaging. In the following, I will give a brief review of the basic preprocessing and imaging methods. A complete and detailed treatment can, e. g., be found in [Yilmaz \(1987\)](#).

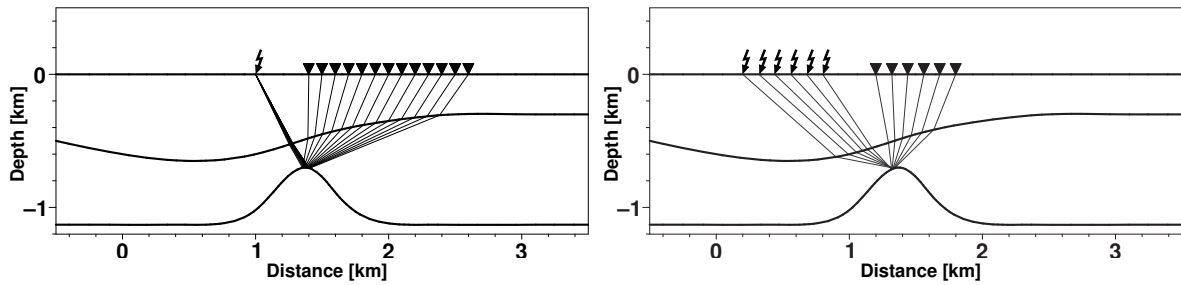


Figure 1.1: 2D sketch of data geometries. Left: after acquisition seismic data is available in the common-shot configuration with source-receiver coordinates. Right: the transformation to midpoint-offset coordinates and the sorting into CMP volumes highlights the redundancy of the data as the reflection points almost coincide (figures taken from Höcht, 2002).

1.3.1 Preprocessing

Preprocessing preconditions the data for further use. It starts with the conversion of the field data to a format which contains the individual traces. Afterwards, corrupt traces are edited and the field geometry is assigned to the data. A gain recovery function may be used to compensate for geometrical spreading and attenuation losses during the wave propagation. For land data, elevation statics are applied to refer the data to a common datum level. Band-pass filters remove noise outside the expected frequency range and frequency-wavenumber filters allow to handle coherent linear noise. The next step in preprocessing is the deconvolution of the data which increases the temporal resolution. In order to bring all traces to a common root-mean-square (RMS) amplitude level trace balancing may be applied afterwards.

After this initial signal processing, the data are usually transformed from source-receiver to midpoint-offset ($\mathbf{m} = (\mathbf{g} + \mathbf{s})/2$, $\mathbf{h} = (\mathbf{g} - \mathbf{s})/2$) coordinates and sorted into common-midpoint (CMP) volumes (see Figure 1.1). This process retains the dimensionality of the data but transforms it from the original hypervolume $D_{CS} = (\mathbf{s}, \mathbf{g}, t)$ to the new hypervolume $D_{CMP} = (\mathbf{m}, \mathbf{h}, t)$. In these data hypervolume the CMP volumes are defined as the subsets $V_{CMP} = (\mathbf{m} = \text{const}, \mathbf{h}, t)$.

1.3.2 Velocity analysis and stacking

If a horizontally layered medium contains only small lateral velocity variations (quasi 1D medium), the depth point for a specific reflection can be considered the same for all traces in a CMP volume (Mayne, 1962). In that case, the kinematic behaviour of a reflection event can be well approximated by a hyperboloid centred at zero-offset (ZO) $\mathbf{h} = \mathbf{0}$, i. e., in the CMP volume the traveltimes of the recorded signal (so-called moveout) increases hyperbolically with increasing absolute offset $|\mathbf{h}|$. Of course, the exact behaviour of the traveltime curve depends on the velocity distribution in the medium. As a consequence, the knowledge of the parameters describing the hyperboloid provide information about the velocities in depth. The task of velocity analysis is to determine this parameter. The outcome of the velocity analysis are so-called stacking or normal moveout (NMO) velocities (v_{stack} or v_{NMO} , respectively) which represent effective velocities of the overburden¹.

¹Often, v_{stack} and v_{NMO} are considered to coincide. However, v_{NMO} is related to a small-spread approximation of the traveltime (and thus to the effective velocity) whereas v_{stack} is given by the hyperboloid that best fits the reflection event over

In the considered case of a quasi 1D medium v_{NMO} equals the weighted average velocity v_{RMS} of the medium above the depth point. For other models, however, v_{RMS} is not strictly defined. Thus, v_{NMO} can no longer be related to the true subsurface velocities. Furthermore, it may even vary with azimuth. Also, additional stacking parameters, e. g., the apparent dip of the reflection events, might be necessary to describe the traveltime curve properly. Methods which utilise such multi-parameter traveltime approximations are, for instance, polystack (de Bazelaire, 1988; Thore et al., 1994), homeomorphic imaging (Gelchinsky, 1989), multifocusing (Gelchinsky et al., 1999; Landa et al., 1999), the common-reflection-point (CRP) stack (Höcht et al., 1997; Perroud et al., 1997), and the common-reflection-surface (CRS) stack (Müller, 1999; Bergler, 2004) which will be discussed in detail in this thesis. Although the determination of these parameters is, strictly speaking, not done by a velocity analysis I will maintain this terminology for the sake of simplicity.

After velocity analysis, the knowledge of the stacking parameters for the different reflection events allows to perform a moveout correction, i. e., the kinematic effect of the source-receiver offset is removed. This process virtually flattens the reflection events and aligns them with the ZO traveltime t_0 which describes the traveltime of the reflection event for coincident source and receiver positions. Summing this data along the offset axis and assigning the result to the midpoint of the corresponding CMP (the ZO location) provides one stacked trace for each CMP volume. If velocity analysis, moveout correction, and stack are applied to the complete set of CMP volumes in the prestack data, a simulated ZO volume $V_{\text{ZO}} = (\mathbf{m}, \mathbf{h} = 0, t)$ is obtained. Such ZO volumes are to a large extent equivalent to the volumes which are generated by an exploding reflector experiment (Loewenthal et al., 1976) with half the medium velocity. The exploding reflector experiment assumes the reflectors to be densely covered with point sources that are all excited at the same time. The emanating wavefield is recorded at the ZO locations on the measurement surface and, thus, provides a first impression of the structures in the medium. Furthermore, the simulated ZO volume has an S/N ratio which is increased by a factor of $\sqrt{N_{\text{st}}}$ (where N_{st} is the number of traces contributing to the stack) compared to the prestack traces (under the assumption that the noise is uncorrelated). Also, stacking significantly reduces the size of the data.

1.3.3 Velocity model building and depth migration

Although stacked data provides a first image of the subsurface, the reflections do not yet allow a precise interpretation of the geological structures: velocity variations in the subsurface distort the shape of reflections and diffraction points and triplications introduce additional complexity. Furthermore, the recorded data may show to unwanted reflection events due to, e. g., multiple reflections. The process that deals with these complications is called migration. It undoes the effects of the wavefield propagation, i. e., it collapses the diffractions to scattering points, unfolds the triplications and maps the reflection events to their proper subsurface position thus providing a structural image of the medium. Migration can be performed on the stacked or on the full prestack data and is referred to as poststack and prestack migration, respectively.

Common to all the different migration methods is the use of the wave equation to propagate or map the wavefield back into the subsurface and the application of an imaging condition to obtain the proper depth image. This task can be implemented using various techniques which basically differ in the treatment of the wave equation. For example, Kirchhoff migration uses an integral solution of

all the offsets in the CMP volume. Due to this dependence on the field geometry, v_{stack} does, in general, not represent the effective velocity of the overburden.

the wave equation which is based on integrations along the diffraction operators of the depth points (e. g., [Schneider, 1978](#)). Downward continuation methods can be either formulated in the space-time domain using finite-difference solutions of the wave equation ([Claerbout, 1985](#)) or in the frequency-wavenumber (f-k) domain ([Stolt, 1978](#); [Gazdag, 1978](#)). However, a common property of all migration methods is that a model of the wave propagation velocities in the medium is required. The parameterisation of the model may vary from smooth models (in general described by means of splines) over gridded models up to models consisting of layers with constant velocity. Each of these model descriptions is especially advantageous in particular situations. For instance, smooth models show a lack of detail but are well suited for Kirchhoff migration (see, e. g., [Versteeg, 1993](#)). In contrast, layered or gridded velocity models are used to extract precise local information, for example for the detection of anomal velocities which may indicate anomalous pressure.

The velocity model is initially unknown and can be obtained by a variety of methods which can be roughly divided into two classes: migration velocity analysis and travelt ime inversion.

Migration velocity analysis

Migration velocity analysis methods make use of the results of the migration process to iteratively determine the velocity model. If the velocity model is consistent with the data, a prestack migration yields a seismic image which is kinematically independent of the used offset. The consistency can be checked in common-image-gathers (CIGs), i. e., gathers containing the offset dependent migration result for a fixed lateral location: models consistent with the data reflect the independence of the offset by showing flat reflection events in the CIGs. In turn, residual moveout on the reflection events indicates inconsistency with the data. Techniques for velocity model updating by residual moveout analysis in CIGs can, amongst others, be found in [Al-Yahya \(1989\)](#) and [Lafond and Levander \(1993\)](#). The drawback of these methods is the computational cost of the repeated applications of prestack depth migration which are required for the iterative updating schemes.

Travelt ime inversion

The second class of techniques for velocity model estimation, travelt ime inversion, does not require migration methods and is usually performed after stacking velocity analysis. These methods determine velocity models which are consistent with the travelt imes and stacking parameters from selected reflection events. The velocity model is obtained iteratively either by updating an initial model or by applying layer-stripping algorithms which construct the model step by step from top to bottom.

First techniques for travelt ime inversion based on a minimisation of the travelt ime misfit between forward modelled and input data have been published by [Gjoystdal and Ursin \(1981\)](#). Tomographic methods using smooth or gridded velocity models are, amongst others, described in [Bishop et al. \(1985\)](#); [Farra and Madariaga \(1988\)](#); [Williamson \(1990\)](#). These methods minimise the misfit by iteratively updating the velocity model as well as the reflector depths by solving linearised systems of equations. Extension of the tomographic methods include additional information in order to stabilise the inversion process. For example, stereotomography ([Billette and Lambaré, 1998](#)) incorporates the local time dip (slope) at the sources and receivers along with the travelt ime from locally coherent reflection events in the prestack data into the update.

Travelt ime inversion based on the layer-stripping inversion technique iteratively determines the velocity model layer by layer. This means that for the construction of the n -th layer the previous $n - 1$

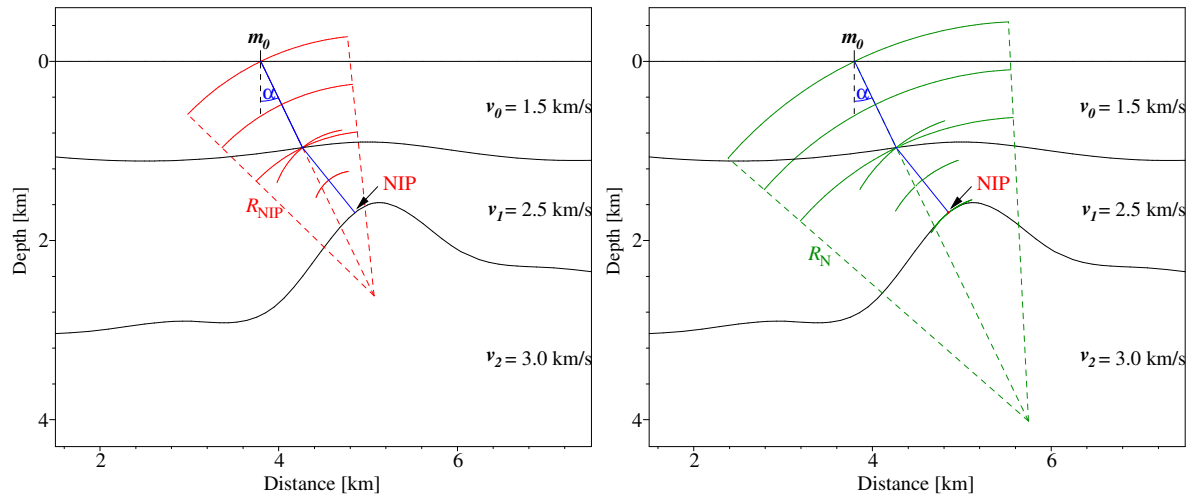


Figure 1.2: 2D sketch illustrating the kinematic wavefield attributes. Left: the NIP wave stems from a point source in the NIP associated with the CMP. Right: the normal wave originates from an exploding reflector experiment and contains information on the local structure of the reflector (figure modified after Mann, 2002).

layers have to be determined first. A layer-stripping algorithm for models consisting of plane horizontal layers was first published by Dix (1955). In addition to the ZO traveltimes of the reflection events this method also requires the stacking parameter v_{RMS} for the determination of the models. Referring to Dix work, layer-stripping is also known as Dix-type inversion. Extensions to this method which overcome the inherent 1D assumption and take plane dipping layers into account are given by Everett (1974) and Kesmarky (1977). A further generalisation to layers separated by curved reflectors is given in Hubral and Krey (1980). Note, however, that most extensions to horizontally layered models require, besides the stacking velocity, additional stacking parameters. These parameters are, in general, obtained by generalised stacking velocity analyses.

1.4 Determination of velocity models from kinematic wavefield attributes

Due to the simplifying assumptions of conventional stacking velocity analysis, the determination of velocity models by traveltime inversion is likely to fail for laterally inhomogeneous media. Multi-parameter traveltime approximations overcome this limitation by providing complete sets of stacking parameters which yield additional information. Most of these approximations are based on second-order traveltime series and have been proven to be useful in media with moderate lateral inhomogeneity. However, it should be noted that in case of strong velocity variations the validity of these approximations is limited.

In the scope of this thesis, the CRS stack technique is used to extract stacking parameters from the prestack data. These so-called kinematic wavefield attributes describe propagation direction and curvatures of two hypothetical wavefronts at the ZO emergence locations \mathbf{m}_0 (see Figure 1.2): the normal-incidence-point (NIP) wave stems from a point source on the reflector at the NIP associated with the

given CMP and the normal (N) wave is related to the exploding reflector experiment. These, in the case of 3D processing eight, parameters are automatically determined by a generalised velocity analysis for each sample of the ZO volume to be simulated.

Traveltime inversion based on the kinematic wavefield attributes of the CRS stack makes use of the fact that the back-propagated NIP wave focuses at traveltime $t = 0$ on the reflector. Thus, a consistent velocity model is found when this condition is fulfilled for each picked set of the quantities traveltime, wavefield attributes, and ZO emergence location. The inversion algorithms can either be based on a tomographic approach (the so-called NIP wave tomography, see [Duvencek, 2004](#)) or on different variants of layer-based inversion methods. Besides the treatment of more complex models the advantages and disadvantages of these methods remain the same as for conventional inversions.

In this thesis, I present a method and an implementation for the determination of layered velocity models with kinematic wavefield attributes. Prior to inversion, the attributes have to be prepared. This leads to an implementation of the CRS stack which is no longer focused on the determination of optimum simulated ZO volumes but on the determination of high-quality wavefield attributes. Using these results an automatic structural picking of reflection events is performed to obtain the input data required for inversion. The Dix-type inversion scheme is combined with the results of NIP wave tomography and is formulated in an iterative layer-stripping manner (following [Hubral and Krey, 1980](#)) for constant velocity layers separated by smoothly curved interfaces.

1.5 Outline of the thesis

This thesis is organised as follows:

A short introduction to seismic reflection imaging as well as a motivation for CRS-based Dix-type inversion is given in this chapter.

In **Chapter 2**, the basics of seismic ray theory required for the further understanding are presented. Here, the kinematic properties of wave propagation in isotropic media is considered.

Chapter 3 introduces the 3D CRS stack and presents several aspects of its implementation. Emphasis is placed on the fast and accurate determination of the stacking parameters of the CRS stack, the so-called kinematic wavefield attributes.

Chapter 4 deals with the spread-length bias inherent to traveltime approximations which have to be applied within finite search apertures. A strategy for the correction of the spread-length bias for the 2D CRS stack is presented here. An extension to 3D is possible but not recommended as the computational cost is too high.

The structural velocity inversion described in the following chapters requires the extraction of continuous reflection events from the CRS stacked volumes. This task is addressed in **Chapter 5** and an algorithm for automated tracking of reflection events based on the kinematic wavefield attributes is presented.

The method for the determination of the layered velocity models requires results that are obtained from NIP wave tomography. This technique is reviewed in **Chapter 6**.

In **Chapter 7**, the CRS-based Dix-type inversion algorithm as well as its combination with NIP wave tomography is discussed. A synthetic data example demonstrates that the proposed combination of the techniques indeed provides better results than a pure Dix-type inversion.

In the scope of the project *High-resolution images of subsurface CO₂ storage sites in time and depth by the CRS methodology (CO₂CRS)* (Trappe et al., 2005), the presented algorithm was applied to a real 3D land dataset. The results of this application are presented in **Chapter 8**. They demonstrate the feasibility of the approach.

Finally, **Chapter 9** contains the summary of this thesis and a short outlook to future research.

A number of additional topics, namely coordinate transformations, properties of the ray propagator matrices, and the calculation of the interface curvature matrix are discussed in the **Appendices A-C**.

1.6 Notation

In this paragraph the notation used throughout the thesis is shortly summarised:

- Scalars are typed as normal letters, e. g., a .
- Vectors with 2 components are described by bold small letters, e. g., \mathbf{a} .
- 2×2 matrices are denoted by bold capital letters, e. g., \mathbf{A} .
- Vectors with three components and 3×3 matrices are underlined.
- Vectors with four components and 4×4 matrices are underlined twice.
- Indices for vectors and matrices start at 1, e. g., $\mathbf{a} = (a_1, a_2, a_3)^T$.
- The superscripts (x) , (r) , (y) , and (z) are appended to quantities that either refer to the global Cartesian, ray-centred, local ray-centred Cartesian or the Cartesian interface coordinate systems, respectively.
- Basis vectors are denoted by $\underline{\mathbf{e}}_1$, $\underline{\mathbf{e}}_2$, and $\underline{\mathbf{e}}_3$. An additional superscript denotes the coordinate system they refer to.
- $\underline{\nabla}$ denotes the Nabla operators with respect to the coordinate system given by an additional superscript. The derivatives are taken with respect to the coordinates or the slowness vector if indicated by the subscript p . For instance, $\underline{\nabla}_p^{(x)} = \left(\frac{\partial}{\partial p_1^{(x)}}, \frac{\partial}{\partial p_2^{(x)}}, \frac{\partial}{\partial p_3^{(x)}} \right)^T$.
- In addition, the Einstein summation convention is used.

Chapter 2

Ray theory

Methods for the qualitative treatment of wave propagation generally assume that the earth behaves like a linear elastic continuum. This allows to describe the propagation of seismic body waves using the elastodynamic wave equation which is provided by classical continuum mechanics. Unfortunately, analytical solutions to this equation for laterally varying media are not known. Thus, the investigation of the propagation processes is done by supplementary methods, e. g., by numerical methods such as finite-difference schemes or by using approximate high-frequency asymptotic solutions.

This thesis focuses on the high-frequency asymptotic methods, namely the ray method. This theory introduces the concept of rays as characteristics of the eikonal equation. The traveltimes of waves, i. e., the time required to propagate along these trajectories, is obtained by an additional integration along the rays. The corresponding ray tracing system can further be extended to the paraxial ray tracing system which approximately describes rays in the close vicinity of a known central ray. This system takes the same form as the dynamic ray tracing system which is used to calculate the partial derivatives of the characteristics with respect to the initial parameters of the system. The quantities obtained from the latter two systems are, amongst others, required for the estimation of paraxial traveltimes, geometrical spreading factors, or kinematic wavefield attributes.

In this chapter, an introduction to the ray method for isotropic media will be given. Special attention will be paid to the methods for ray tracing in smooth and layered media as they are of particular interest for the inversion techniques. Due to their use in the CRS stack, the relationship between the kinematic wavefield attributes and the quantities involved in dynamic ray tracing will also be highlighted. However, the complexity of the topic allows to give an introduction to selected aspects, only. A detailed description of the ray method and other related techniques can, for instance, be found in [Kravtsov and Orlov \(1990\)](#); [Červený \(2001\)](#); [Chapman \(2004\)](#). The considerations made in this chapter basically follow the lines of [Červený \(2001\)](#).

2.1 From the elastodynamic wave equation to the eikonal equation

The assumption of a linear elastic continuum leads to the elastodynamic wave equation (e. g., [Aki and Richards, 1980](#)). This equation describes the propagation of body waves in an unbounded, anisotropic, inhomogeneous, and perfectly elastic medium. In absence of body forces it reads

$$\left(C_{ijkl} u_k^{[l]}\right)^{[j]} = \rho \ddot{u}_i, \quad i, j, k, l = 1, 2, 3, \quad (2.1)$$

with $\underline{\mathbf{u}}(\underline{\mathbf{x}}, t)$ being the particle displacement vector which depends on position ($\underline{\mathbf{x}}$) and time dependent (t). Here, the notation $u_i^{[j]}$ denotes the partial derivative $\partial u_i / \partial x_j$ and the dots denote time derivatives, e. g., $\ddot{u}_i = \partial^2 u_i / \partial t^2$. The quantities $\rho(\underline{\mathbf{x}})$ and $C_{ijkl}(\underline{\mathbf{x}})$ constitute the density and the elastic tensor with its 21 independent parameters, respectively.

In the case of an isotropic medium the elastic tensor C_{ijkl} can be simplified and expressed in terms of two independent parameters. These so-called Lamé's elastic moduli λ and μ are related to C_{ijkl} by

$$C_{ijkl} = \lambda \delta_{ij} \delta_{kl} + \mu (\delta_{ik} \delta_{jl} + \delta_{il} \delta_{jk}), \quad i, j, k, l = 1, 2, 3. \quad (2.2)$$

Inserting this relation into equation (2.1) yields the elastodynamic wave equation for an isotropic medium. In vector notation it reads

$$(\lambda + \mu) \nabla \nabla \cdot \underline{\mathbf{u}} + \mu \nabla^2 \underline{\mathbf{u}} + \nabla \lambda \nabla \cdot \underline{\mathbf{u}} + \nabla \mu \times \nabla \times \underline{\mathbf{u}} + 2(\nabla \mu \cdot \nabla) \underline{\mathbf{u}} = \rho \ddot{\underline{\mathbf{u}}}. \quad (2.3)$$

For homogeneous unbounded media equation (2.3) can be solved analytically and yields two independently propagating plane waves: a compressional (P) and a shear (S) wave. Also, the transmission and reflection of the waves at plane interfaces between two homogeneous media can be described analytically. For inhomogeneous media the solution of the wave equation is considerably more complex and the wavefield can, in general, no longer be separated into several independent waves. The solution to this problem is the consideration of high-frequency wave propagation. This assumption leads to waves which satisfy the elastodynamic equation approximately and separates the wavefield into P and S waves. The properties of these high-frequency P and S waves propagating in smoothly inhomogeneous media are locally similar to the properties of the P and S waves propagating in homogeneous media. Also, the interaction of high-frequency waves with smooth structural interfaces can be formulated similar to the behaviour of plane waves at a plane interface. However, assuming high-frequency wave propagation only provides an approximate solutions to propagation, transmission, and reflection. Furthermore, the condition that the frequency of the propagating waves should be high is not precisely defined. In seismic literature basically qualitative explanations are given. A common statement is that the prevailing wavelength of the wave must be significantly smaller than the length scale of the variations of the medium's parameters. A more detailed treatment of the validity conditions can be found in [Ben-Menachem and Beydoun \(1985\)](#).

The most common approach to the theoretical description of high-frequency wave propagation is the ray method. Its solution to the elastodynamic wave equation is based on the so-called ray-series which is a series in terms of high-frequency analytical signals:

$$\underline{\mathbf{u}} = \sum_{n=0}^{\infty} \underline{\mathbf{a}}_n F_n(t - T). \quad (2.4)$$

Here, t denotes the travelttime and the amplitude function $\underline{\mathbf{a}}_n(\underline{\mathbf{x}})$ and the eikonal $T(\underline{\mathbf{x}})$ are arbitrary but slowly varying functions of the position $\underline{\mathbf{x}}$. $F_n(t - T)$ represent high-frequency analytical signals, i. e., their Fourier spectrum is assumed to effectively vanish for low frequencies. The latter results in the relationship $|\ddot{F}_n(t)| \gg |\dot{F}_n(t)| \gg |F_n(t)|$.

In practice, often the leading term of the ray series (2.4) is used only, thus leading to the so-called zero-order ray method. The general ansatz for the displacement vector $\underline{\mathbf{u}}$ then reads

$$\underline{\mathbf{u}} = \underline{\mathbf{a}} F(t - T). \quad (2.5)$$

Note, that in order to simplify the following expressions $\underline{\mathbf{a}} = \underline{\mathbf{a}}_0$ and $F(t - T) = F_0(t - T)$ are used.

Inserting ansatz (2.5) into the elastodynamic equation (2.3) yields

$$\underline{\mathbf{n}}\ddot{F} - \underline{\mathbf{m}}\dot{F} + \underline{\mathbf{l}}F = 0, \quad (2.6)$$

with

$$n_i = -\rho a_i + (\lambda + \mu)a_j T^{[i]} T^{[j]} + \mu a_i T^{[j]} T^{[j]}, \quad (2.7)$$

$$m_i = (\lambda + \mu) \left[a_j^{[i]} T^{[j]} + a_j^{[j]} T^{[j]} + a_j T^{[ij]} \right] + \mu \left[2a_i^{[j]} T^{[j]} + a_i T^{[ij]} \right] \\ + \lambda^{[i]} a_j T^{[j]} + \mu^{[j]} \left[a_i T^{[j]} + a_j T^{[i]} \right], \quad (2.8)$$

$$l_i = (\lambda + \mu) a_j^{[ij]} + \mu a_i^{[jj]} + \lambda^{[i]} a_j^{[j]} + \mu^{[j]} (a_i^{[j]} + a_j^{[i]}), \quad i, j = 1, 2, 3. \quad (2.9)$$

For high frequencies the first two terms in equation (2.6) are expected to dominate and the third term for $\underline{\mathbf{l}}$ may thus be neglected. Also, in order to solve equation (2.6) approximately $\underline{\mathbf{n}}$ and $\underline{\mathbf{m}}$ have to vanish independently:

$$\underline{\mathbf{n}} = 0, \quad (2.10)$$

$$\underline{\mathbf{m}} = 0. \quad (2.11)$$

In order to solve equation (2.10) it is altered to read

$$(\Gamma_{ij} - \delta_{ij})a_j = 0, \quad i, j = 1, 2, 3, \quad (2.12)$$

with

$$\Gamma_{ij} = \frac{\lambda + \mu}{\rho} T^{[i]} T^{[j]} + \frac{\mu}{\rho} \delta_{ij} T^{[k]} T^{[k]}. \quad (2.13)$$

Equation (2.12) represents an eigenvalue problem with two independent non-trivial solutions which constitute the so-called eikonal equations

$$(\underline{\nabla}T)^2 = \frac{\rho}{\lambda + 2\mu} = \frac{1}{v_P^2}, \quad (2.14)$$

$$(\underline{\nabla}T)^2 = \frac{\rho}{\mu} = \frac{1}{v_S^2}. \quad (2.15)$$

These equations describe the traveltime fields of high-frequency P and S waves propagating through media with smoothly varying P and S wave velocities $v_P(\underline{\mathbf{x}})$ and $v_S(\underline{\mathbf{x}})$, respectively. The surfaces of constant T are interpreted as wavefronts. Defining the slowness vector $\underline{\mathbf{p}}^{(x)} = \underline{\nabla}T$ which is perpendicular to the wavefront and v being either v_P or v_S , equations (2.14) and (2.15) may also be written as

$$\underline{\mathbf{p}}^{(x)2} = \frac{1}{v^2}. \quad (2.16)$$

Note that $\underline{\mathbf{p}}^{(x)}$ denotes the slowness vector in the general Cartesian coordinate system.

The amplitudes $\underline{\mathbf{a}}$ of the waves can be obtained from equation (2.11) which constitutes the so-called transport equations for the P and S waves. However, as amplitudes are not required in the scope of this thesis the formal solution to equation (2.11) will not be presented here.

2.2 The ray tracing system as solution of the eikonal equation

The eikonal equation (2.16) represents a first-order nonlinear partial differential equation which can be solved by the method of characteristics (e. g., Herzberger, 1958; Bleistein, 1984).

For that purpose, the eikonal equation (2.16) is transformed into a Hamilton-Jacobi equation

$$\mathcal{H}(\underline{\mathbf{x}}, \underline{\mathbf{p}}^{(x)}) = 0, \quad (2.17)$$

which can be replaced by the so-called characteristic system

$$\frac{d\underline{\mathbf{x}}}{dl} = \underline{\nabla}_{\underline{\mathbf{p}}} \mathcal{H} \quad , \quad \frac{d\underline{\mathbf{p}}^{(x)}}{dl} = -\underline{\nabla}_{\underline{\mathbf{x}}} \mathcal{H}, \quad (2.18)$$

$$\frac{dT}{dl} = \underline{\mathbf{p}}^{(x)} \cdot \underline{\nabla}_{\underline{\mathbf{p}}} \mathcal{H}. \quad (2.19)$$

Here, the variable l denotes an monotonously increasing parameter along the ray which depends on the specific form of the Hamiltonian \mathcal{H} . Equations (2.18) define a system of ordinary differential equations of the first order which satisfy condition (2.17). The solution to these equations are the characteristics $\underline{\mathbf{x}}(l)$ and $\underline{\mathbf{p}}^{(x)}(l)$. In the particular case of the eikonal equation, the trajectories of $\underline{\mathbf{x}}$ describe rays. Therefore, the characteristic system (2.18) is also called ray tracing system. Equation (2.19) for the traveltime along the ray is not coupled to the system (2.18). For that reason it can be solved by an additional integration as soon as the characteristics are known.

The Hamiltonian \mathcal{H} can be defined in several ways. An appropriate choice for it is

$$\mathcal{H} = |\underline{\mathbf{p}}^{(x)}| - 1/v = 0. \quad (2.20)$$

Inserting this definition into the characteristic system (2.18) leads to the system of six coupled equations

$$\frac{d\underline{\mathbf{x}}}{ds} = v \underline{\mathbf{p}}^{(x)}, \quad (2.21)$$

$$\frac{d\underline{\mathbf{p}}^{(x)}}{ds} = \underline{\nabla} \frac{1}{v}. \quad (2.22)$$

Here, the quantity l in equations (2.18) represents the arclength s . According to equation (2.21) the rays are tangent to the slowness vector $\underline{\mathbf{p}}^{(x)}$ in isotropic inhomogeneous media. Thus, the rays are orthogonal trajectories to the wavefronts.

After the calculation of the ray trajectory the traveltime $T(s)$ along the ray is finally given by the additional path integration from starting point S to end point G (according to equation (2.19)):

$$T = \int_S^G \frac{1}{v} ds. \quad (2.23)$$

In order to determine the entire traveltime field the ray tracing system (2.21) and (2.22) and traveltime equation (2.23) must be solved for all possible rays.

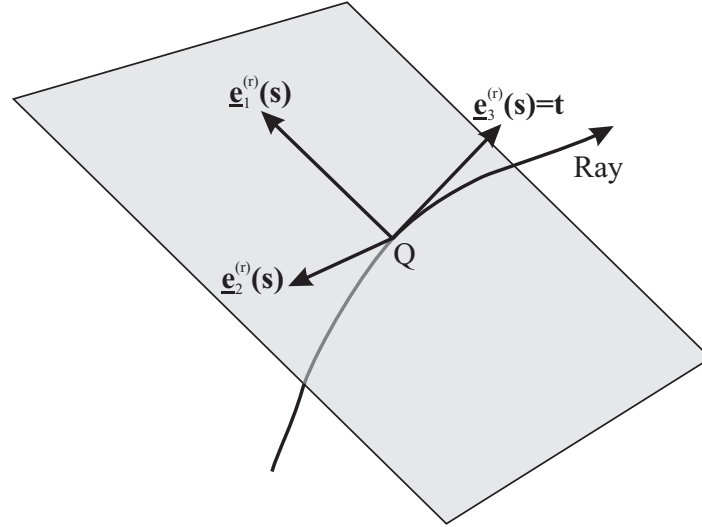


Figure 2.1: Definition of the ray-centred coordinate system. At point Q on the ray the three mutually orthogonal and right-handed basis vectors $\underline{\mathbf{e}}_1^{(r)}(s)$, $\underline{\mathbf{e}}_2^{(r)}(s)$, and $\underline{\mathbf{e}}_3^{(r)}(s)$ are defined such that $\underline{\mathbf{e}}_1^{(r)}(s)$ and $\underline{\mathbf{e}}_2^{(r)}(s)$ fall into the plane normal to the ray and $\underline{\mathbf{e}}_3^{(r)}(s)$ is tangent to the ray.

2.3 Paraxial and dynamic ray tracing

Many applications require the determination of rays in the close vicinity of a given central ray. An approximation to these so-called paraxial rays, the paraxial ray tracing system, can be derived from the ray tracing system (2.21) and (2.22). Closely related to the paraxial ray tracing system is the dynamic ray tracing system which allows to determine the partial derivatives of the characteristics with respect to the initial parameters of the system along the ray. The dynamic ray tracing system is especially interesting as its propagator matrix can be used to easily compute traveltime fields in the vicinity of the central ray. Also, curvatures of wavefronts (see, e. g., Hubral, 1979, 1980) and geometrical spreading factors (see, e. g., Popov and Pšenčík, 1978) can be evaluated with little effort.

Although not explicitly required, the dynamic ray tracing system will be formulated in ray-centred coordinates as this yields the simplest version of the ray tracing system.

2.3.1 Ray-centred coordinates

The ray-centred coordinate system ($q_1, q_2, q_3 = s$) is a curvilinear orthogonal coordinate system established along a known (central) ray, i. e., the ray itself is one of the coordinate axes and the origin for q_1 and q_2 . Following this definition a point Q on the ray has the coordinates $(0, 0, s)$. The three corresponding mutually orthogonal and right-handed basis vectors of the ray-centred coordinate system are given by $\underline{\mathbf{e}}_1^{(r)}(s)$, $\underline{\mathbf{e}}_2^{(r)}(s)$, and $\underline{\mathbf{e}}_3^{(r)} = \underline{\mathbf{t}}^{(x)}(s)$ where $\underline{\mathbf{t}}^{(x)}(s)$ is the unit vector tangent to the ray ($\underline{\mathbf{t}}^{(x)}(s) = v(s)\underline{\mathbf{p}}^{(x)}(s)$). The unit vectors $\underline{\mathbf{e}}_1^{(r)}(s)$ and $\underline{\mathbf{e}}_2^{(r)}(s)$ fall into the plane normal to the ray at Q (see Figure 2.1). The orientation of $\underline{\mathbf{e}}_1^{(r)}(s)$ and $\underline{\mathbf{e}}_2^{(r)}(s)$ along the ray can be obtained by the system of

ordinary differential equations

$$\frac{d\mathbf{e}_i^{(r)}}{ds} = (\mathbf{e}_i^{(r)} \cdot \nabla v) \underline{\mathbf{p}}^{(x)}, \quad i = 1, 2. \quad (2.24)$$

Note that ray-centred coordinates are only suitable to describe points in the vicinity of the central ray. A unique representation is only obtained as long as there exists only one plane perpendicular to the central ray containing a specific point. As a consequence the region of validity for ray-centred coordinates depends on the curvature of the central ray.

For the transformation of vectorial equations from global Cartesian coordinates into ray-centred coordinates the scale factors h_1 , h_2 , and h_3 of the ray-centred coordinate system are required. They are obtained from equation (2.24) and read

$$h_1 = h_2 = 1, \quad h_3 = h, \quad (2.25)$$

where

$$h = 1 + \left[\frac{1}{v} \left(q_1 \frac{\partial v}{\partial q_1} \Big|_{(q_1=0, q_2=0)} + q_2 \frac{\partial v}{\partial q_2} \Big|_{(q_1=0, q_2=0)} \right) \right]. \quad (2.26)$$

Using the scale factors (2.25), the Nabla operator $\underline{\nabla}^{(r)}$ for ray-centred coordinates is given by the relation

$$\underline{\nabla}^{(r)} = \left(\frac{\partial}{\partial q_1}, \frac{\partial}{\partial q_2}, \frac{\partial}{h \partial q_3} \right)^T. \quad (2.27)$$

At a point Q on the ray, the ray-centred coordinate system coincides with a local Cartesian coordinate system $\underline{\mathbf{y}}$ with origin Q and basis vectors $\underline{\mathbf{e}}_1^{(y)} = \underline{\mathbf{e}}_1^{(r)}(s)$, $\underline{\mathbf{e}}_2^{(y)} = \underline{\mathbf{e}}_2^{(r)}(s)$, and $\underline{\mathbf{e}}_3^{(y)} = \underline{\mathbf{e}}_3^{(r)}(s)$. Thus, for points on the ray, the transformation from the ray-centred coordinate system (or equivalently from the local Cartesian ray-centred coordinate system $\underline{\mathbf{y}}$) to the global Cartesian coordinate system is given by the relationship

$$d\underline{\mathbf{x}} = \underline{\mathbf{H}} d\underline{\mathbf{q}} \quad \text{or} \quad d\underline{\mathbf{x}} = \underline{\mathbf{H}} d\underline{\mathbf{y}}, \quad (2.28)$$

where $\underline{\mathbf{H}}$ is the orthonormal transformation matrix on the ray with elements $\underline{\mathbf{H}} = (\underline{\mathbf{e}}_1^{(y)}, \underline{\mathbf{e}}_2^{(y)}, \underline{\mathbf{e}}_3^{(y)})$. Alternatively, $\underline{\mathbf{H}}$ can be expressed in terms of orthogonal rotation matrices (see Appendix A). Note that for points off the ray the transformation matrix is not that simple.

As the ray-centred coordinate $q_3 = s$ is measured along the ray and the local Cartesian ray-centred coordinate y_3 along the tangent to the ray at Q it is furthermore necessary that

$$ds = h^{-1} dy_3. \quad (2.29)$$

Finally, note that the slowness vector at Q is given by

$$\underline{\mathbf{p}}^{(r)} = \underline{\mathbf{p}}^{(y)} = \begin{pmatrix} 0 \\ 0 \\ 1/v \end{pmatrix}, \quad (2.30)$$

as $\underline{\mathbf{e}}_3^{(r)}$ and $\underline{\mathbf{e}}_3^{(y)}$ are tangent to the ray.

2.3.2 The ray tracing system in ray-centred coordinates

Using the Nabla operator (2.27) for ray-centred coordinates and considering the relation $\underline{\mathbf{p}}^{(r)} = \underline{\nabla}^{(r)}T$, the eikonal equation (2.16) can be transformed into ray-centred coordinates:

$$p_1^{(r)2} + p_2^{(r)2} + \frac{1}{h^2}p_3^{(r)2} = \frac{1}{v^2}. \quad (2.31)$$

The corresponding Hamiltonian may be written as

$$\begin{aligned} \mathcal{H}^{(r)}(\underline{\mathbf{q}}, \underline{\mathbf{p}}^{(r)}) &= p_3^{(r)} - h \sqrt{\frac{1}{v^2} - \mathbf{p}^{(r)2}} \\ &= p_3^{(r)} + \mathcal{H}_R^{(r)}(\underline{\mathbf{q}}, \underline{\mathbf{p}}^{(r)}), \end{aligned} \quad (2.32)$$

where $\mathcal{H}_R^{(r)}$ denotes the so-called reduced Hamiltonian.

Inserting Hamiltonian (2.32) into the characteristic system (2.18) yields

$$\frac{dq_1}{dl} = -\frac{h^2 p_1^{(r)}}{\mathcal{H}_R^{(r)}}, \quad \frac{dp_1^{(r)}}{dl} = -\frac{h^2}{\mathcal{H}_R^{(r)}} \left[\frac{1}{2} \frac{\partial}{\partial q_1} \left(\frac{1}{v} \right) - \frac{1}{h^3} \mathcal{H}^{(r)2} \frac{\partial h}{\partial q_1} \right], \quad (2.33)$$

$$\frac{dq_2}{dl} = -\frac{h^2 p_2^{(r)}}{\mathcal{H}_R^{(r)}}, \quad \frac{dp_2^{(r)}}{dl} = -\frac{h^2}{\mathcal{H}_R^{(r)}} \left[\frac{1}{2} \frac{\partial}{\partial q_2} \left(\frac{1}{v} \right) - \frac{1}{h^3} \mathcal{H}^{(r)2} \frac{\partial h}{\partial q_2} \right], \quad (2.34)$$

$$\frac{dq_3}{dl} = 1, \quad \frac{dp_3^{(r)}}{dl} = -\frac{\partial \mathcal{H}_R^{(r)}}{\partial q_3}. \quad (2.35)$$

In view of equations (2.35) and $q_3 = s$ it can be concluded that $l = s$. Thus, the ray tracing system in ray-centred coordinates consists of only four equations and may be written as

$$\frac{d\mathbf{q}}{ds} = -\frac{h^2}{\mathcal{H}_R^{(r)}} \mathbf{p}^{(r)}, \quad \frac{d\mathbf{p}^{(r)}}{ds} = -\frac{h^2}{2\mathcal{H}_R^{(r)}} \nabla^{(r)} v^{-1} + \frac{\mathcal{H}_R^{(r)}}{h} \nabla^{(r)} h. \quad (2.36)$$

Note that the ray-centred coordinate system of ray tracing system (2.36) is connected to a given central ray Ω . Thus, ray tracing in ray-centred coordinates allows to compute rays in the vicinity of Ω .

2.3.3 The paraxial ray tracing system

So far, the ray tracing system (2.36) has no distinct advantage over the standard ray tracing system (2.21) and (2.22). In order to simplify the ray tracing system (2.36) the medium velocity v is approximated by a Taylor expansion up to second order in q_1 and q_2 :

$$v = v_s + \mathbf{q}^T \nabla^{(r)} v_s + \frac{1}{2} \mathbf{q}^T \mathbf{V} \mathbf{q}, \quad (2.37)$$

with $v_s = v(0, 0, s)$ and $V_{ij} = \partial^2 v_s / \partial q_1 \partial q_2 |_{q_1=0, q_2=0}$.

Using equation (2.37), the approximate expression of Hamiltonian $\mathcal{H}^{(r)}$ in the paraxial vicinity of a central ray Ω reads

$$\mathcal{H}^{(r)} = p_3^{(r)} - \frac{1}{v_s} \left[1 - \frac{1}{2v_s} \mathbf{q}^T \mathbf{V} \mathbf{q} - \frac{v_s^2}{2} \mathbf{p}^{(r)2} \right]. \quad (2.38)$$

This Hamiltonian yields the paraxial ray tracing system in ray-centred coordinates

$$\frac{d\mathbf{q}}{ds} = v_s \mathbf{p}^{(r)}, \quad \frac{d\mathbf{p}^{(r)}}{ds} = -\frac{1}{v_s^2} \mathbf{V} \mathbf{q}^{(r)}. \quad (2.39)$$

Introducing the 4×1 column matrix $\underline{\underline{\mathbf{w}}}_p$ and the 4×4 system matrix $\underline{\underline{\mathbf{S}}}$

$$\underline{\underline{\mathbf{w}}}_p = \begin{pmatrix} \mathbf{q} \\ \mathbf{p}^{(r)} \end{pmatrix}, \quad (2.40)$$

$$\underline{\underline{\mathbf{S}}} = \begin{pmatrix} \mathbf{0} & v_s \mathbf{I} \\ -\frac{1}{v_s^2} \mathbf{V} & \mathbf{0} \end{pmatrix}, \quad (2.41)$$

finally allows to express the paraxial ray tracing system (2.39) in the more compact form

$$\frac{d}{ds} \underline{\underline{\mathbf{w}}}_p = \underline{\underline{\mathbf{S}}} \underline{\underline{\mathbf{w}}}_p. \quad (2.42)$$

The linear paraxial ray tracing system (2.42) can be used to trace rays in the paraxial vicinity of a central ray Ω . Its range of validity depends on how well the Hamiltonian (2.38) is approximated around this ray. Basically, this region is controlled by the degree of inhomogeneity in the velocity distribution near Ω .

2.3.4 The dynamic ray tracing system

Whole systems of rays corresponding to a specified wave may be parameterised by the so-called ray parameter γ . Dynamic ray tracing aims at determining the partial derivatives of the characteristics with respect to the ray parameter of the central ray. Taking this derivatives for ray tracing system (2.39) yields

$$\frac{d}{ds} \left(\frac{\partial \mathbf{q}}{\partial \gamma_j} \right) = v_s \frac{\partial \mathbf{p}^{(r)}}{\partial \gamma_j}, \quad \frac{d}{ds} \left(\frac{\partial \mathbf{p}^{(r)}}{\partial \gamma_j} \right) = -\frac{1}{v_s^2} \mathbf{V} \frac{\partial \mathbf{q}^{(r)}}{\partial \gamma_j}, \quad j = 1, 2. \quad (2.43)$$

Defining the matrices \mathbf{Q} and $\mathbf{P}^{(r)}$ with

$$Q_{ij} = \left. \frac{\partial q_i}{\partial \gamma_j} \right|_{q_1=0, q_2=0}, \quad P_{ij}^{(r)} = \left. \frac{\partial p_i^{(r)}}{\partial \gamma_j} \right|_{q_1=0, q_2=0}, \quad i, j = 1, 2, \quad (2.44)$$

allows to express the dynamic ray tracing system (2.43) in compact matrix notation

$$\frac{d}{ds} \underline{\underline{\mathbf{w}}}_d = \underline{\underline{\mathbf{S}}} \underline{\underline{\mathbf{w}}}_d. \quad (2.45)$$

Here, $\underline{\underline{\mathbf{S}}}$ is given by equation (2.41) and $\underline{\underline{\mathbf{w}}}_d$ denotes the 4×2 matrix

$$\underline{\underline{\mathbf{w}}}_d = \begin{pmatrix} \mathbf{Q} \\ \mathbf{P}^{(r)} \end{pmatrix}. \quad (2.46)$$

Note that the paraxial and the dynamic ray tracing systems (2.42) and (2.45) have identical form. They only differ in the quantities that are calculated.

Using matrices \mathbf{Q} and $\mathbf{P}^{(r)}$ another useful quantity, the symmetric matrix $\mathbf{M}^{(r)}$ of second derivatives of the travelttime field with respect to \mathbf{q} , can be introduced as

$$M_{ij}^{(r)} = \left. \frac{\partial^2 T}{\partial q_i \partial q_j} \right|_{q_1=0, q_2=0} = \frac{\partial^2 T}{\partial q_i \partial \gamma_k} \frac{\partial \gamma_k}{\partial q_j} = \frac{\partial p_i^{(r)}}{\partial \gamma_k} \frac{\partial \gamma_k}{\partial q_j} = P_{ij}^{(r)} Q_{ij}^{-1}, \quad i, j, k = 1, 2. \quad (2.47)$$

In matrix notation this reads

$$\mathbf{M}^{(r)} = \mathbf{P}^{(r)} \mathbf{Q}^{-1}. \quad (2.48)$$

2.3.5 The ray propagator matrix

The ray tracing systems (2.42) and (2.45) consist of linear ordinary differential equations of first order. Thus, their general solution may be written in terms of a fundamental matrix $\underline{\underline{\mathbf{\Pi}}}^{(r)}$. This matrix, which is also called ray propagator matrix, solves the system

$$\frac{d}{ds} \underline{\underline{\mathbf{\Pi}}}^{(r)} = \underline{\underline{\mathbf{S}}} \underline{\underline{\mathbf{\Pi}}}^{(r)} \quad (2.49)$$

for the initial condition $\underline{\underline{\mathbf{\Pi}}}^{(r)}(s_0, s_0) = \underline{\underline{\mathbf{I}}}$.

Once the propagator matrix $\underline{\underline{\mathbf{\Pi}}}^{(r)}(R, S)$ for a ray $\Omega(R, S)$ from S to R is known, the solution $\underline{\underline{\mathbf{w}}}(R)$ to an arbitrary initial condition $\underline{\underline{\mathbf{w}}}(S)$ can be obtained from the continuation relation

$$\underline{\underline{\mathbf{w}}}(R) = \underline{\underline{\mathbf{\Pi}}}^{(r)}(R, S) \underline{\underline{\mathbf{w}}}(S). \quad (2.50)$$

Here, $\underline{\underline{\mathbf{w}}}(S)$ and $\underline{\underline{\mathbf{w}}}(R)$ can either be given by $\underline{\underline{\mathbf{w}}}_p$ or $\underline{\underline{\mathbf{w}}}_d$.

Usually, the propagator matrix $\underline{\underline{\mathbf{\Pi}}}^{(r)}(R, S)$ is expressed in terms of four 2×2 submatrices

$$\underline{\underline{\mathbf{\Pi}}}^{(r)}(R, S) = \begin{pmatrix} \mathbf{Q}_1(R, S) & \mathbf{Q}_2(R, S) \\ \mathbf{P}_1^{(r)}(R, S) & \mathbf{P}_2^{(r)}(R, S) \end{pmatrix}. \quad (2.51)$$

These submatrices $\mathbf{Q}_1(R, S)$, $\mathbf{Q}_2(R, S)$, $\mathbf{P}_1^{(r)}(R, S)$, and $\mathbf{P}_2^{(r)}(R, S)$ may be assigned a simple physical meaning: $\mathbf{Q}_1(R, S)$ and $\mathbf{P}_1^{(r)}(R, S)$ are the solution to normalised plane wave and $\mathbf{Q}_2(R, S)$ and $\mathbf{P}_2^{(r)}(R, S)$ to normalised point source initial conditions. A number of useful properties of the propagator matrix $\underline{\underline{\mathbf{\Pi}}}^{(r)}(R, S)$ and its submatrices are discussed in Appendix B.

In view of equations (2.48) and (2.51) the continuation relation (2.50) for matrix $\mathbf{M}^{(r)}$ reads

$$\mathbf{M}^{(r)}(R) = \left(\mathbf{P}_1^{(r)}(R, S) + \mathbf{P}_2^{(r)}(R, S) \mathbf{M}^{(r)}(S) \right) \left(\mathbf{Q}_1(R, S) + \mathbf{Q}_2(R, S) \mathbf{M}^{(r)}(S) \right)^{-1}, \quad (2.52)$$

where $\mathbf{M}^{(r)}(R)$ is the solution to an arbitrary initial condition $\mathbf{M}^{(r)}(S)$.

According to the initial conditions for the submatrices of the ray propagator matrix a point source situated at S is given by $\mathbf{Q}(S) = \mathbf{0}$. Using the notations $\mathbf{Q}(R, S)$ and $\mathbf{P}^{(r)}(R, S)$ in this case, the continuation relation (2.50) then yields

$$\mathbf{Q}(R, S) = \mathbf{Q}_2(R, S) \mathbf{P}^{(r)}(S), \quad \mathbf{P}^{(r)}(R, S) = \mathbf{P}_2^{(r)}(R, S) \mathbf{P}^{(r)}(S). \quad (2.53)$$

For a point source at R , i. e., $\mathbf{Q}(R) = \mathbf{0}$, the corresponding relations read

$$\mathbf{Q}(S, R) = -\mathbf{Q}_2^T(R, S) \mathbf{P}^{(r)}(R) \quad , \quad \mathbf{P}^{(r)}(S, R) = \mathbf{Q}_1^T(R, S) \mathbf{P}^{(r)}(R). \quad (2.54)$$

Combining the two relationships (2.53) and (2.54) with equation (2.48) allows to express matrices $\mathbf{M}^{(r)}(R, S)$ and $\mathbf{M}^{(r)}(S, R)$ for point sources located at S and R , respectively:

$$\mathbf{M}^{(r)}(R, S) = \mathbf{P}_2^{(r)}(R, S) \mathbf{Q}_2^{-1}(R, S) \quad , \quad \mathbf{M}^{(r)}(S, R) = -\mathbf{Q}_2^{-1}(R, S) \mathbf{Q}_1(R, S). \quad (2.55)$$

2.4 Paraxial traveltimes

The traveltimes of rays in the paraxial vicinity of a central ray can either be calculated exactly by standard ray tracing or approximately, e. g., by means of a Taylor expansion. In the following approximate expressions for the paraxial traveltimes will be presented. These expressions are, for instance, required for the determination of stacking operators or two-point eikonals.

Now, a point $R' = (q_1, q_2, s)$ in the close vicinity of a point $R = (0, 0, s_0)$ on the central ray is considered. A Taylor expansion for the paraxial traveltime $T(R')$ up to second-order terms then reads

$$T(R') = T(R) + \frac{s - s_0}{v(R)} - \frac{(s - s_0)^2}{2v^2(R)} \frac{\partial v}{\partial s} \Big|_R + \frac{1}{2} \mathbf{q}^T(R') \mathbf{M}^{(r)}(R) \mathbf{q}(R'). \quad (2.56)$$

Here, it has been used that

$$\frac{\partial T}{\partial s} \Big|_R = \frac{1}{v(R)} \quad , \quad \frac{\partial^2 T}{\partial s^2} \Big|_R = -\frac{1}{v(R)^2} \frac{\partial v}{\partial s} \Big|_R. \quad (2.57)$$

Note that the linear terms in $\mathbf{q}(R')$ are missing in equation (2.56) as the wavefront is perpendicular to the central ray.

A representation of the paraxial traveltimes which is more convenient for the following considerations is obtained by transforming (2.56) into Cartesian coordinates. Here, $\underline{\mathbf{y}}(R', R)$ denotes the coordinate of R' with respect to the local Cartesian ray-centred coordinate system of R . Considering the relation (2.29) the traveltime approximation (2.56) in the local Cartesian ray-centred coordinate system at R is given by

$$T(R') = T(R) + \underline{\mathbf{y}}^T(R', R) \underline{\mathbf{p}}^{(y)}(R) + \frac{1}{2} \underline{\mathbf{y}}^T(R', R) \underline{\mathbf{M}}^{(y)}(R) \underline{\mathbf{y}}(R', R), \quad (2.58)$$

where $\underline{\mathbf{p}}^{(y)}(R) = (0, 0, 1/v(R))^T$ denotes the components of the slowness vector in the local Cartesian ray-centred coordinates. The upper left 2×2 -submatrix of $\underline{\mathbf{M}}^{(y)}(R)$ coincides with matrix $\mathbf{M}^{(r)}(R)$. The full 3×3 matrix is given by additional components which depend on the velocity $v(R)$ and its spatial derivatives at R :

$$\underline{\mathbf{M}}^{(y)}(R) = \begin{pmatrix} M_{11}^{(r)}(R) & M_{12}^{(r)}(R) & -v^{-2}(R) \frac{\partial v}{\partial y_1} \Big|_R \\ M_{12}^{(r)}(R) & M_{22}^{(r)}(R) & -v^{-2}(R) \frac{\partial v}{\partial y_2} \Big|_R \\ -v^{-2}(R) \frac{\partial v}{\partial y_1} \Big|_R & -v^{-2}(R) \frac{\partial v}{\partial y_2} \Big|_R & -v^{-2}(R) \frac{\partial v}{\partial y_3} \Big|_R \end{pmatrix}. \quad (2.59)$$

Equation (2.58) can be transformed from the local ray-centred Cartesian coordinate system to general Cartesian coordinates by considering transformation relation (2.28) and introducing $\underline{\mathbf{x}}(R', R) = \underline{\mathbf{x}}(R') -$

$\underline{\mathbf{x}}(R)$, $\underline{\mathbf{p}}^{(x)} = \underline{\mathbf{H}}(R) \underline{\mathbf{p}}^{(y)}(R)$, and the matrix of second derivatives of the travelttime field with respect to general Cartesian coordinates $\underline{\mathbf{M}}^{(x)}(R) = \underline{\mathbf{H}}(R) \underline{\mathbf{M}}^{(y)}(R) \underline{\mathbf{H}}^T(R)$:

$$T(R') = T(R) + \underline{\mathbf{x}}^T(R', R) \underline{\mathbf{p}}^{(x)}(R) + \frac{1}{2} \underline{\mathbf{x}}^T(R', R) \underline{\mathbf{M}}^{(x)}(R) \underline{\mathbf{x}}(R', R). \quad (2.60)$$

Note that travelttime approximations (2.58) and (2.60) have a local character: they are valid in the close vicinity of point R only. The range of validity depends on the complexity of the underlying model.

2.5 Ray tracing in media with structural interfaces

So far, the ray tracing with the systems (2.21) and (2.22), (2.42), and (2.45) is limited to media which are formed by smooth velocity distributions. However, in the scope of this thesis it is necessary to introduce methods for ray tracing in media containing structural interfaces, i. e., surfaces across which the wave propagation velocities are discontinuous (so-called zero-order discontinuities). These media are constituted by a set of blocks with smoothly varying velocities which are separated by the interfaces. The ray tracing within the blocks is performed by the above mentioned ray tracing systems. The interactions of the rays with the interfaces, i. e., the transmission and reflection of the quantities involved in the ray tracing, are treated separately as boundary value problem by additional formulas which will be presented in this chapter.

For the derivation of these relations a ray is considered which strikes the interfaces at point Q with the incident slowness $\underline{\mathbf{p}}(Q)$. After reflection/transmission this point is denoted as \tilde{Q} . Although points Q and \tilde{Q} coincide due to the continuity of the ray trajectory, this discrimination is required as many quantities may be discontinuous across the interface, e. g., $\underline{\mathbf{p}}^{(x)}(Q) \neq \underline{\mathbf{p}}^{(x)}(\tilde{Q})$ or $\underline{\mathbf{M}}^{(x)}(Q) \neq \underline{\mathbf{M}}^{(x)}(\tilde{Q})$. In terms of medium velocities the notations $v(Q)$ and $v(\tilde{Q})$ with the following meaning are introduced: $v(Q)$ denotes the velocity on the side of the interface where the incident ray is situated. For a reflected ray $v(\tilde{Q})$ represents the corresponding medium velocity on the incident side (in case of unconverted reflected rays $v(\tilde{Q})$ equals $v(Q)$), for a transmitted ray $v(\tilde{Q})$ represents the velocity on the other side of the interface.

2.5.1 Definition of the interfaces

In the following an interface Σ is considered. Both the interface and its first and second derivatives are assumed to be continuous at point Q . The two halfspaces on either side of the interface are assumed to be in welded contact. This means that the displacement and traction components acting across the surface are the same on both sides. According to Červený (2001), these boundary conditions yield the phase matching relations which state that the traveltimes $T(\tilde{Q})$ of the reflected or transmitted waves are equal to the travelttime $T(Q)$ of the incident wave along Σ . In addition, this implies that the tangential derivatives of $T(\tilde{Q})$ and $T(Q)$ at Q and \tilde{Q} are equal (and thus the tangential components of the slownesses).

A point \tilde{Q} in the vicinity of Q the interface is approximated by the second-order series

$$x_3(Q') = \frac{1}{2} \underline{\mathbf{x}}^T(Q', Q) \underline{\mathbf{B}}^{(x)}(Q) \underline{\mathbf{x}}(Q', Q) + \underline{\mathbf{b}}^{(x)T}(Q) \underline{\mathbf{x}}(Q', Q), \quad (2.61)$$

with $\mathbf{x}(Q', Q) = \mathbf{x}(Q') - \mathbf{x}(Q)$, the symmetric curvature matrix $\mathbf{B}^{(x)}(Q)$, and the vector of first derivatives $\mathbf{b}^{(x)}(Q)$:

$$\mathbf{B}^{(x)}(Q) = \begin{pmatrix} \left. \frac{\partial^2 x_3}{\partial x_1^2} \right|_Q & \left. \frac{\partial^2 x_3}{\partial x_1 \partial x_2} \right|_Q \\ \left. \frac{\partial^2 x_3}{\partial x_1 \partial x_2} \right|_Q & \left. \frac{\partial^2 x_3}{\partial x_2^2} \right|_Q \end{pmatrix} \quad (2.62)$$

$$\mathbf{b}^{(x)}(Q) = \begin{pmatrix} \left. \frac{\partial x_3}{\partial x_1} \right|_Q \\ \left. \frac{\partial x_3}{\partial x_2} \right|_Q \end{pmatrix}. \quad (2.63)$$

At point Q a local Cartesian coordinate system $\underline{\mathbf{z}}$ with basis vectors $\underline{\mathbf{e}}_1^{(z)}(Q)$, $\underline{\mathbf{e}}_2^{(z)}(Q)$, and $\underline{\mathbf{e}}_3^{(z)}(Q)$ is introduced. It is specified such that $\underline{\mathbf{e}}_3^{(z)}(Q)$ coincides with the interface normal at Q and points in direction of the incident ray:

$$\underline{\mathbf{e}}_3^{(z)}(Q) = \underline{\mathbf{n}}^{(x)} = \frac{\text{sgn}(p_3^{(x)}(Q))}{\sqrt{b_1^{(x)2}(Q) + b_2^{(x)2}(Q) + 1}} \begin{pmatrix} b_1^{(x)}(Q) \\ b_2^{(x)}(Q) \\ -1 \end{pmatrix} = \frac{\text{sgn}(p_3^{(x)}(Q))}{\|\underline{\mathbf{b}}^{(x)}(Q)\|} \underline{\mathbf{b}}^{(x)}(Q). \quad (2.64)$$

The basis vectors $\underline{\mathbf{e}}_1^{(z)}(Q)$ and $\underline{\mathbf{e}}_2^{(z)}(Q)$ are chosen such that $\underline{\mathbf{e}}_1^{(z)}(Q)$ is situated in the plane of incidence, i. e., the plane that is defined by the rays slowness vector $\underline{\mathbf{p}}^{(x)}(Q)$ and interface normal $\underline{\mathbf{n}}^{(x)}(Q)$. Consequently, $\underline{\mathbf{e}}_2^{(z)}(Q)$ is normal to that plane:

$$\underline{\mathbf{e}}_2^{(z)}(Q) = \frac{\underline{\mathbf{n}}^{(x)}(Q) \times \underline{\mathbf{p}}^{(x)}(Q)}{\|\underline{\mathbf{n}}^{(x)}(Q) \times \underline{\mathbf{p}}^{(x)}(Q)\|}, \quad \underline{\mathbf{e}}_1^{(z)}(Q) = \underline{\mathbf{e}}_2^{(z)}(Q) \times \underline{\mathbf{e}}_3^{(z)}(Q). \quad (2.65)$$

Note that $\underline{\mathbf{e}}_2^{(z)}(Q)$ and $\underline{\mathbf{e}}_1^{(z)}(Q)$ cannot be determined by these formulas if $\underline{\mathbf{n}}^{(x)}(Q)$ is parallel to $\underline{\mathbf{p}}^{(x)}(Q)$. In that case they can be chosen arbitrary but such that they form a local Cartesian coordinate system with $\underline{\mathbf{e}}_3^{(z)}(Q)$. In literature, the definitions (2.64) and (2.65) of the basis vectors are often referred to as standard option.

The transformation from this local Cartesian to the general Cartesian coordinate system is specified by the transformation matrix $\underline{\mathbf{Z}}(Q)$ and the transformation relation

$$d\underline{\mathbf{x}} = \underline{\mathbf{Z}}(Q) d\underline{\mathbf{z}}. \quad (2.66)$$

In addition, matrix $\underline{\mathbf{G}}(Q)$ describes the transformation from ray-centred coordinates to local Cartesian coordinates of the interface at point Q :

$$d\underline{\mathbf{z}} = \underline{\mathbf{G}}(Q) d\underline{\mathbf{q}}. \quad (2.67)$$

Thus, transformation matrix $\underline{\mathbf{H}}(Q)$ which describes the transformation from the ray-centred coordinate system at Q to the general Cartesian coordinate system is written as

$$\underline{\mathbf{H}}(Q) = \underline{\mathbf{Z}}(Q) \underline{\mathbf{G}}(Q). \quad (2.68)$$

As $\underline{\mathbf{e}}_3^{(z)}(Q)$ is parallel to $\underline{\mathbf{b}}^{(x)}(Q)$ it follows that the interface is approximated in the local Cartesian coordinate system of point Q by

$$z_3(Q') = -\frac{1}{2} \mathbf{z}^T(Q') \mathbf{B}^{(z)}(Q) \mathbf{z}(Q'). \quad (2.69)$$

The Matrix $\mathbf{B}^{(z)}(Q)$ is referred to as interface curvature matrix. It is connected to the curvature Matrix $\mathbf{B}^{(x)}(Q)$ by the relation (see Appendix C)

$$\mathbf{B}^{(z)}(Q) = \frac{1}{\mathbf{e}_3^{(z)}(Q) \cdot \underline{\mathbf{b}}^{(x)}(Q)} \mathbf{Z}^T(Q) \mathbf{B}^{(x)}(Q) \mathbf{Z}(Q). \quad (2.70)$$

Here, $\mathbf{Z}(Q)$ is the upper left 2×2 submatrix of $\underline{\mathbf{Z}}(Q)$. This equation is of special practical importance as interfaces are commonly described in general Cartesian coordinates and the transformation formulas for wavefronts require curvature matrices in local Cartesian coordinates.

2.5.2 Rays across the interface

Consider the incident ray at Q with slowness vector $\underline{\mathbf{p}}^{(x)}(Q)$. After transmission/reflection the slowness vector of the corresponding ray is denoted by $\underline{\mathbf{p}}^{(x)}(\tilde{Q})$ and its location by $\tilde{Q} = Q$. As the ray is completely defined by slowness vector and location the problem of ray reflection/transmission is reduced to the determination of $\underline{\mathbf{p}}^{(x)}(\tilde{Q})$.

The derivation of the transmission/reflection formula for $\underline{\mathbf{p}}^{(x)}(\tilde{Q})$ is based on the phase matching relations for the tangential components of the slowness vectors. In order to apply these conditions the incident and transmitted/reflected slowness vectors are decomposed into components that are tangential and normal to the interface:

$$\underline{\mathbf{p}}^{(x)}(Q) = \underline{\mathbf{a}}^{(x)}(Q) + \sigma(Q) \underline{\mathbf{n}}^{(x)}(Q) \quad , \quad \underline{\mathbf{p}}^{(x)}(\tilde{Q}) = \underline{\mathbf{a}}^{(x)}(\tilde{Q}) + \sigma(\tilde{Q}) \underline{\mathbf{n}}^{(x)}(Q). \quad (2.71)$$

Here, $\sigma(Q)$ and $\sigma(\tilde{Q})$ are constants and $\underline{\mathbf{a}}^{(x)}(Q)$ and $\underline{\mathbf{a}}^{(x)}(\tilde{Q})$ are the tangential components of the corresponding slowness vectors. In addition the identity $\underline{\mathbf{n}}^{(x)}(Q) = \underline{\mathbf{n}}^{(x)}(\tilde{Q})$ has been used.

The quantity $\sigma(Q)$ can be expressed as

$$\sigma(Q) = \underline{\mathbf{p}}^{(x)}(Q) \cdot \underline{\mathbf{n}}^{(x)}(Q). \quad (2.72)$$

Using equations (2.71) and (2.72) together with phase matching condition $\underline{\mathbf{a}}^{(x)}(\tilde{Q}) = \underline{\mathbf{a}}^{(x)}(Q)$ the slowness vector $\underline{\mathbf{p}}^{(x)}(\tilde{Q})$ can be written as

$$\underline{\mathbf{p}}^{(x)}(\tilde{Q}) = \underline{\mathbf{p}}^{(x)}(Q) - (\underline{\mathbf{p}}^{(x)}(Q) \cdot \underline{\mathbf{n}}^{(x)}(Q)) \underline{\mathbf{n}}^{(x)}(Q) + \sigma(\tilde{Q}) \underline{\mathbf{n}}^{(x)}(Q). \quad (2.73)$$

For the complete description of the transmitted/reflected slowness vector $\underline{\mathbf{p}}^{(x)}(\tilde{Q})$ the unknown quantity $\sigma(\tilde{Q})$ is determined from equation (2.16) for \tilde{Q}

$$\underline{\mathbf{p}}^{(x)2}(\tilde{Q}) = \frac{1}{v^2(\tilde{Q})}. \quad (2.74)$$

Inserting equation (2.73) into (2.74) yields

$$\sigma(\tilde{Q}) = \pm \sqrt{\frac{1}{v^2(\tilde{Q})} - \frac{1}{v^2(Q)} + (\underline{\mathbf{p}}^{(x)}(Q) \cdot \underline{\mathbf{n}}^{(x)}(Q))^2}. \quad (2.75)$$

Combining equations (2.75) and (2.73), the final relation for the reflection/transmission of a ray at point Q reads

$$\underline{\mathbf{p}}^{(x)}(\tilde{Q}) = \underline{\mathbf{p}}^{(x)}(Q) - \left[\underline{\mathbf{p}}^{(x)}(Q) \cdot \underline{\mathbf{n}}^{(x)}(Q) \pm \sqrt{\frac{1}{v^2(\tilde{Q})} - \frac{1}{v^2(Q)} + (\underline{\mathbf{p}}^{(x)}(Q) \cdot \underline{\mathbf{n}}^{(x)}(Q))^2} \right] \underline{\mathbf{n}}^{(x)}(Q). \quad (2.76)$$

Here, the negative root corresponds to the transmitted and the positive to the reflected ray. In order to apply (2.76) it must be assured that the radicand of the square-root is positive. Otherwise the solution gets imaginary and describes an overcritical reflection.

Note that (2.76) represents a general formulation of Snell's law

$$\frac{\sin \alpha(Q)}{v(Q)} = \frac{\sin \alpha(\tilde{Q})}{v(\tilde{Q})}, \quad (2.77)$$

where $\alpha(Q)$ and $\alpha(\tilde{Q})$ denote the angles between slowness vectors $\underline{\mathbf{p}}^{(x)}(Q)$ or $\underline{\mathbf{p}}^{(x)}(\tilde{Q})$ and the interface normal $\underline{\mathbf{n}}^{(x)}(Q)$, respectively.

After transmission or reflection the new ray-centred coordinate system at \tilde{Q} is not fully specified. Its basis vector $\underline{\mathbf{e}}_3^{(r)}(\tilde{Q})$ is given by the ray itself, $\underline{\mathbf{e}}_1^{(r)}(\tilde{Q})$ and $\underline{\mathbf{e}}_2^{(r)}(\tilde{Q})$ may be chosen arbitrarily but such that the triplet $\underline{\mathbf{e}}_1^{(r)}(\tilde{Q})$, $\underline{\mathbf{e}}_2^{(r)}(\tilde{Q})$, and $\underline{\mathbf{e}}_3^{(r)}(\tilde{Q})$ is mutually orthogonal and right-handed. A convenient choice is the so-called reciprocal choice which requires that the angle between $\underline{\mathbf{e}}_2^{(z)}(Q)$ and $\underline{\mathbf{e}}_2^{(r)}(\tilde{Q})$ is equal to the angle between $\underline{\mathbf{e}}_2^{(z)}(Q)$ and $\underline{\mathbf{e}}_2^{(r)}(Q)$. This implies that $\underline{\mathbf{e}}_1^{(r)}(\tilde{Q})$ and $\underline{\mathbf{e}}_2^{(r)}(\tilde{Q})$ approach $\underline{\mathbf{e}}_1^{(r)}(Q)$ and $\underline{\mathbf{e}}_2^{(r)}(Q)$ for $v(Q) \rightarrow v(\tilde{Q})$, which means that the basis vectors are continuous for the limiting case of a vanishing interface.

According to Červený (2001) the reciprocal choice reads

$$\underline{\mathbf{e}}_2^{(r)}(\tilde{Q}) = \frac{(\underline{\mathbf{e}}_2^{(r)}(Q) \cdot \underline{\mathbf{e}}_2^{(z)}(Q) \times \underline{\mathbf{p}}^{(x)}(Q))(\underline{\mathbf{e}}_2^{(z)}(Q) \times \underline{\mathbf{p}}^{(x)}(\tilde{Q})) + (\underline{\mathbf{e}}_2^{(r)}(Q) \cdot \underline{\mathbf{e}}_2^{(z)}(Q))\underline{\mathbf{e}}_2^{(z)}(Q)}{\left| (\underline{\mathbf{e}}_2^{(r)}(Q) \cdot \underline{\mathbf{e}}_2^{(z)}(Q) \times \underline{\mathbf{p}}^{(x)}(Q))(\underline{\mathbf{e}}_2^{(z)}(Q) \times \underline{\mathbf{p}}^{(x)}(\tilde{Q})) + (\underline{\mathbf{e}}_2^{(r)}(Q) \cdot \underline{\mathbf{e}}_2^{(z)}(Q))\underline{\mathbf{e}}_2^{(z)}(Q) \right|} \quad (2.78)$$

$$\underline{\mathbf{e}}_1^{(r)}(\tilde{Q}) = \frac{\underline{\mathbf{e}}_2^{(r)}(\tilde{Q}) \times \underline{\mathbf{p}}^{(x)}(\tilde{Q})}{\left| \underline{\mathbf{e}}_2^{(r)}(\tilde{Q}) \times \underline{\mathbf{p}}^{(x)}(\tilde{Q}) \right|} \quad (2.79)$$

2.5.3 Matrix $\mathbf{M}^{(r)}(Q)$ across the interface

In order to determine a relation for the transmission/reflection of matrix $\mathbf{M}^{(r)}(Q)$ across the interface Σ the distribution of the traveltimes along Σ in the vicinity of point Q has to be known. Therefore, the traveltimes approximation (2.60) is transformed into the local Cartesian coordinate system of the interface. At point Q' , situated close to Q , this yields

$$T(Q') = T(Q) + \underline{\mathbf{z}}^T(Q') \underline{\mathbf{p}}^{(z)}(Q) + \frac{1}{2} \underline{\mathbf{z}}^T(Q') \underline{\mathbf{Z}}^T(Q) \underline{\mathbf{H}}(Q) \underline{\mathbf{M}}^{(y)}(Q) \underline{\mathbf{H}}^T(Q) \underline{\mathbf{Z}}(Q) \underline{\mathbf{z}}(Q') \quad (2.80)$$

$$= T(Q) + \underline{\mathbf{z}}^T(Q') \underline{\mathbf{p}}^{(z)}(Q) + \frac{1}{2} \underline{\mathbf{z}}^T(Q') \underline{\mathbf{G}}(Q) \underline{\mathbf{M}}^{(y)}(Q) \underline{\mathbf{G}}^T(Q) \underline{\mathbf{z}}(Q'). \quad (2.81)$$

If point Q' is situated on Σ its position is specified as $Q' \equiv [z_1, z_2, z_3 = -\frac{1}{2} \underline{\mathbf{z}}^T \underline{\mathbf{B}}^{(z)}(Q) \underline{\mathbf{z}}]$ (see equation (2.69)). Inserting this condition into equation (2.81) and retaining terms up to second-order only

yields the traveltimes T^Σ along the interface as a function of two variables $\mathbf{z}(Q')$, only:

$$T^\Sigma(Q') = T(Q) + \mathbf{z}^T(Q')\mathbf{p}^{(z)}(Q) + \frac{1}{2}\mathbf{z}^T(Q')\mathbf{F}(Q)\mathbf{z}(Q'), \quad (2.82)$$

with

$$\mathbf{F}(Q) = \mathbf{G}(Q)\mathbf{M}^{(r)}(Q)\mathbf{G}^T(Q) + \mathbf{E}(Q) - p_3^{(z)}(Q)\mathbf{B}^{(z)}(Q), \quad (2.83)$$

$$\begin{aligned} E_{ij}(Q) &= G_{i3}(Q)G_{jm}(Q)M_{3m}^{(y)}(Q) + G_{ik}(Q)G_{j3}(Q)M_{k3}^{(y)}(Q) \\ &\quad + G_{i3}(Q)G_{j3}(Q)M_{33}^{(y)}(Q) \quad , \quad i, j, k, m = 1, 2. \end{aligned} \quad (2.84)$$

In equation (2.83) the identity $\mathbf{M}^{(y)}(Q) = \mathbf{M}^{(r)}(Q)$ has been used (see equation (2.59)). Furthermore, \mathbf{G} denotes the upper left 2×2 -submatrix of $\underline{\mathbf{G}}$.

For the transmitted/reflected waves in the vicinity of point \tilde{Q} similar traveltimes expansions $T^\Sigma(\tilde{Q}')$ to (2.82) can be obtained. Therefore, the relation between incident and transmitted/reflected matrices $\mathbf{M}^{(r)}(Q)$ and $\mathbf{M}^{(r)}(\tilde{Q})$ can be established by applying the phase matching relation $T^\Sigma(Q') = T^\Sigma(\tilde{Q}')$. This yields

$$T(Q) + \mathbf{z}^T(Q')\mathbf{p}^{(z)}(Q) + \frac{1}{2}\mathbf{z}^T(Q')\mathbf{F}(Q)\mathbf{z}(Q') = T(\tilde{Q}) + \mathbf{z}^T(Q')\mathbf{p}^{(z)}(\tilde{Q}) + \frac{1}{2}\mathbf{z}^T(Q')\mathbf{F}(\tilde{Q})\mathbf{z}(Q'), \quad (2.85)$$

and thus

$$T(Q) = T(\tilde{Q}) \quad , \quad \mathbf{p}^{(z)}(Q) = \mathbf{p}^{(z)}(\tilde{Q}) \quad , \quad \mathbf{F}(Q) = \mathbf{F}(\tilde{Q}). \quad (2.86)$$

The main result is given by the relation $\mathbf{F}(Q) = \mathbf{F}(\tilde{Q})$ as it constitutes the transformation of matrix $\mathbf{M}^{(r)}(Q)$ across the interface:

$$\mathbf{M}^{(r)}(\tilde{Q}) = \mathbf{G}^{-1}(\tilde{Q}) \left[\mathbf{G}(Q)\mathbf{M}^{(r)}(Q)\mathbf{G}(Q)^T + \mathbf{E}(Q) - \mathbf{E}(\tilde{Q}) - u\mathbf{B}^{(z)}(Q) \right] \mathbf{G}^{-T}(\tilde{Q}), \quad (2.87)$$

where

$$u = p_3^{(z)}(Q) - p_3^{(z)}(\tilde{Q}) = \frac{G_{33}(Q)}{v(Q)} - \frac{G_{33}(\tilde{Q})}{v(\tilde{Q})}. \quad (2.88)$$

Note that $\mathbf{M}^{(r)}(\tilde{Q})$ is given in the ray-centred coordinates of the transmitted/reflected ray. Thus, the ray-centred coordinate system at \tilde{Q} has to be known. This system can, for instance, be determined by the ray transmission formula (2.76) and the standard option.

The physical interpretation of equation (2.87) is as follows: $\mathbf{G}^{-1}(\tilde{Q})\mathbf{G}(Q)\mathbf{M}^{(r)}(Q)\mathbf{G}(Q)^T\mathbf{G}^{-T}(\tilde{Q})$ describes the transformation of matrix $\mathbf{M}^{(r)}(Q)$ from the ray-centred coordinate system at Q to the respective system at \tilde{Q} , $\mathbf{G}^{-1}(\tilde{Q})[\mathbf{E}(Q) - \mathbf{E}(\tilde{Q})]\mathbf{G}^{-T}(\tilde{Q})$ introduces effects due to inhomogeneities of the medium in the vicinity of Q and \tilde{Q} , and $u\mathbf{G}^{-1}(\tilde{Q})\mathbf{B}^{(z)}(Q)\mathbf{G}^{-T}(\tilde{Q})$ considers the effect of the curvature of the interface at Q .

2.5.4 Matrices $\mathbf{Q}(Q)$ and $\mathbf{P}^{(r)}(Q)$ across the interface

The continuity of rays requires the continuity of the ray parameter γ across the interface. If the continuity of rays is also assumed to be valid for paraxial rays this condition reads

$$\left. \frac{\partial \gamma}{\partial z_j} \right|_Q = \left. \frac{\partial \gamma}{\partial z_j} \right|_{\tilde{Q}} \quad , \quad j = 1, 2. \quad (2.89)$$

This condition, which may be rewritten as

$$\left. \frac{\partial \gamma}{\partial q_k(Q)} \right|_Q \left. \frac{\partial q_k(Q)}{\partial z_j} \right|_Q = \left. \frac{\partial \gamma}{\partial q_k(\tilde{Q})} \right|_{\tilde{Q}} \left. \frac{\partial q_k(\tilde{Q})}{\partial z_j} \right|_{\tilde{Q}}, \quad j, k = 1, 2, \quad (2.90)$$

yields, together with the definition for the transformation matrix \mathbf{G} , the relation for the transmission/reflection of matrix $\mathbf{Q}(Q)$:

$$\mathbf{Q}(\tilde{Q}) = \mathbf{G}^T(\tilde{Q}) \mathbf{G}^{-T}(Q) \mathbf{Q}(Q). \quad (2.91)$$

The expression for the transmission/reflection of matrix $\mathbf{P}^{(r)}(Q)$ can now be obtained from equations (2.48), (2.87), and (2.91):

$$\mathbf{P}^{(r)}(\tilde{Q}) = \mathbf{G}^{-1}(\tilde{Q}) \left[\mathbf{G}(Q) \mathbf{P}^{(r)}(Q) + (\mathbf{E}(Q) - \mathbf{E}(\tilde{Q}) - u \mathbf{B}^{(z)}(Q)) \mathbf{G}^{-T}(Q) \mathbf{Q}(Q) \right]. \quad (2.92)$$

2.5.5 The ray propagator matrix $\underline{\underline{\Pi}}^{(r)}$ across the interface

The last expression required for a complete treatment of ray tracing in layered media is the transformation relation $\underline{\underline{\Pi}}^{(r)}(\tilde{Q}, Q)$ for the ray propagator matrix across interfaces. According to equation (2.50) the continuation relation reads

$$\begin{pmatrix} \mathbf{Q}(\tilde{Q}) \\ \mathbf{P}^{(r)}(\tilde{Q}) \end{pmatrix} = \underline{\underline{\Pi}}^{(r)}(\tilde{Q}, Q) \begin{pmatrix} \mathbf{Q}(Q) \\ \mathbf{P}^{(r)}(Q) \end{pmatrix}. \quad (2.93)$$

A comparison with the transformation equations for $\mathbf{Q}(\tilde{Q})$ and $\mathbf{P}^{(r)}(\tilde{Q})$, (2.91) and (2.92), respectively, reveals that $\underline{\underline{\Pi}}^{(r)}(\tilde{Q}, Q)$ is given by

$$\underline{\underline{\Pi}}^{(r)}(\tilde{Q}, Q) = \begin{pmatrix} \mathbf{G}^T(\tilde{Q}) \mathbf{G}^{-T}(Q) & \mathbf{0} \\ \mathbf{G}^{-1}(\tilde{Q}) (\mathbf{E}(Q) - \mathbf{E}(\tilde{Q}) - u \mathbf{B}^{(z)}(Q)) \mathbf{G}^{-T}(Q) & \mathbf{G}^{-1}(\tilde{Q}) \mathbf{G}(Q) \end{pmatrix}. \quad (2.94)$$

Furthermore, the propagator matrix $\underline{\underline{\Pi}}^{(r)}(\tilde{Q}, Q)$ can be expressed as a product of two matrices

$$\underline{\underline{\Pi}}^{(r)}(\tilde{Q}, Q) = \underline{\underline{\mathbf{Y}}}^{-1}(\tilde{Q}) \underline{\underline{\mathbf{Y}}}(Q), \quad (2.95)$$

where the so-called projection matrix $\underline{\underline{\mathbf{Y}}}(A)$ for an arbitrary point A is given by

$$\underline{\underline{\mathbf{Y}}}(A) = \begin{pmatrix} \mathbf{G}^{-T}(A) & \mathbf{0} \\ (\mathbf{E}(A) - p_3^{(z)}(A) \mathbf{B}^{(z)}(A)) \mathbf{G}^{-T}(A) & \mathbf{G}(A) \end{pmatrix}. \quad (2.96)$$

Matrix $\underline{\underline{\mathbf{Y}}}(A)$ describes the projection of paraxial quantities on the interface Σ . Therefore, it can be used to establish a propagator matrix for a central ray $\Omega(R, S)$ and paraxial rays that emanate from sources that are located on a surface containing point S (the anterior surface) and impinge at receivers located on a surface that contains point R (the posterior surface). This surface-to-surface ray propagator matrix $\underline{\underline{\mathbf{T}}}(R, S)$ is obtained by multiplying $\underline{\underline{\Pi}}^{(r)}(R, S)$ by $\underline{\underline{\mathbf{Y}}}^{-1}(S)$ and $\underline{\underline{\mathbf{Y}}}(R)$ from the right and left, respectively:

$$\begin{aligned} \underline{\underline{\mathbf{T}}}(R, S) &= \underline{\underline{\mathbf{Y}}}(R) \underline{\underline{\Pi}}^{(r)}(R, S) \underline{\underline{\mathbf{Y}}}^{-1}(S) \\ &= \begin{pmatrix} \mathbf{A}(R, S) & \mathbf{B}(R, S) \\ \mathbf{C}(R, S) & \mathbf{D}(R, S) \end{pmatrix}. \end{aligned} \quad (2.97)$$

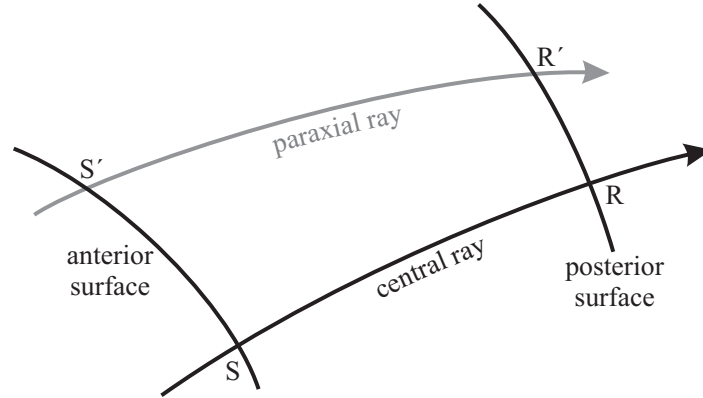


Figure 2.2: The surface-to-surface two-point eikonal allows to calculate traveltimes for paraxial rays that emanate at point S' on the anterior surface and impinge at point R' on the posterior surface.

The propagator matrix $\underline{\underline{\mathbf{T}}}(R, S)$ has the same properties as propagator matrix $\underline{\underline{\mathbf{\Pi}}}^{(r)}(R, S)$. Especially important is the continuation relation

$$\begin{pmatrix} \mathbf{z}(R') \\ \mathbf{p}^{(z)}(R') - \mathbf{p}^{(z)}(R) \end{pmatrix} = \underline{\underline{\mathbf{T}}}(R, S) \begin{pmatrix} \mathbf{z}(S') \\ \mathbf{p}^{(z)}(S') - \mathbf{p}^{(z)}(S) \end{pmatrix}. \quad (2.98)$$

From equation (2.97) the following relations between the submatrices of the propagator matrices can be obtained:

$$\mathbf{D}(R, S) \mathbf{B}^{-1}(R, S) = \mathbf{G}(R) \mathbf{P}_2^{(r)} \mathbf{Q}_2^{-1}(R, S) \mathbf{G}^T(R) + \mathbf{E}(R) - p_3^{(z)}(R) \mathbf{B}^{(z)}(R), \quad (2.99)$$

$$-\mathbf{B}(R, S)^{-1} \mathbf{A}(R, S) = -\mathbf{G}(S) \mathbf{Q}_2^{-1} \mathbf{Q}_1(R, S) \mathbf{G}^T(S) + \mathbf{E}(S) - p_3^{(z)}(R) \mathbf{B}^{(z)}(S). \quad (2.100)$$

The meaning of these relations is obvious from equations (2.83) and (2.55): $\mathbf{D}(R, S) \mathbf{B}^{-1}(R, S)$ represents a symmetric 2×2 matrix of the second derivatives of the traveltime field along the posterior surface Σ_p . In agreement with equation (2.55) this matrix $\mathbf{M}^{(z), \Sigma_p}(R, S) = \mathbf{D}(R, S) \mathbf{B}^{-1}(R, S)$ corresponds to a point source situated at S , that is, on the anterior surface Σ_a . The matrix product $-\mathbf{B}(R, S)^{-1} \mathbf{A}(R, S)$ represents a similar quantity: the matrix $\mathbf{M}^{(z), \Sigma_a}(S, R) = -\mathbf{B}(R, S)^{-1} \mathbf{A}(R, S)$ describes the second derivatives of the traveltime field along the anterior surface due to a point source at R .

2.6 The two-point eikonal

Many applications, e. g., two-point ray tracing or, in the scope of this thesis, the derivation of the CRS stacking operator, require the knowledge of traveltimes along paraxial rays $\Omega_p(R', S')$ where R' and S' are situated close to the points R and S on the central ray. In the following, such a traveltime approximation for surface-to-surface paraxial rays is presented, i. e., S and S' are situated on the anterior and R and R' on the posterior surface (see Figure 2.2). The corresponding traveltime approximation, the so-called surface-to-surface two-point eikonal $T^\Sigma(R', S')$, is constructed from the traveltimes $T^\Sigma(R')$ and $T^\Sigma(S')$ as

$$T^\Sigma(R', S') = T^\Sigma(R') - T^\Sigma(S'). \quad (2.101)$$

For that purpose, the relation between slowness vectors $\mathbf{p}^{(z)}(R')$ and $\mathbf{p}^{(z)}(S')$ of the paraxial ray are determined from the continuation relation (2.98) for the propagator matrix $\underline{\mathbf{T}}(R, S)$. Making use of the symplectic properties and assuming that $\mathbf{z}(R', R)$ and $\mathbf{z}(S', S)$ are known, equation (2.98) can be solved for $\mathbf{p}^{(z)}(S')$ and $\mathbf{p}^{(z)}(R')$:

$$\mathbf{p}^{(z)}(R') = \mathbf{p}^{(z)}(R) - \mathbf{B}^{-T}(R, S) \mathbf{z}(S', S) + \mathbf{D}(R, S) \mathbf{B}^{-1}(R, S) \mathbf{z}(R', R), \quad (2.102)$$

$$\mathbf{p}^{(z)}(S') = \mathbf{p}^{(z)}(S) - \mathbf{B}^{-1}(R, S) \mathbf{A}(R, S) \mathbf{z}(S', S) + \mathbf{B}^{-1}(R, S) \mathbf{z}(R', R). \quad (2.103)$$

Deriving traveltimes approximation (2.82) yields the paraxial slowness vectors $\mathbf{p}^{(z)}(R')$ and $\mathbf{p}^{(z)}(S')$

$$\mathbf{p}^{(z)}(R') = \mathbf{p}^{(z)}(R) + \mathbf{F}(R) \mathbf{z}(R', R) \quad , \quad \mathbf{p}^{(z)}(S') = \mathbf{p}^{(z)}(S) + \mathbf{F}(S) \mathbf{z}(S', S), \quad (2.104)$$

which allow to express the traveltimes approximation (2.82) in terms of slowness vectors only:

$$T^\Sigma(R') = T(R) + \frac{1}{2} \mathbf{z}^T(R', R) [\mathbf{p}^{(z)}(R) + \mathbf{p}^{(z)}(R')], \quad (2.105)$$

$$T^\Sigma(S') = T(S) + \frac{1}{2} \mathbf{z}^T(S', S) [\mathbf{p}^{(z)}(S) + \mathbf{p}^{(z)}(S')]. \quad (2.106)$$

Inserting equations (2.102) and (2.103) into (2.105) and (2.106), respectively, yields the paraxial traveltimes approximations $T^\Sigma(R')$ and $T^\Sigma(S')$:

$$\begin{aligned} T^\Sigma(R') &= T(R) + \mathbf{z}^T(R', R) \mathbf{p}^{(z)}(R) - \frac{1}{2} \mathbf{z}^T(R', R) \mathbf{B}^{-T}(R, S) \mathbf{z}(S', S) \\ &\quad + \frac{1}{2} \mathbf{z}^T(R', R) \mathbf{D}(R, S) \mathbf{B}^{-1}(R, S) \mathbf{z}(R', R), \end{aligned} \quad (2.107)$$

$$\begin{aligned} T^\Sigma(S') &= T(S) + \mathbf{z}^T(S', S) \mathbf{p}^{(z)}(S) - \frac{1}{2} \mathbf{z}^T(S', S) \mathbf{B}^{-1}(R, S) \mathbf{A}(R, S) \mathbf{z}(S', S) \\ &\quad + \frac{1}{2} \mathbf{z}^T(S', S) \mathbf{B}^{-1}(R, S) \mathbf{z}(R', R). \end{aligned} \quad (2.108)$$

Using these results the surface-to-surface two-point eikonal (2.101) is finally given by

$$\begin{aligned} T^\Sigma(R', S') &= T(R, S) + \mathbf{z}^T(R', R) \mathbf{p}^{(z)}(R) - \mathbf{z}^T(S', S) \mathbf{p}^{(z)}(S) \\ &\quad + \frac{1}{2} \mathbf{z}^T(R', R) \mathbf{D}(R, S) \mathbf{B}^{-1}(R, S) \mathbf{z}(R', R) + \frac{1}{2} \mathbf{z}^T(S', S) \mathbf{B}^{-1}(R, S) \mathbf{A}(R, S) \mathbf{z}(S', S) \\ &\quad - \mathbf{z}^T(S', S) \mathbf{B}^{-1}(R, S) \mathbf{z}(R', R). \end{aligned} \quad (2.109)$$

Equation (2.109) can also be expressed in terms of the matrices of second derivatives of the traveltimes field

$$\begin{aligned} T^\Sigma(R', S') &= T(R, S) + \mathbf{z}^T(R', R) \mathbf{p}^{(z)}(R) - \mathbf{z}^T(S', S) \mathbf{p}^{(z)}(S) \\ &\quad + \frac{1}{2} \mathbf{z}^T(R', R) \mathbf{M}^{(z), \Sigma_p}(R, S) \mathbf{z}(R', R) - \frac{1}{2} \mathbf{z}^T(S', S) \mathbf{M}^{(z), \Sigma_a}(S, R) \mathbf{z}(S', S) \\ &\quad + \mathbf{z}^T(S', S) \mathbf{M}^{(z), \Sigma_{ap}}(R, S) \mathbf{z}(R', R). \end{aligned} \quad (2.110)$$

Here, $\mathbf{M}^{(z), \Sigma_{ap}}(R, S)$ denotes the matrix of mixed second derivatives of the traveltimes field

$$M_{ij}^{(z), \Sigma_{ap}}(R, S) = -\mathbf{B}^{-1}(R, S) = \left. \frac{\partial^2 T^\Sigma(R', S')}{\partial z_i(S', S) \partial z_j(R', R)} \right|_{R'=R, S'=S}, \quad (2.111)$$

i. e., one derivative is taken along the anterior, the other along the posterior surface. Note that this matrix is, in contrast to $\mathbf{M}^{(z), \Sigma_p}(R, S)$ and $\mathbf{M}^{(z), \Sigma_a}(S, R)$, not symmetric.

2.7 Wavefront curvatures

The matrix $\mathbf{M}^{(y)}(R)$ can be related to the more descriptive matrix $\mathbf{K}^{(y)}(R)$ which describes the curvature of a wavefront passing through point R on the central ray in local ray-centred Cartesian coordinates. This wavefront is, similar to interface approximation (2.69), defined by the relation

$$y_3(R') = -\frac{1}{2}\mathbf{y}^T(R') \mathbf{K}^{(y)}(R) \mathbf{y}(R'), \quad (2.112)$$

with R' being a point situated on the wavefront.

Definition (2.112) is inserted into traveltime approximation (2.58) in order to obtain the traveltimes along the wavefront. Retaining only terms up to second order and considering that $T(R') = T(R)$ on the wavefront yields

$$y_3(R') = -\frac{1}{2}\mathbf{y}^T(R') v(R) \mathbf{M}^{(y)}(R) \mathbf{y}(R'). \quad (2.113)$$

A comparison of equations (2.112) and (2.113) immediately shows that

$$\mathbf{M}^{(y)}(R) = \frac{1}{v(R)} \mathbf{K}^{(y)}(R). \quad (2.114)$$

Curvature matrices define, together with slowness vectors, the so-called kinematic wavefield attributes.

Chapter 3

The common-reflection-surface stack

As discussed in Section 1.2 seismic data acquisition is conducted such that the wavefields excited from different sources and measured at the receivers illuminate the same structures in the subsurface. Therefore, the corresponding seismic dataset contains redundant information in the sense that energy, reflected at one depth point, is present in the recorded wavefield for different source/receiver combinations. As the plain seismic data is of very limited use, the identification of the coherent redundant information is of fundamental importance. Usually, this task is accomplished by means of stacking velocity analyses. These techniques yield one or more stacking parameters which define traveltimes curves describing the spatial behaviour of selected events throughout the dataset. In conjunction with certain model assumptions the knowledge of these quantities allows to extract medium parameters that are required to deduce the geological properties of the subsurface. For instance, the kinematic behaviour of the identified coherent events can be used to calculate the distribution of the wave propagation velocities in the subsurface whereas the dynamic properties allow to calculate reflection coefficients. In addition, a summation along the traveltimes curves produces a stacked image which simulates a new dataset for a specific source-receiver combination. Thus, stacking velocity analysis plus stacking also provides a first unmigrated time domain image of the subsurface.

Nowadays, there exist a number of different techniques for the determination of stacking parameters; a few of them are mentioned in Chapter 1.3.2. Throughout this thesis the ZO common-reflection-surface (CRS) stack technique (in the following simply called CRS stack), which simulates a poststack volume with coincident source and receiver locations, is used. The underlying assumption of the CRS stack is that the central ray hits a reflector in depth perpendicularly at the so-called normal-incidence point (NIP) and that the down-going and up-going ray segments are identical. In the following these rays will be called normal rays¹. In this case a number of simplifications in the ray-theoretical traveltimes approximations can be made. The resulting stacking operator of the CRS stack depends on eight stacking parameters, the so-called kinematic wavefield attributes, which describe the curvature and orientation of two wavefronts related to two hypothetical experiments.

A detailed description of the ZO CRS stack for 2D and 3D acquired data can, amongst others, be found in Jäger (1999), Müller (1999), Mann (2002) and Müller (2003), Bergler (2004), respectively. In general, the CRS technique is not restricted to the simulation of ZO volumes. The extension to finite offset (e. g., Bergler, 2001) provides a stacking operator depending on five or fourteen stacking parameters for 2D and 3D, respectively.

¹Precisely, a normal ray only requires to hit a reflector perpendicularly. The assumption of coincident up- and down-going ray segments is a further constraint but for the sake of simplicity the term normal ray implies this property here.

3.1 Midpoint and half-offset coordinates

In the following, it is assumed that sources S and receivers R are spread out along a single surface which is planar and coincides with the (x, y) -plane of the general Cartesian coordinate system, i. e., the location of a point is fully described by a 2D vector. In this situation, particular convenient coordinates for the description of the ZO CRS stack are midpoint $\mathbf{m}^{(x)}(R, S)$ and half-offset $\mathbf{h}^{(x)}(R, S)$ coordinates. Given a source at $\mathbf{x}(S)$ and a receiver at $\mathbf{x}(R)$ they are defined as

$$\mathbf{m}^{(x)}(R, S) = \frac{1}{2} [\mathbf{x}(R) + \mathbf{x}(S)] \quad , \quad \mathbf{h}^{(x)}(R, S) = \frac{1}{2} [\mathbf{x}(R) - \mathbf{x}(S)] \quad . \quad (3.1)$$

If S and R denote start and endpoints of a central ray, anterior and posterior surfaces are identical and the basis vectors of the local Cartesian coordinate systems of the two surfaces coincide with the ones of the general Cartesian system. Therefore, a paraxial ray from S' on the anterior surface to R' on the posterior surface has the displacement vectors (as used in the two-point eikonal (2.110))

$$\mathbf{z}(S', S) = \mathbf{x}(S', S) - \mathbf{x}(S) \quad , \quad \mathbf{z}(R', R) = \mathbf{x}(R', R) - \mathbf{x}(R) \quad . \quad (3.2)$$

Inserting these equations into the definition (3.1) yields displacements relative to the central ray's midpoint and half-offset coordinates:

$$\mathbf{m}_D^{(x)}(R', S') = \mathbf{m}^{(x)}(R', S') - \mathbf{m}^{(x)}(R, S) = \frac{1}{2} (\mathbf{x}(R', R) + \mathbf{x}(S', S)) \quad , \quad (3.3)$$

$$\mathbf{h}_D^{(x)}(R', S') = \mathbf{h}^{(x)}(R', S') - \mathbf{h}^{(x)}(R, S) = \frac{1}{2} (\mathbf{x}(R', R) - \mathbf{x}(S', S)) \quad . \quad (3.4)$$

Solving equations (3.3) and (3.4) for $\mathbf{x}(S', S)$ and $\mathbf{x}(R', R)$ immediately leads to

$$\mathbf{x}(S', S) = \mathbf{m}_D^{(x)}(R', S') - \mathbf{h}_D^{(x)}(R', S') \quad , \quad \mathbf{x}(R', R) = \mathbf{m}_D^{(x)}(R', S') + \mathbf{h}_D^{(x)}(R', S') \quad . \quad (3.5)$$

3.2 The surface-to-surface two-point eikonal in midpoint and half-offset coordinates

Using the relations (3.5) the two-point eikonal (2.110) is transformed into midpoint and half-offset coordinates:

$$\begin{aligned} T(R', S') &= T(R, S) + \mathbf{m}_D^{(x)T}(R', S') \mathbf{p}_M^{(x)}(R, S) + \mathbf{h}_D^{(x)T}(R', S') \mathbf{p}_H^{(x)}(R, S) \\ &\quad + \frac{1}{2} \mathbf{m}_D^{(x)T}(R', S') \mathbf{M}_{MM}^{(x)}(R, S) \mathbf{m}_D^{(x)}(R', S') + \frac{1}{2} \mathbf{h}_D^{(x)T}(R', S') \mathbf{M}_{HH}^{(x)}(R, S) \mathbf{h}_D^{(x)}(R', S') \\ &\quad + \mathbf{m}_D^{(x)T}(R', S') \mathbf{M}_{MH}^{(x)}(R, S) \mathbf{h}_D^{(x)}(R', S') \quad , \end{aligned} \quad (3.6)$$

where

$$\mathbf{p}_M^{(x)}(R, S) = \mathbf{p}^{(x)}(R) - \mathbf{p}^{(x)}(S) = \frac{\partial T(R', S')}{\partial \mathbf{m}_D^{(x)}(R', S')}, \quad (3.7)$$

$$\mathbf{p}_H^{(x)}(R, S) = \mathbf{p}^{(x)}(R) + \mathbf{p}^{(x)}(S) = \frac{\partial T(R', S')}{\partial \mathbf{h}_D^{(x)}(R', S')}, \quad (3.8)$$

$$\begin{aligned} \mathbf{M}_{MM}^{(x)}(R, S) &= \mathbf{M}^{(x), \Sigma_a}(S, R) + \mathbf{M}^{(x), \Sigma_p}(R, S) + \mathbf{M}^{(x), \Sigma_{ap}}(R, S) + \mathbf{M}^{(x)T, \Sigma_{ap}}(R, S) \\ &= \frac{\partial^2 T(R', S')}{\partial \mathbf{m}_D^{(x)2}(R', S')}, \end{aligned} \quad (3.9)$$

$$\begin{aligned} \mathbf{M}_{HH}^{(x)}(R, S) &= \mathbf{M}^{(x), \Sigma_a}(S, R) + \mathbf{M}^{(x), \Sigma_p}(R, S) - \mathbf{M}^{(x), \Sigma_{ap}}(R, S) - \mathbf{M}^{(x)T, \Sigma_{ap}}(R, S) \\ &= \frac{\partial^2 T(R', S')}{\partial \mathbf{h}_D^{(x)2}(R', S')}, \end{aligned} \quad (3.10)$$

$$\begin{aligned} \mathbf{M}_{MH}^{(x)}(R, S) &= -\mathbf{M}^{(x), \Sigma_a}(S, R) + \mathbf{M}^{(x), \Sigma_p}(R, S) + \mathbf{M}^{(x), \Sigma_{ap}}(R, S) - \mathbf{M}^{(x)T, \Sigma_{ap}}(R, S) \\ &= \frac{\partial^2 T(R', S')}{\partial \mathbf{m}_D^{(x)}(R', S') \partial \mathbf{h}_D^{(x)}(R', S')}. \end{aligned} \quad (3.11)$$

Similar to the two-point eikonal (2.110) the matrices $\mathbf{M}_{MM}^{(x)}(R, S)$ and $\mathbf{M}_{HH}^{(x)}(R, S)$ are symmetric, whereas $\mathbf{M}_{MH}^{(x)}(R, S)$ is not symmetric, i. e., it consists of four independent elements.

Note that the two-point eikonal (3.6) is only valid if posterior and anterior surface are planar and identical. Expressions for non-planar surfaces can also be found. However, this requires the use of a more general two-point eikonal (see, e. g., [Zhang, 2003](#)).

3.3 The surface-to-surface two-point eikonal for normal rays

So far, equation (3.6) provides a travelttime approximation for finite-offset central rays, i. e., rays where R and S do not necessarily coincide. However, the ZO CRS stack assumes the central ray to be a normal ray with coincident up- and down-going ray segments. Such rays are described by the condition $R = S$ or, correspondingly, $\mathbf{h}^{(x)}(R, S) = \mathbf{0}$ and, thus, $\mathbf{h}_D^{(x)}(R', S') = \mathbf{h}^{(x)}(R', S')$. Furthermore, the coincidence of the identical down-going and up-going ray segments immediately implies

$$\mathbf{p}^{(x)}(R) = -\mathbf{p}^{(x)}(S), \quad (3.12)$$

and, under consideration of equations (3.7) and (3.8)

$$\mathbf{p}_M^{(x)}(R, S) = \mathbf{p}_M^{(x)} = \frac{\partial T(R', S')}{\partial \mathbf{m}_D^{(x)}(R', S')} = 2 \mathbf{p}^{(x)}(R) \quad (3.13)$$

$$\mathbf{p}_H^{(x)}(R, S) = \mathbf{p}_H^{(x)} = \frac{\partial T(R', S')}{\partial \mathbf{h}_D^{(x)}(R', S')} = \mathbf{0}. \quad (3.14)$$

As equation (3.14) is valid for all midpoints it can also be concluded that

$$\mathbf{M}_{MH}^{(x)}(R, S) = \mathbf{M}_{MH}^{(x)} = \frac{\partial^2 T(R', S')}{\partial \mathbf{m}_D^{(x)}(R', S') \partial \mathbf{h}_D^{(x)}(R', S')} = \mathbf{0}. \quad (3.15)$$

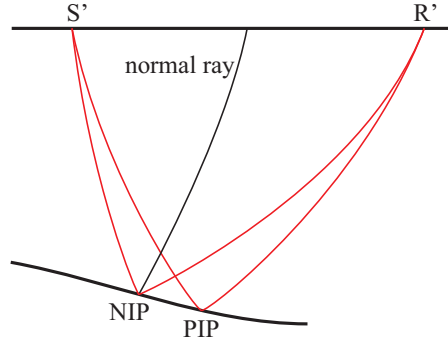


Figure 3.1: The NIP wave theorem states that, up to second-order, the traveltimes of paraxial rays S' -PIP- R' are equal to the traveltimes of non-Snell rays S' -NIP- R' in the CMP domain.

Inserting the relations (3.12)-(3.15) into the two-point eikonal (3.6) finally yields the two-point eikonal for ZO central rays

$$T(\mathbf{m}_D^{(x)}, \mathbf{h}^{(x)}) = T_0 + 2 \mathbf{p}^{(x)T} \mathbf{m}_D^{(x)} + \frac{1}{2} \mathbf{m}_D^{(x)T} \mathbf{M}_{MM}^{(x)} \mathbf{m}_D^{(x)} + \frac{1}{2} \mathbf{h}^{(x)T} \mathbf{M}_{HH}^{(x)} \mathbf{h}^{(x)}. \quad (3.16)$$

For the sake of simplicity the annotations (R' , S') have been omitted and T_0 denotes the traveltime of the (normal) central ray with midpoint coordinate $\mathbf{m}^{(x)}(R, S)$. As up- and down-going raypaths coincide this traveltime is also referred to as two-way traveltime of the normal rays for from the reflection point in depth to the measurement surface.

It should be noted that, in general, ZO rays are not necessarily normal rays. ZO rays only require the coincidence of source and receiver locations whereas normal rays additionally require that the rays hit the reflectors in depth perpendicularly and that the up- and down-going raypaths coincide. As the raypaths are not known in practice, it is difficult to decide whether a certain ZO reflection is associated with a normal ray or not. Luckily, in most cases the ZO reflections in the data are related to normal rays. Therefore, ZO reflections are usually considered to be constituted from normal rays and the term ZO ray is presumed to be equivalent with the term normal ray. However, one should be aware that this assumption, and thus the above traveltime approximation, does not hold for non-normal rays.

3.4 The common-reflection-surface stacking operator

Equation (3.16) already represents a valid ZO stacking operator. However, its parameterisation in terms of traveltime derivatives is not very vivid. Therefore, the stacking parameters $\mathbf{p}^{(x)}$, $\mathbf{M}_{MM}^{(x)}$, and $\mathbf{M}_{HH}^{(x)}$ are related to two hypothetical experiments which allow to assign them a geometric interpretation in terms of wavefront curvatures and emergence angles of the central ray.

3.4.1 The common-midpoint experiment

The first experiment is carried out in the CMP domain which is characterised by $\mathbf{m}_D^{(x)} = \mathbf{0}$ or, equivalently, by a constant midpoint $\mathbf{m}^{(x)}(R, S)$. The traces in the prestack data that satisfy this condition

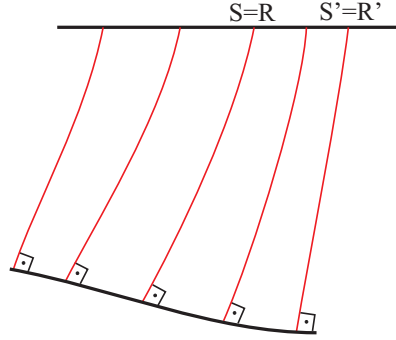


Figure 3.2: The ZO configuration only considers rays with coincident source and receiver locations. These rays are assumed to be normal rays.

constitute a so-called CMP volume. In this domain the traveltime approximation (3.16) simplifies to

$$T(\mathbf{0}, \mathbf{h}^{(x)}) = T_0 + \frac{1}{2} \mathbf{h}^{(x)\text{T}} \mathbf{M}_{\text{HH}}^{(x)} \mathbf{h}^{(x)}. \quad (3.17)$$

According to equation (2.114) and under consideration of the relation $\mathbf{M}_{\text{HH}}^{(x)} = \mathbf{H} \mathbf{M}_{\text{HH}}^{(y)} \mathbf{H}^{\text{T}}$ (see Section 2.4) this traveltime approximation may be written in terms of a symmetric wavefront curvature matrix $\mathbf{K}_{\text{NIP}}^{(y)}$ as

$$T(\mathbf{0}, \mathbf{h}^{(x)}) = T_0 + \frac{1}{v_0} \mathbf{h}^{(x)\text{T}} \mathbf{H} \mathbf{K}_{\text{NIP}}^{(y)} \mathbf{H}^{\text{T}} \mathbf{h}^{(x)}, \quad (3.18)$$

where v_0 denotes the so-called near-surface velocity at $\mathbf{m}^{(x)}(R, S)$. Note that the factor two has been included into $\mathbf{K}_{\text{NIP}}^{(y)}$.

Following the NIP wave theorem (see Chernjak and Gritsenko, 1979; Hubral and Krey, 1980; Hubral, 1983) the traveltimes of paraxial rays $\Omega(R', S')$ reflected at the paraxial-incidence-point (PIP) are, in the CMP configuration, up to second-order equal to the traveltimes of non-Snell rays $\Omega(R', S')$ that pass through the NIP (see Figure 3.1). Hence, all these rays can be seen as passing through NIP and may, thus, be kinematically related to a point source situated at the NIP. The corresponding wavefront propagates upwards along the central ray and emerges at S with the curvature $\mathbf{K}_{\text{NIP}}^{(y)}$. As this describes a one-way experiment whereas the traveltime approximation (3.18) is related to the two-way experiment a factor of two was included into $\mathbf{K}_{\text{NIP}}^{(y)}$ in equation (3.18).

3.4.2 The zero-offset experiment

The ZO section is defined by the condition $\mathbf{h}^{(x)} = \mathbf{0}$, i. e., only traces with coincident source and receiver locations are considered. Under this condition the traveltime approximation (3.16) reduces to

$$T(\mathbf{m}_{\text{D}}^{(x)}, \mathbf{0}) = T_0 + 2 \mathbf{p}^{(x)\text{T}} \mathbf{m}_{\text{D}}^{(x)} + \frac{1}{2} \mathbf{m}_{\text{D}}^{(x)\text{T}} \mathbf{M}_{\text{MM}}^{(x)} \mathbf{m}_{\text{D}}^{(x)}. \quad (3.19)$$

Similar to the CMP experiment this equation can be rewritten in terms of a symmetric wavefront curvature matrix $\mathbf{K}_{\text{N}}^{(y)}$:

$$T(\mathbf{m}_{\text{D}}^{(x)}, \mathbf{0}) = T_0 + 2 \mathbf{p}^{(x)\text{T}} \mathbf{m}_{\text{D}}^{(x)} + \frac{1}{v_0} \mathbf{m}_{\text{D}}^{(x)\text{T}} \mathbf{H} \mathbf{K}_{\text{N}}^{(y)} \mathbf{H}^{\text{T}} \mathbf{m}_{\text{D}}^{(x)}. \quad (3.20)$$

Obviously, the ZO experiment considers paraxial rays that are also normal rays (see Figure 3.2). Thus, the parameters $\mathbf{p}^{(x)}$ and $\mathbf{K}_N^{(y)}$ can kinematically be related to the so-called exploding reflector model of [Loewenthal et al. \(1976\)](#). In this experiment the reflector in the vicinity of the NIP is densely covered with point sources that are excited at the same time. The generated wavefront has initially the same shape as the reflector. Therefore the corresponding rays are normal to the interface. This so-called normal wave propagates along the central ray and emerges at S . There, its direction is given by $\mathbf{p}^{(x)}$ and its curvature by $\mathbf{K}_N^{(y)}$. Thus, these parameters provide information on the shape of the reflectors in depth. Similar to the NIP wave experiment the exploding reflector model describes a one-way experiment and therefore a factor of two has to be included into $\mathbf{K}_N^{(y)}$.

3.4.3 The CRS stacking operator in terms of kinematic wavefield attributes

Using equations (3.18) and (3.20) the traveltimes approximation (3.16) can be expressed in terms of the eight kinematic wavefield attributes $\mathbf{K}_{NIP}^{(y)}$, $\mathbf{K}_N^{(y)}$, and $\mathbf{p}^{(x)}$. The resulting equation is the CRS stacking operator for a 3D measurement configuration

$$T(\mathbf{m}_D^{(x)}, \mathbf{h}^{(x)}) = T_0 + 2 \mathbf{p}^{(x)T} \mathbf{m}_D^{(x)} + \frac{1}{v_0} \mathbf{h}^{(x)T} \mathbf{H} \mathbf{K}_{NIP}^{(y)} \mathbf{H}^T \mathbf{h}^{(x)} + \frac{1}{v_0} \mathbf{m}_D^{(x)T} \mathbf{H} \mathbf{K}_N^{(y)} \mathbf{H}^T \mathbf{m}_D^{(x)}. \quad (3.21)$$

In accordance with Section 2.4 and equation (A.15) the slowness vector $\mathbf{p}^{(x)}$ and the transformation matrix \mathbf{H} may also be written in terms of two angles α and β :

$$\mathbf{p}^{(x)} = \frac{1}{v_0} \begin{pmatrix} \cos \alpha \sin \beta \\ \sin \alpha \sin \beta \end{pmatrix} = \frac{1}{v_0} \mathbf{w}^{(x)}, \quad (3.22)$$

$$\mathbf{H} = \mathbf{R}_3^{(y)}(\alpha) \mathbf{R}_2^{(y)}(\beta) = \mathbf{R}^{(x)}(\alpha, \beta). \quad (3.23)$$

Usually, α and β are referred to as emergence angles of the central ray, i. e., they describe the direction of the central ray at S in terms of an azimuth α and a dip β .

Inserting these relations into (3.21) leads to the typically used representation of the CRS stacking operator:

$$\begin{aligned} T(\mathbf{m}_D^{(x)}, \mathbf{h}^{(x)}) &= T_0 + \frac{2}{v_0} \mathbf{w}^{(x)T} \mathbf{m}_D^{(x)} + \frac{1}{v_0} \mathbf{h}^{(x)T} \mathbf{R}^{(x)}(\alpha, \beta) \mathbf{K}_{NIP}^{(y)} \mathbf{R}^{(x)T}(\alpha, \beta) \mathbf{h}^{(x)} \\ &\quad + \frac{1}{v_0} \mathbf{m}_D^{(x)T} \mathbf{R}^{(x)}(\alpha, \beta) \mathbf{K}_N^{(y)} \mathbf{R}^{(x)T}(\alpha, \beta) \mathbf{m}_D^{(x)}. \end{aligned} \quad (3.24)$$

Although the parabolic traveltimes formula (3.24) represents a full second-order stacking operator it is rarely used in practice as numerical investigations suggest that a hyperbolic approximation is in many cases more accurate (e. g., [Ursin, 1982](#)). Such a representation can easily be obtained by squaring the parabolic equation and retaining only first- and second-order terms. Applied to the CRS stacking operator (3.24) this yields

$$\begin{aligned} T^2(\mathbf{m}_D^{(x)}, \mathbf{h}^{(x)}) &= \left(T_0 + \frac{2}{v_0} \mathbf{w}^{(x)T} \mathbf{m}_D^{(x)} \right)^2 + \frac{2T_0}{v_0} \mathbf{h}^{(x)T} \mathbf{R}^{(x)}(\alpha, \beta) \mathbf{K}_{NIP}^{(y)} \mathbf{R}^{(x)T}(\alpha, \beta) \mathbf{h}^{(x)} \\ &\quad + \frac{2T_0}{v_0} \mathbf{m}_D^{(x)T} \mathbf{R}^{(x)}(\alpha, \beta) \mathbf{K}_N^{(y)} \mathbf{R}^{(x)T}(\alpha, \beta) \mathbf{m}_D^{(x)}. \end{aligned} \quad (3.25)$$

The physical interpretation of the CRS stacking operators is straightforward. The traveltimes approximations (3.24) and (3.25) describe the traveltimes of paraxial rays that are reflected on the same

reflector as the central ray. Their reflection points are situated in the vicinity of the central ray's reflection point. Thus the traveltimes approximations consider a continuous reflecting surface around this point (for that reason the method is called CRS). Following this interpretation, the normal wavefront, specified by the matrix $\mathbf{K}_N^{(y)}$ and the two emergence angles, accounts for the local structure of the reflector and the NIP wavefront (parameterised by $\mathbf{K}_{\text{NIP}}^{(y)}$) for the additional kinematic effect of the source/receiver offset $\mathbf{h}^{(x)}$. In addition, all the attributes also incorporate the effect of the overburden. As already mentioned, the CRS stacking operators have a limited range of validity. This range depends, next to the desired accuracy, on the structure of the subsurface. A quantitative criterion for this range can therefore only be given if the subsurface is known.

With the knowledge of the eight stacking parameters the above traveltimes approximations can be used to produce a stacked ZO volume from the prestack data. For that purpose, a loop over all output locations sums up the data along the traveltimes surface associated with the current output location. The summation result is then assigned to its respective output position $(\mathbf{m}^{(x)}(R, S), T_0)$. Such a simulated ZO volume is, however, not a true ZO volume as obtained by ray tracing: due to the approximative nature of the CRS stacking operators the ZO reflections may be mispositioned in space and time for complex subsurface structures. Also, stacking does in general not simulate the forward modelled ZO amplitudes properly.

3.4.4 A comparison between the CRS operator and a conventional stacking operator

In general, the traveltimes approximations used in conventional processing are much simpler than the CRS operators (3.24) or (3.25). An often used stacking operator for processing in the CMP volumes is given by the hyperbolic form (e. g., [Schneider and Backus, 1968](#))

$$T^2(\mathbf{h}^{(x)}) = T_0^2 + \frac{4 \mathbf{h}^{(x)2}}{v_{\text{NMO}}^2(\gamma)}, \quad (3.26)$$

where the stacking parameter $v_{\text{NMO}}(\gamma)$ denotes the so-called normal moveout (NMO) velocity which is a function of the azimuth γ . In general, the second-order quantity $v_{\text{NMO}}(\gamma)$ cannot be determined exactly from the data by a single coherence analyses as this yields a best fit quantity $v_{\text{stack}}(\gamma)$ (the so-called stacking velocity) which also incorporates, for instance, higher-order contributions of the traveltimes surface. A detailed description of this effect (which also applies to the CRS stacking operator) and its consequences is given in Chapter 4. For 1D media $v_{\text{NMO}}(\gamma)$ is independent of the azimuth and equals the root means square (RMS) velocity v_{RMS} ([Dix, 1955](#))

$$v_{\text{NMO}} = v_{\text{RMS}} = \sqrt{\frac{1}{T_0} \int_0^{T_0} v^2(t) dt}. \quad (3.27)$$

Here, $v(t)$ represent the subsurface velocity along the normal ray. Thus, for 1D media the NMO velocity constitutes an integral velocity of the overburden of the reflection point. For more complex media a simple relationship to the subsurface velocities can, in general, no longer be provided but if the half-offset vector $\mathbf{h}^{(x)}$ is expressed in terms of polar coordinates, i. e.,

$$\mathbf{h}^{(x)}(\gamma) = |\mathbf{h}^{(x)}| \begin{pmatrix} \cos \gamma \\ \sin \gamma \end{pmatrix}, \quad (3.28)$$

the NMO velocity can be obtained from the NIP wavefront by (see equation (3.25))

$$\frac{1}{v_{\text{NMO}}^2(\gamma)} = \frac{T_0}{2v_0} (\cos \gamma, \sin \gamma) \mathbf{R}^{(x)}(\alpha, \beta) \mathbf{K}_{\text{NIP}}^{(y)} \mathbf{R}^{(x)\text{T}}(\alpha, \beta) \begin{pmatrix} \cos \gamma \\ \sin \gamma \end{pmatrix}. \quad (3.29)$$

Consequently, the NMO velocity in equation (3.26) may also be written in terms of a symmetric 2×2 matrix \mathbf{P}_{NMO} which contains NMO velocities in three different azimuths, e. g., in 0° , 45° , and 90° :

$$\mathbf{P}_{\text{NMO}} = \begin{pmatrix} \frac{4}{v_{\text{NMO}}^2(0^\circ)} & \frac{4}{v_{\text{NMO}}^2(45^\circ)} - \left(\frac{2}{v_{\text{NMO}}^2(0^\circ)} + \frac{2}{v_{\text{NMO}}^2(90^\circ)} \right) \\ \frac{4}{v_{\text{NMO}}^2(45^\circ)} - \left(\frac{2}{v_{\text{NMO}}^2(0^\circ)} + \frac{2}{v_{\text{NMO}}^2(90^\circ)} \right) & \frac{4}{v_{\text{NMO}}^2(90^\circ)} \end{pmatrix}. \quad (3.30)$$

The corresponding stacking operator then reads

$$T^2(\mathbf{h}^{(x)}) = T_0^2 + \mathbf{h}^{(x)\text{T}} \mathbf{P}_{\text{NMO}} \mathbf{h}^{(x)}, \quad (3.31)$$

i. e., it is parameterised in terms of three stacking parameters.

A comparison of this operator with the hyperbolic CRS stacking operator (3.25) immediately reveals that equation (3.26) uses far less data for stacking than the CRS operator as the midpoint direction is not considered. As a consequence, the improvement in the S/N ratio due to stacking is smaller compared to the CRS technique. Furthermore, the conventional stacking operator suffers from reflection point dispersal as it does not consider the spatial structure of the subsurface: in case of dipping or curved reflectors the corresponding reflection events in the CMP volumes have different reflection points on the reflectors in depth and the stacking operator (3.26) leads to incorrect stacking results and biased stacking parameters. Although this effect can be partly compensated by a dip-moveout (DMO) correction (Hale, 1984) there remains the problem that the stacking parameter has no physical meaning for media beyond 1D. In addition, as the azimuthal dependency of v_{NMO} is often neglected, a single stacking parameter may be insufficient for the description of reflection events in complex media. In contrast, the CRS stacking operator inherently accounts for reflection point dispersal by considering a reflection surface around the central ray's reflection point. Also, the azimuthal dependencies are correctly treated by the use of curvature matrices instead of scalar stacking parameters. Finally, the conventional approach only provides three quantities that can be used for the determination of the structures of the subsurface whereas the CRS stacking parameter offers eight independent attributes.

3.4.5 Relation to the 2D case

The CRS stacking operator for 2D measurement configurations can be obtained as a special case from the 3D operator (3.25). The parabolic operator (3.24) is not considered here as it is virtually not used in practice.

The 2D CRS stacking operator describes the traveltimes for sources and receivers that are deployed along a straight line with a constant azimuth α_l . As only this azimuth is covered by the data, the azimuth α of the central ray is necessarily assumed to coincide with α_l . This also means that the emergence angle β is measured in a plane perpendicular to the measurement surface and with an azimuth α_l . So, these 2D emergence angles are only identical to the true emergence angles if the normal ray lies in this plane when it emerges on the measurement surface (this is, for instance, the case

if 2D media are considered). In case of out-of-plane normal rays the measured emergence angle β^{2D} is an apparent emergence angle, i. e., the dip of the slowness vector in direction of the measurement line.

In the 3D CRS stacking operator (3.25) the 2D situation can be simulated by expressing $\mathbf{m}_D^{(x)}$ and $\mathbf{h}^{(x)}$ in polar coordinates

$$\mathbf{m}_D^{(x)}(\alpha_l) = |\mathbf{m}_D^{(x)}| \mathbf{e}(\alpha_l) \quad , \quad \mathbf{h}^{(x)}(\alpha_l) = |\mathbf{h}^{(x)}| \mathbf{e}(\alpha_l) \quad , \quad \mathbf{e}(\alpha_l) = \begin{pmatrix} \cos \alpha_l \\ \sin \alpha_l \end{pmatrix} \quad , \quad (3.32)$$

and by setting $\alpha = \alpha_l$ and $\beta = \beta^{2D}$. Inserting these relations into equation (3.25) yields the hyperbolic 2D CRS stacking operator

$$T^2(m_D, h) = \left(T_0 + 2 \frac{\sin \beta^{2D}}{v_0} m_D \right)^2 + \frac{2t_0 \cos^2 \beta^{2D}}{v_0} \left(K_{\text{NIP}}^{2D} h^2 + K_N^{2D} m_D^2 \right) \quad , \quad (3.33)$$

where $K_{\text{NIP}}^{2D} = K_{\text{NIP},11}$, $K_N^{2D} = K_{N,11}$, $|\mathbf{m}_D^{(x)}| = m_D$, and $|\mathbf{h}^{(x)}| = h$. Note, that the two curvatures are given in direction of the measurement line and that they are, due to their scaling with β^{2D} , also apparent curvatures if the normal ray is out-of-plane.

The relations between the apparent and the full 3D kinematic wavefield attributes are obtained by evaluating the 3D CRS stacking operator (3.25) with the 3D wavefield attributes for the measurement azimuth α_l (given by equations (3.32)). The comparison of the resulting terms with the 2D operator (3.33) then yields

$$\beta^{2D} = \arcsin(\cos \alpha_l \cos \alpha \sin \beta + \sin \alpha_l \sin \alpha \sin \beta) \quad , \quad (3.34)$$

$$K^{2D} = \frac{\mathbf{e}^T(\alpha_l) \mathbf{R}^{(x)}(\alpha, \beta) \mathbf{K}^{(y)} \mathbf{R}^{(x)T}(\alpha, \beta) \mathbf{e}(\alpha_l)}{\cos^2 \beta^{2D}} \quad , \quad (3.35)$$

where K^{2D} and $\mathbf{K}^{(y)}$ may either denote the curvatures of the NIP or the normal wavefronts.

The complete set of 3D attributes cannot be calculated from the apparent attributes as the problem is under-determined. For this reason it can be concluded that the 2D CRS stack and its attributes may be inadequate for the use in applications that rely on the knowledge of the complete curvatures and emergence angles as, e. g., velocity inversion methods.

3.5 Implementation of the CRS stack method

The implementation of the CRS stack method based on the hyperbolic traveltime approximation (3.25) consists of two basic parts. First, the determination of the eight kinematic wavefield attributes α , β , $\mathbf{K}_{\text{NIP}}^{(y)}$, and $\mathbf{K}_N^{(y)}$ for the desired reflection events is required. Then, summations along the reflection responses defined by these attributes in the five-dimensional prestack data provides the ZO stacks for the respective output locations $(\mathbf{m}^{(x)}(R, S), T_0)$. As these ZO locations are not known a priori a gridded ZO output volume is defined and the above mentioned steps are performed for each of the grid locations. The spatial and temporal sampling of the grid is usually chosen such that it coincides with the midpoints of the individual CMP volumes and the temporal sampling rate in the prestack data, respectively. In this way, the CRS stack is performed throughout the whole prestack data, irrespective whether there is a reflection event at a specific location or not. In the latter case, the kinematic

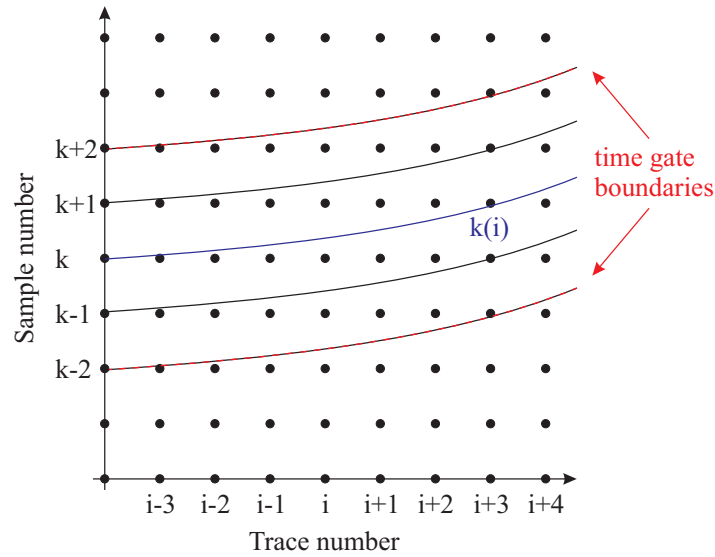


Figure 3.3: The semblance value S for a sample k is evaluated from a multitude of time shifted CRS operators within a time window that is disposed symmetrically around the test sample.

wavefield attributes are physically meaningless and the stacking process sums up uncorrelated signals only and does therefore lead to a negligible stacked amplitude. For locations that are related to actual reflection events the wavefield attributes are well defined and the stacking process sums coherent energy thus leading to significant stacked amplitudes. Drawback of this method is that any kind of correlated energy is imaged. Therefore, it might be difficult to identify the desired reflection events in the simulated ZO volume.

3.5.1 Coherence analysis

In order to automate the implementation of the CRS stack it is required that the kinematic wavefield attributes are determined without human interaction. For that purpose the CRS operator (3.25) is tested within a range of different attribute values for its fit to the actual reflection response. This so-called coherence analysis provides the fit of the individual test operators by evaluating an underlying coherence criterion. Thus, the determination of the wavefield attributes is formulated as a non-linear eight parameter global optimisation problem in the five-dimensional prestack data. The coherence criterion used in the current implementation of the CRS stack is the widely used semblance criterion (Neidell and Taner, 1971)

$$S = \frac{\sum_{j=-W/2}^{W/2} \left(\sum_{i=1}^N f_{i,j+k(i)} \right)^2}{N \sum_{j=-W/2}^{W/2} \sum_{i=1}^N f_{i,j+k(i)}^2}. \quad (3.36)$$

Here, $f_{i,j}$ denotes the amplitude of the j^{th} sample on the i^{th} of N traces. A time window of width W which is disposed symmetrically around the CRS operator at $k(i)$ (see Figure 3.3) accounts for the limited frequency bandwidth and increases the stability of the process. A reasonable size of this

window is the length of the wavelet. The semblance criterion is normalised such that it yields a value between 0 and 1.

Drawback of the semblance criterion is that it presumes the amplitude and phase of the wavefield to be constant along the CRS operator. Unfortunately, this assumption is not necessarily fulfilled, e. g., due to angle dependent reflection coefficients. Therefore, semblance may yield coherence maxima for incorrect wavefield attributes. A number of coherence criteria that incorporate amplitude and phase variations are presented in [Gelchinsky et al. \(1985\)](#). However, as they come along with a significantly higher computational cost they are not considered here.

3.5.2 Optimisation and parallelisation strategies

Unfortunately, the global optimisation problem for the determination of the wavefield attributes does not allow to make assumptions on the distribution of the coherence values within the parameter space. For that reason sophisticated search routines which require the evaluation of the smallest possible number of test operators are the key to an efficient implementation of the CRS stack. In the following, a grid search which provides initial attributes and a simulated annealing approach for the refinement of the attributes are discussed. Furthermore, a parallelisation technique for the CRS stack is presented. A detailed description of these techniques can be found in [Müller \(2003\)](#) and [Bergler \(2004\)](#).

Initial grid search

The grid search serves as an initial search with the aim to confine a region where the searched-for global coherence maximum is situated. This search requires at least the definition of two sets of parameters:

- An upper and a lower boundary for each of the involved wavefield attributes.
- A grid size that defines the locations where the coherence analysis is performed.

The application of the grid search is quite simple: on each of the grid points between upper and lower boundary the coherence value is calculated. The grid point with the highest value finally defines the set of attributes that fits the reflection event best. As an option the search can be refined by decreasing the grid size and repeating the process in a small area centred around the current coherence maximum. In addition, the grid search can be further constrained by using initial attributes that are obtained by means of other methods, e. g., manual picking.

Although the implementation of this search is straightforward its performance is rather poor. If n parameters are to be optimised simultaneously, the coherence has to be evaluated on $N = \prod_{i=1}^n m_n$ grid points (where m_n is the number of values that the n^{th} parameter can take). Therefore, the grid search can, in general, only serve as an initial guess. However, despite the actual differences in the stacked volumes might be quite significant for attributes determined with different resolutions, they are often hardly visible to the human eye (see [Figure 3.4](#)). Thus, if only a stacked volume is required the grid search may already be sufficiently accurate.

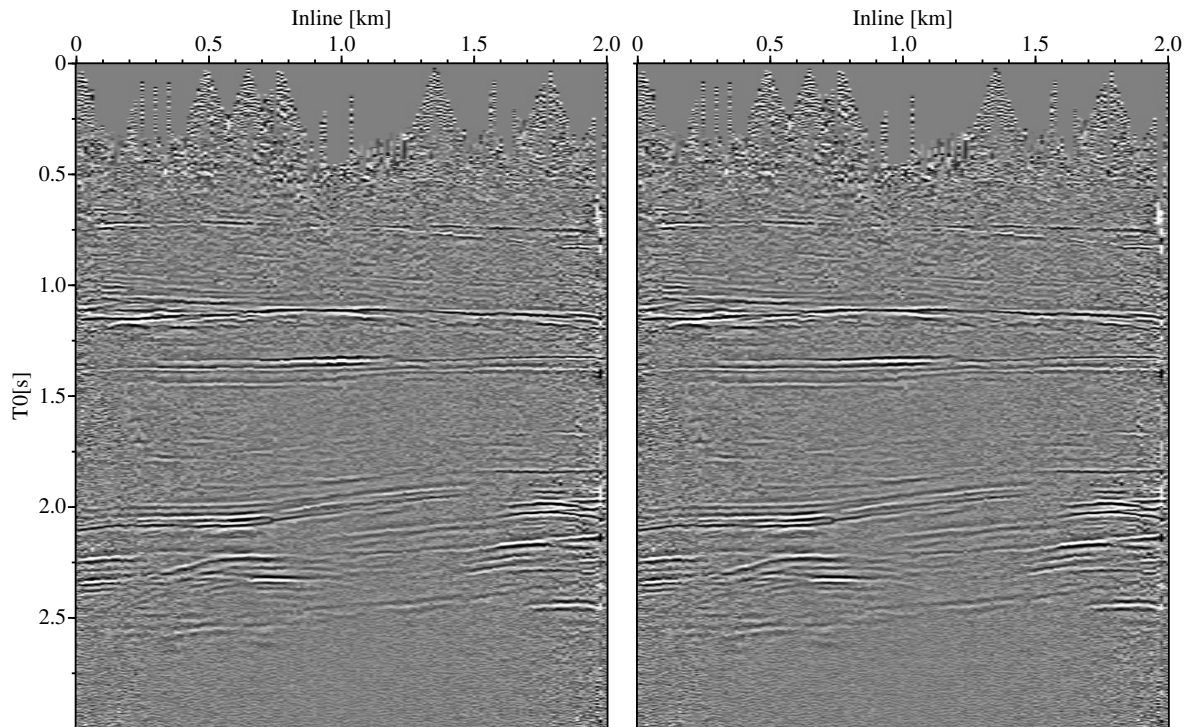


Figure 3.4: In many cases stacked sections or volumes appear to be largely insensitive to the accuracy of the stacking parameters: the figure on the left, which was obtained by a low resolution grid search, shows only minor differences to the human eye compared to the figure on the right, which is the result of a high resolution grid search. The inline sections were obtained from conventional CMP processing with the stacking operator (3.31). The grid spacing of the stacking parameters \mathbf{V}_{NMO} was 40 m/s for the low resolution result and 10 m/s for the high resolution result.

Simulated annealing optimisation

In order to refine the attributes determined by the grid search a technique based on the simulated annealing method (Kirkpatrick et al., 1983) is employed. This so-called continuous optimisation by simulated annealing (Press et al., 2002) is an extension to the uphill simplex method according to Nelder and Mead (1965).

The uphill simplex method is designed to find local maxima of an objective function (e. g., the semblance) by means of a simplex. For that purpose, the simplex, which is a polyhedron with $N + 1$ vertices in the N -dimensional space, takes a number of steps which alters its orientation, size, and shape according to the values of the objective function at the vertices (see Figure 3.5). In general, each single step is performed such that the vertex with the lowest objective function value moves to a position with a higher value. Thus, the simplex continuously advances towards the local maximum of the objective function. The process is terminated when some termination criteria are reached, e. g., a number of iterations is reached or the difference of the objective function values at the vertices is fractionally smaller than some threshold.

The simulated annealing approach modifies the uphill simplex method such that it is suitable to detect the global maximum of the objective function. Therefore, two additional elements are included into

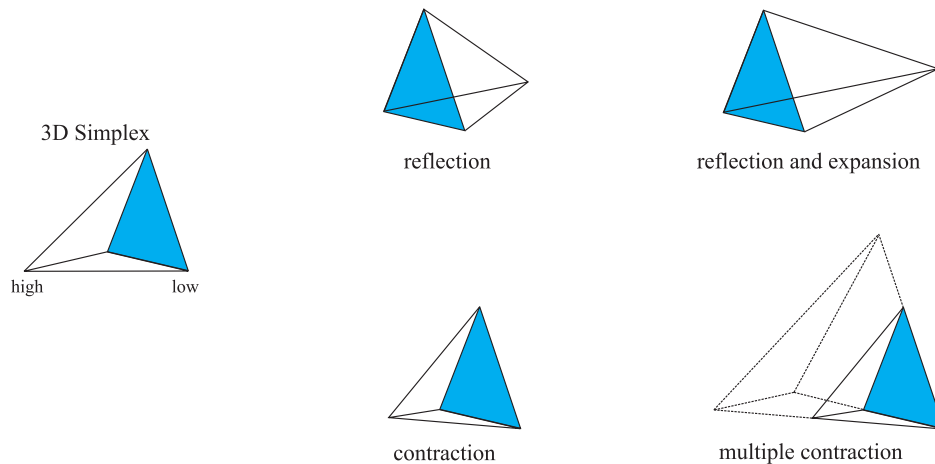


Figure 3.5: A simplex is a geometrical figure consisting of $N + 1$ vertices and their interconnecting line segments in the N -dimensional space. During the simulated annealing optimisation the vertices are moved such that they transform and move the simplex according to a number of predefined rules (here shown for a tetrahedron, i. e., the simplex for the 3D space).

the algorithm:

- at each movement step of the simplex a logarithmically distributed random value is subtracted from the objective function values associated with each vertex. A similar random variable is added to every new point that is tried as a replacement point. Thus, the simplex is given a chance to perform a movement towards a position with a worse objective function.
- a temporal decreasing control parameter $T(\tau)$ defines the amplitude of the random distribution at the time τ . This parameter actually defines the probability of performing a movement in direction of a worse objective function. In the limit $T(\tau) \rightarrow 0$ the algorithm reduces exactly to the uphill simplex method.

The consequence of these random configuration changes is that the simplex is given a chance to leave local maxima as long as $T(\tau) > 0$. If $T(\tau)$ is reduced sufficiently slow it becomes likely that the simplex migrates into the region containing the global maximum. Finally, in the limit $T(\tau) \rightarrow 0$ the algorithm will then converge to the maximum. Due to the ability to vary the size of the simplex the simulated annealing optimisation does, in general, provide attributes with a higher resolution than the grid search.

The difficulty in the application of the simulated annealing is the appropriate choice of the annealing schedule $T(\tau)$. If $T(\tau)$ is decreased too fast the simplex may get stuck in local maxima, if lowered too slow unnecessary and time consuming computations are performed. Actually, reasonable choices for $T(\tau)$ cannot be quantified easily. Therefore the simulated annealing methods basically rely on the users experience. However, if the optimisation already starts close to the searched-for global maximum of the objective function, $T(\tau)$ can be chosen such that the simulated annealing has a significantly better performance than a grid search with a comparable resolution. For that reason, the determination of the wavefield attributes is implemented as a combination of a grid search and a simulated annealing

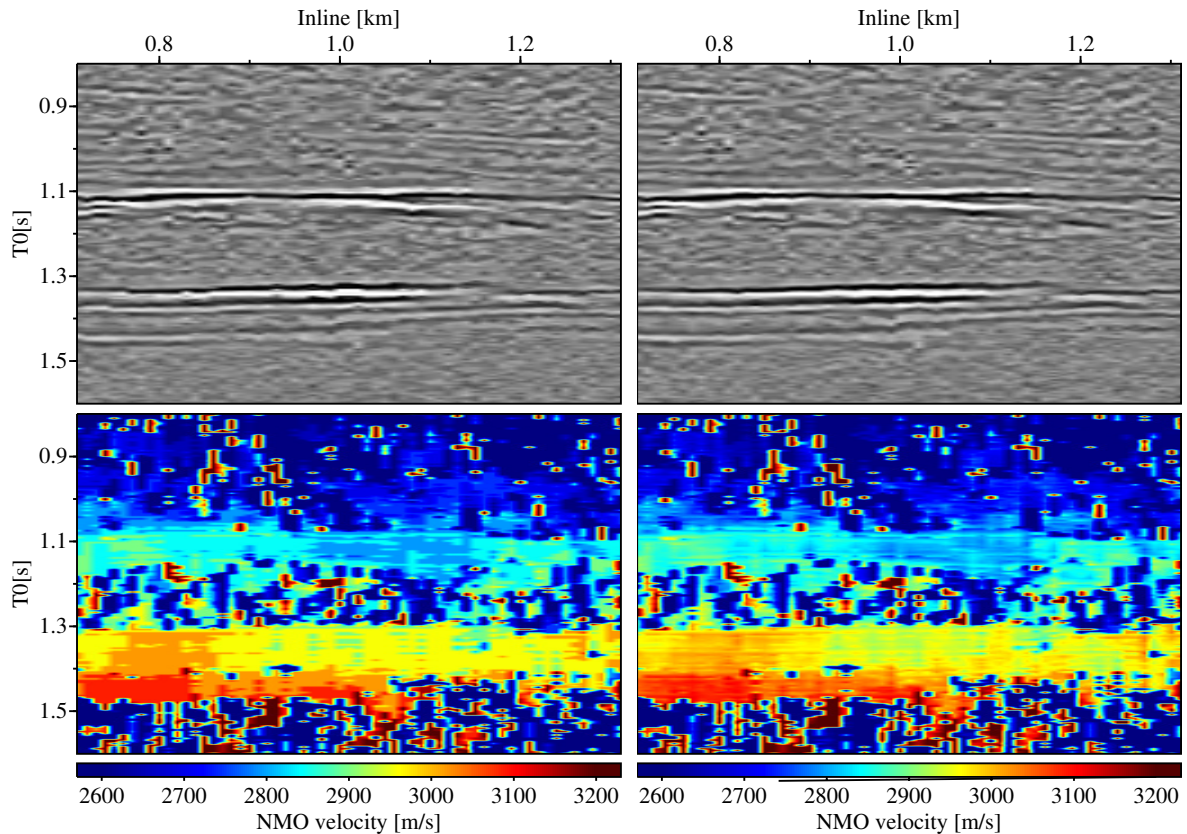


Figure 3.6: Details of the inline section shown in Figure 3.4 after simulated annealing optimisation. The figures on the left hand side show details of the stacked section and the determined NMO velocities $v_{\text{NMO}}(0^\circ)$ from the low resolution grid search. On the right hand side the results of the simulated annealing optimisation are depicted. Again, the differences in the stacked sections are hardly visible whereas the NMO velocities vary significantly. In general, the NMO velocities obtained from the simulated annealing optimisation have a higher resolution than the ones obtained from the grid search.

optimisation: the coarse grid search aims at detecting the region where the global maximum is located and the optimisation refines these results.

Figure 3.6 shows detailed results of this strategy applied to the same data as presented in Figure 3.4. Similar to the latter figure, the variations in the optimised and initial stacked sections are hardly visible to the human eye. In contrast, the sections containing the NMO velocities show significant differences: the section obtained from the grid search clearly reveals the step size of the search whereas the optimised section contains far more details. Nevertheless, it can also be seen that the stacking parameters are still subject to unphysical fluctuations and outliers. These unwanted effects which are, e. g., related to noise in the prestack data, cannot be avoided by the search routines itself. A so-called event consistent smoothing method designed to eliminate such artifacts in the kinematic wavefield attributes is discussed in [Hertweck et al. \(2005\)](#). The presented technique acts as a post-processing step that uses the wavefield attributes determined so far to define the orientation of smoothing windows. The event consistent smoothing does not smooth the stacked section but the attributes themselves. The new stacked section is obtained by re-stacking with the smoothed attributes. The danger of such

types of smoothing is, however, the possible inconsistency with the data.

Parallelisation

An important aspect in the implementation of the CRS stack is the parallelisation of the code, i. e., the computation of independent parts of the algorithms simultaneously on different nodes. This allows to speed up the processing time without loss of accuracy and without simplifications of the problem. Fortunately, the CRS stack (or even stacking in general) is perfectly suited for parallelisation. Its stacking operator (3.25) reveals that the result for one output sample ($\mathbf{m}^{(x)}(R, S), T_0$) is independent of results from other samples. Therefore, a sample is the smallest unit that can be computed independently and without communication with other nodes (which would degrade the performance). Nevertheless, a sample is not the appropriate unit for parallelisation. A more natural choice is a parallelisation based on traces, that is, all the samples that belong to a certain output location $\mathbf{m}^{(x)}(R, S)$. The reason is that seismic data is usually organised in traces which contain all the necessary information to treat its samples independent from the rest of the dataset, e. g., geometrical information and sampling rate. Thus, traces may, in contrast to samples, be stored unordered. Furthermore, the communication with a load balancer is significantly reduced due to the reduced number of units but this number still remains large enough for typical clusters.

In the 3D CRS stack software the parallelisation is implemented as follows:

- One master process performs the load balancing, the slave processes perform the CRS stack.
- Each slave requests a trace from the master to be processed.
- After processing a trace the result is stored in an individual file and the slave repeats the previous step.
- If no more traces are to be processed the master collects all the results from the individual files and merges them into a single output file.

In principle, it is not necessary to store the results in individual files. However, for the chosen data formats (Seismic Unix and SEG-Y) this simplifies on-the-fly quality control and avoids delays due to file locks.

3.5.3 Apertures

For the implementation of the search and optimisation strategies it is required to specify the data that enters into the coherence analyses. Usually, this is done by using traces within an area around the emergence location of the central ray, i. e., the location $\mathbf{m}^{(x)}(R, S)$. This so-called search aperture may be specified arbitrarily but it is common to define it elliptically with respect to the midpoint and half-offset coordinates. In that case, a trace with midpoint displacement $\mathbf{m}_D^{(x)}$ and half-offset $\mathbf{h}^{(x)}$ is within the search aperture with size $(\mathbf{m}_D^{(x)SA}, \mathbf{h}^{(x)SA})$ if the condition

$$\frac{m_{D,1}^{(x)2}}{(m_{D,1}^{(x)SA})^2} + \frac{m_{D,2}^{(x)2}}{(m_{D,2}^{(x)SA})^2} + \frac{h_1^{(x)2}}{(h_1^{(x)SA})^2} + \frac{h_2^{(x)2}}{(h_2^{(x)SA})^2} \leq 1 \quad (3.37)$$

is fulfilled. Note that the principal axes of the ellipse coincide with the midpoint and half-offset coordinate axes. If required, a different alignment can be obtained by introducing an additional component describing the rotation.

In general, the search aperture coincides with the stacking aperture which specifies the data used for the simulation of the ZO volume. However, a distinction of these two apertures is necessary as they may differ in certain cases.

The choice of the search and stacking apertures have a large impact on the accuracy of the results. On the one hand, too small an aperture introduces instability to the parameter determination. On the other hand, too large an aperture is undesirable as it does no longer allow to describe the attributes as local properties of the reflection response. A quantitative measure for the optimum apertures is difficult to define. However, in practice values for the apertures in midpoint displacement direction are a few hundred meters whereas in half-offset direction the expected depths of the reflection events should be estimated (e. g., [Sheriff and Geldart, 1982](#)).

3.5.4 Processing steps

Even with the use of sophisticated search techniques the simultaneous determination of the eight kinematic wavefield attributes is very inefficient without a priori information that allows to constrain the search ranges and steps substantially. For that reason the optimisation is usually decomposed into three subsequent steps which are carried out in different subsets of the data space, respectively.

Hyperbolic CMP search

In a first step the CRS stacking operator (3.25) is applied to the CMP domain. As this domain is defined by the condition $\mathbf{m}_D^{(x)} = \mathbf{0}$ and the corresponding CRS operator reads

$$T^2(\mathbf{h}^{(x)}) = T_0^2 + \frac{2T_0}{v_0} \mathbf{h}^{(x)T} \mathbf{R}^{(x)}(\alpha, \beta) \mathbf{K}_{\text{NIP}}^{(y)} \mathbf{R}^{(x)T}(\alpha, \beta), \quad \mathbf{h}^{(x)} = T_0^2 + \mathbf{h}^{(x)T} \mathbf{M} \mathbf{h}^{(x)}, \quad (3.38)$$

where the symmetric 2×2 matrix \mathbf{M} is given by

$$\mathbf{M} = \frac{2T_0}{v_0} \mathbf{R}^{(x)}(\alpha, \beta) \mathbf{K}_{\text{NIP}}^{(y)} \mathbf{R}^{(x)T}(\alpha, \beta). \quad (3.39)$$

Thus, the CRS operator for the CMP domain is parameterised in terms of three parameters \mathbf{M} which are constituted by the five kinematic wavefield attributes $\mathbf{w}^{(x)}$ and $\mathbf{K}_{\text{NIP}}^{(y)}$. A comparison with equation (3.31) shows that this operator is closely related to the conventional one. In fact, the optimisation for the three parameters can also be conducted by means of conventional procedures, e. g., stacking velocity analysis.

The application of the stacking operator (3.38) requires full azimuthal coverage of the traces in the CMP volumes. If this condition is not satisfied, as for instance for narrow azimuth marine data, further simplifications have to be applied. The most prominent is the reduction to a one parameter operator by setting

$$\mathbf{M} = m \mathbf{I}. \quad (3.40)$$

As a one parameter optimisation is computationally very effective it is also suited to determine initial values for a highly constrained three parameter optimisation. Furthermore, it represents the stacking operator for 1D media and may, thus, be used if simple subsurface structures are encountered.

The basic result of the hyperbolic CMP search is, besides the parameter and coherence volumes, the CMP stacked ZO volume obtained by applying the stacking operator (3.38) to the prestack data.

Linear ZO search

The ZO volume obtained from the hyperbolic CMP search serves as input for the next two steps. The ZO domain, defined by $\mathbf{h}^{(x)} = \mathbf{0}$, yields the stacking operator

$$\begin{aligned} T^2(\mathbf{m}_D^{(x)}) &= \left(T_0 + \frac{2}{v_0} \mathbf{w}^{(x)\text{T}} \mathbf{m}_D^{(x)} \right)^2 + \frac{2T_0}{v_0} \mathbf{m}_D^{(x)\text{T}} \mathbf{R}^{(x)}(\alpha, \beta) \mathbf{K}_N^{(y)} \mathbf{R}^{(x)\text{T}}(\alpha, \beta) \mathbf{m}_D^{(x)} \\ &= \left(T_0 + \frac{2}{v_0} \mathbf{w}^{(x)\text{T}} \mathbf{m}_D^{(x)} \right)^2 + \mathbf{m}_D^{(x)\text{T}} \mathbf{N} \mathbf{m}_D^{(x)}. \end{aligned} \quad (3.41)$$

Similar to the CMP domain the 2×2 matrix \mathbf{N} is here given by

$$\mathbf{N} = \frac{2T_0}{v_0} \mathbf{R}^{(x)}(\alpha, \beta) \mathbf{K}_N^{(y)} \mathbf{R}^{(x)\text{T}}(\alpha, \beta), \quad (3.42)$$

and the CRS operator for the ZO domain is therefore parameterised in terms of five independent quantities $\mathbf{w}^{(x)}$ and \mathbf{N} .

Still, an initial grid search for five parameters is not practicable with todays computer hardware. For that purpose, the two factors $\mathbf{w}^{(x)}$ and \mathbf{N} are determined independently. First, the vector $\mathbf{w}^{(x)}$ is determined under the assumption $\mathbf{N} = \mathbf{0}$, i. e., the normal wave is assumed to be a plane wave at the measurement surface. Inserting this condition into equation (3.41) yields the respective stacking operator

$$T(\mathbf{m}_D^{(x)}) = T_0 + \frac{2}{v_0} \mathbf{w}^{(x)\text{T}} \mathbf{m}_D^{(x)}. \quad (3.43)$$

Due to the linear form of this equation the two parameter optimisation for $\mathbf{w}^{(x)}$ is also called linear ZO search.

Hyperbolic ZO search

With the knowledge of $\mathbf{w}^{(x)}$ the matrix \mathbf{N} is determined as a last optimisation step. This optimisation is based on the stacking operator (3.41). Similar to the hyperbolic CMP search, a fast initial one parameter search, i. e., $\mathbf{N} = n \mathbf{I}$, may be used to constrain the three parameter optimisation.

After this step, the eight parameters \mathbf{M} , \mathbf{N} , and $\mathbf{w}^{(x)}$ are known and the eight kinematic wavefield attributes α , β , $\mathbf{K}_{\text{NIP}}^{(y)}$, and $\mathbf{K}_N^{(y)}$ can be obtained from simple algebraic transformations.

Note that the two ZO searches do not only yield the stacking parameters but also coherence volumes and, if desired, stacked volumes (the so-called ZO stacked ZO volumes).

CRS stack

The last task in the CRS processing chain is the generation of the CRS stacked ZO volume. This stack is performed on the prestack data using the complete stacking operator (3.25) and the previously determined attributes. In addition, a CRS coherence volume is provided by evaluating the coherence criterion for the determined attributes.

Attribute refinements

In general, the refinement of the attributes based on the simulated annealing approach can be performed after each of the previously discussed steps. However, only a few combinations of initial search and refinement are actually useful in terms of accuracy and performance. For instance, a simultaneous five parameter refinement of $\mathbf{w}^{(x)}$ and \mathbf{N} is more reasonable than two subsequent refinements due to two reasons: the performance of the refinement is far less sensitive to the number of parameters than the initial grid search and the five parameter refinement provides a higher accuracy as the full CRS operator for the ZO domain (3.41) is used. Therefore, the proposed refinements are either

- an eight parameter refinement applied on the prestack data with the full CRS operator (3.25) or
- a three parameter refinement of matrix \mathbf{M} based on the stacking operator (3.38) followed by a five parameter refinement of vector $\mathbf{w}^{(x)}$ and matrix \mathbf{N} with the stacking operator (3.41).

Obviously, the eight parameter refinement is the better choice as it makes use of the complete CRS operator in the five dimensional prestack data whereas the two subsequent refinements are applied to different 3D subsets of this 5D domain. However, the large number of traces involved in an eight parameter optimisation may severely degrade the computational efficiency. In that case, the second approach provides a good compromise between achievable accuracy and computational cost.

3.6 Further aspects

The techniques discussed in this chapter only cover the aspects of the CRS stack that are actually required for the applications in this thesis. A complete treatment of the CRS method requires the presentation of far more processing schemes and optimisation methods. For instance, this includes the implementation of the method in the common-shot or common-receiver configuration (Dümmong, 2005) as an alternative to the midpoint and half-offset configuration. In case of land data the estimation and correction of residual static time shifts (Koglin, 2005) and the handling of surface topography (Zhang, 2003; von Steht, 2004; Heilmann et al., 2006) are of particular importance. Furthermore, the CRS stack method was recently extended to arbitrary acquisition geometries and multi-component data (Boelsen, 2005). An application of these extensions is the use of the CRS technology for the processing of data obtained by vertical seismic profiling (VSP) (von Steht, 2006).

Note also that there exist alternatives to the presented optimisation strategies. For example, the eight kinematic wavefield attributes can be determined by a series of 2D CRS stacks applied to different azimuthal directions (Höcht, 2002). In this way, the computational cost can be minimised but the stability and accuracy may be decreased as an appropriate azimuthal distribution of the traces is required.

Chapter 4

Spread-length bias

The CRS stack technology is based on the assumption that reflection events can be described by a second-order approximation of the traveltime. Thus, the coherence analysis which is used for the determination of the kinematic wavefield attributes is influenced by the range of validity of this approximation: as the semblance yields optimum fit quantities, for non-second-order reflection events the actually obtained stacking parameters differ from the searched-for parameters. In the same way the estimated optimum fit ZO traveltimes (in the following called stack times), and thus the simulated ZO section, do, in general, not coincide with the true ZO stack times. As the misfit in stacking parameters and stack times basically depends on the search aperture used in the coherence analyses this behaviour is called spread-length bias (see, e.g., [Shah and Levin, 1973](#); [Al-Chalabi, 1973](#); [Hubral and Krey, 1980](#)). Outcome of this effect are a stacked section with reflection events mispositioned in time and stacking parameter sections which are biased by high-order contributions. As a consequence, applications based on these quantities will also yield incorrect results.

In this chapter, a technique for the treatment of the spread-length bias is presented for the 2D CRS stack. Although an extension to 3D is straightforward it is not considered here as the computational cost is too high. However, the presented 2D example shows that the spread-length bias can significantly affect the results of subsequent applications based on the determined attributes and traveltimes. [Al-Chalabi \(1974\)](#) presented a first approach for the correction of the spread-length bias of stacking velocities in a conventional stacking operator. Similar to the technique presented here, it makes use of a series of coherence analyses with different search apertures but, in contrast, it does not correct for the stack times and is not suitable for high-density velocity analyses as no automatic picking is involved.

4.1 Spread-length bias

As stated before, the spread-length bias arises when the traveltime approximation used in a coherence analysis is insufficient to describe the shape of a reflection event. Common coherence criteria, e. g., the semblance as used in the implementation of the CRS stack, are usually based on the maximisation of correlated energy which can be understood as a determination of the optimum fit between the actual reflection event and the operator defined by the traveltime approximation. As most traveltime approximations are basically series expansions, this means that their coefficients (which are defined

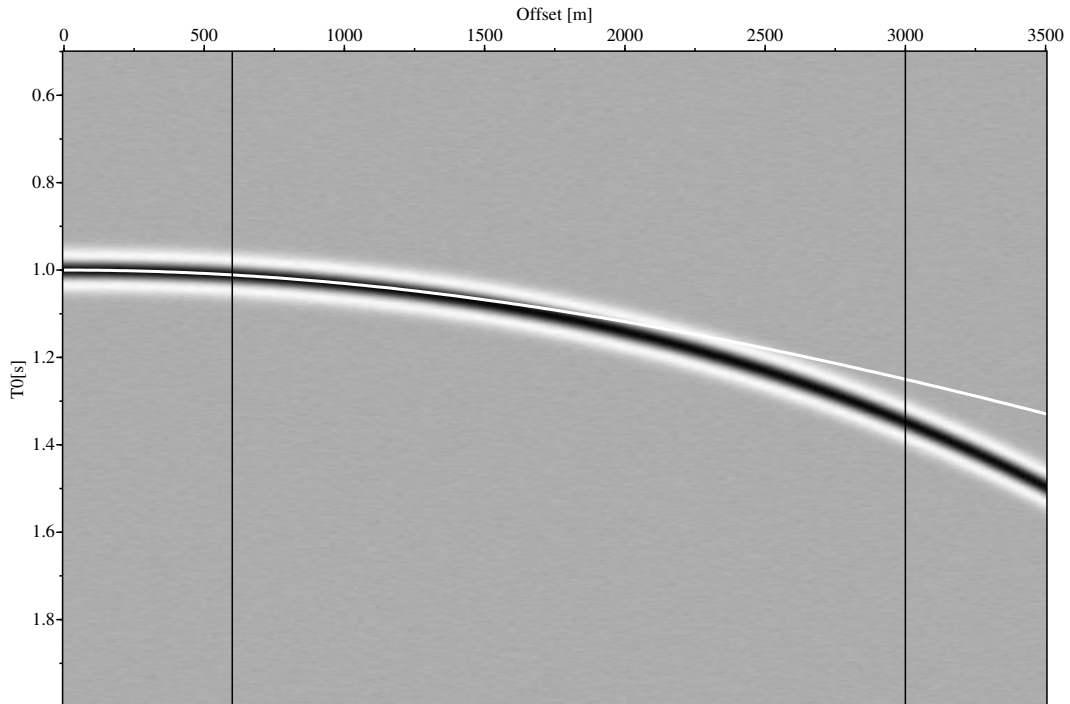


Figure 4.1: CMP gather with a non-hyperbolic reflection event. White trajectory: corresponding hyperbolic traveltimes curve. Black lines: absolute minimum and maximum search apertures used in the coherence analyses.

at the expansion point) obtained by coherence analysis do not coincide with the true coefficients when using large search apertures. In addition, when used for stacking purposes, these biased coefficients lead to stacked sections with the reflection events mispositioned in time. Of course, this problem can be neglected when using relatively small search apertures. However, in many cases this decreases the stability of the coherence analysis and might even totally fail in case of poor data quality and/or a too low number of traces in the vicinity of the expansion point. So, the consideration of these misfits is unavoidable if high quality stack times and stacking parameters are required.

For a given dataset, the exact behaviour of the misfits depends, besides the search aperture (the so-called spread-length), on a multitude of quantities, e. g., coherence criterion, wavelet type, trace distribution, and amplitude and phase changes. Thus, a simple expression of the misfit cannot be given. However, if all quantities except the search aperture are kept constant between two coherence analyses, the bias depends on the spread-length only. For that reason it is called spread-length bias.

Although spread-length bias occurs for every traveltimes approximation used in coherence analyses it is especially problematic for low-order series approximations like the second-order traveltimes formula used by the CRS stack. Higher-order approximations, e. g., fourth-order series approximations, partially reduce the effects of the spread-length bias. However, this requires to perform multiparameter coherence analyses which are quite ineffective in terms of computational cost.

In order to demonstrate the effect of the spread-length bias, a synthetic 2D CMP gather with a non-second-order reflection event was modelled using a zero-phase Ricker wavelet (see Figure 4.1). For

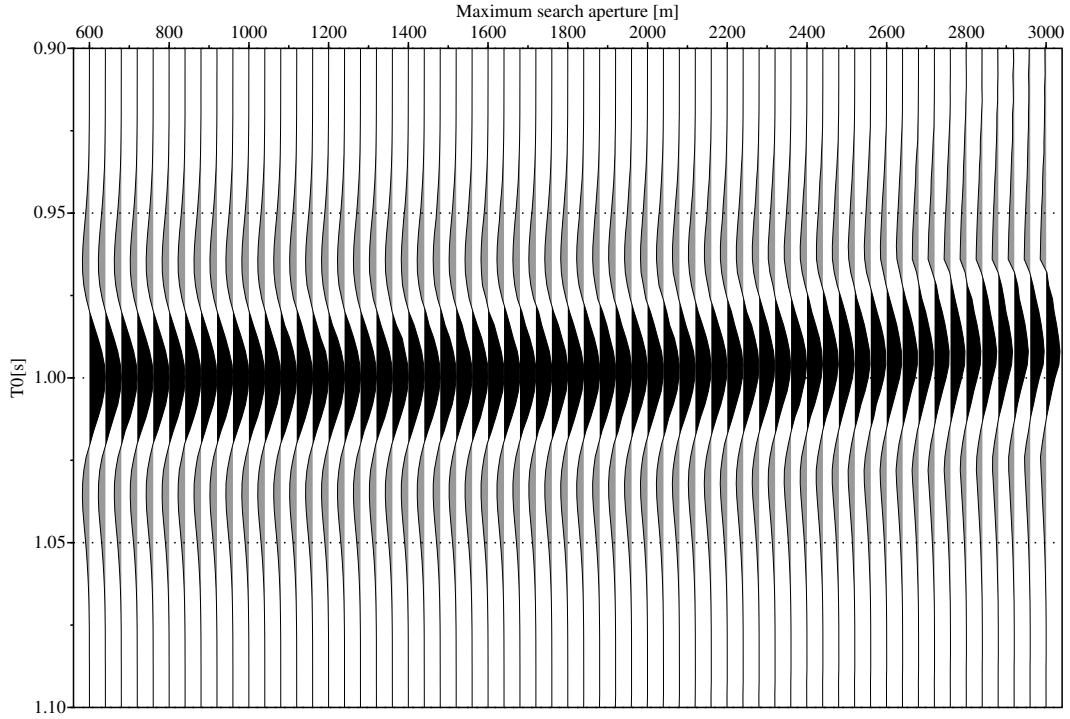


Figure 4.2: CMP stacked traces obtained from coherence analyses with different search apertures. Each trace is related to a specific coherence analysis with the corresponding maximum search aperture.

the ZO traveltime $T_0 = 1$ s the white trajectory denotes the searched-for traveltime curve for a coherence analysis based on a hyperbolic ZO traveltime approximation. Such a 2D stacking operator with its expansion point at half-offset $h = 0$ reads

$$T^2 = T_0^2 + M h^2, \quad (4.1)$$

with $M = 2T_0 \partial^2 T / \partial h^2|_{h=0}$ being the stacking parameter. A comparison of this series expansion with the 2D CRS stacking operator (3.33) shows that M is related to K_{NIP}^{2D} and β_a by

$$M = \frac{2T_0 \cos^2 \beta_a}{v_0} K_{\text{NIP}}^{2D}. \quad (4.2)$$

Correctly stacked, the results should show a CMP stacked trace with a zero-phase wavelet centred around $T_0 = 1$ s and a respective stacking parameter value of $M = 2.5 \times 10^{-7} \text{ s}^2/\text{m}^2$. Note that M should vary systematically along the wavelet (see, e. g., Mann and Höcht, 2003). This will become evident in Figures 4.3 and 4.8.

On this dataset, a number of coherence analyses with different maximum search apertures (ranging from 600 m to 3000 m, increment 40 m, the black lines in Figure 4.1 denote the absolute minimum and maximum search apertures) were performed. The resulting CMP stacked traces and the traces containing the optimum fit stacking parameter M_S form new sections which can be sorted according to their corresponding maximum search aperture (see Figures 4.2 and 4.3). These figures show the effect

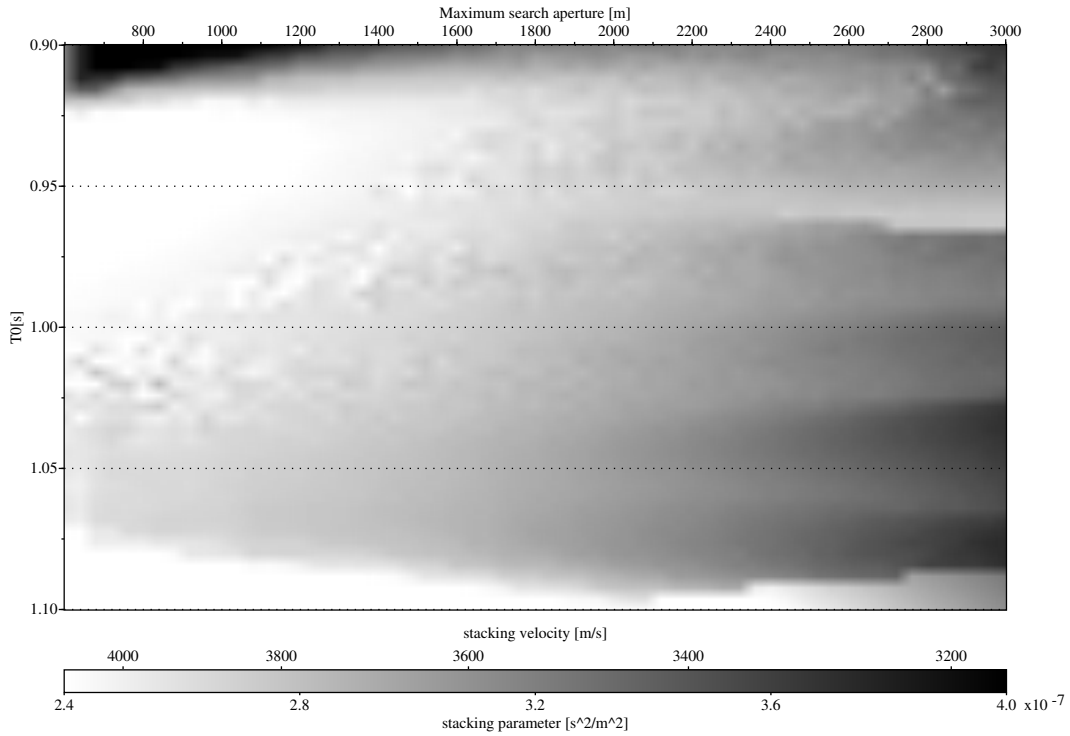


Figure 4.3: Stacking parameter M section obtained from coherence analyses with different maximum search apertures. Note the variation of parameter M with increasing aperture in the time range covered by the wavelet (around $T = 1$ s, see Figure 4.2). Note that the stacking velocity scale is nonlinear.

of the spread-length bias, i. e., an increasing bias in stack time as well as in the stacking parameter with increasing aperture size.

More insight into the spread-length bias can be obtained by picking the maxima of the wavelets and the corresponding optimum fit stacking parameters M_S in the respective sections. Figures 4.4 and 4.5 depict these values over the mean-square aperture

$$\sigma = \frac{1}{N} \sum_{i=1}^N h_i^2, \quad (4.3)$$

which represents a squared average offset of all N stacked traces. The spread-length bias in stack time T_S and stacking parameter M_S shows an almost linear trend starting from the correct intercept at $\sigma = 0$. The latter is not surprising as $\sigma = 0$ equals zero search aperture, i. e., only the expansion point (where stack time and stacking parameter are defined) is considered. In fact, the representation in terms of (T_S, σ) and (M_S, σ) , respectively, turns out to constitute the most accurate linear representation of the spread-length bias in the CMP domain¹. Thus, it may be approximated by the first order

¹For other domains the relationship may differ but in the scope of this thesis the consideration of the CMP domain is sufficient.

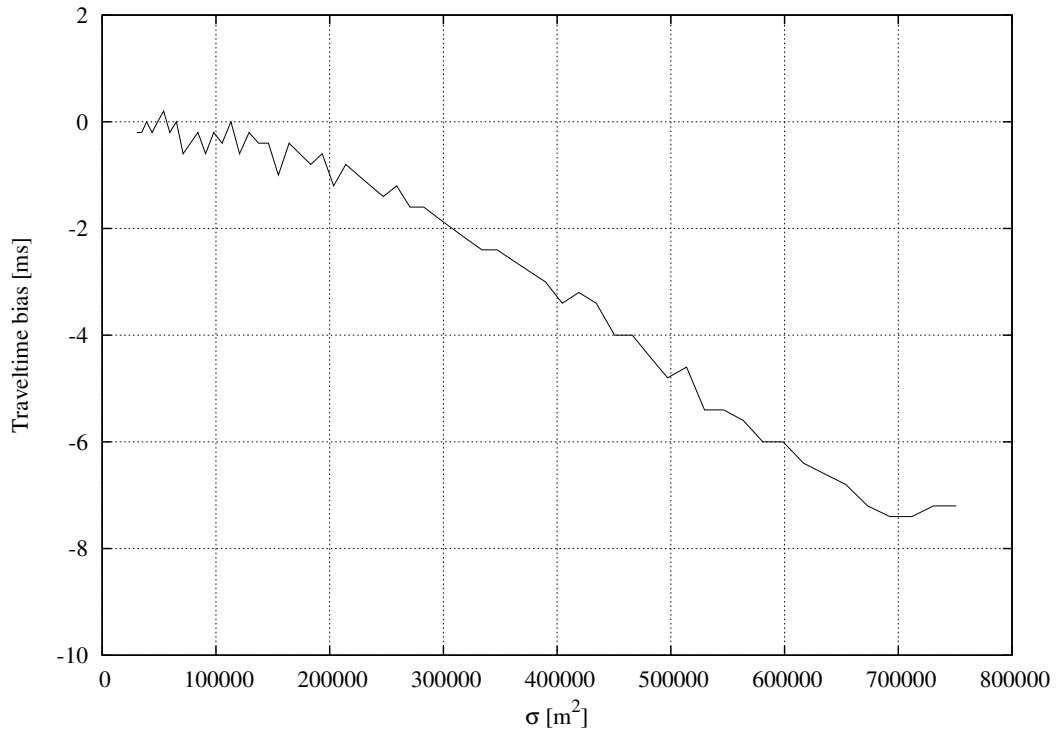


Figure 4.4: Traveltime bias over mean-square aperture σ picked at the maximum of the wavelet.

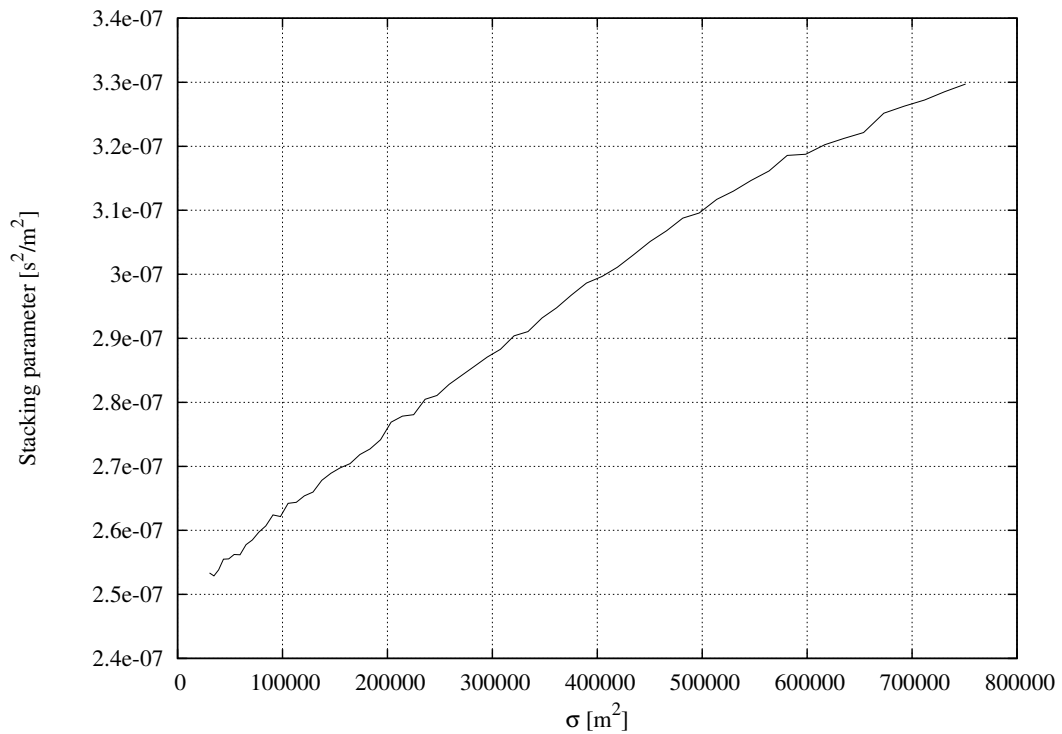


Figure 4.5: Value of the optimum fit stacking parameter M_S over mean-square aperture σ picked at the maximum of the wavelet. In terms of stacking velocities v_{st} the displayed stacking parameter ranges from 4082 ($M = 2.4 \times 10^{-7} \text{ s}^2/\text{m}^2$) to 3430 m/s ($M = 3.4 \times 10^{-7} \text{ s}^2/\text{m}^2$).

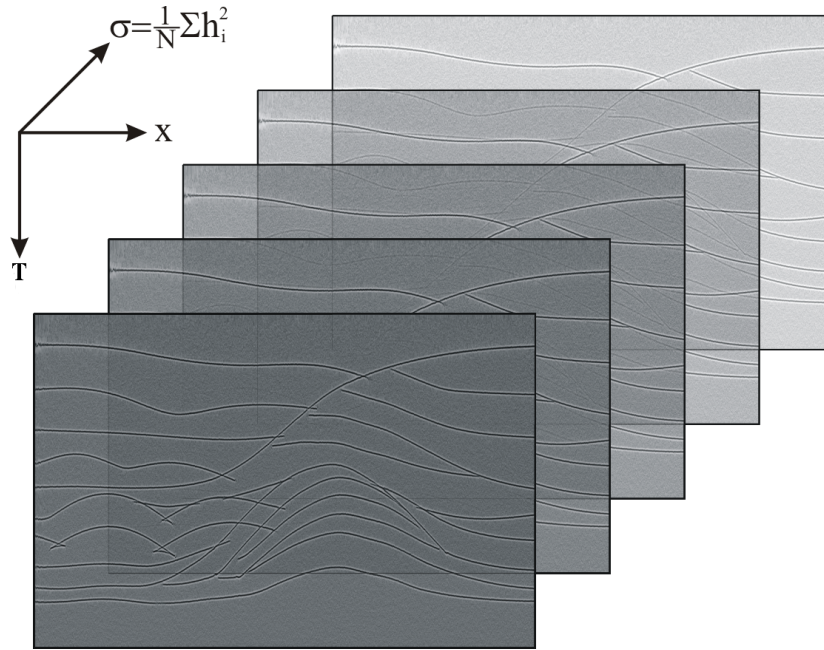


Figure 4.6: Definition of the multi-section volume. Each plane represents a CMP stacked section for a particular mean-square aperture σ . All these planes together form the MSS volume.

expansion

$$T_S(\sigma) = T_{ZO} + a \cdot \sigma, \quad (4.4)$$

$$M_S(\sigma, t_S) = M_{T_{ZO}} + b \cdot \sigma, \quad (4.5)$$

where T_{ZO} and $M_{T_{ZO}}$ denote the actually searched-for true ZO stack times and stacking parameters. Equations (4.4) and (4.5) state that with the knowledge of the attributes a and b which describe the spread-length bias the optimum fit quantities T_S and M_S can be approximately computed from correct attributes T_{ZO} and $M_{T_{ZO}}$ and vice versa.

For horizontally layered media the linear relationship can also be justified by theory (Al-Chalabi, 1974). For more complex moveouts this approximation may be insufficient. However, in practice equations (4.4) and (4.5) appear to provide a good compromise between computational cost and achievable accuracy.

4.2 Correction of the spread-length bias

Based on equations (4.4) and (4.5) the spread-length bias can be corrected in two subsequent automated steps. Firstly, the stack time bias is corrected. This yields a stacked section with correctly positioned reflection events and a section containing the attribute a which describes the spread-length bias of the stack time. In the second step this attribute is used to correct the stacking parameter M_S to obtain $M_{T_{ZO}}$.

The corrections are carried out in multi-section volumes (see Figure 4.6). These volumes are defined by the mean-square aperture σ , stack time T_s , and trace location x and can be obtained as follows:

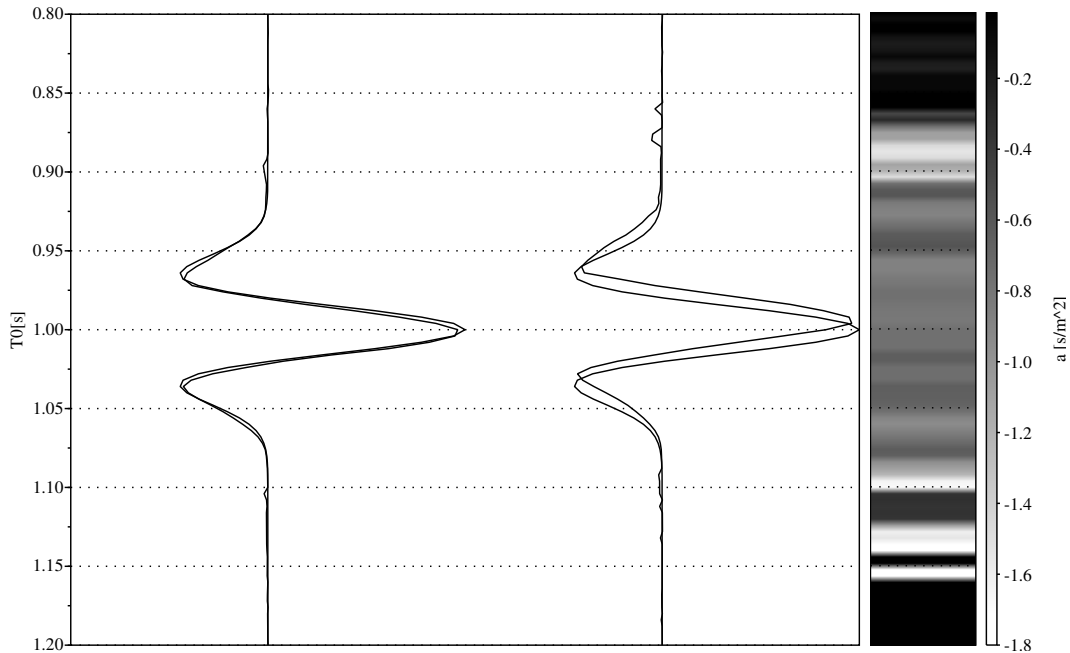


Figure 4.7: Results of the stack time correction. Left: overlay of the forward modelled ZO trace with the corrected (left part) and the conventional stack (right part), respectively. Right: corresponding section with attribute a . Note that this attribute is only meaningful for traveltimes covered by the wavelet.

when performing coherence analyses on a full 2D dataset, one conventional (x, T_s) -section is obtained for each specific maximum search aperture (which is related to a respective mean-square aperture σ). Arranging all these sections according to their mean-square aperture σ builds the multi-section volume. As coherence analyses yield stacked sections as well as one additional section for each stacking parameter in the traveltime approximation, I distinguish between Multi-Section-Stack (MSS) volumes and Multi-Section-Attribute (MSA) volumes, respectively.

4.2.1 Correction of the stack time

The stack time is corrected by introducing an additional coherence analysis in the MSS volume. The respective stacking operator is based on the linear approximation of the spread-length bias given by equation (4.4). This stacking operator is related to the searched-for true ZO stack time T_{ZO} which corresponds to mean-square aperture $\sigma = 0$. In terms of the MSS volume this is equivalent to the section $MSS(x, T_s(\sigma = 0) = T_{ZO}, \sigma = 0)$. Outcome of this coherence analysis is a section containing the stacking parameter a which parameterises the spread-length bias in the stack time. As this attribute is available for each sample of the output section it can be used to perform a stack and, thus, to construct a stacked section with stack time corrected reflection events.

Figure 4.7 shows the results of this correction for the dataset introduced above. On the right hand side, the section containing attribute a is shown and on the left hand side an overlay of the correct ZO trace with the one obtained after correction. Compared to the overlay with a conventionally stacked trace

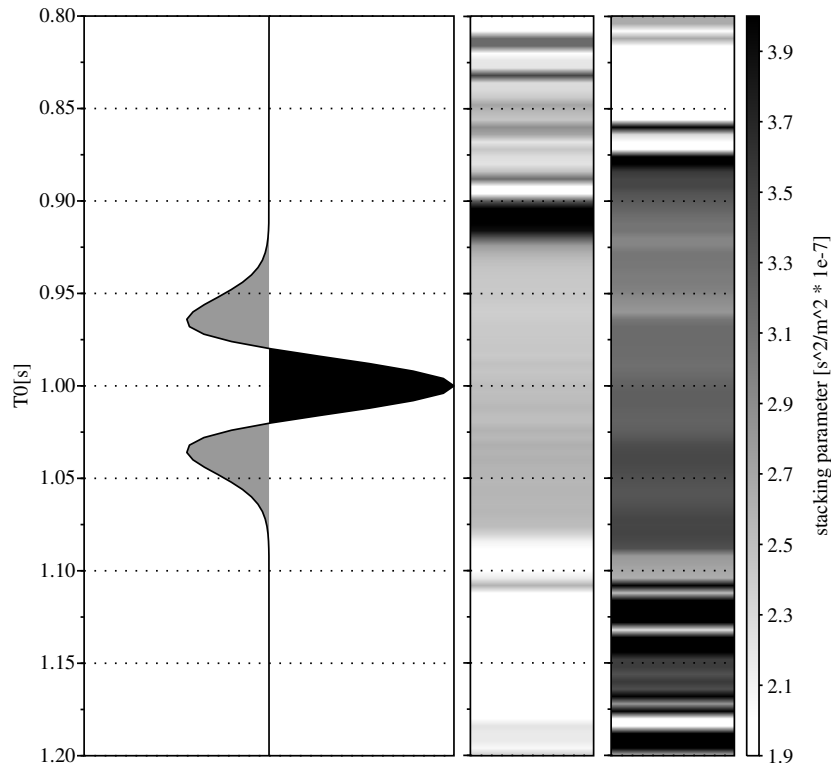


Figure 4.8: Results of the stacking parameter correction. Left: forward modelled ZO trace. Middle: stacking parameter after correction. Right: conventionally obtained stacking parameter (maximum search aperture of 2500 m). Note the systematic variation of the stacking parameter along the wavelet.

(search aperture of 2500 m, right part) it can be seen that the stack time bias has almost completely vanished.

4.2.2 Correction of the stacking parameter bias

With the knowledge of attribute a from the previous step, stacking parameters $M_S(\sigma, T_s)$ can now be corrected to $M_{T_{ZO}}$. Again, the correction is carried out in a multi-section volume, this time in the MSA volume. Similar to the correction of the stack time the output section is related to $\sigma = 0$ and, thus, to the section $MSA(x, T_s(\sigma = 0) = T_{ZO}, \sigma = 0)$. As attribute a describes the amount of spread-length bias in stack time it can be used (together with stacking operator (4.4)) to construct trajectories in the MSA volume which denote data belonging to a specific point (x, T_{ZO}) . That means, for a specific location on the stacking parameter output section the trajectory of the corresponding attribute a can be used to automatically pick all the stacking parameters M_S related to this position in the MSA volume. These picks form a set of points $(M_S(\sigma), \sigma)$ which can, according to equation (4.5), be used in a linear regression to extrapolate $M_S(\sigma = 0) = M_{T_{ZO}}$. Performed for each sample on the output section this correction yields a section with corrected stacking parameters $M_{T_{ZO}}(T_{ZO}, x)$.

Figure 4.8 shows the results of this procedure applied to the same dataset as above. As can be seen in the middle part of the figure the value of the corrected stacking parameter is now very close to the

searched-for value of $M = 2.5 \times 10^{-7} \text{ s}^2/\text{m}^2$. The difference to a conventionally obtained parameter (right part) is quite significant. Note that coherence analyses only yield reliable results in time ranges with actual reflection events. This explains the strange behaviour of the stacking parameter outside of the wavelet.

4.3 Implementation of the CRS stack for the treatment of the spread-length bias

The structure of the CRS workflow for the treatment of the spread-length bias is basically the same as the conventional one presented in Chapter 3.5. Again, the first step is carried out in the CMP domain. However, instead of a single coherence analysis, a number of analyses with different maximum search apertures are performed. The obtained MSS and MSA volumes are corrected for the spread-length bias according to the previously described method. Outcome of this step are a stack-time-corrected ZO stack and a section with a corrected stacking parameter M_{corr} . In case of spread-length bias both sections differ from the sections obtained from conventional processing.

Similar to the conventional implementation the corrected stacked section now enters into the two ZO searches for α and K_N . In principle, it is now possible to perform multiple coherence analyses and the respective spread-length bias corrections for these two searches. However, due to the improved signal-to-noise ratio in the stacked ZO section compared to the prestack data, these searches can be applied with significantly smaller search apertures than the automatic CMP stack. This means that the spread-length bias is also significantly smaller and can be neglected in practice which allows to perform conventional searches. The attribute sections obtained by these two searches will nevertheless be different from the conventional ones as the input is a stacked section with correctly positioned reflection events. As a consequence, the two attributes α and K_N will automatically have the (for the presented search strategy) optimum achievable quality.

So, the results of this processing scheme are three sections with the corrected kinematic wavefield attributes $K_{\text{NIP,corr}}$, $K_{\text{N,corr}}$, and α_{corr} and the stack-time-corrected ZO section obtained by the spread-length bias correction of the MSS volume of the automatic CMP stack.

Note that it is not reasonable to perform a full CRS stack on the prestack data with corrected attributes $K_{\text{NIP,corr}}$, $K_{\text{N,corr}}$, and α_{corr} . These attributes are not designed to maximise the coherence value and, thus, to produce the best image. In order to perform a CRS stack, the attributes have to be extrapolated back to the desired stacking aperture. Besides the fact that this is only possible for the attribute $K_{\text{NIP,corr}}$ ($K_{\text{N,corr}}$ and α_{corr} are not explicitly corrected and, thus, no extrapolation operator is available), it is pointless to use corrected quantities to obtain uncorrected results. A conventional processing is in that case faster and yields, due to the missing extrapolation, a CRS stacked section of better quality.

Drawback of the presented implementation is that the stack-time-corrected section is not a CRS stacked section. However, as the focus is not on image quality (i. e., the optimisation of the signal-to-noise ratio) this is actually not a problem. Another point which may be considered as problematic is the computational cost of the method as the correction is based on multiple coherence analyses and the calculation of linear regressions. In the current implementation the computing time for the correction itself, i. e., the application of the additional coherence analysis and the linear regression, can be neglected compared to full CRS processing sequence. What remains is the calculation of the multiple coherence analyses in the CMP domain. Here, the implementation makes use of the results

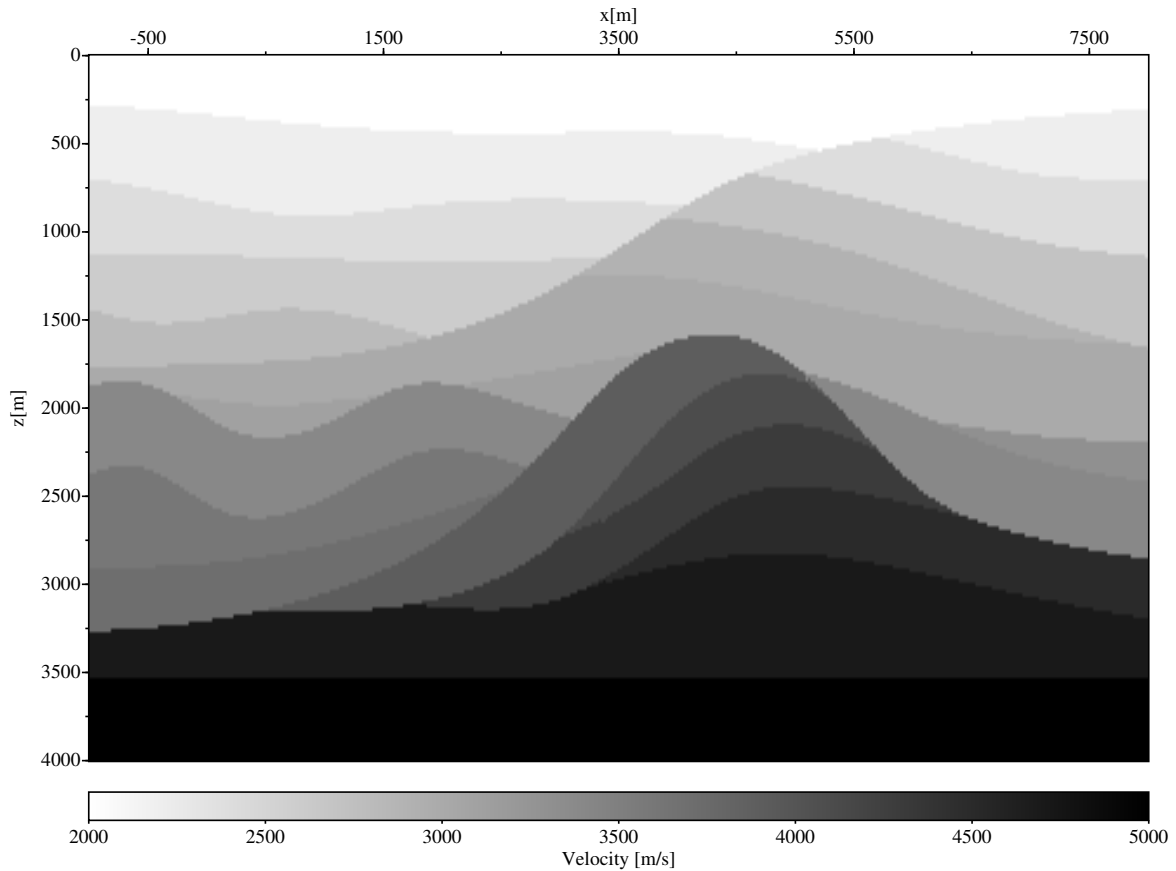


Figure 4.9: P-wave velocity model used for the generation of the synthetic dataset.

of the previous step to perform the subsequent coherence analysis. That means, that the required CPU time for n coherence analyses is significantly less than n times the CPU time for one analysis and so this should be no problem, especially as 2D processing is considered here.

4.4 Synthetic data example

The proposed technique has been applied to a synthetic data example based on the P-wave velocity model displayed in Figure 4.9. The corresponding S-wave velocity and density model are not depicted as only primary P-waves are modelled. Amplitude and phase variations with offset were not considered in the modelling. Thus, only the kinematics of the reflection events enter into the subsequent applications. In context with spread-length bias, the interesting part of this model is the dome in the centre. In this region the prestack data shows the largest deviations to the hyperbolic approximation used in the CRS stack.

The modelled prestack data consists of 933 CMP gathers with a midpoint spacing of 15 m and an offset spacing of 60 m. For data generation a 30Hz zero-phase Ricker wavelet was used. In addition, a high noise level was added to the data. Figure 4.10 shows a forward modelled ZO section corresponding to

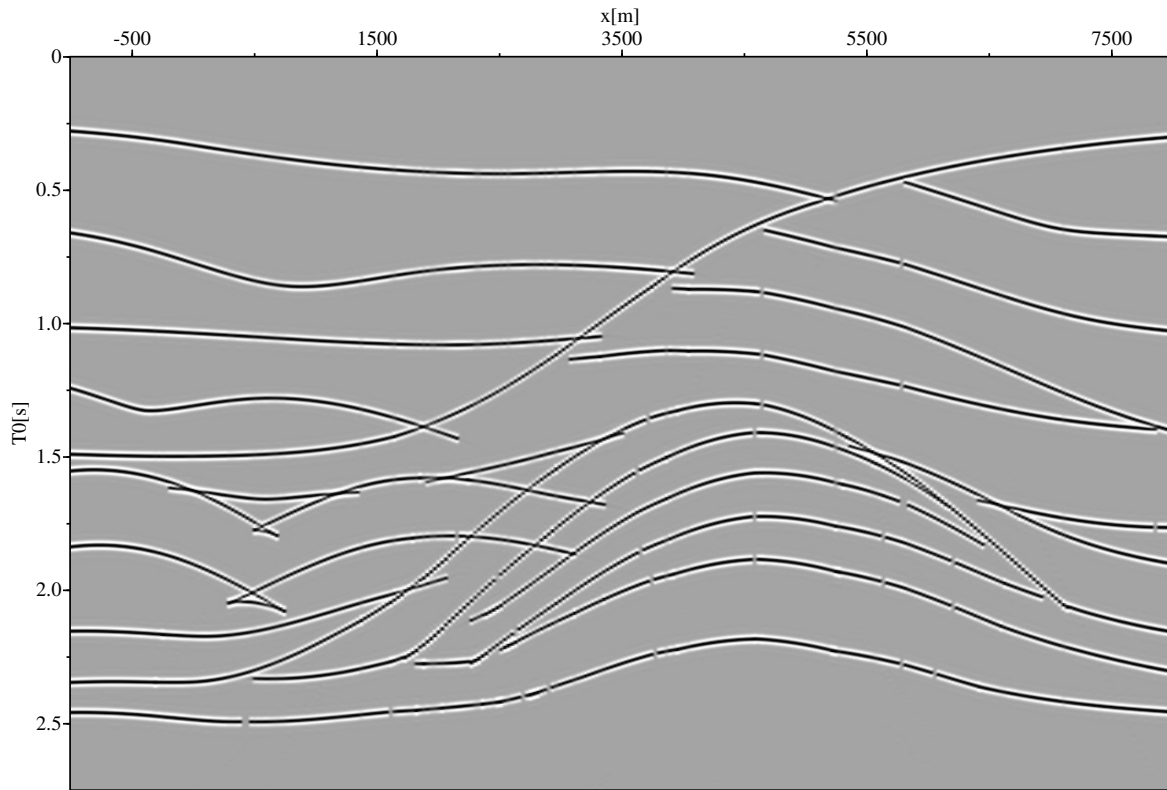


Figure 4.10: Forward modelled ZO section. Gaps on the reflection events, e. g., at $x = 4500$ m and $t = 0.8$ s, are due to missing diffractions and artifacts of the ray-tracing.

this model (without noise). Holes on the reflection events are due to missing diffractions and artifacts of the wavefront construction method.

The data was CRS processed according to the procedure described above. In a first step, multiple CMP stacks with maximum search apertures ranging from 1000 m to 3200 m were performed. The corresponding MSS and MSA volumes were then corrected for the spread-length bias. The results of this step were a stacked ZO section with corrected stack times and a section containing the corrected stacking parameter M_{corr} . The attributes α_{corr} and R_{NC} were finally obtained using the stack time corrected ZO section as input for the linear and hyperbolic ZO search, respectively.

Figure 4.11 shows two close-ups of the dome. The figure on top is an overlay of the forward modelled ZO section with the stack time corrected section. The stack times are significantly less biased compared with the lower figure which depicts an overlay with a conventionally obtained ZO section.

A comparison of the corrected and the conventionally obtained parameter M_{corr} is displayed in Figure 4.12 and reveals differences up to 50%.

Figure 4.13 finally illustrates the differences that appear in the kinematic wavefield attribute α when using corrected or conventional ZO sections as input, respectively. Similar results are obtained for the deviations of K_{N} (not shown).

At this point, a stack-time-corrected ZO section as well as the three corrected kinematic wavefield

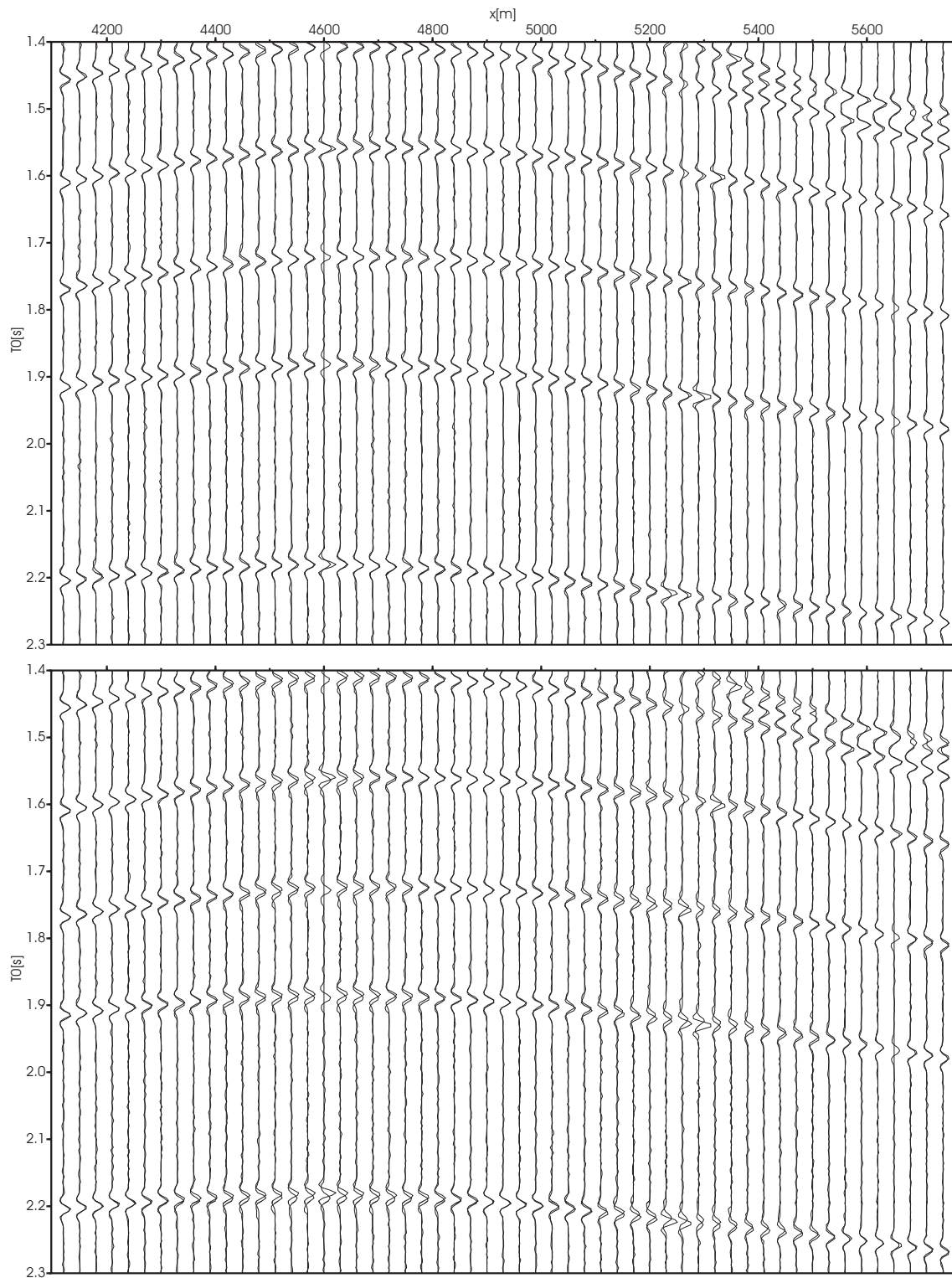


Figure 4.11: Detailed view at the dome. Bottom: overlay of the forward modelled ZO section (with-noise) with a conventionally obtained ZO section (maximum search aperture: 3200 m). Note the stack time bias which is up to a quarter of the wavelet length. Top: overlay with the stack time corrected section. This figure shows that the spread-length bias almost completely vanishes after stack time correction.

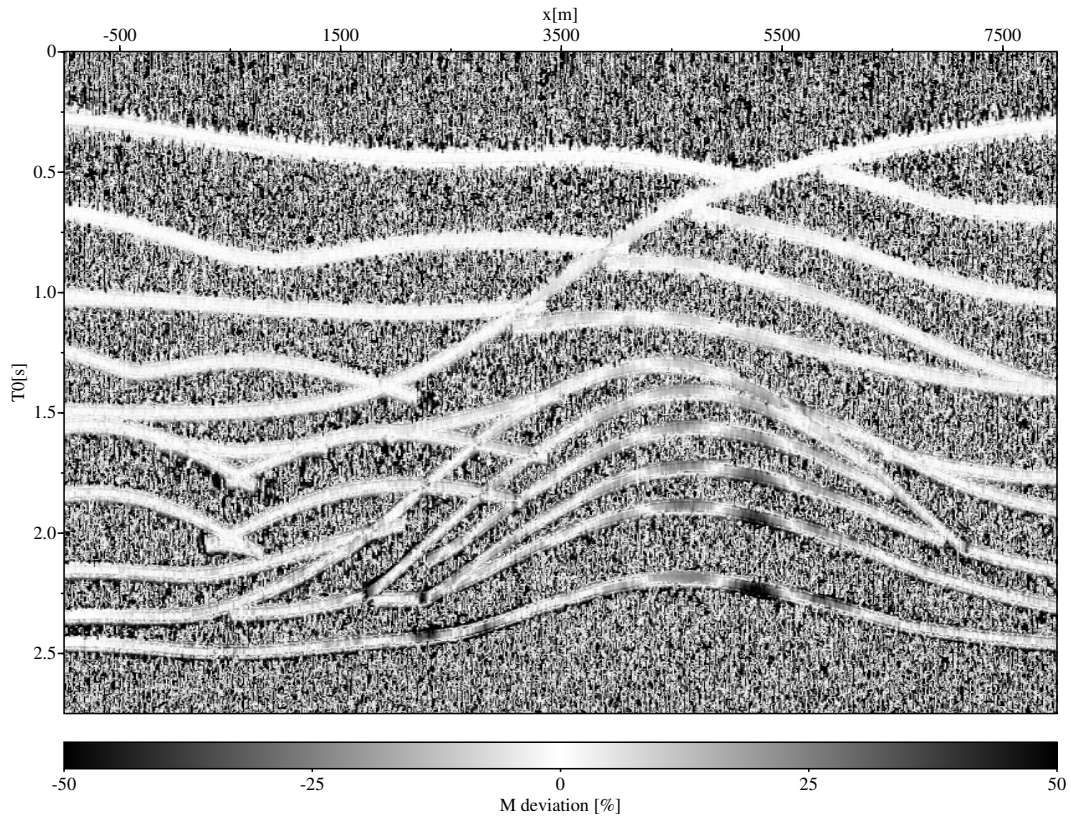


Figure 4.12: Percentile difference between the spread-length bias corrected stacking parameter M_{corr} and a conventionally obtained stacking parameter (maximum search aperture: 3200 m). The largest bias occurs in the region of the dome. Due to the stack time bias the differences should only be considered in the centres of the time ranges containing reflection events.

attribute sections are available for further processing. In order to check the quality of these quantities they were used in a CRS-based tomographic inversion for the determination of a smooth migration velocity model (Duveneck, 2004). As will be shown in Chapter 6 this model is obtained by minimising a cost function, i. e., an optimum model m is sought, such that the misfit between the input data $d_{\text{in}} = (x_0, t_0, \alpha, K_{\text{NIP}})$ and the corresponding forward modelled values $d_{\text{mod}} = f(m)$ is minimised. So, the input data d_{in} mainly consist of the quantities affected by the spread-length bias. A subsequent prestack depth migration (PSDM) allows to indirectly check the consistency of the corrected attributes with the data. The processing was performed with the same setup for the corrected and for the conventional workflow.

Figure 4.14 (top) shows the velocity model obtained by the tomographic inversion with spread-length bias corrected input data. Due to the smooth parameterisation the result shows far less details compared to the original velocity model in Figure 4.9. However, the general structure, e. g., the dome in the centre, can still be identified. A comparison with the tomographic velocity model obtained from conventional attributes (maximum search aperture of 3200 m) reveals that the velocities differ up to 250 m/s in the dome (Figure 4.14 (bottom)). As depicted in Figure 4.15, these differences can, of course, not be ignored when performing depth migration. In general, the common-image gath-

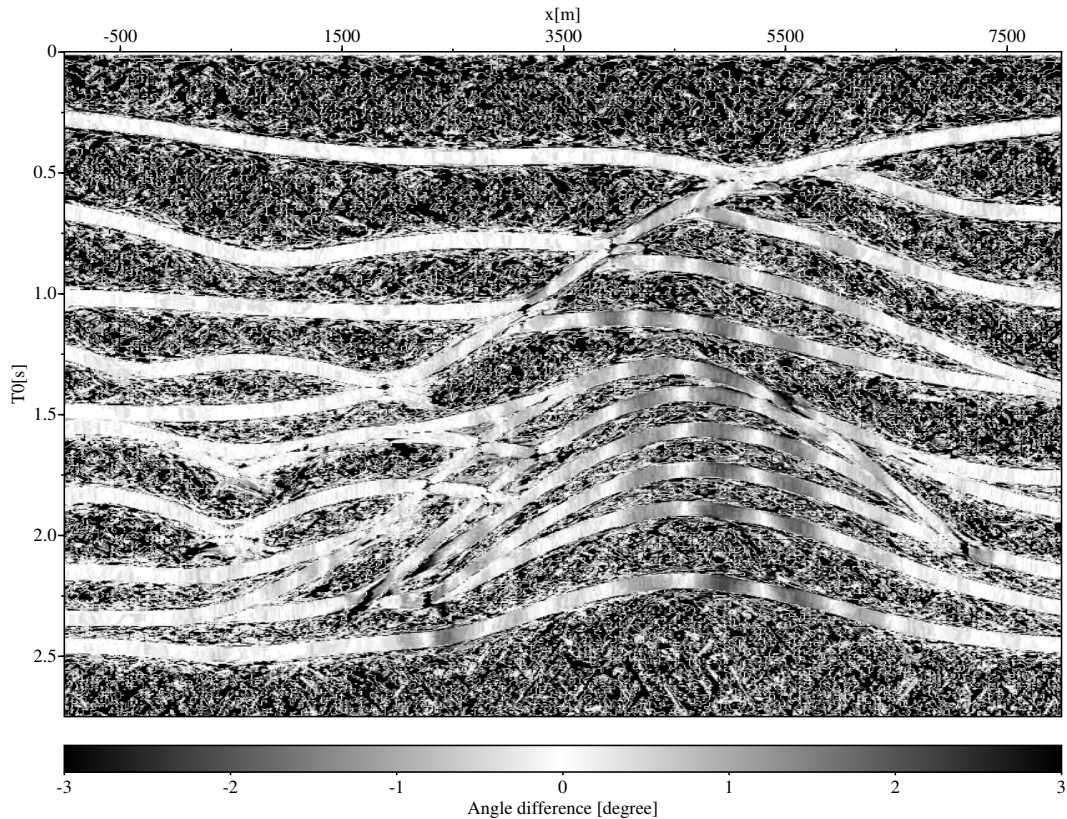


Figure 4.13: Differences between the kinematic wavefield attribute α_{corr} and a conventional α (maximum search aperture in the CMP gathers: 3200 m) due to the use of different stacked input sections in the search routine. Similar to Figure 4.12 only the centres of the time ranges containing reflection events should be considered.

ers (here with offsets up to 2000 m) obtained with the velocity model from corrected quantities have significantly less moveout than the ones obtained with the conventional velocity model. Also the locations of the reflectors are in many cases more accurate when using corrected attributes. This demonstrates that the spread-length bias correction indeed results in improved attributes and stack times.

4.5 Further aspects

Currently, an implementation of the correction technique is, under consideration of the computational cost, only reasonable for the 2D CRS stack. For the 3D CRS stack it is required to perform multiple searches for three parameters which is beyond the possibilities of today's computer hardware. However, a transition from the 2D to the 3D correction technique is theoretically straightforward. First, the five-dimensional MSS and MSA volumes are created from three-parameter CMP searches. The MSS volume is then used by a coherence analysis for the correction of the stack time bias. The corresponding stacking operator is a three-dimensional extension to the 2D operator (4.4). Afterwards, the results

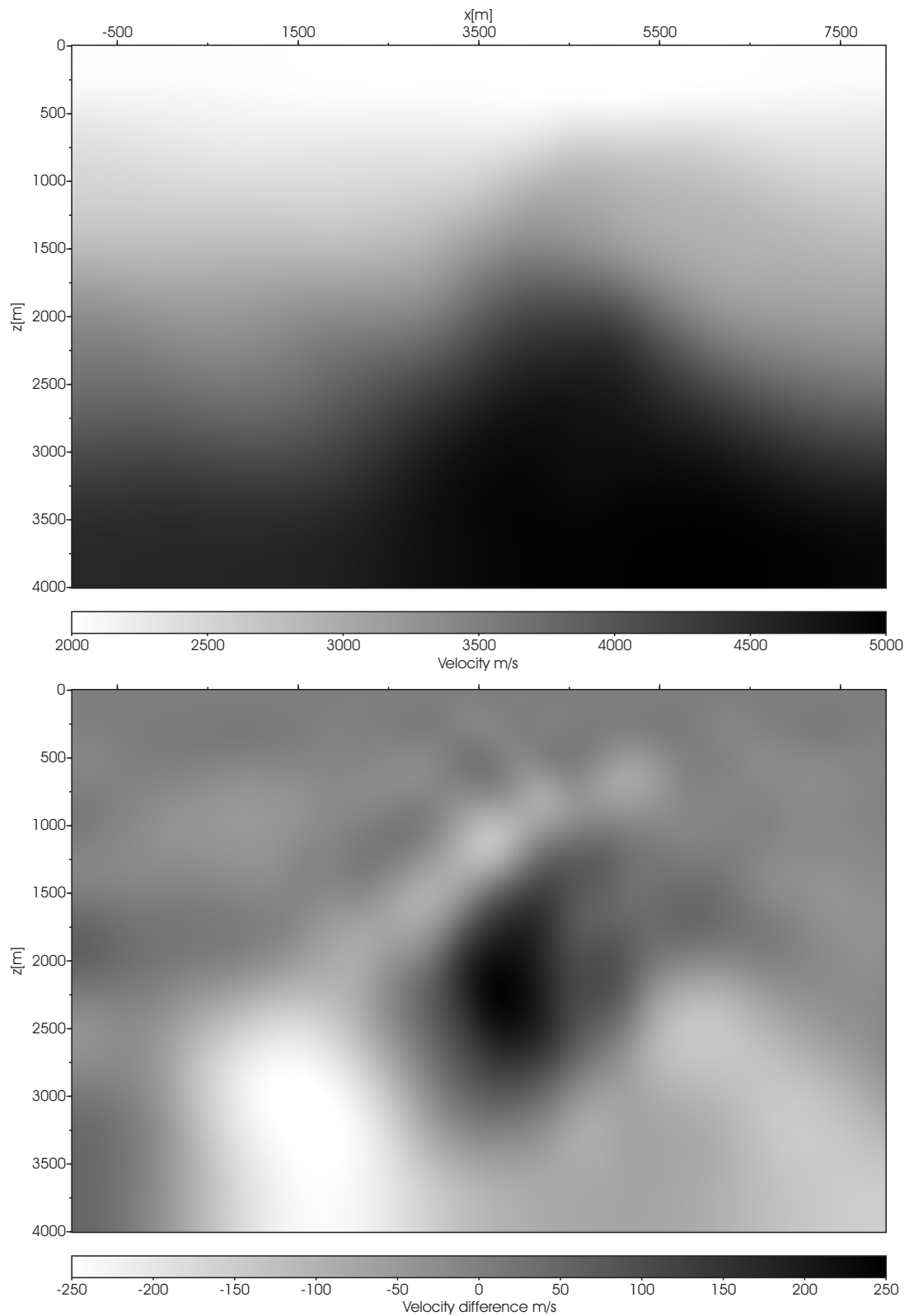


Figure 4.14: Top: smooth velocity model obtained from CRS-based tomographic inversion with spread-length bias corrected attributes and stack times. Bottom: difference in velocity models obtained by tomographic inversion with corrected and conventional attributes, respectively.

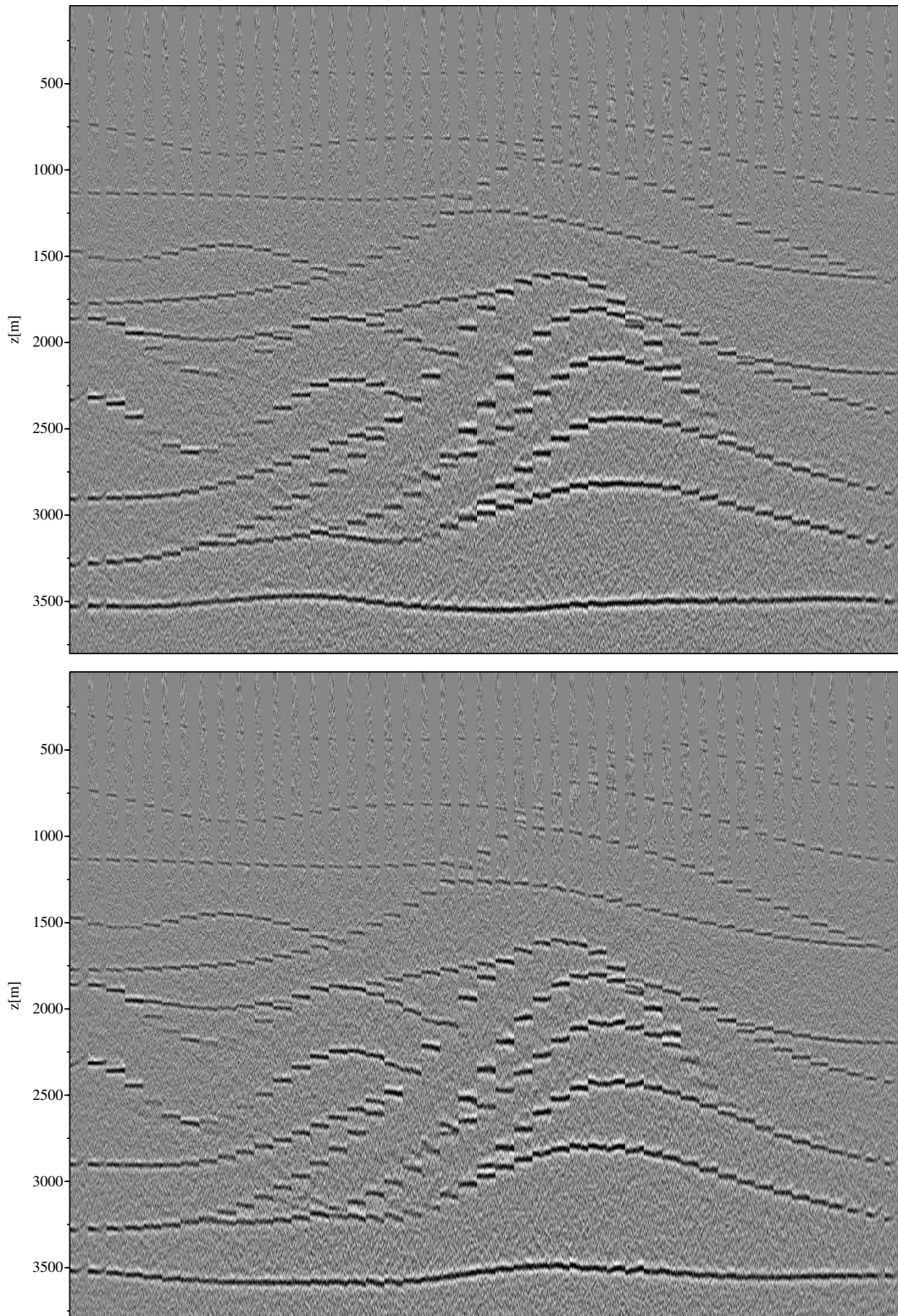


Figure 4.15: Results of prestack depth migration (PSDM). Top: common-image gathers (maximum offset 2000 m, common-image gathers every 200 m) after PSDM based on the velocity model from corrected attributes and stack times. Bottom: the same common-image gathers obtained by PSDM based on a velocity model determined from conventional attributes.

of this step are used in the linear regression which yields the corrected wavefield attributes. Again, the correction is carried out on a three-dimensional operator based on equation (4.5). Finally, the remaining steps, i. e., the determination of the emergence angles and the curvatures of the normal wavefront, are carried out similar to the conventional implementation.

As a last point, it should be noted that the corrected attributes are, similar to the conventional ones, still second-order attributes. That means that the described method is especially useful for data which do not deviate significantly from second-order. In that case, the subsequent second-order applications will yield more reliable results.

Chapter 5

Automatic picking of reflection events

The use of techniques that are applied to exactly defined stratigraphic sequences on the stacked data, e. g., layer-based inversion methods, require the extraction of continuous reflection events and stacking parameters from the respective data volumes. If performed manually, this task is rather cumbersome and errorprone. Furthermore, in case of 3D data, an appropriate visualisation of the data is difficult. Therefore, algorithms that allow an automatic tracking of events are desirable. In this chapter a technique that uses the kinematic wavefield attributes of the 3D CRS stack is presented. The method is suited for arbitrary acquisition geometries and automatically bypasses areas with insufficient information for reliable tracking.

5.1 Event tracking in ZO volumes with the CRS operator

The CRS stacking operator (3.25) provides the curvature matrix \mathbf{K}_N and the direction vector $\mathbf{w}^{(x)}$ of the normal wave at the surface. Actually, these quantities are directly related to the local curvature and orientation of the reflection event at the respective location in the ZO stack volume. Thus, if a point A on an arbitrary event is considered and the corresponding wavefield attributes are known, the ZO representation (3.41) of the complete CRS operator can be used to approximate the spatial continuation to a point B of the event on a trace in the vicinity of A (see Figure 5.1, left). As the CRS stack is usually performed for each sample of the stacked ZO volume, the wavefield attributes and, thus, an approximation for the continuation is also known at each sample. This means that a reflection event can be tracked automatically if only a single seed point on the selected event is given. However, an implementation based solely on the calculation of the continuation is insufficient to perform a consistent tracking as it does not account for discontinuous events which may occur, e. g., at faults or in regions of poor signal-to-noise ratio. In that case, continuations can be evaluated but they are actually meaningless as they point to positions where the reflection event does not exist (see Figure 5.1, right). Therefore, additional criteria to validate the consistency of the continuations are required. Depending on the available data arbitrary criteria can be defined. A restriction to information that is available from the CRS technique only yields, amongst others, the following conditions:

Continuity of the kinematic wavefield attributes. Along the reflection events the wavefield attributes should vary smoothly (Hertweck et al., 2005). Thus, the attributes at point A should not substantially differ from the attributes on the continuation point B . Therefore, a user given variational threshold can be used as a validation criterion.

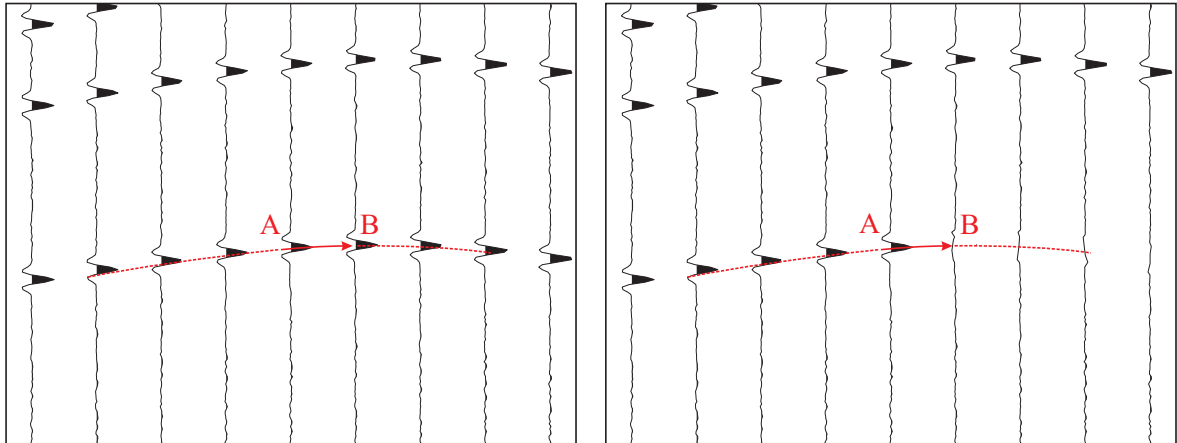


Figure 5.1: Left: if a point A on the event is given the corresponding wavefield attributes together with the ZO representation (3.41) of the CRS operator yield an approximation for the spatial continuation B of the reflection. Right: an event tracking solely based on kinematic wavefield attributes does not account for discontinuous reflection events. The continuation evaluated at point A leads to a location B where the reflection event does not exist.

Continuity of the coherence values. Similar to the wavefield attributes the coherence value should vary smoothly from A to B . Thus, a threshold for the coherence variation can be used, too.

Coherence threshold. The coherence values are highest on the reflection events. Therefore, a threshold for the minimal accepted coherence value indicates whether B is considered to lie on the reflection event.

Stack amplitude differences. Similar to the other quantities the stack amplitude is assumed to vary smoothly. Thus, a threshold for the stack amplitude variation can be introduced, too.

Other criteria, which are not related to the CRS technique, are, for instance, thresholds based on instantaneous quantities (e. g., instantaneous phase or frequency). Also, additional coherence criteria may be applied to the data.

In addition to the above mentioned validation criteria the evaluated continuation has to be refined. This is due to the fact that the attributes used for the calculation of the continuation are determined from data within a search aperture, i. e., they are obtained as best fit attributes from a number of traces. Therefore, the calculated continuation B will most likely not coincide with the true continuation B_T . However, as the spatial distance to the continuation is usually significantly smaller than the search aperture, it can be expected that B is at least located within the wavelet that defines the reflection event. As B_T is usually defined to be associated with the absolute maximum stack energy of the wavelet the refinement consists of the determination of this energy within a user-defined window centred around B .

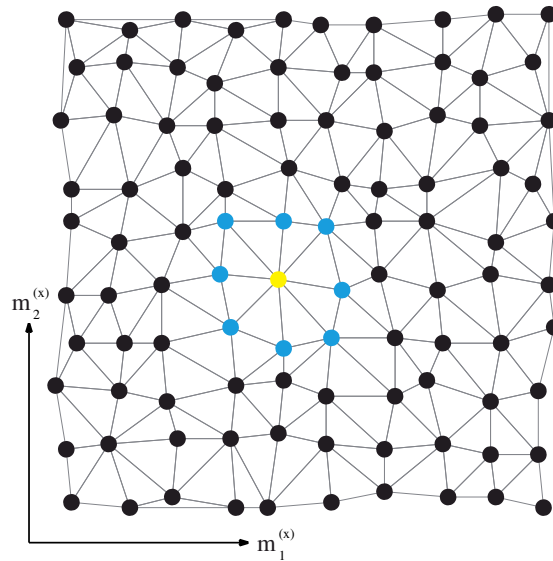


Figure 5.2: After Delaunay triangulation the nearest neighbouring traces (depicted in blue) to an arbitrary central trace (yellow) are given by all the traces that share a triangle with it.

5.2 Navigation in ZO volumes

For 3D data the proper selection of the traces for the calculation of the continuation is essential as it defines the movement scheme and the regions in the data that are covered by the algorithm. In the following it is assumed that the selected reflection events appear only once on each trace, respectively. If this is not the case, e. g., along triplications, the tracking has to be performed independently for each of the segments. Using this assumption the navigation in the ZO data volumes $(T, \mathbf{m}^{(x)})$ can be split into two independent routines, one which controls the movement along the T -axis and one for the movement in the midpoint plane $\mathbf{m}^{(x)}$. Actually, the former movement defines the continuation and therefore it is given by the evaluation of the CRS operator (3.41) with the proper wavefield attributes and validation criteria. In contrast, the movement in the $\mathbf{m}^{(x)}$ plane defines the traces along which the continuations are evaluated, i. e., it provides the input and the extrapolation direction for the tracking of the reflection events. For traces that are regularly distributed along the midpoint plane the navigation may be simply specified but for an irregular distribution of the traces the movement and the treatment of discontinuous reflection events has to be more sophisticated. Therefore, the movement scheme is realized by means of a recursive function that acts on the triangulated trace locations.

In a first step, the trace locations are triangulated using a Delaunay triangulation (Delaunay, 1934). The triangulation yields the nearest neighbouring traces to an arbitrary trace (in the following called central trace). They are given by all the traces that share a triangle with the central trace (see Figure 5.2). The spatial continuation of the selected reflection event is now evaluated for the neighbouring traces which have not yet been successfully validated (the latter condition is necessary to prevent repeated tracking of a trace from different central traces for a given seed point A). Whenever a valid continuation to any of these neighbours is found this trace becomes successor of the central trace and the above process is repeated. If no continuation is found (this may either be the case if all remaining continuations are invalid or all neighbouring traces are processed) the current central trace is discarded

and its predecessor becomes active again and continues the validation of the remaining neighbouring traces. The process terminates automatically if the active trace does not have a predecessor, i. e., it coincides with the initial trace that started the navigation, and if this trace has validated all of its neighbours. In the implementation this algorithm is realized by means of a recursive function that has the form

```
function track_event(central_trace){
  // Loop over all neighboring traces except the predecessor and
  // successfully validated neighbors
  loop(remaining_neighbouring_traces){
    // validate the current neighbor in the loop (cnl)
    validate_continuation(cnl)
    // if a valid continuation to cnl is found mark it as active
    if(cnl is valid) track_event(cnl)
    // otherwise continue with next neighbour in the loop
  }
  // if no continuation is found return to predecessor
  return
}
```

Although such a recursive function generally degrades the memory and runtime efficiency of the implementation it provides a vivid and simple solution to the navigation problem. It automatically keeps track of the movement path, i. e., it records where and when valid continuations are found, and is, thus, able to bypass regions of invalidity in the data. However, the presented algorithm is not able to track isolated valid areas in the data as each valid trace must be connected to the initial trace by a path of valid continuations. The consideration of such regions would not only require the consideration of the nearest neighbours but also the calculation of continuations to traces that are further away from the central trace which, in turn, decreases the stability of the process.

5.3 Automatic picking of a reflection event in real data

The proposed technique has been applied to a real dataset with the aim to extract primary reflection events that serve as input for layer-based inversion. For the sake of simplicity, only a selected tracked event will be presented and discussed here. Also, the detailed description of the dataset will follow later in Chapter 8.

The result of the first step, the Delaunay triangulation, is shown in Figure 5.3. As can be seen, the trace distribution is irregular in the midpoint plane. This is especially visible at the borders of the measurement area where a number of traces are missing. In the centre of the covered area the distribution is, to a large extent, regular but regions of irregularity can also be observed.

The event tracking was started in the central part of the measurement area as indicated by the cross in Figure 5.3. All the previously discussed validation criteria were applied for the validation of the continuations. Instead of the CRS stacked ZO volume a stacked volume obtained from the hyperbolic ZO search was used for the determination of the continuity of the stack amplitude. On the one hand, these volumes are characterised by reflection events with a better continuity than in CRS stacked

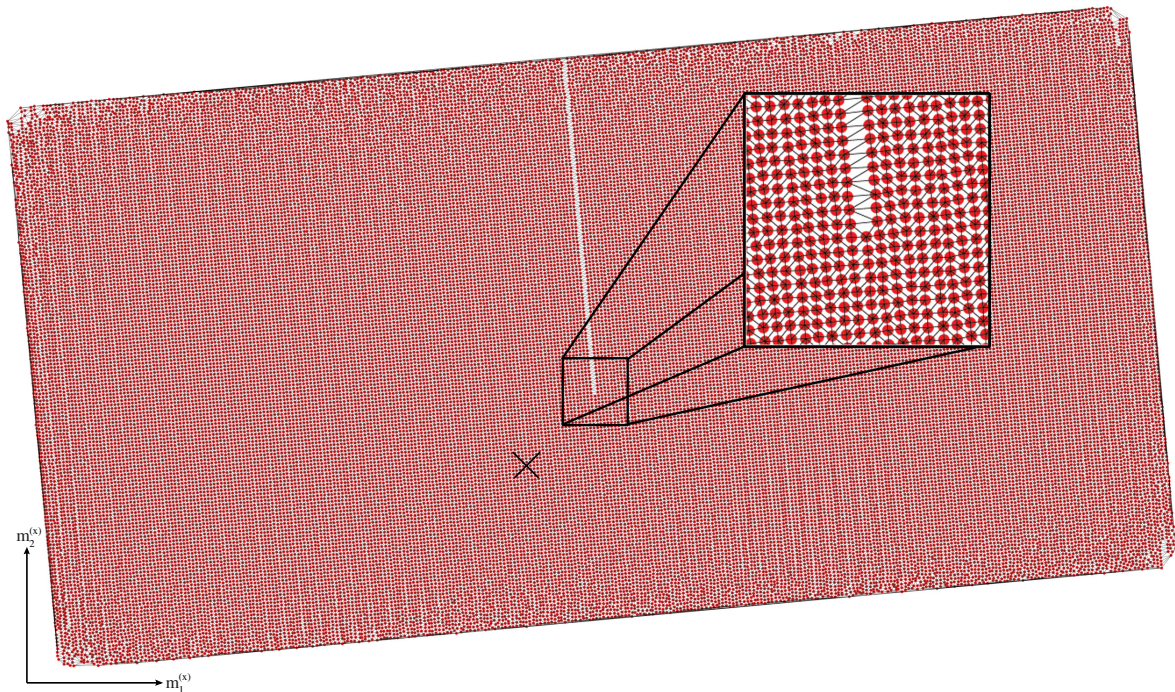


Figure 5.3: Delaunay triangulation of the trace locations (red dots). As can be seen, the distribution of the traces is irregular in the midpoint plane. The cross indicates the starting trace used for the tracking.

volumes. On the other hand, they suffer from strong artifacts. Therefore, they are well suited for the tracking if the desired event can be specified. However, for interpretation they are inadequate as it may be difficult to distinguish between artifacts and reflection events.

The results of the event tracking is depicted in Figure 5.4. Here, the tracked event is displayed together with an inline and a crossline section of the CRS stacked ZO volume. The figure shows the complete tracked event which is colour-coded with the coherence values used in the respective validation criterion. As can be seen, the extracted event almost covers the full measurement area but is also subject to a number of gaps. Figure 5.5 shows a detailed view of one of the gaps together with an inline and a crossline section of the stacked volume obtained from the hyperbolic ZO search. This figure reveals that the gaps are, in fact, due to low coherence values at their borders. Also, it can be observed that the stack amplitudes of the displayed inline and crossline strongly decrease within the area of the gap. As both quantities, coherence and stack amplitude, do enter into the validation criteria the algorithm is consequently not able to track the event in these areas.

5.4 Further aspects

In principle, the algorithm can be generalised such that reflection events can be tracked in prestack data. For that purpose, a CRS stacking operator for finite offsets (FO) is required that provides kinematic wavefield attributes describing the shape of reflection events for arbitrary locations in the data.

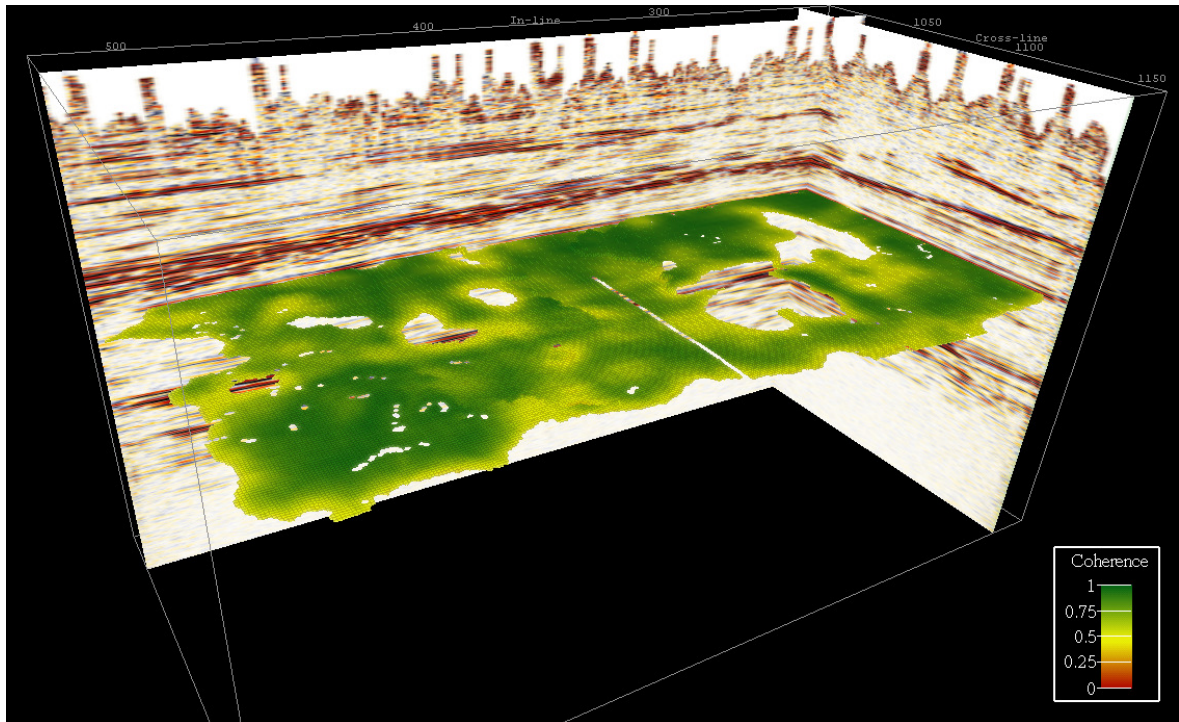


Figure 5.4: Automatically tracked reflection event. The colours on the surface indicate the respective coherence values. The inline and crossline sections are taken from the CRS stack volume.

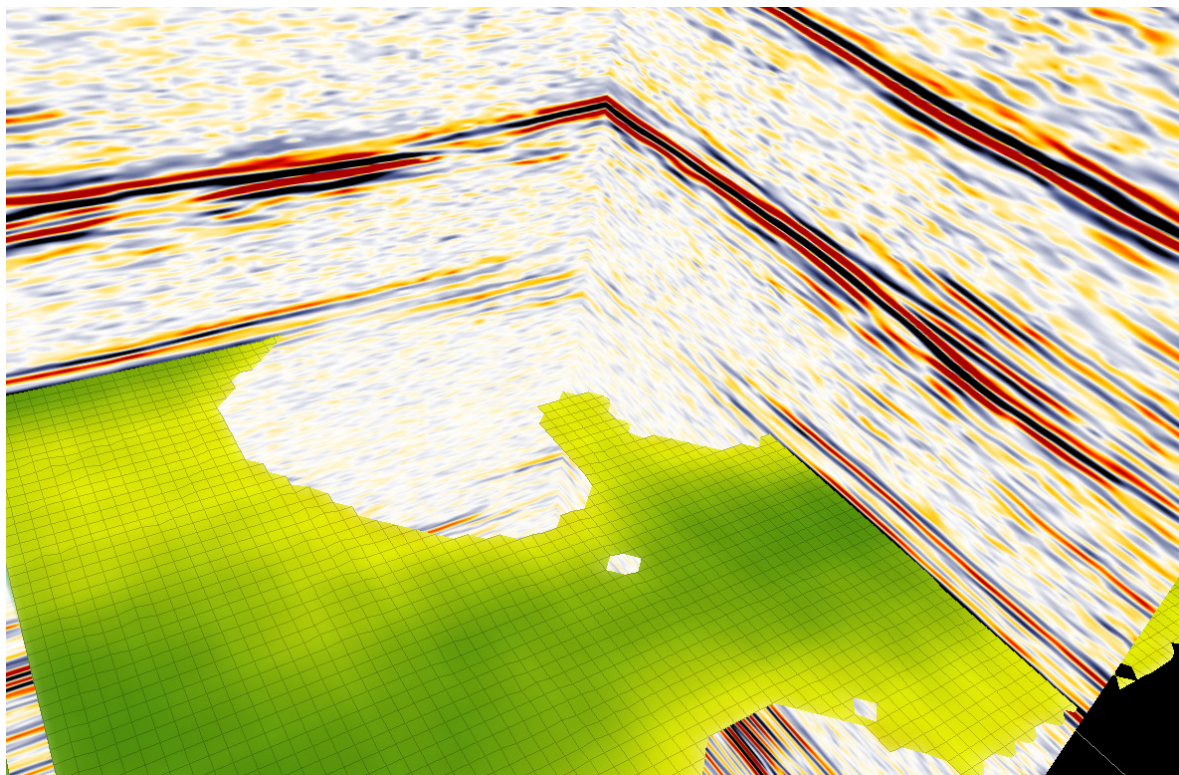


Figure 5.5: Detailed view of a gap in the tracked reflection event. The gaps are due to areas where no valid continuations were found. The colours have the same meaning as in Figure 5.4 but the inline and crossline sections are taken from the stack volume obtained by the hyperbolic ZO search.

Obviously, this also allows to calculate continuations for arbitrary locations. Thus, if the FO CRS stack is performed for all available offsets the continuations can be evaluated for the complete prestack data.

Unfortunately, the 3D FO CRS stacking operator, which is based on equation (3.6), is parameterised in terms of 14 wavefield attributes (e. g., [Bergler, 2004](#)) and requires, similar to the 3D ZO CRS stack, a number of simultaneous multi-parameter optimisations. For the event tracking these optimisations have to be performed for each required offset and, therefore, tracking in 3D acquired prestack data is far to time consuming with current technology.

For 2D acquired data the situation is different. The FO CRS stacking operator is parameterised in terms of five wavefield attributes and can be performed such that only two of them have to be optimised simultaneously ([Bergler, 2001](#)). Therefore, the computational cost is significantly lower than for 3D and prestack tracking should be feasible.

Chapter 6

NIP wave tomography

Once the CRS stack is performed and the kinematic wavefield attributes are determined this information can be used in an inversion scheme for the estimation of velocity models of the subsurface. The basic idea of the different CRS-based inversion methods is always the same: a velocity model is sought which is consistent with the determined kinematic wavefield attributes and corresponding ZO traveltimes of unconverted primary reflection events. For that purpose, the geometrical interpretation of the NIP wave is used. As it describes a wavefront that stems from a point source on the reflector, each NIP wavefront determined by the CRS stack on the measurement surface focuses, i. e., collapses to a point, at zero traveltimes if the correct velocity model is used for the back-propagation. This concept has the distinct advantage that it allows to treat the samples in the CRS stacked volumes independent from each other and does not necessarily require the structural extraction of reflection events (however, if structural velocity models are desired the structural extraction of reflection events has to be performed nonetheless).

In this chapter, a tomographic approach to the velocity inversion problem, the so-called NIP wave tomography, is presented. This technique, which was developed by [Duveneck \(2004\)](#), provides a smooth velocity model parameterised in terms of B-Splines and is obtained by an iterative global optimisation of the input data. The particular advantage of NIP wave tomography compared to other tomographic methods, e. g., stereotomography ([Billette and Lambaré, 1998](#)), is that the input data is obtained by picking locally coherent events in the CRS stacked volumes instead of the extraction of continuous, interpreted horizons in the prestack data.

In the scope of this thesis the NIP wave tomography is used as the resulting velocity models allow to perform a ray tracing for the determination of structural skeletons, i. e., the reflector positions, for the calculation of layered velocity models.

6.1 Formulation of the tomographic inverse problem

In the tomographic inversion method a velocity model consistent with the seismic data is obtained by minimising a cost function which describes the misfit between picked and forward modelled data. For that purpose, data and model components as well as the inverse problem have to be specified.

6.1.1 Data components

The input data for the tomography is directly related to the hypothetical NIP wavefronts emerging at the measurement surface. Each of these n_{data} wavefronts is associated with a ZO sample ($T_0, \mathbf{m}^{(x)}$) on a primary reflection event, the corresponding slowness vector $\mathbf{p}^{(x)}$, and the curvature matrix $\mathbf{K}_{\text{NIP}}^{(y)}$ (in fact, a single curvature into a specified direction is already sufficient). Therefore, each NIP wave can be represented by a data point

$$d_i = (\tau_0, \mathbf{K}_{\text{NIP}}^{(y)}, \mathbf{p}^{(x)}, \mathbf{m}^{(x)})_i, \quad i = 1, 2, \dots, n_{\text{data}}, \quad (6.1)$$

where $\tau_0 = T_0/2$ denotes the normal ray traveltime. These data points can, for instance, be obtained by picking locally coherent reflection events (e. g., Klüver and Mann, 2005) or, if additional information on the spatial continuity of the data is required, by a tracking of reflection events as described in Chapter 5. In the following, the letter \mathbf{d} denotes a whole set of data points.

6.1.2 Model components

The model components define the data to be inverted for. Besides the components required to describe the velocity model this includes the true subsurface locations and associated local reflector dips of the NIPs.

The velocity model in terms of B-Splines

The velocity model used in the tomography is represented by means of B-Splines (e. g., de Boor, 1978). A B-spline of m th degree provides an analytical, smooth model description with continuous analytical derivatives up to $(m-1)$ st order and is therefore well suited for the ray tracing as described in Chapter 2. On a three-dimensional grid of size $n_{x_1} \times n_{x_2} \times n_{x_3}$ with a strictly increasing knot sequence, i. e.,

$$\dots < x_{j,i} < x_{j,i+1} < \dots, \quad j = 1, 2, 3, \quad i = 1, 2, \dots, n_{x_j}, \quad (6.2)$$

the velocity model $v(\mathbf{r})$ in terms of B-Splines is given by the piecewise polynomial function

$$v(\mathbf{r}) = \sum_{j=1}^{n_{x_1}} \sum_{k=1}^{n_{x_2}} \sum_{l=1}^{n_{x_3}} v_{jkl} \beta_j^{[m]}(r_1) \beta_k^{[m]}(r_2) \beta_l^{[m]}(r_3), \quad (6.3)$$

where the v_{jkl} are the so-called B-Spline coefficients and $\beta_j^{[m]}(x_1)$, $\beta_k^{[m]}(x_2)$, and $\beta_l^{[m]}(x_3)$ are the B-Spline basis functions (here, the superscript $^{[m]}$ indicates the degree of the B-Spline). The basis functions are non-zero on $m+1$ consecutive knot intervals and can be defined recursively by the relation

$$\beta_i^{[m]}(r_j) = \frac{r_j - x_{j,i}}{x_{j,i+m} - x_{j,i}} \beta_i^{[m-1]}(r_j) + \frac{x_{j,i+m+1} - r_j}{x_{j,i+m+1} - x_{j,i+1}} \beta_{i+1}^{[m-1]}(r_j), \quad (6.4)$$

with

$$\beta_i^{[0]}(r_j) = \begin{cases} 1 & \text{for } r_j \in [x_{j,i}, x_{j,i+1}) \\ 0 & \text{else} \end{cases}, \quad (6.5)$$

and $j = 1, 2, 3$ and i being either the corresponding j , k , or l . Thus, B-Splines provide a model description with localised basis functions and a limited number of model parameters. These two

properties are especially useful for tomographic inversion as they allow for an efficient and unique solution of the inversion problem.

The derivatives of a B-Spline can easily be obtained from equation (6.3). They read

$$\frac{\partial^{(p+q+r)}v(\mathbf{r})}{\partial r_1^p \partial r_2^q \partial r_3^r} = \sum_{j=1}^{n_{x_1}} \sum_{k=1}^{n_{x_2}} \sum_{l=1}^{n_{x_3}} v_{jkl} \frac{\partial^p \beta_j^{[m]}(r_1)}{\partial r_1^p} \frac{\partial^q \beta_k^{[m]}(r_2)}{\partial r_2^q} \frac{\partial^r \beta_l^{[m]}(r_3)}{\partial r_3^r}, \quad (6.6)$$

where the derivatives of the basis function are given by (e. g., Butterfield, 1976)

$$\frac{\partial^p \beta_i^{[m]}(r_j)}{\partial r_j^p} = m \left(\frac{1}{x_{j,i+m} - x_{j,i}} \frac{\partial^{p-1} \beta_i^{[m-1]}(r_j)}{\partial r_j^{p-1}} - \frac{1}{x_{j,i+m+1} - x_{j,i+1}} \frac{\partial^{p-1} \beta_{i+1}^{[m-1]}(r_j)}{\partial r_j^{p-1}} \right). \quad (6.7)$$

In the tomographic inversion the B-Spline coefficients v_{jkl} are the quantities to be determined.

Locations and local reflector dips of the NIPs

For the tomographic inversion process it is necessary to forward model the NIP waves corresponding to the n_{data} data points through the velocity model. If this ray tracing is started in the subsurface the n_{data} associated unit normal vectors $\mathbf{e}_{(\text{NIP})}^{(x)}$ to the local reflector dip and NIP locations $\mathbf{m}_{(\text{NIP})}^{(x)}$ are initially unknown. Thus, they have to be considered as additional model parameters

$$d_{i,(\text{NIP})} = \left(\mathbf{m}_{(\text{NIP})}^{(x)}, \mathbf{e}_{(\text{NIP})}^{(x)} \right)_i, \quad i = 1, 2, \dots, n_{\text{data}}. \quad (6.8)$$

Note that only the two horizontal components $\mathbf{e}_{(\text{NIP})}^{(x)}$ of the full normal vector $\underline{\mathbf{e}}_{(\text{NIP})}^{(x)}$ are required. The third component is automatically obtained from the condition $|\underline{\mathbf{e}}_{(\text{NIP})}^{(x)}| = 1$. The complete set of additional model parameters will in the following be denoted by the letter $\mathbf{d}_{(\text{NIP})}$.

The model vector \mathbf{c}

All the model components mentioned above, i. e., the B-Spline coefficients v_{jkl} and the NIP parameters $\mathbf{d}_{(\text{NIP})}$, are arranged into a model vector \mathbf{c} with $n_{\text{mod}} = n_{x_1} \cdot n_{x_2} \cdot n_{x_3} + n_{\text{data}}$ components

$$\mathbf{c} = (v_{1,1,1}, \dots, v_{n_{x_1} n_{x_2} n_{x_3}}, d_{1,(\text{NIP})}, \dots, d_{n_{\text{data}},(\text{NIP})}) = (\mathbf{c}_{(v)}, \mathbf{d}_{(\text{NIP})}). \quad (6.9)$$

6.1.3 The inverse problem

The tomographic approach to the inversion problem is formulated in terms of the model vector \mathbf{c} and the data vector \mathbf{d} as follows: given the data points \mathbf{d} a model \mathbf{c} is sought which minimises the misfit between the forward modelled data points $\mathbf{d}_{\text{mod}} = \mathbf{f}(\mathbf{c})$ and the given input data \mathbf{d} obtained from the CRS stack results. Here, the forward modelling is symbolised by the nonlinear operator \mathbf{f} . Using the least-squares norm as a measure of the misfit the inversion problem can be formulated as a problem of minimising the cost function

$$S(\mathbf{c}) = \frac{1}{2} \|\mathbf{d} - \mathbf{f}(\mathbf{c})\|^2 = \frac{1}{2} \|\Delta \mathbf{d}(\mathbf{c})\|^2, \quad (6.10)$$

with $\Delta \mathbf{d}(\mathbf{c}) = \mathbf{d} - \mathbf{f}(\mathbf{c})$.

Equation (6.10) can be further extended by the matrix \mathbf{C}_D which allows to assign different weights to the individual data points:

$$S(\mathbf{c}) = \frac{1}{2} \|\Delta \mathbf{d}(\mathbf{c})\|^2 = \frac{1}{2} \Delta \mathbf{d}(\mathbf{c})^T \mathbf{C}_D^{-1} \Delta \mathbf{d}(\mathbf{c}). \quad (6.11)$$

Matrix \mathbf{C}_D , which is often referred to as data covariance matrix, is symmetric and positive definite. In the NIP wave tomography it is furthermore assumed to be diagonal, thus, implying uncorrelated data errors. Therefore, its basic use is to stabilise the tomography by bringing the different types of data with their different physical dimensions to a comparable size. Suitable choices for the elements of \mathbf{C}_D are discussed in [Duvneck \(2004\)](#).

Additional constraints on the model are either introduced by adding extra terms to the cost function or, e. g., in case of a priori velocity information, by appending them to the data vector \mathbf{d} . A physically justified constraint to the model parameters is to require the velocity model to have minimum second derivatives. These derivatives are related to the curvature and, thus, to the roughness of the velocity model. This implies that the simplest model consistent with the data is sought. Furthermore it ensures a sufficient range of validity for the ray tracing. Applying this additional regularisation to the cost function yields

$$S(\mathbf{c}) = \frac{1}{2} \Delta \mathbf{d}(\mathbf{c})^T \mathbf{C}_D^{-1} \Delta \mathbf{d}(\mathbf{c}) + \frac{1}{2} \epsilon \mathbf{c}_{(v)}^T \mathbf{D} \mathbf{c}_{(v)}, \quad (6.12)$$

where ϵ is a positive weighting factor. The symmetric and positive definite matrix \mathbf{D} is related to the second derivatives of the velocity model by the condition

$$\mathbf{c}_{(v)}^T \mathbf{D} \mathbf{c}_{(v)} = \int_{\mathbf{x}} \left[v(\mathbf{x}) + \sum_{i=1}^3 \epsilon_i \left(\frac{\partial^2 v(\mathbf{x})}{\partial x_i^2} \right)^2 \right] d\mathbf{x}, \quad (6.13)$$

Note that in addition to the second derivatives also the velocity itself is used for the regularisation. Similar to ϵ in equation (6.12) the ϵ_i denote weighting factors that allow a relative weighting of the different terms.

The nonlinear modelling operator \mathbf{f} implies that the inverse problem, i. e., the minimisation of the cost function $S(\mathbf{c})$, is also nonlinear. Therefore, its solution requires the application of global nonlinear optimisations as, for instance, Monte-Carlo methods. As these methods are computationally very expensive an iterative, local approach is used in NIP wave tomography. For that purpose it is assumed that the modelling operator can be approximated in the vicinity of a given model \mathbf{c}_n corresponding to the n th iteration by the linear relationship

$$\mathbf{f}(\mathbf{c}_n + \Delta \mathbf{c}) = \mathbf{f}(\mathbf{c}_n) + \mathbf{F} \Delta \mathbf{c}. \quad (6.14)$$

The matrix $F_{ij} = \partial f_i / \partial c_j$ is known as the Matrix of Fréchet derivatives of \mathbf{f} at \mathbf{c}_n . These derivatives can be calculated during the ray tracing by applying ray perturbation theory (e. g., [Červený, 2001](#)). A detailed description of their calculation is given in [Duvneck \(2004\)](#).

The linearised modelling operator (6.14) allows to apply a Newton-type algorithm to solve the inverse problem (e. g., [Press et al., 2002](#)). These methods make use of the condition that the gradient of equation (6.12) with respect to the model parameters vanishes if a minimum is encountered, i. e., $\nabla^{(c)} S(\mathbf{c}) = \mathbf{0}$. The application of this condition leads to the so-called normal equations ([Lines and Treitel, 1984](#))

$$\hat{\mathbf{F}}^T \hat{\mathbf{F}} \Delta \mathbf{c} = \hat{\mathbf{F}}^T \Delta \hat{\mathbf{d}}, \quad (6.15)$$

with

$$\hat{\mathbf{F}} = \begin{pmatrix} \mathbf{C}_D^{-1} \mathbf{F} \\ \mathbf{B} \end{pmatrix} \quad \text{and} \quad \Delta \hat{\mathbf{d}} = \begin{pmatrix} \mathbf{C}_D^{-1} \Delta \mathbf{d}(\mathbf{c}_n) \\ -\mathbf{B} \mathbf{c}_n \end{pmatrix} \quad (6.16)$$

and matrix \mathbf{B} chosen such that it satisfies the condition

$$\mathbf{c}^T \mathbf{B}^T \mathbf{B} \mathbf{c} = \epsilon \mathbf{c}_{(v)}^T \mathbf{D} \mathbf{c}_{(v)}. \quad (6.17)$$

This matrix can, for instance, be obtained by a Cholesky decomposition of \mathbf{D} .

From equation (6.15) it follows that an update $\Delta \mathbf{c}$ to the current model vector \mathbf{c}_n is obtained by computing the least-squares solution to the equation

$$\hat{\mathbf{F}} \Delta \mathbf{c} = \Delta \hat{\mathbf{d}}. \quad (6.18)$$

Numerical methods for solving such systems of equations include, e. g., singular value decomposition or LSQR algorithms (e. g., Press et al., 2002).

Once the model update vector $\Delta \mathbf{c}$ is obtained, the updated model vector \mathbf{c}_{n+1} is given by

$$\mathbf{c}_{n+1} = \mathbf{c}_n + \lambda \Delta \mathbf{c}. \quad (6.19)$$

Here, the factor $\lambda \leq 1$ is required to account for the linearisation applied to the modelling operator \mathbf{f} .

6.2 The inversion algorithm

Following the considerations in this chapter, the NIP wave tomography can be described by a general inversion scheme. Assuming that the data components \mathbf{d} are available the scheme reads as follows:

1. The initial velocity model is set up by assigning initial values to \mathbf{c}_v . Also, additional regularisation weights need to be specified.
2. The data points \mathbf{d} are traced into the model until the traveltimes τ_0 is encountered. This is done by means of the ray tracing system (2.21)-(2.23). The resulting locations and ray direction vectors in depth define the vector \mathbf{d}_{NIP} . Thus, at this stage the complete model vector \mathbf{c} is known.
3. Dynamic ray tracing based on the ray tracing system (2.45) is used to forward model the vector \mathbf{d}_{mod} and the Fréchet derivatives \mathbf{F} .
4. The cost function (6.12) is evaluated from \mathbf{d} , \mathbf{d}_{mod} , and the regularisation term for the velocity model.
5. The system (6.18) is solved to obtain the model update vector $\Delta \mathbf{c}$.
6. According to equation (6.19) an updated model is calculated. Within this model ray tracing is performed to obtain a new vector \mathbf{d}_{mod} .
7. The cost function (6.12) is evaluated with the newly obtained \mathbf{d}_{mod} .
8. If the cost function has increased, the model update is rejected, λ is decreased and the last two steps are repeated until the cost function decreases or λ falls below a specified threshold. A minimum of the cost function is found if it does not decrease even for small λ .

9. If the cost function has decreased the updated model is used in the next iteration starting with step 3. The process is repeated until a maximum number of iterations is reached or the cost function falls below a threshold.

Note that NIP wave tomography only provides a velocity model which is consistent with the input data. Such a consistent model is not to be confused with the true model. A homogeneous subsurface with a plane interface can, for instance, also be consistently described by a velocity model that contains a vertical gradient. It is even possible, that tomography yields a consistent model that focuses the NIP wavefronts at completely wrong locations, i. e., the solution may not be unique. However, the successful use of the velocity models in prestack depth migration shows that in most cases, they yield subsurface locations of the focused NIP wavefronts that are very close to the true locations.

Chapter 7

Dix-type inversion

The smooth velocity models obtained, e. g., by NIP wave tomography provides sufficient information for many depth migration methods. Nonetheless, due to their representation in terms of smoothly varying B-Splines they are often inappropriate when local velocity variations are sought for. In that case it is advantageous to use Dix-type or layer-stripping velocity inversion methods. These techniques assume the subsurface to consist of constant velocity layers separated by structural interfaces (such models will be called layered media in the following). The layer velocities and the positions of the separating interfaces are obtained in a recursive manner starting from the shallowest layer.

In this chapter a technique for the estimation of layered velocity models based on [Hubral and Krey \(1980\)](#) is presented. The method uses the kinematic wavefield attributes provided by the CRS stack to obtain a layered medium. In contrast to the 1D models of the pure Dix-type inversion (e. g., [Dix, 1955](#)) this medium is characterised by smoothly curved, dipping structural interfaces. Similar to NIP wave tomography, the consistency of the velocity models with the measured data is enforced by requiring the NIP wavefronts to collapse on their corresponding interfaces in depth. However, due to the additional stratigraphic information that is provided by the inversion method a structural extraction of reflection events in the CRS stacked ZO volumes is required (see [Chapter 5](#)). Drawback of any layer-based inversion technique is the error propagation: an error in the velocity of a given layer affects the positions and velocities of all the layers illuminated by rays travelling through this layer. In order to partially compensate for this effect the results of the NIP wave tomography are used for the spatial positioning of the interfaces. The layer-based inversion then reduces to the calculation of the layer velocities.

Alternative algorithms for the determination of layered media are described by [Chernjak and Gritsenko \(1979\)](#). A technique based on multifocusing is presented by [Keydar et al. \(1995\)](#) and a 2D algorithm for models consisting of layers with a constant velocity gradient by [Biloti et al. \(2002\)](#).

7.1 Ray tracing in layered media

As the Dix-type inversion algorithms consider layered media the ray tracing procedures as described in [Chapter 2](#) simplify considerably. This is due to the fact that the spatial derivatives of the velocities vanish within the individual constant velocity layers, i. e.,

$$\underline{\nabla}^{(x)} v_l = \underline{\mathbf{0}}, \quad (7.1)$$

with v_l denoting the velocity in the l th layer.

In general, the ray tracing in layered media consists of two parts. One describes the ray tracing inside the layers and the other one across the interfaces. In the following, the individual techniques will be derived and then combined to a general ray tracing scheme.

7.1.1 Ray tracing in layers of constant velocity

Applying condition (7.1) to the ray tracing system (2.21)-(2.23) immediately yields the solutions

$$\underline{\mathbf{x}}(s) = \underline{\mathbf{x}}_0 + v_l \underline{\mathbf{p}}_0 (s - s_0), \quad (7.2)$$

$$\underline{\mathbf{p}}(s) = \underline{\mathbf{p}}_0, \quad (7.3)$$

$$T(s) = T_0 + (s - s_0)/v_l, \quad (7.4)$$

with $\underline{\mathbf{x}}_0$, $\underline{\mathbf{p}}_0$, T_0 , and s_0 being the initial location, slowness, traveltime, and arclength along the ray, respectively. In view of these equations it is evident that rays are straight lines in constant velocity media.

In a similar way the dynamic ray tracing system for constant velocity media is obtained: inserting condition (7.1) into equations (2.43) yields

$$\frac{d\mathbf{Q}}{ds} = v_l \mathbf{P}^{(r)}, \quad \frac{d\mathbf{P}^{(r)}}{ds} = \mathbf{0}. \quad (7.5)$$

The solution to this system for a ray $\Omega(R, S)$ from S to R reads

$$\mathbf{Q}(R) = \mathbf{Q}(S) + v_l (s - s_0) \mathbf{P}^{(r)}(S), \quad (7.6)$$

$$\mathbf{P}^{(r)}(R) = \mathbf{P}^{(r)}(S). \quad (7.7)$$

According to equation (2.51) this provides the propagator matrix

$$\underline{\underline{\mathbf{\Pi}}}^{(r)}(R, S) = \begin{pmatrix} \mathbf{I} & v_l (s - s_0) \mathbf{I} \\ \mathbf{0} & \mathbf{I} \end{pmatrix}. \quad (7.8)$$

Using the propagator matrix $\underline{\underline{\mathbf{\Pi}}}^{(r)}(R, S)$ yields the continuation relation (2.52) for matrix $\mathbf{M}^{(r)}$:

$$\mathbf{M}^{(r)}(R) = \left[\left(\mathbf{M}^{(r)}(S) \right)^{-1} + v_l (s - s_0) \mathbf{I} \right]^{-1}. \quad (7.9)$$

The latter equation is especially useful as it describes the propagation of the NIP wave within the constant velocity layers. In view of equations (2.28), (2.59), and (2.114) relation (7.9) transforms to an equation describing the continuation of wavefront curvatures $\mathbf{K}^{(y)}$ or, equivalently, radii $\mathbf{R}^{(y)} = (\mathbf{K}^{(y)})^{-1}$:

$$\mathbf{K}^{(y)}(R) = \left[\left(\mathbf{K}^{(y)}(S) \right)^{-1} + (s - s_0) \mathbf{I} \right]^{-1}, \quad (7.10)$$

$$\mathbf{R}^{(y)}(R) = \mathbf{R}^{(y)}(S) + (s - s_0) \mathbf{I}. \quad (7.11)$$

From equation (7.11) it immediately follows that the radius of curvature of a wavefront in a constant velocity medium is linearly related to the length of the ray.

The last point to consider for the ray tracing is the behaviour of the basis vectors of the ray-centred coordinate system. Inserting condition (7.1) into the relevant equation (2.24) yields

$$\frac{d\mathbf{e}_i^{(r)}}{ds} = 0 \quad \Leftrightarrow \quad \mathbf{e}_i^{(r)}(R) = \mathbf{e}_i^{(r)}(S). \quad (7.12)$$

Thus, the three basis vectors are constant along the ray.

7.1.2 Ray tracing across interfaces

Equations (2.76) and (2.94) describe the reflection/transmission of the ray and the ray propagator matrix across an interface Σ , respectively. As the generalised Snell's law (2.76) does not depend on derivatives of the velocity field it remains unchanged here. However, equation (2.94) simplifies as $\mathbf{E}(Q)$ and $\mathbf{E}(\tilde{Q})$ vanish according to equations (2.84) and (2.59). Thus, the propagator matrix $\underline{\underline{\Pi}}^{(r)}(\tilde{Q}, Q)$ across an interface reads

$$\underline{\underline{\Pi}}^{(r)}(\tilde{Q}, Q) = \begin{pmatrix} \mathbf{G}^T(\tilde{Q}) \mathbf{G}^{-T}(Q) & \mathbf{0} \\ -u \mathbf{G}^{-1}(\tilde{Q}) \mathbf{B}^{(z)}(Q) \mathbf{G}^{-T}(Q) & \mathbf{G}^{-1}(\tilde{Q}) \mathbf{G}(Q) \end{pmatrix}. \quad (7.13)$$

With the knowledge of $\underline{\underline{\Pi}}^{(r)}(\tilde{Q}, Q)$ the transmitted/reflected quantities $\mathbf{M}^{(r)}(\tilde{Q})$, $\mathbf{Q}(\tilde{Q})$, and $\mathbf{P}^{(r)}(\tilde{Q})$ can be calculated by means of the respective continuation relation, e. g., equation (2.93) for $\mathbf{Q}(\tilde{Q})$ and $\mathbf{P}^{(r)}(\tilde{Q})$.

If only wavefront curvatures are to be considered for reflection/transmission the respective matrix $\mathbf{K}^{(y)}(\tilde{Q})$ can be obtained from equations (2.87) and (2.114). Under consideration of $\mathbf{E}(Q) = \mathbf{E}(\tilde{Q}) = \mathbf{0}$ this directly yields

$$\mathbf{K}^{(y)}(\tilde{Q}) = \frac{v(\tilde{Q})}{v(Q)} \mathbf{G}^{-1}(\tilde{Q}) \left[\mathbf{G}(Q) \mathbf{K}^{(y)}(Q) \mathbf{G}(Q)^T - u \mathbf{B}^{(z)}(Q) \right] \mathbf{G}^{-T}(\tilde{Q}), \quad (7.14)$$

Of course, a similar expression can also be obtained for the wavefront radii matrix $\mathbf{R}^{(y)}(\tilde{Q})$ by applying $\mathbf{R}^{(y)} = \left(\mathbf{K}^{(y)} \right)^{-1}$ to the last equation.

In view of equations (7.13) and (7.14) the principle task is the determination of the transformation matrices $\mathbf{G}(Q)$ and $\mathbf{G}(\tilde{Q})$. If the basis vectors of the interface coordinate system and the ray-centred coordinate systems at Q and \tilde{Q} are chosen according to the standard option (2.64)-(2.65) and to the reciprocal choice (2.78) the transformation matrices are either given directly by evaluation of equation (A.9) or by the combination of rotation matrices (A.15)

$$\mathbf{G}(Q) = \mathbf{R}_3^{(y)}(\gamma) \mathbf{R}_2^{(y)}(i_Q), \quad (7.15)$$

$$\mathbf{G}(\tilde{Q}) = \mathbf{R}_3^{(y)}(\gamma) \mathbf{R}_2^{(y)}(i_{\tilde{Q}}), \quad (7.16)$$

with i_Q and $i_{\tilde{Q}}$ being the incidence and emergence angles of the ray and γ the angle between $\mathbf{e}_2^{(z)}(Q)$ and $\mathbf{e}_2^{(r)}(Q)$ (e. g., Červený, 2001).

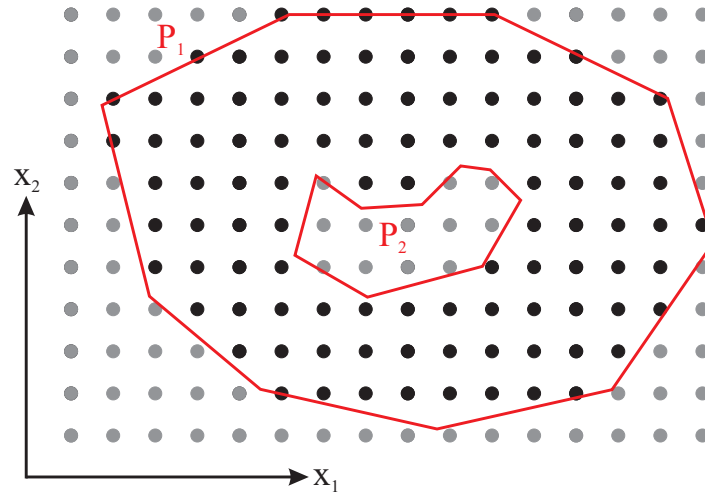


Figure 7.1: Interfaces are represented by a combination of B-Splines on a regular knot interval (denoted by the dots) and polygons P_i that define the lateral extension. The polygons allow to evaluate if a point Q lies on the interface. In this figure, the valid region of the interface is denoted by the black dots, i. e., points on the interface are inside the polygon P_1 and outside of P_2 .

7.1.3 Description of the interfaces

The definition of the interfaces plays an important role in ray tracing. Their mathematical representation must provide well-defined first and second order spatial derivatives as, e. g., required for the evaluation of the interface curvature matrix $\mathbf{B}^{(z)}(Q)$. Furthermore, a representation that is able to handle irregular shapes for the correct treatment of fault structures or holes that are due to missing data, is desirable.

A representation of the interfaces well suited for these needs is given by a combination of B-Splines (see Chapter 6.1.2) and polygons: the polygons define the shape of the interface and, thus, provide a criterion whether the B-Spline can be evaluated at a point Q or not. For that purpose, the even-odd rule (e. g., [Hormann and Agathos, 2001](#)) is used to determine if Q lies inside or outside of the different polygons. Considering, for instance, the interface depicted in Figure 7.1 the point Q lies on the interface if it is inside the polygon P_1 and outside the polygon P_2 . If Q is located on the interface the B-Spline can be evaluated in a second step for $x_3(Q)$ and its spatial derivatives.

The presented representation of the interfaces has, however, two drawbacks. Firstly, the B-Splines require regular knot intervals. Thus, if an interface is created from irregularly distributed points an interpolation to the knot sequence is necessary. Secondly, the intersections of rays and interfaces can not be obtained analytically. Instead, iterative methods have to be used.

7.1.4 A ray tracing scheme for layered media

The individual results (7.2)-(7.16) can be combined into a single ray tracing scheme for layered media. For that purpose, a ray starting at point \tilde{Q}_0 and ending at point Q_{N+1} is considered. Along the raypath the ray is subject to N reflections and/or transmissions. The corresponding incidence and emergence

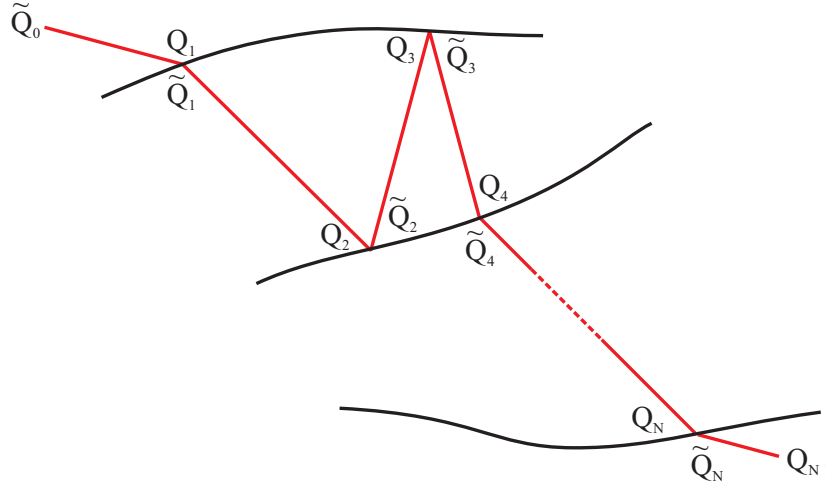


Figure 7.2: The ray tracing of an arbitrary, multiply reflected and transmitted ray in a layered medium starts at point \tilde{Q}_0 and ends at Q_{N+1} . The reflection or transmission points corresponding to Q_1, Q_2, \dots, Q_N are denoted by $\tilde{Q}_1, \tilde{Q}_2, \dots, \tilde{Q}_N$. Note that the locations of Q_i and \tilde{Q}_i coincide.

points on interface Σ_i , $i = 1, 2, \dots, N$ are denoted by Q_i and \tilde{Q}_i , respectively (see Figure 7.2), and the basis vectors of the ray-centred coordinate system by $\mathbf{e}_1^{(r)}(Q_i)$, $\mathbf{e}_2^{(r)}(Q_i)$, and $\mathbf{e}_3^{(r)}(Q_i)$. Correspondingly, the basis vectors of the interface coordinate system are given by $\mathbf{e}_1^{(z)}(Q_i)$, $\mathbf{e}_2^{(z)}(Q_i)$, and $\mathbf{e}_3^{(z)}(Q_i)$.

The ray tracing scheme starts with an initialisation of the coordinates \mathbf{x}_0 , the slowness vector \mathbf{p}_0 , the arclength $s_0 = 0$, and the traveltimes $T_0 = 0$ along the ray, the ray-centred coordinate system $\mathbf{e}_1^{(r)}(\tilde{Q}_0)$, $\mathbf{e}_2^{(r)}(\tilde{Q}_0)$, and $\mathbf{e}_3^{(r)}(\tilde{Q}_0)$, and the propagator matrix $\underline{\underline{\mathbf{\Pi}}}^{(r)}(\tilde{Q}_0, \tilde{Q}_0) = \underline{\underline{\mathbf{I}}}$. For all considered points $\tilde{Q}_0, Q_1, \dots, Q_{N+1}$ the following steps are applied:

1. Given a point \tilde{Q}_i the intersection Q_{i+1} of the straight ray (7.2) with the interface Σ_{i+1} is sought and the length of the ray segment, i. e., $s_{i+1} - s_i$, is evaluated.
2. Equation (7.4) is evaluated to add the traveltimes of the ray segment from \tilde{Q}_i to Q_{i+1} to the total traveltimes of the ray. The coordinates \mathbf{x}_0 are set to the coordinates of the intersection point Q_{i+1} .
3. An intermediate propagator matrix $\underline{\underline{\mathbf{\Pi}}}^{(r)}(Q_{i+1}, \tilde{Q}_i)$ is determined from equation (7.8). This propagator matrix is used to update $\underline{\underline{\mathbf{\Pi}}}^{(r)}(\tilde{Q}_i, \tilde{Q}_0)$ by means of the chain rule (B.7), i. e.,

$$\underline{\underline{\mathbf{\Pi}}}^{(r)}(Q_{i+1}, \tilde{Q}_0) = \underline{\underline{\mathbf{\Pi}}}^{(r)}(Q_{i+1}, \tilde{Q}_i) \underline{\underline{\mathbf{\Pi}}}^{(r)}(\tilde{Q}_i, \tilde{Q}_0). \quad (7.17)$$

If i equals $N - 1$ the scheme ends here.

4. The interface coordinate system $\mathbf{e}_1^{(z)}(Q_{i+1})$, $\mathbf{e}_2^{(z)}(Q_{i+1})$, and $\mathbf{e}_3^{(z)}(Q_{i+1})$ is determined from the standard option (2.64) and (2.65). In addition, the interface curvature matrix $\mathbf{B}^{(z)}(Q_{i+1})$ is evaluated by means of equation (2.70).
5. The generalised Snell's law (2.76) is used to calculate the reflected or transmitted slowness vector \mathbf{p}_{i+1} across the interface to point \tilde{Q}_{i+1} . Afterwards, the ray-centred coordinate system $\mathbf{e}_1^{(r)}(\tilde{Q}_{i+1})$, $\mathbf{e}_2^{(r)}(\tilde{Q}_{i+1})$, and $\mathbf{e}_3^{(r)}(\tilde{Q}_{i+1})$ is determined according to the reciprocal choice (2.78).

6. The transformation matrices $\mathbf{G}(Q_{i+1})$ and $\mathbf{G}(\tilde{Q}_{i+1})$ are determined either from equations (7.15) and (7.16) or by means of equation (A.15). For that purpose the basis vectors $\underline{\mathbf{e}}_1^{(r)}(Q_i)$, $\underline{\mathbf{e}}_2^{(r)}(Q_i)$, and $\underline{\mathbf{e}}_3^{(r)}(Q_i)$ of the ray-centred coordinate system are used for the evaluation of $\mathbf{G}(Q_{i+1})$ and the basis vectors $\underline{\mathbf{e}}_1^{(r)}(\tilde{Q}_{i+1})$, $\underline{\mathbf{e}}_2^{(r)}(\tilde{Q}_{i+1})$, and $\underline{\mathbf{e}}_3^{(r)}(\tilde{Q}_{i+1})$ for the calculation of $\mathbf{G}(\tilde{Q}_{i+1})$.
7. An intermediate propagator matrix $\underline{\underline{\mathbf{\Pi}}}_I^{(r)}(\tilde{Q}_{i+1}, Q_{i+1})$ is determined from equation (7.13). Similar to step 3, this matrix is used to update $\underline{\underline{\mathbf{\Pi}}}_I^{(r)}(Q_{i+1}, \tilde{Q}_0)$ by means of the chain rule (B.7), i. e.,

$$\underline{\underline{\mathbf{\Pi}}}_I^{(r)}(\tilde{Q}_{i+1}, \tilde{Q}_0) = \underline{\underline{\mathbf{\Pi}}}_I^{(r)}(\tilde{Q}_{i+1}, Q_{i+1}) \underline{\underline{\mathbf{\Pi}}}_I^{(r)}(Q_{i+1}, \tilde{Q}_0). \quad (7.18)$$

After reaching Q_N the corresponding traveltime T , location $\underline{\mathbf{x}}_N$, and slowness vector $\underline{\mathbf{p}}_N$ of the ray as well as the propagator matrix $\underline{\underline{\mathbf{\Pi}}}_I^{(r)}(Q_N, \tilde{Q}_0)$ are known and can be used for further applications. Note, however, that $\underline{\underline{\mathbf{\Pi}}}_I^{(r)}(Q_N, \tilde{Q}_0)$ is not a surface-to-surface propagator matrix. If this is required additional multiplications with an projection matrix $\underline{\underline{\mathbf{Y}}}$ adapted to layered media have to be applied, see equations (2.96) and (2.97).

7.2 Dix-type inversion with kinematic wavefield attributes

The knowledge of the relations (7.2)-(7.16) for ray tracing in layered media allows to establish a recursive algorithm for the determination of velocity models of the subsurface from unconverted primary ZO reflections and the corresponding kinematic wavefield attributes. For that purpose it is assumed that the velocity distribution in the subsurface can be exactly represented by a medium with iso-velocity layers. In order to keep the following considerations simple it is furthermore assumed that the subsurface consists of N layers that are continuous across the complete model and do not intersect each other.

7.2.1 Data components

In principle, the input data for the Dix-type inversion is the same as used for NIP wave tomography. However, as a structural inversion is performed also a structural instead of a locally coherent picking is required. This task is performed by means of the picking algorithm described in Chapter 5 which provides for each available spatial location of a primary reflection event a data point d_i as defined by equation (6.1). Thus, each reflection event n , $n = 1, 2, \dots, L$, yields a data vector \mathbf{d}^n which contains the data required for the inversion as well as inherent structural information. As will be shown in the next sections the inversion algorithm is based on the back-propagation of the NIP wave into the medium. For that purpose, it is required to additionally invert the direction of the emerging normal ray as well as the orientation of the NIP wave. Furthermore, the traveltime τ_0 along the normal ray is inverted to account for the focusing of the NIP wave at zero traveltime $\tau_0 = 0$. The application of these transformations provide data vectors $\tilde{\mathbf{d}}^n$ that read

$$\tilde{d}_i^n = (-\tau_0, \tilde{\mathbf{K}}_{\text{NIP}}^{(y)}, -\mathbf{p}^{(x)}, \mathbf{m}^{(x)})_i \quad , \quad i = 1, 2, \dots, n_{\text{data}} \quad (7.19)$$

with

$$\tilde{\mathbf{K}}_{\text{NIP}}^{(y)} = \begin{pmatrix} -K_{\text{NIP},11}^{(y)} & K_{\text{NIP},12}^{(y)} \\ K_{\text{NIP},12}^{(y)} & -K_{\text{NIP},22}^{(y)} \end{pmatrix}. \quad (7.20)$$

The complete input data is finally constituted by the data vector

$$\mathbf{D} = (\tilde{\mathbf{d}}^n) \quad , \quad n = 1, 2, \dots, L. \quad (7.21)$$

7.2.2 Velocity inversion and construction of the interfaces

In the following it is assumed that the solution to the velocity model has already been obtained down to the $(L - 1)$ th layer. The Dix-type inversion then reduces to the determination of the velocity v_L and the interface of the L th layer. Thus, the velocity model is obtained in a recursive manner starting from the shallowest layer.

Redatuming

The first step in the determination of the velocity of the L th layer consists in the redatuming of the data vector $\tilde{\mathbf{d}}^L$ defined on the measurement surface onto the $(L - 1)$ th interface. This is achieved by means of the previously described ray tracing scheme for layered media which immediately provides the locations $\underline{\mathbf{x}}_i$, slowness vectors $\underline{\mathbf{p}}_i$, and remaining traveltimes $\tau_{0,i}$ along the normal rays on the $(L - 1)$ th interface. The individual curvature matrices $\tilde{\mathbf{K}}_{\text{NIP},i}^{(y)}$ are redatumed by applying the continuation relation (2.52) to the propagator matrices $\underline{\mathbf{\Pi}}_i^{(r)}$. In addition, the ray-centred coordinate systems of the data points are transformed such that the basis vectors $\underline{\mathbf{e}}_{2,i}^{(r)}$ coincide with the corresponding basis vectors $\underline{\mathbf{e}}_{1,i}^{(z)}$ of the $(L - 1)$ th interface. This is achieved by an rotation with respect to the $\underline{\mathbf{e}}_{3,i}^{(r)}$ axis. Thus, the curvature matrices transform to

$$\tilde{\mathbf{K}}_{\text{NIP,rot},i}^{(y)} = \begin{pmatrix} m_{I11,i} & m_{I12,i} \\ m_{I12,i} & m_{I22,i} \end{pmatrix} = \mathbf{R}_3^{(y)\text{T}}(\kappa_i) \tilde{\mathbf{K}}_{\text{NIP},i}^{(y)} \mathbf{R}_3^{(y)}(\kappa_i), \quad (7.22)$$

where κ_i is the angle between $\underline{\mathbf{e}}_{2,i}^{(r)}$ and $\underline{\mathbf{e}}_{1,i}^{(z)}$. Actually, this transformation is not necessary but it simplifies equation (7.14) considerably for the further operations:

$$\mathbf{K}^{(y)}(\tilde{Q}) = \frac{v(\tilde{Q})}{v(Q)} \mathbf{S}_1(Q) \mathbf{K}^{(y)}(Q) \mathbf{S}_1(Q) + u_{R/T} \mathbf{S}_2(Q) \mathbf{B}^{(z)}(Q) \mathbf{S}_2(Q), \quad (7.23)$$

with

$$\mathbf{S}_1 = \begin{pmatrix} \cos i_Q / \cos i_{\tilde{Q}} & 0 \\ 0 & 1 \end{pmatrix}, \quad \mathbf{S}_2 = \begin{pmatrix} 1 / \cos i_{\tilde{Q}} & 0 \\ 0 & 1 \end{pmatrix}, \quad (7.24)$$

and

$$u_R = \frac{v(\tilde{Q})}{v(Q)} \cos i_Q - \cos i_{\tilde{Q}} \quad \text{for transmission,} \quad (7.25)$$

$$u_T = \frac{v(\tilde{Q})}{v(Q)} \cos i_Q + \cos i_{\tilde{Q}} \quad \text{for reflection.} \quad (7.26)$$

Determination of the layer velocity

After redatuming the data vector $\tilde{\mathbf{d}}^L$ is in an appropriate form to determine the velocity of the L th layer. For that purpose, three systems of equations that provide three layer velocities $v_{L,i}$ for each data

point contained in $\tilde{\mathbf{d}}^L$ are defined. The first condition that enters into these systems is given by the fact that the NIP wavefronts focus on the L th interface, i. e., the radii of the focused NIP wavefronts vanish. Due to the constant velocity of the layers this also implies, according to equation (7.10), that the NIP wavefronts are spherical after transmission into the L th layer. Denoting the curvature matrices of the transmitted NIP wavefronts by $\tilde{\mathbf{K}}_{\text{NIP,rot}}^{(y)}$ this condition reads

$$\tilde{\mathbf{K}}_{\text{NIP,rot},i}^{(y)} = \frac{1}{s - s_0} \mathbf{I} = m_{T,i} \mathbf{I}, \quad i = 1, 2, \dots, n_{\text{data}}. \quad (7.27)$$

Considering that $\tau_{0,i} = 0$ for the focused NIP wavefronts, the application of equation (7.27) to relation (7.4) provides the first condition for the systems of equations:

$$\frac{1}{m_{T,i}} = v_{L,i} \tau_{0,i}, \quad i = 1, 2, \dots, n_{\text{data}}. \quad (7.28)$$

As this condition introduces two unknowns, the velocity $v_{L,i}$ and the curvatures $m_{T,i}$ an additional condition is required. Here, Snell's law (2.77)

$$\frac{\sin \epsilon_{I,i}}{v_{L-1}} = \frac{\sin \epsilon_{T,i}}{v_{L,i}}, \quad i = 1, 2, \dots, n_{\text{data}}, \quad (7.29)$$

is used for this purpose. In this equation $\epsilon_{I,i}$ and $\epsilon_{T,i}$ denote the incidence and transmission angles of the rays related to the individual data points, respectively. The incidence angle is obtained from the slowness vector and interface normal of the corresponding data point and its associated ray whereas the transmission angle is a third unknown entering into the system of equations. Thus, another condition has to be introduced which takes the latter unknown into account. The proper relation is given by the transmission law (7.23) and equation (7.27) and reads for $i = 1, 2, \dots, n_{\text{data}}$

$$\begin{pmatrix} m_{T,i} & 0 \\ 0 & m_{T,i} \end{pmatrix} = \begin{pmatrix} \frac{v_{L,i} \cos^2 \epsilon_{I,i}}{v_{L-1} \cos^2 \epsilon_{T,i}} m_{I11,i} + \frac{u_T}{\cos^2 \epsilon_{T,i}} \mathbf{B}_{11,i}^{(z)} & \frac{v_{L,i} \cos \epsilon_{I,i}}{v_{L-1} \cos \epsilon_{T,i}} m_{I12,i} + \frac{u_T}{\cos \epsilon_{T,i}} \mathbf{B}_{12,i}^{(z)} \\ \frac{v_{L,i} \cos \epsilon_{I,i}}{v_{L-1} \cos \epsilon_{T,i}} m_{I12,i} + \frac{u_T}{\cos \epsilon_{T,i}} \mathbf{B}_{12,i}^{(z)} & \frac{v_{L,i}}{v_{L-1}} m_{I22,i} + u_T \mathbf{B}_{22,i}^{(z)} \end{pmatrix}, \quad (7.30)$$

where u_T is given by the relation (7.25) for transmission and the interface curvature matrix $\mathbf{B}^{(z)}$ is evaluated at the location of the respective data point.

Actually, the last condition (7.30) provides three equations. Therefore, for each data point d_i^L three systems of equations can be established that solve the inverse problem:

$$\frac{1}{m_{T,i}} = v_{L,i} \tau_{0,i} \wedge \frac{\sin \epsilon_{I,i}}{v_{L-1}} = \frac{\sin \epsilon_{T,i}}{v_{L,i}} \wedge m_{T,i} = \frac{v_{L,i} \cos^2 \epsilon_{I,i}}{v_{L-1} \cos^2 \epsilon_{T,i}} m_{I11,i} + \frac{u}{\cos^2 \epsilon_{T,i}} \mathbf{B}_{11,i}^{(z)}, \quad (7.31)$$

$$\frac{1}{m_{T,i}} = v_{L,i} \tau_{0,i} \wedge \frac{\sin \epsilon_{I,i}}{v_{L-1}} = \frac{\sin \epsilon_{T,i}}{v_{L,i}} \wedge 0 = \frac{v_{L,i} \cos \epsilon_{I,i}}{v_{L-1} \cos \epsilon_{T,i}} m_{I12,i} + \frac{u}{\cos \epsilon_{T,i}} \mathbf{B}_{12,i}^{(z)}, \quad (7.32)$$

$$\frac{1}{m_{T,i}} = v_{L,i} \tau_{0,i} \wedge \frac{\sin \epsilon_{I,i}}{v_{L-1}} = \frac{\sin \epsilon_{T,i}}{v_{L,i}} \wedge m_{T,i} = \frac{v_{L,i}}{v_{L-1}} m_{I22,i} + u \mathbf{B}_{22,i}^{(z)}. \quad (7.33)$$

Considering that $v_{L,i}$ must be positive the three physically reasonable solutions to these systems read

$$v_{L,i} = \frac{2v_{L-1}}{F_1}, \quad (7.34)$$

$$m_{T,i} = \frac{F_1}{2v_{L-1}\tau_{0,i}}, \quad (7.35)$$

$$\sin \epsilon_{T,i} = \frac{2 \sin \epsilon_{L,i}}{F_1}, \text{ with} \quad (7.36)$$

$$F_1 = \sqrt{4 \sin^2 \epsilon_{L,i} + 2H_1^2 + 4 \cos^2 \epsilon_{L,i} m_{I11,i} v_{L-1} \tau_{0,i} + 4H_1 \cos \epsilon_{L,i} + 2G_1}, \quad (7.37)$$

$$G_1 = \pm \sqrt{H_1^4 + 4H_1^3 \cos \epsilon_{L,i} (1 + \cos \epsilon_{L,i} m_{I11,i})}, \quad (7.38)$$

$$H_1 = B_{11,i}^{(z)} v_{L-1} \tau_{0,i}, \quad (7.39)$$

for system (7.31),

$$v_{L,i} = \frac{B_{12,i}^{(z)} v_{L-1}}{F_2}, \quad (7.40)$$

$$m_{T,i} = \frac{F_2}{B_{12,i}^{(z)} v_{L-1} \tau_{0,i}}, \quad (7.41)$$

$$\sin \epsilon_{T,i} = \frac{\sin \epsilon_{L,i} B_{12,i}^{(z)}}{F_2}, \text{ with} \quad (7.42)$$

$$F_2 = \sqrt{B_{12,i}^{(z)2} + \cos^2 \epsilon_{L,i} m_{I12,i} (2B_{12,i}^{(z)2} + m_{I12,i})}, \quad (7.43)$$

for system (7.32), and

$$v_{L,i} = \frac{\sqrt{2} v_{L-1}}{F_3}, \quad (7.44)$$

$$m_{T,i} = \frac{F_3}{\sqrt{2} v_{L-1} \tau_{0,i}}, \quad (7.45)$$

$$\sin \epsilon_{T,i} = \frac{\sqrt{2} \sin \epsilon_{L,i}}{F_3}, \text{ with} \quad (7.46)$$

$$F_3 = \sqrt{2v_{L-1} \tau_{0,i} m_{I22,i} + H_3^2 + 2H_3 \cos \epsilon_{L,i} \pm G_3}, \quad (7.47)$$

$$G_3 = \pm \sqrt{H_3^4 + 4H_3^3 (m_{I22,i} + \cos \epsilon_{L,i}) - 4H_3^2 \sin \epsilon_{L,i}}, \quad (7.48)$$

$$H_3 = B_{22,i}^{(z)2} v_{L-1} \tau_{0,i}, \quad (7.49)$$

for system (7.33).

As can be seen, the systems (7.31) and (7.33) provide two physically valid solutions due to the signs of the square roots of G_1 and G_3 , respectively. The correct solution can be determined by using the transmission law (7.23) to reconstitute the input values from the gained solutions. Another possibility is to compare the results of the three systems and to select the proper solution. This method does, however, require accurate results which are, in general, not available for real data.

As each data point \tilde{d}_i^L provides three solutions to the layer velocity the complete data vector $\tilde{\mathbf{d}}^L$ yields a velocity field \mathbf{v}_L with $3 \times n_{\text{data}}$ components. This vector is median filtered for the removal of outliers and finally averaged to determine the layer velocity v_L .

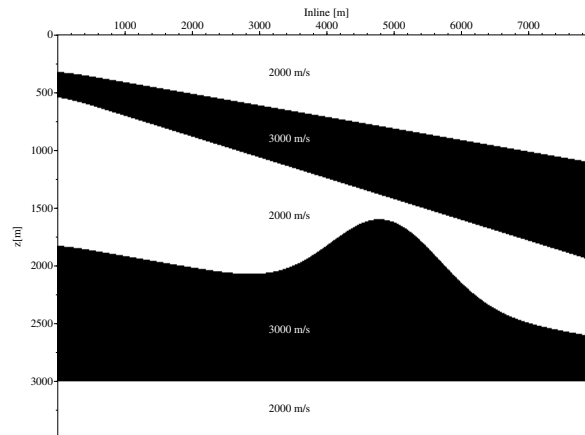


Figure 7.3: Inline section of the model used for the synthetic data example. It is characterised by strong velocity contrasts and dipping and curved layers.

Construction of the interface

Once the velocity v_L is known the corresponding interface can be constructed. Therefore, the data points pertaining the individual rays at the $(L - 1)$ th interface are transmitted into the L th layer by means of the transmission law (7.23) for wavefronts. Afterwards, equation (7.2) is used to determine the location where the NIP wavefronts focus using $m_{T,i}^{-1} = (s - s_0)$. According to the geometrical interpretation of the NIP wave these points define locations on the interface under construction. Thus, the final interface can be constructed by these points and by means of the technique described in Section 7.1.3.

Special case: the first layer

Although the Dix-type inversion is a recursive process which is applied in a similar manner to each layer the first layer requires a special treatment. Actually, the CRS stack already provides the layer velocity in terms of the near-surface velocity v_0 . In addition, the normal rays are already transmitted into the first layer. Therefore, the construction of this layer reduces to the focusing of the NIP wavefronts and the construction of the first interface. However, if the near-surface velocity is wrongly chosen for the CRS stack, the wavefield attributes are incorrectly scaled and the NIP wavefronts will focus at the wrong positions. In order to avoid this effect an additional layer with zero thickness and layer velocity v_0 is introduced at the measurement surface. As a consequence, the true velocity of the first layer can be obtained by means of the inversion algorithm which is applied directly to the measurement surface. Furthermore, the wavefield attributes are scaled to the correct values due to the additional transmission.

7.3 Synthetic data example

In order to test the Dix-type inversion a synthetic dataset was generated. The corresponding model (see Figure 7.3) shows no lateral velocity variations in crossline direction, the inline direction is charac-

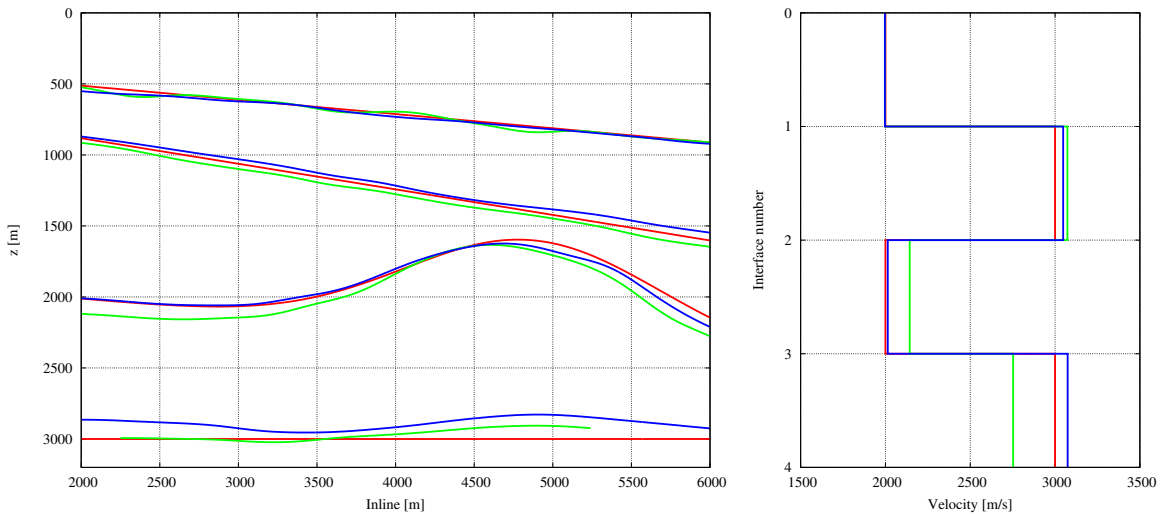


Figure 7.4: Left: interfaces of the true model (red) compared to the interface locations obtained by pure Dix-type inversion (green) and Dix-type inversion combined with tomography (blue), respectively. Except for the last interface, the locations from the combined approach better fit the original model. Right: layer velocities obtained by the two inversion algorithms compared to the original velocities (displayed using the same color scheme). Again, the combined approach provides better results.

terised by strong velocity contrasts and dipping and curved layers. The kinematic wavefield attributes and traveltimes of primary reflection events were forward modelled by means of the same ray tracing algorithm that enters into the inversion scheme. Thus, the Dix-type inversion yields the exact layer velocities and interfaces if the input data is not modified. In general, such optimal data is not available due to, e. g., noise on the prestack data or numerical inaccuracies of algorithms used for the determination of the wavefield attributes. Therefore, random noise in the range of $\pm 5^\circ$ for the angles, ± 100 m for the curvature radii, and ± 0.01 s for the traveltimes was added to the data prior to the inversion.

The result of the Dix-type inversion is depicted in Figure 7.4. It can be observed that the interface locations and the layer velocities are generally well recovered. However, the results also show an error accumulation and the introduction of systematic errors with increasing depth. This is due to the iterative inversion approach which yields the L th layer in dependency of the results obtained for its overburden. Thus, errors in the overburden directly influence the deeper layers. This effect can also be observed in Figure 7.5 which shows the determined layer velocities for each data point \tilde{d}_i^L . Here, the error accumulation is noticeable by the increasing scattering of the individual values and by the systematic error they introduce. For instance, the velocities of the fourth layer are systematically too small.

7.4 Combined Dix-type inversion

In order to improve the quality of the inversion result a combination of NIP wave tomography and Dix-type inversion is proposed. According to Duveneck (2004), the NIP wave tomography is stable with respect to noisy input data. Albeit the locations of the individual data points in depth may

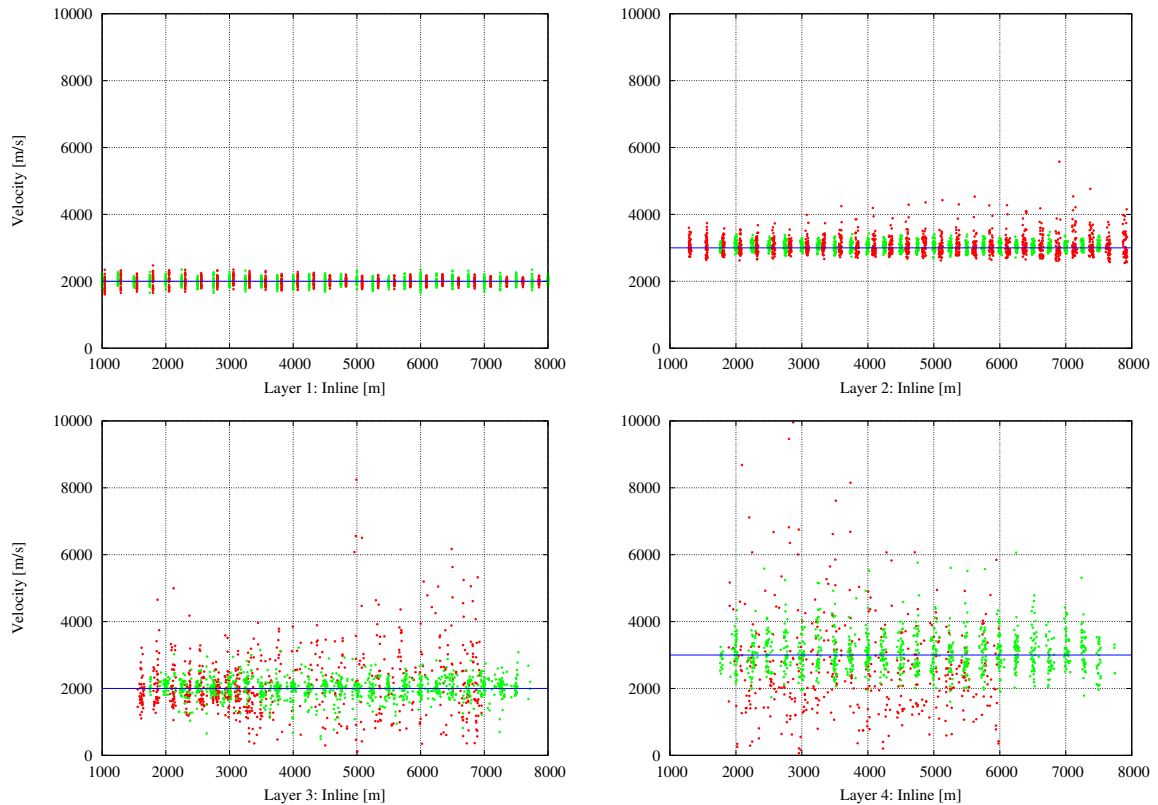


Figure 7.5: Layer velocities determined for the individual data points \tilde{d}_i^L by pure Dix-type (red) and combined inversion (green). The error accumulation introduces systematic errors and causes the velocities to scatter around the original values. In general, the velocities from combined inversion show less scattering and are closer to the reference velocities (blue lines).

scatter significantly the overall interface structures are well reconstructed, i. e., no systematic errors are introduced in the depth positioning. As the input data for tomography is equivalent to the data used in Dix-type inversion this actually means that the locations of the individual interfaces can be determined correctly within the smooth velocity model obtained by the tomography. For that purpose, the interfaces $\tilde{\mathbf{d}}^L$ are back-propagated into depth using the smooth velocity model and the ray tracing system (2.21)-(2.23). The ray tracing for a single interface is performed individually for each data point \tilde{d}_i^L until the corresponding traveltimes $\tau_{0,i}$ is used up. Similar to the Dix-type inversion the final interface is then constructed from the depth positioned points by means of the technique described in Section 7.1.3. The outcome of this process is a structural skeleton of the model, i. e., a model that consists of all the interfaces. The layer velocities are not yet defined.

This technique has been applied to the synthetic data example. The smooth velocity model (Figure 7.6) gives a first impression of the overall structure of the model. However, due to its smoothness structural information can hardly be extracted. The ray traced interfaces are depicted in Figure 7.4. Although not perfectly matching the original interfaces the structural skeleton better fits the first three interfaces compared to the results of pure Dix-type inversion. The large misfit of the last interface is due to low ray coverage for the deeper parts of the model (only 25% of the available data was used in the tomography) as well as to the model parameterisation in terms of B-Splines which is not sufficient to

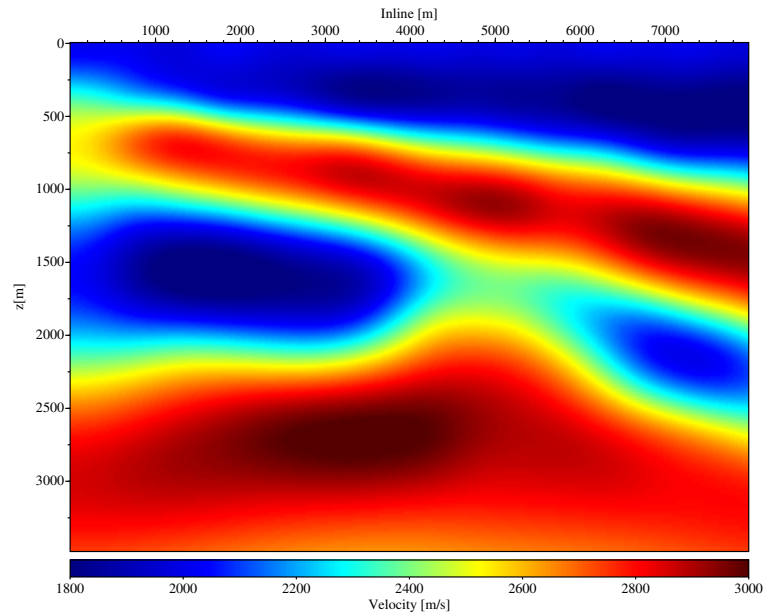


Figure 7.6: Inline section of the smooth velocity model obtained by NIP wave tomography. In general, the structure of the original velocity model can be identified but conclusions on layer locations and velocities can hardly be drawn.

accurately describe the strong velocity contrasts. Thus, such misfits may be further reduced by using different model parameterisations and, to a certain extent, by increasing the amount of input data.

After the construction of the structural skeleton, the last step consists in the determination of the layer velocities. This is again done by means of the iterative Dix-type inversion method. However, as the interfaces are already known the inversion scheme is used to provide velocities only. As can be seen in Figure 7.4 these velocities are, due to the more accurate interface locations, closer to the original velocities than the pure Dix-type inversion. Furthermore, Figure 7.5 demonstrates that the scattering of the individual velocities and the systematic errors are significantly reduced. In addition, a larger number of data points could be used as the ray tracing is not spatially restricted to a model defined by the shapes of the interfaces.

So, in the combined Dix-type inversion the interfaces are constructed independently and, therefore, without error accumulations whereas the velocities still suffer from error accumulation as the iterative Dix-type scheme is used. The alternative construction of the interfaces does, however, reduce this error accumulation as far as possible.

7.5 Further aspects

So far, the model is assumed to be exactly described by means of a layered medium. Furthermore, the availability of structural data from all primary reflection events is expected. When dealing with real data both assumptions are, in general, not satisfied. For NIP wave tomography deviations from these assumptions are not critical. As long as the parameterisation in terms of B-Splines allows to

determine a model consistent with the data the subsequently created structural skeleton will provide accurate interface locations. The Dix-type velocity inversion behaves differently. If the medium shows only slight lateral velocity variations a calculated layer velocity represents an RMS velocity of all the true layers between the assumed layer boundaries (e. g., [Hubral and Krey, 1980](#)) but with increasing lateral variations this interpretation loses its meaning. Thus, the application of Dix-type inversion methods is generally questionable for complex data that does not allow to extract a sufficiently large fraction of the primary reflection events.

The quality of the inversion result can be further enhanced by involving the normal wavefront into the process. The corresponding curvature matrices can be included in the ray tracing algorithm that back-propagates the interfaces into depth. There, the normal wavefronts provide information on the local curvatures and orientations of the interfaces and can, for instance, be used to additionally constrain the interfaces or to close small gaps on the interface. However, The danger of this attempt is that subtle details of the interface may be obscured.

Chapter 8

Application to real data

In the scope of the project *High-resolution images of subsurface CO₂ storage sites in time and depth by the CRS methodology (CO₂CRS)* (Trappe et al., 2005) the 3D CRS stack and the inversion algorithm were applied to a real onshore dataset.

The application of the combined Dix-type inversion approach demonstrates the feasibility of the method for real data. Unfortunately, no results of a prestack depth migration were available for this data and, thus, the results cannot be verified quantitatively. However, as the velocities obtained from NIP wave tomography and layer-stripping inversion complement each other it can be expected that they will at least give a reasonable impression of the velocity distribution in the subsurface.

8.1 Prestack data

The data under investigation were acquired such that the azimuthal coverage allows to perform the CRS stack with eight parameters, i. e., the distribution of the traces in the CMP bins covers a wide range of offset azimuths and the ZO locations of the CMP stacked traces are spread over the complete 2D acquisition area (see Figure 8.1).

Midpoint and half-offset geometry	
Number of CMP bins in inline/crossline direction	up to 319, up to 159
Total number of CMP bins	50936
Maximum CMP fold	100
Maximum inline/crossline length	7975 m, 3975 m
CMP bin interval	≈25 m
Offset range, azimuthal coverage	up to 5000 m, full coverage

Recording parameters	
Recording time	4 s
Sampling interval	4 ms

Table 8.1: Acquisition geometry and recording parameters.

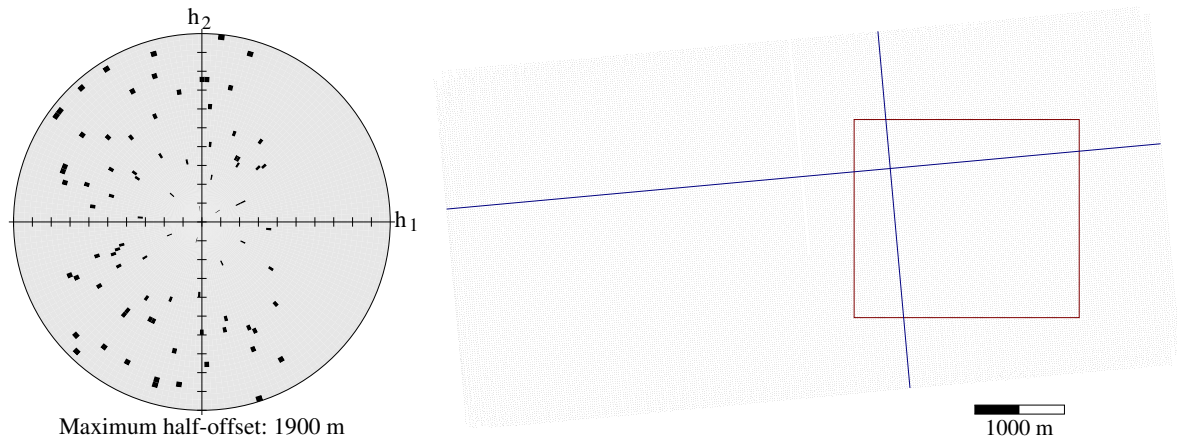


Figure 8.1: Left: azimuthal coverage of traces in a sample CMP bin. Black areas denote regions where traces are located. As a large range of azimuths is covered a three-parameter search for \mathbf{M} is feasible. Right: distribution of the ZO locations of the CMP stacked traces on the acquisition area. The traces cover the complete 2D area. The velocity inversion was carried out within the region enclosed by the red rectangle. The blue lines indicate the locations of the inline and crossline sections that will be displayed throughout this chapter.

The prestack data were already preprocessed and the results presented in this chapter all refer to these preprocessed data. The size of the dataset amounts to over six gigabytes. The CRS stack was performed on the complete dataset leading to a ZO volume covering an approximately rectangular area of $8000 \text{ m} \times 4000 \text{ m}$ with an average distance of 25 m between the CMP bins. This rectangular area is rotated counter-clockwise by approximately 5° with respect to the global coordinate system. In the following, inline and crossline direction are defined as the axes which form an acute angle of 5° with the $m_1^{(x)}$ and $m_2^{(x)}$ axes of the acquisition area, respectively. Thus, they are aligned with the rectangular area. A summary of the midpoint and half-offset geometry and the recording parameters is given in Table 8.1.

8.2 3D CRS processing

The CRS processing parameters have been selected according to the needs of the inversion methods. This means that emphasis was put on the quality of the kinematic wavefield attributes rather than on the image quality of the CRS stacked volume. For a quick overview the processing parameters are listed in Table 8.2.

8.2.1 CMP processing

The data was provided with a conventionally obtained stacking velocity volume that served as a guide for the determination of the stacking parameter \mathbf{M} . This allowed to significantly constrain the search range of the one-parameter initial grid search. In addition, the processing time was reduced due to the smaller parameter ranges to be sampled. The choice of the search apertures was based on the inspection of the moveouts of reflection events at several CMP locations. They ensure both stability

General output parameters	
CMP bins processed in inline direction	up to 319
CMP bins processed in crossline direction	up to 159
Interval of simulated ZO traces	≈ 25 m
Simulated ZO traveltimes	0...3.3 s
Sampling interval of the simulated ZO traces	4 ms
General search parameters	
Near surface velocity	1900 m/s
Total width of coherence window	36 ms
Search parameters of CMP processing	
Number of search parameters for initial search	1
Attributes for guided search	provided
Search range around guide values (expressed as stacking velocity)	±250 m/s
Search steps (initial/refinement)	40/5
Number of search parameters for simulated annealing refinement	3
Initial temperature, steps/temperature, total temperatures	0.06, 50, 6
Circular search aperture (linear interpolation)	100 m at 0.2 s 4000 m at 2 s
Search parameters of ZO processing	
Number of search parameters for initial searches (linear, hyperbolic)	2,1
Search range (α, N)	±30°, ±10 ⁻⁵ s ² /m ²
Search steps for linear search (initial/refinement)	60/4
Search steps for hyperbolic search (initial/refinement)	75/7
Circular search apertures for linear search	200 m
Circular search apertures for hyperbolic search	200 m
Number of search parameters for simulated annealing refinement	5 (2+3)
Initial temperature, steps/temperature, total temperatures	0.1, 60, 10
Circular search aperture	200 m
Search parameters of CRS processing	
Number of search parameters for simulated annealing refinement	8 (3+2+3)
Initial temperature, steps/temperature, total temperatures	0.005, 90, 9
Circular offset search aperture (linear interpolation)	100 m at 0.2 s 3000 m at 2 s
Circular midpoint search aperture	80 m
Circular smoothing aperture	105 m
Time window used for smoothing	0.03 s
Coherence threshold used for smoothing	0.01
Percentile threshold for median filter	60%

Table 8.2: Processing parameters of the CRS stack.

of the coherence analyses due to a large number of traces and reliability concerning the spread-length bias. After initial processing a three-parameter simulated annealing refinement was applied for the simultaneous determination of the three independent elements of matrix \mathbf{M} . Figures 8.2 and 8.3 show an inline and a crossline section obtained by the simulated annealing optimisation. In the CMP stacked sections a number of reflection events can be clearly identified. Also, the corresponding stacking parameters (here expressed as stacking velocity for the azimuth 0°) show reasonable values along the events. They are, however, still subject to fluctuation due to noise in the prestack data.

8.2.2 ZO processing

The processing in the ZO volumes followed the procedure as described in Chapter 3.5. Based on the ZO volume obtained from the CMP processing, a two-parameter initial grid search for the emergence angles α and β followed by a search for a one-parameter normal wave were performed. In order to determine the complete matrix \mathbf{N} and to refine the emergence angles an additional five-parameter simulated annealing optimisation was conducted. The emergence angle sections depicted in Figures 8.4 and 8.5 show the result of this optimisation. As expected, only smooth variations along the reflection events can be observed. Furthermore, the generally small dips, which does not exceed 15° along the events, indicates that the structure of the subsurface is close to a 1D medium, i. e., the lateral velocity variations can be expected to be relatively small.

8.2.3 CRS processing

In order to take full advantage of the 3D CRS operator an additional eight-parameter simulated annealing optimisation was performed. Due to the limitations of the available computer facilities (a single PC with a dual-processor) the search apertures in midpoint and half-offset direction had to be reduced significantly (see Table 8.2) but the optimisation was still carried out on up to 310 traces per CRS gather. However, it should be noted that the small search aperture may decrease the stability of the detection of \mathbf{N} .

Following this optimisation, an additional event consistent smoothing of the attributes (Hertweck et al., 2005) was performed. Its sole purpose was to remove remaining outliers and, thus, a small smoothing radius of only 105 m was used (this amounts to a maximum of 57 traces contributing to the smoothing process of a sample). A subset of the final results is depicted in Figures 8.6-8.9. The figures show that the CRS stacked sections generally have an improved signal-to-noise ratio and more distinct reflection events compared to the CMP stacked sections. Furthermore, the attribute sections show better continuity and are no longer subject to outliers and unphysical fluctuations. Finally, it can be observed that the coherence values significantly increased on the reflection events, thus, indicating reliably determined attributes.

8.3 Automatic picking of reflection events

Based on the results of the CRS processing reflection events were automatically tracked and extracted for the velocity inversion methods. As most reflection events are not continuous across the complete CRS stacked volume the tracking and, thus, the velocity inversion was restricted to a subset of the

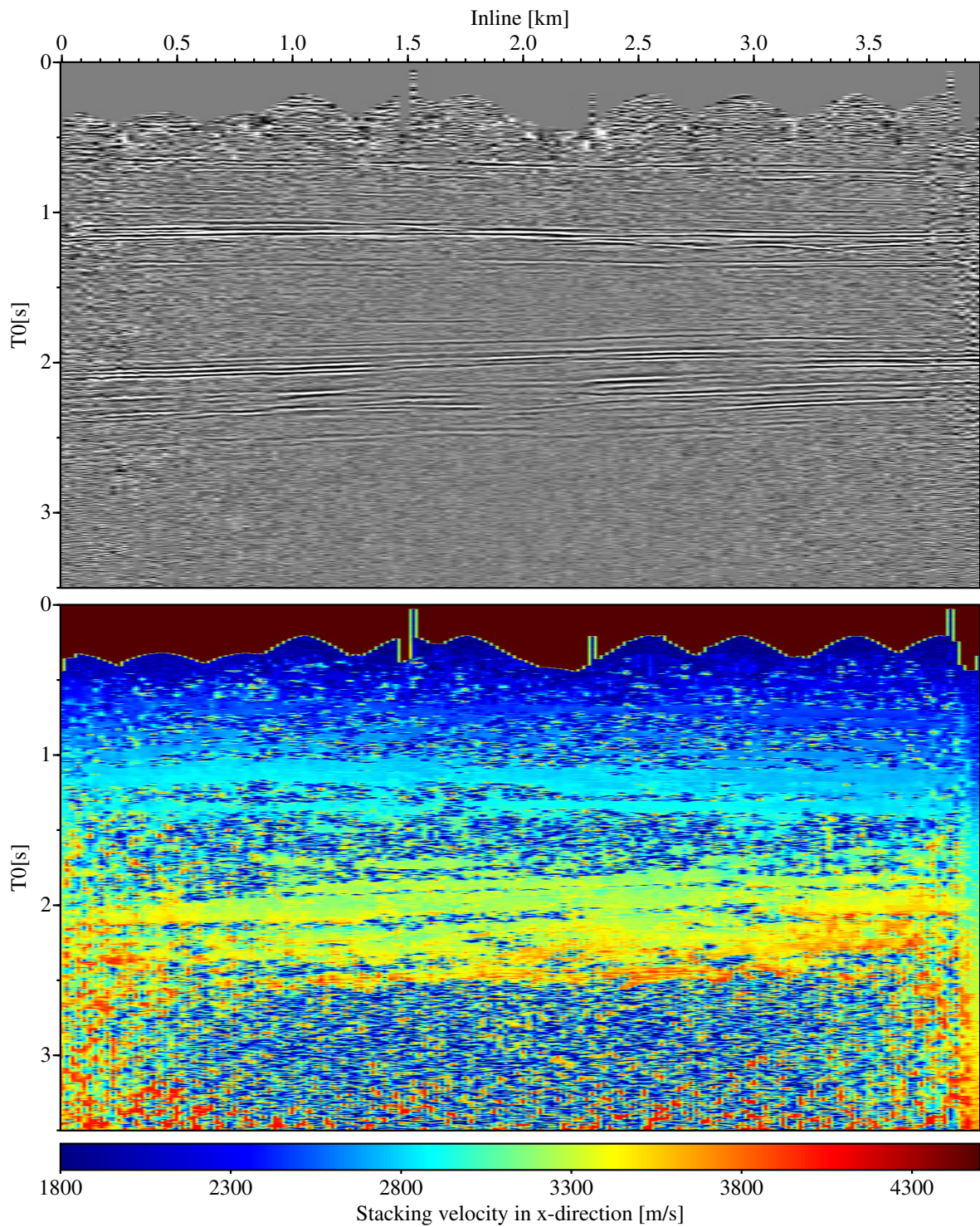


Figure 8.2: Inline CMP stack and stacking velocity sections obtained from the three-parameter simulated annealing optimization.

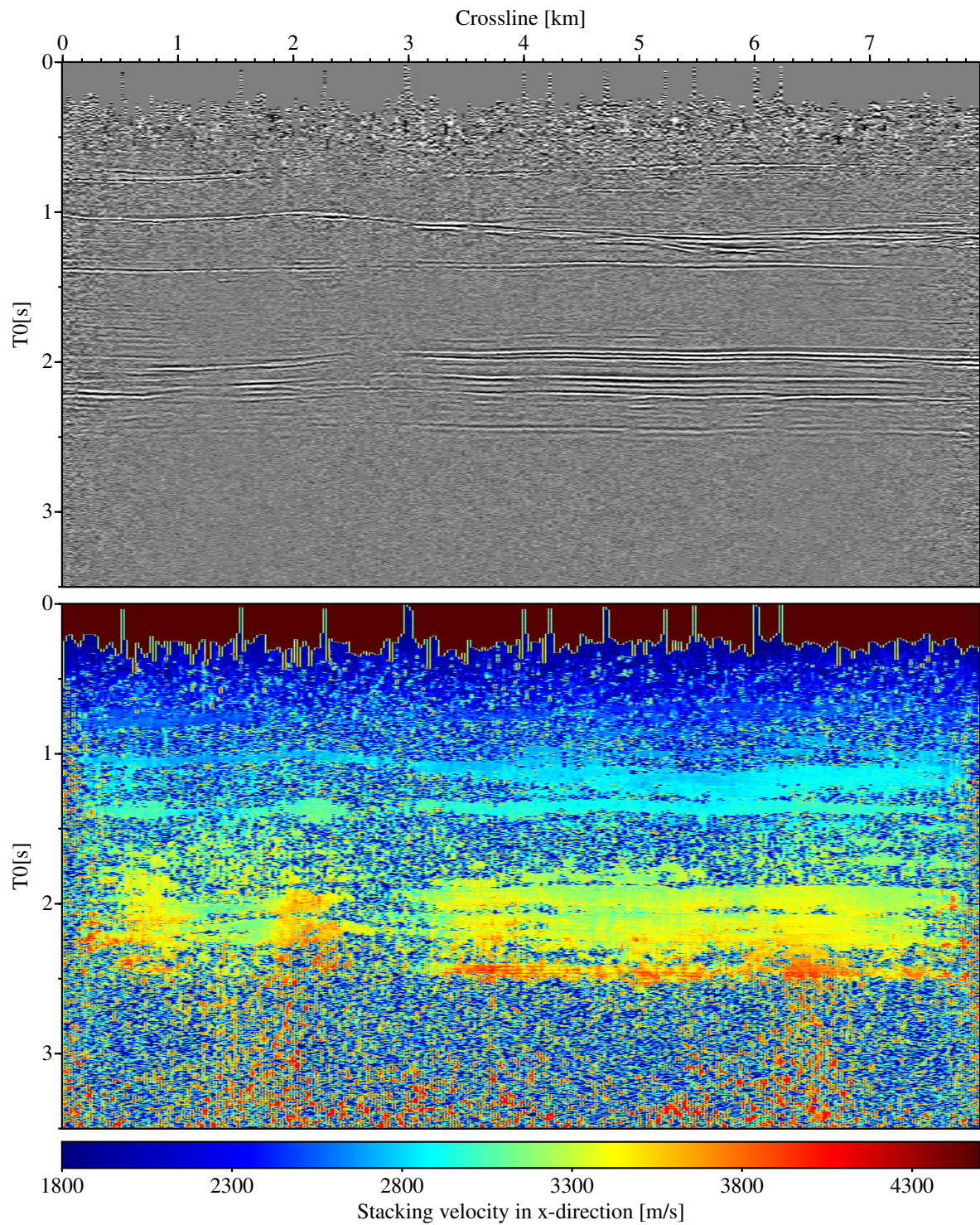


Figure 8.3: Crossline CMP stack and stacking velocity sections obtained from the three-parameter simulated annealing optimisation.

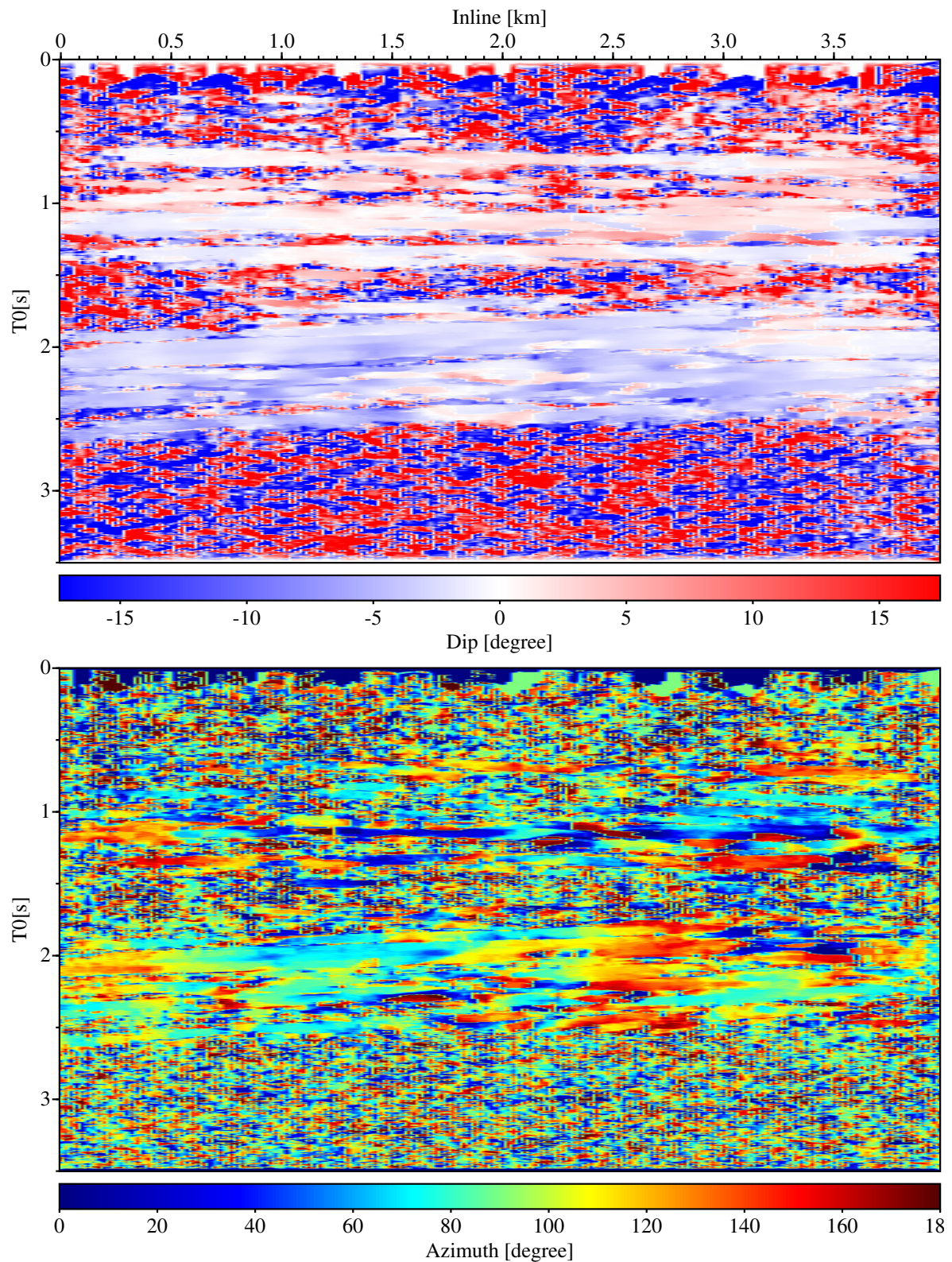


Figure 8.4: Inline dip (top) and azimuth (bottom) sections obtained from the five-parameter simulated annealing optimisation.

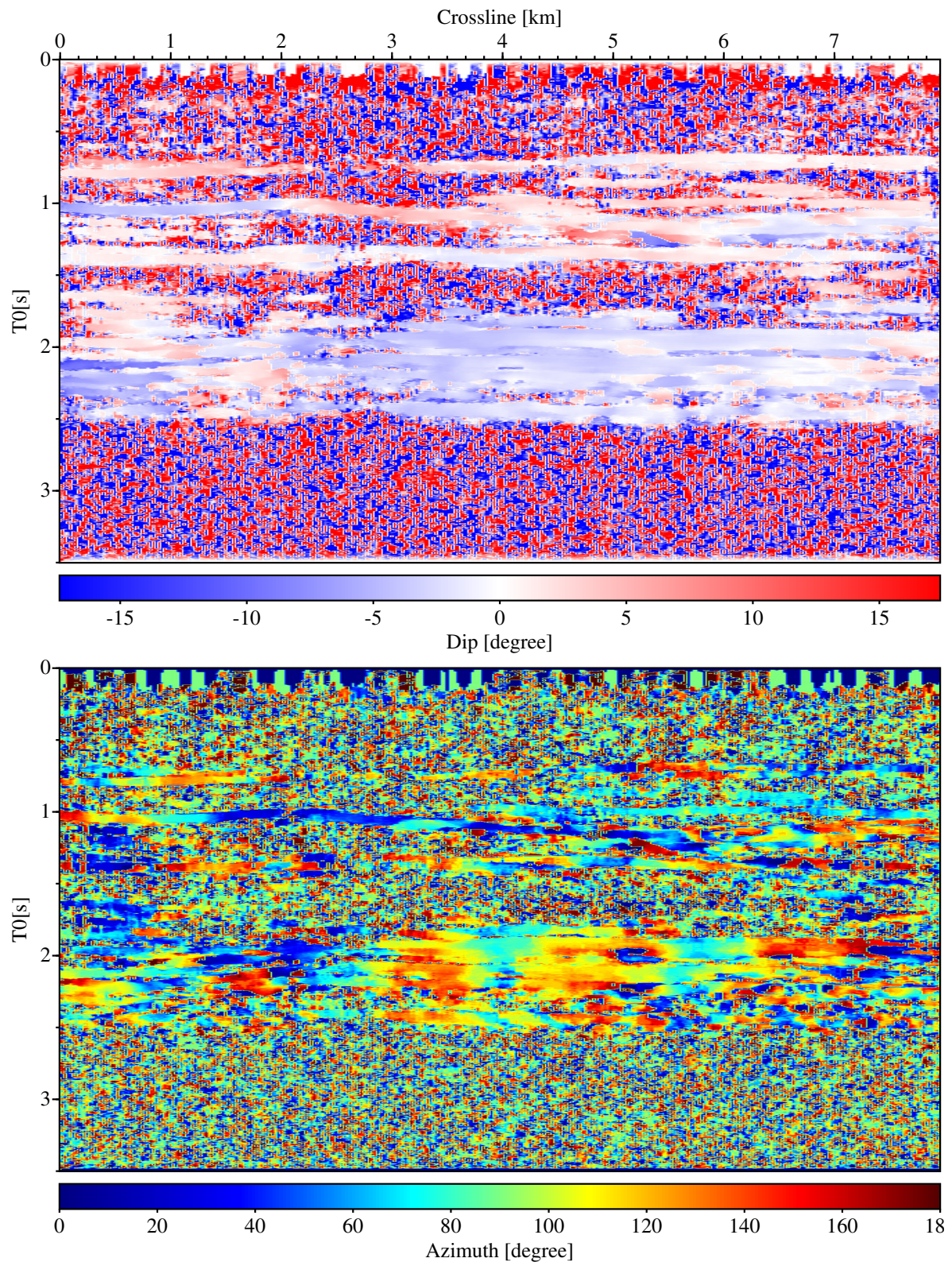


Figure 8.5: Crossline dip (top) and azimuth (bottom) sections obtained from the five-parameter simulated annealing optimisation.

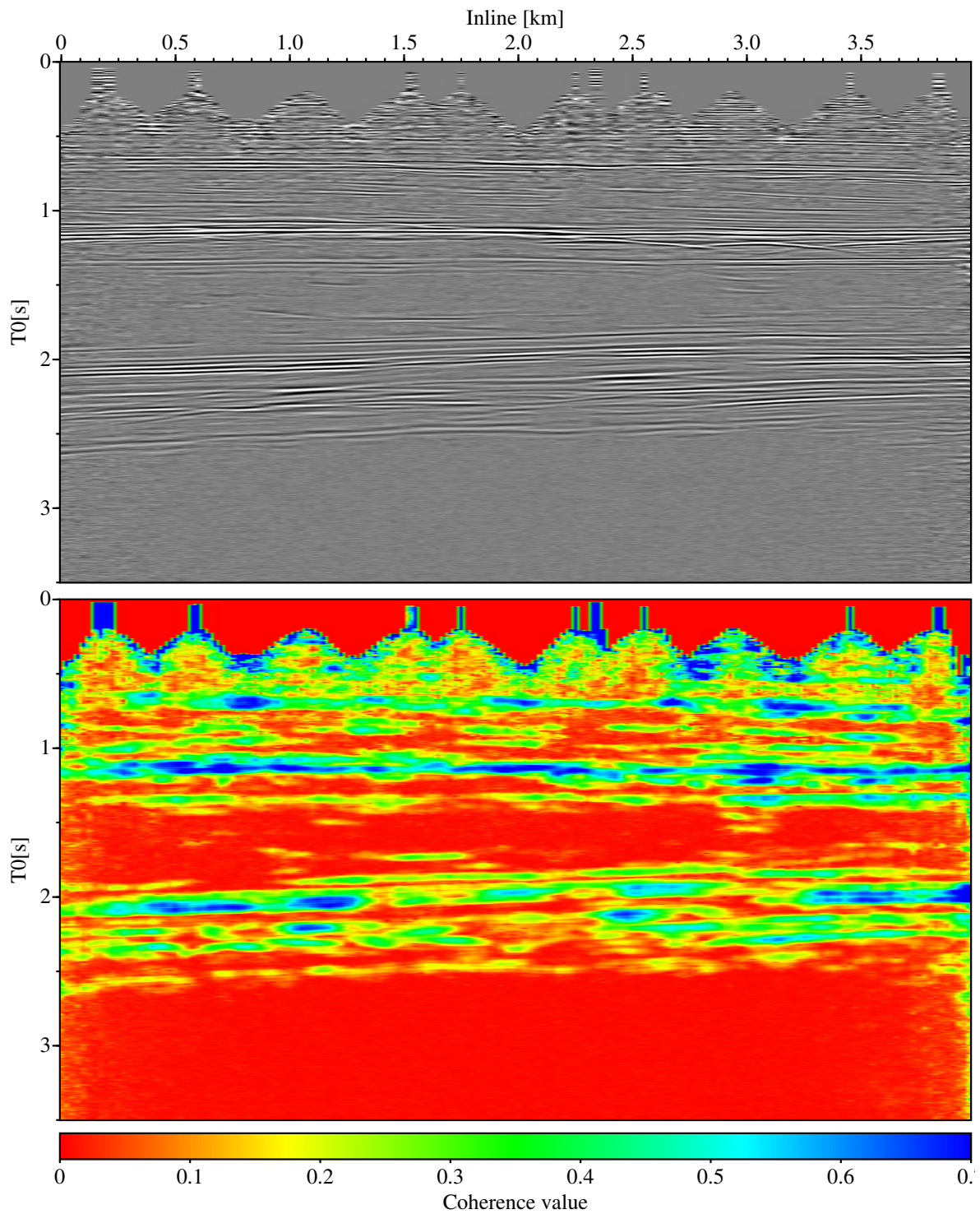


Figure 8.6: Inline CRS stack and coherence sections obtained after event consistent smoothing and restacking.

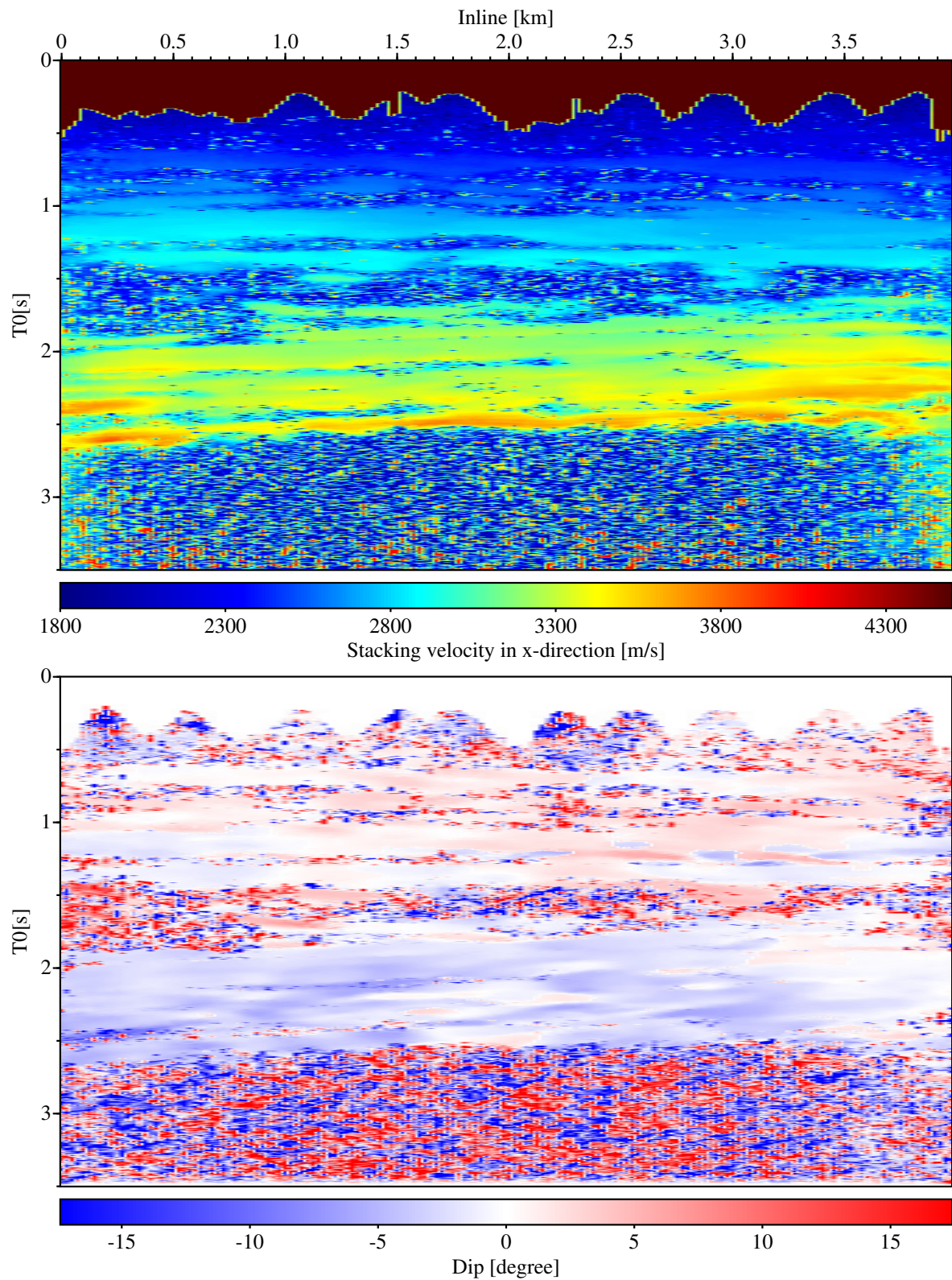


Figure 8.7: Inline stacking velocity (top) and dip (bottom) sections obtained after event consistent smoothing and restacking.

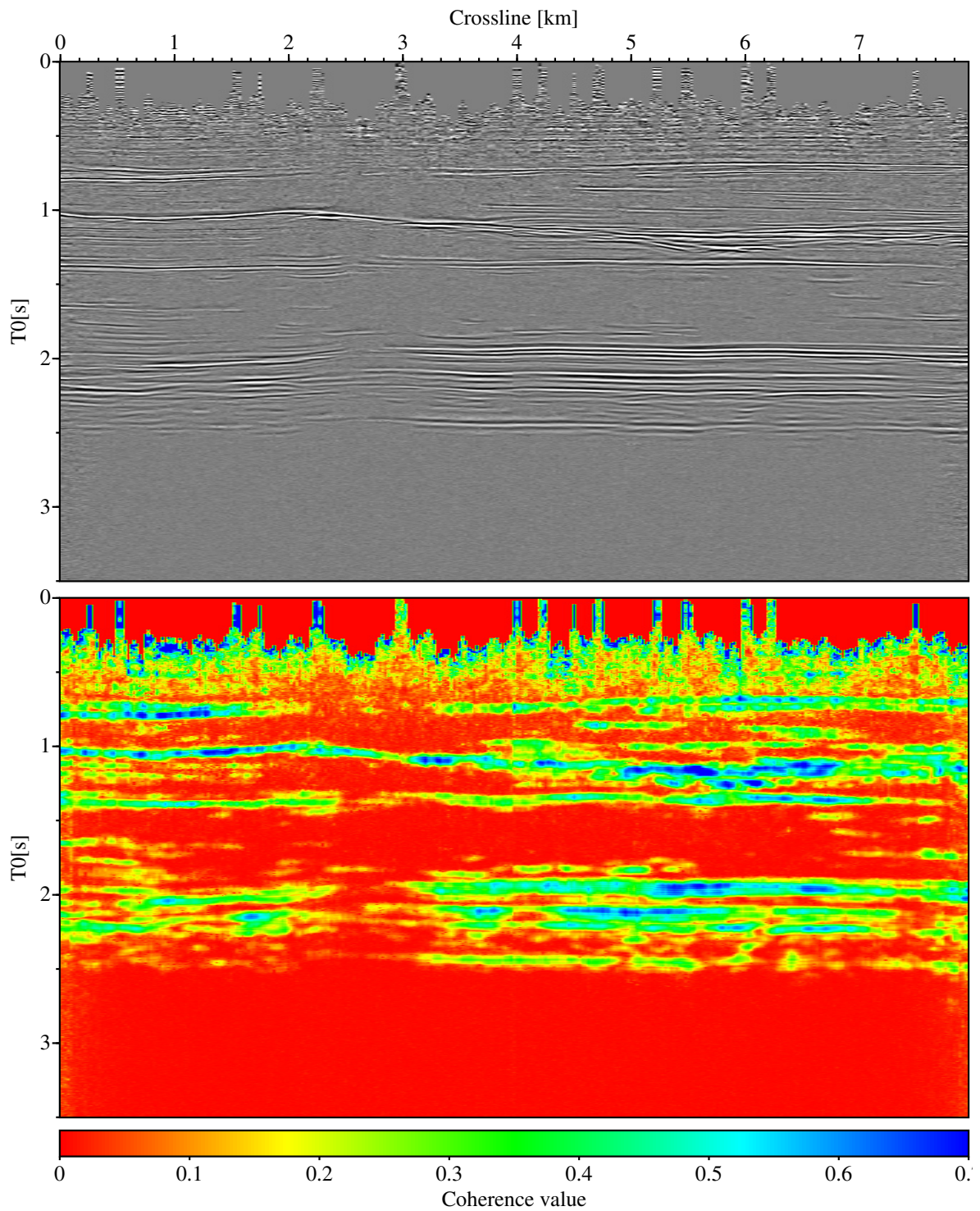


Figure 8.8: Crossline CRS stack and coherence sections obtained after event consistent smoothing and restacking.

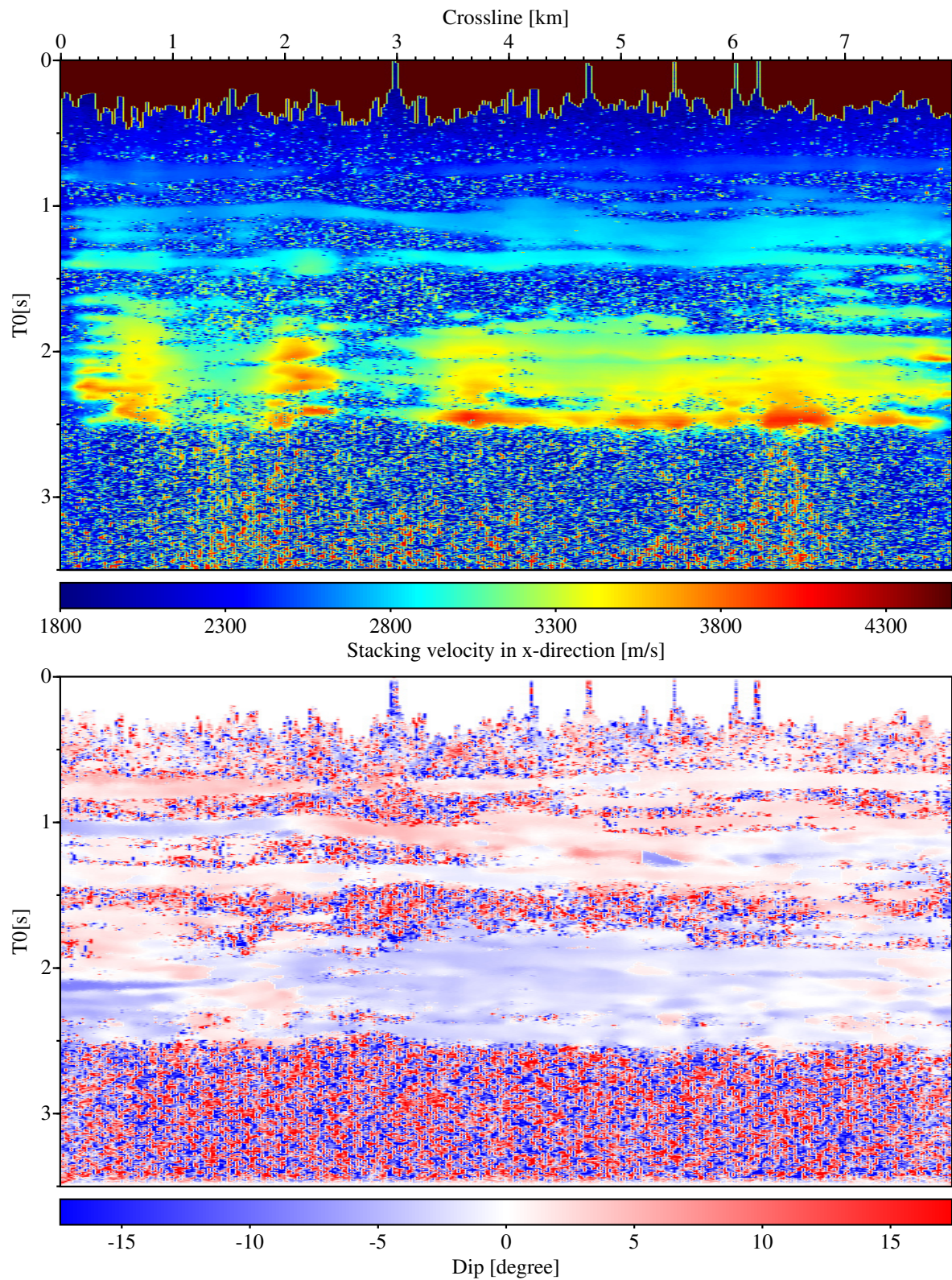


Figure 8.9: Crossline stacking velocity (top) and dip (bottom) sections obtained after event consistent smoothing and restacking.

Processing parameters	
Stack volume for validation of amplitude threshold	from hyperbolic ZO search
Allowed stack amplitude variation ⁽¹⁾	30%...10000%
Volume for validation of coherence threshold	from CRS stack
Allowed coherence variation ⁽¹⁾	30%-...100%
Coherence threshold ⁽¹⁾	0.001...0.075
Attribute volumes	from smoothed 8-parameter opt. (Normal wave not considered)
Allowed emergence angle deviation ⁽¹⁾	0.2° ...0.5°
Refinement window	0.02 s
⁽¹⁾ : Depends on the reflection event; is constant for a given event.	

Table 8.3: Processing parameters used for the tracking of reflection events.

Processing parameters	
Dimension of the velocity model	4400 × 4400 × 4400 m ³
Spacing of the B-Spline knots	400 × 400 × 400 m ³
Input data points	2683
Fixed near-surface velocity	1900 m/s
Step size in ray tracing	50 m
Number of iterations	20
Velocity model forced to follow local reflector structure	yes
Additional regularisations or constraints	none

Table 8.4: Processing parameters used for the NIP wave tomography.

data with a size of 2500 m × 2200 m (indicated by the rectangle in Figure 8.1). Within this region it was possible to extract a total of seven reflection events and the corresponding wavefield attributes that largely cover the respective area (see Figures 8.10 and 8.11 and Table 8.3 for technical details). The ZO traveltimes of these events range from approximately 0.7 s to 2.5 s. As can be seen, the events suffer from a number of gaps that will be closed by extrapolation during the the layer-stripping approach. Although this may degrade the quality of the results it simplifies the processing considerably as no interface hulls have to be defined.

In general, it cannot be expected that all reflectors in the model are detected. Especially in the shallow part of the data additional reflection events are visible but the tracking of these events was not possible due to the poor quality of the kinematic wavefield attributes as a result of the small number of traces contributing to the optimisations. However, as the data indicates a medium with little lateral variation, missing events should not falsify the velocity trend obtained by layer-stripping.

8.4 NIP wave tomography

The smooth velocity model was obtained by applying NIP wave tomography to the target area. For that purpose, the number of data points from the extracted reflection events were reduced by a factor of 20. This resulted in a total of 2683 input picks (see Figure 8.12). The velocity model with a size of 4400 × 4400 × 4400 m³ was disposed symmetrically around the target area and the tomography was

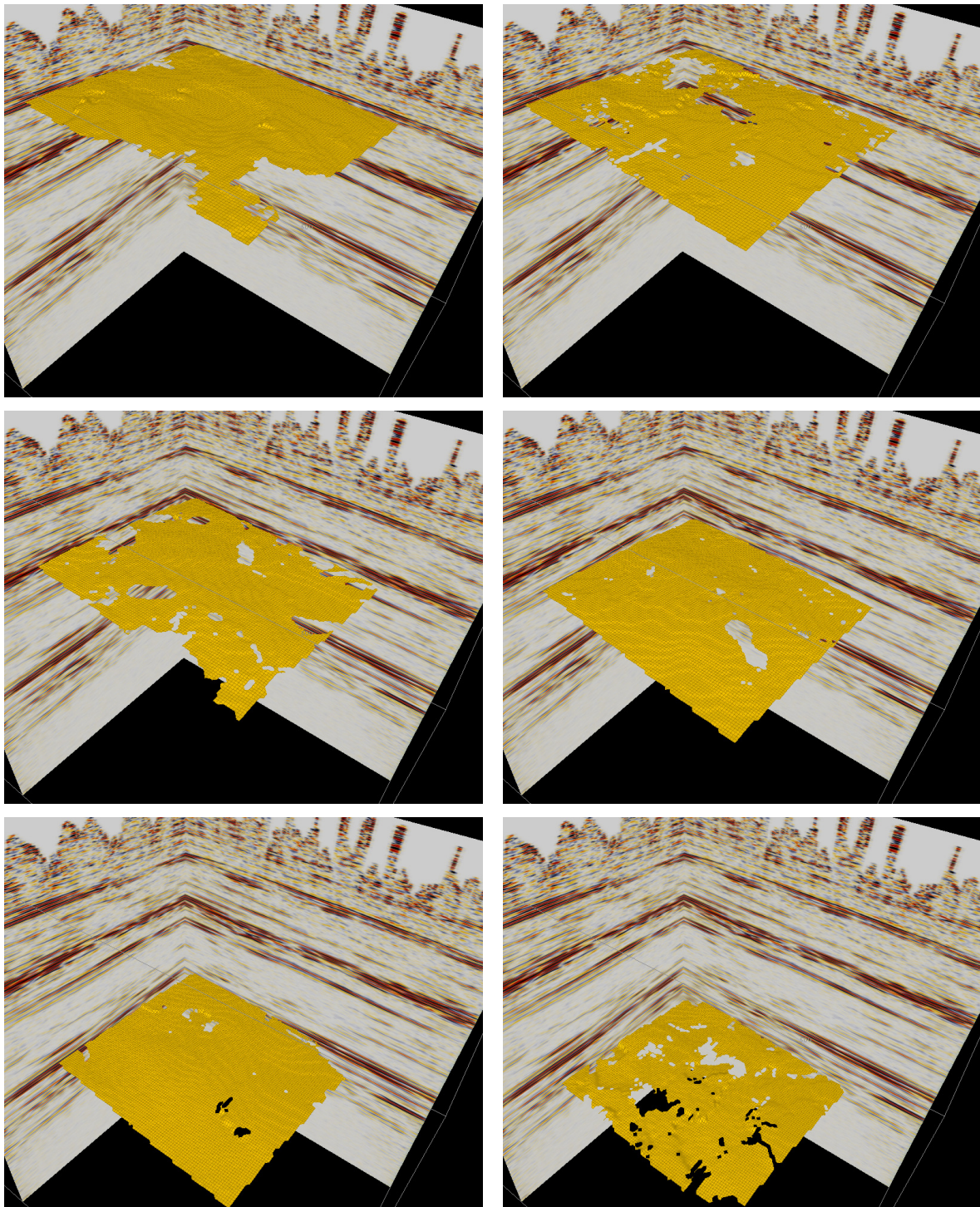


Figure 8.10: The first six reflection events extracted by the automatic tracking technique.

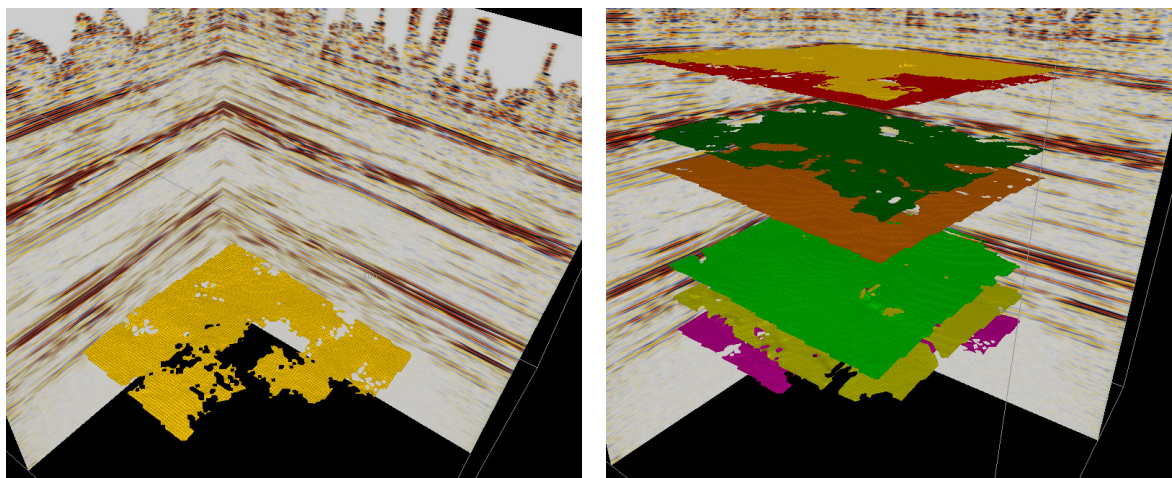


Figure 8.11: Left: the seventh reflection event extracted by the automatic tracking technique. Right: an overlay of all the extracted events.

performed with a total of 20 iterations. Additional details on the processing parameters are given in Table 8.4.

Figure 8.13 shows an inline and a crossline section of the resulting smooth velocity model. As expected, the distribution of the velocities is close to 1D and approximates a velocity gradient. The consistency of this model with the data is verified by inspecting the residual misfits between the forward modelled data components and the corresponding input data. As depicted in Figure 8.14, these misfits are small, thus indicating a result of the tomographic inversion that is consistent with the given data.

8.5 Combined Dix-type inversion

For the determination of the layered velocity model the tracked reflection events were firstly transformed to the depth domain. The required kinematic ray tracing was based on the velocity model obtained from the NIP wave tomography. Afterwards, the traced events were subject to extrapolation and smoothing. The purpose of this process was to close gaps on the events, remove unphysical fluctuations, and to define a regular grid for the description of the reflectors by means of B-Splines. In order to prevent fundamental changes to the reflector structures the smoothing bandwidth was chosen as small as possible to still close the gaps (see Table 8.5). The results of these processes are depicted in Figures 8.15 and 8.16: this structural skeleton resembles the structure of the smooth velocity model, i. e., the reflectors only show small lateral variations.

As a last step, the layer velocities were determined using the Dix-type velocity inversion equations. The obtained velocities are depicted in Figure 8.17 and show a trend that coincides in most instances with the results from the NIP wave tomography. The only remarkable difference is given by the slight velocity inversion between the fifth and the sixth layer. In order to evaluate the reliability of the results Figure 8.18, which shows the individual velocity estimates of each data point, must be considered. These velocity fields clearly demonstrate the error accumulation which is inherent to the

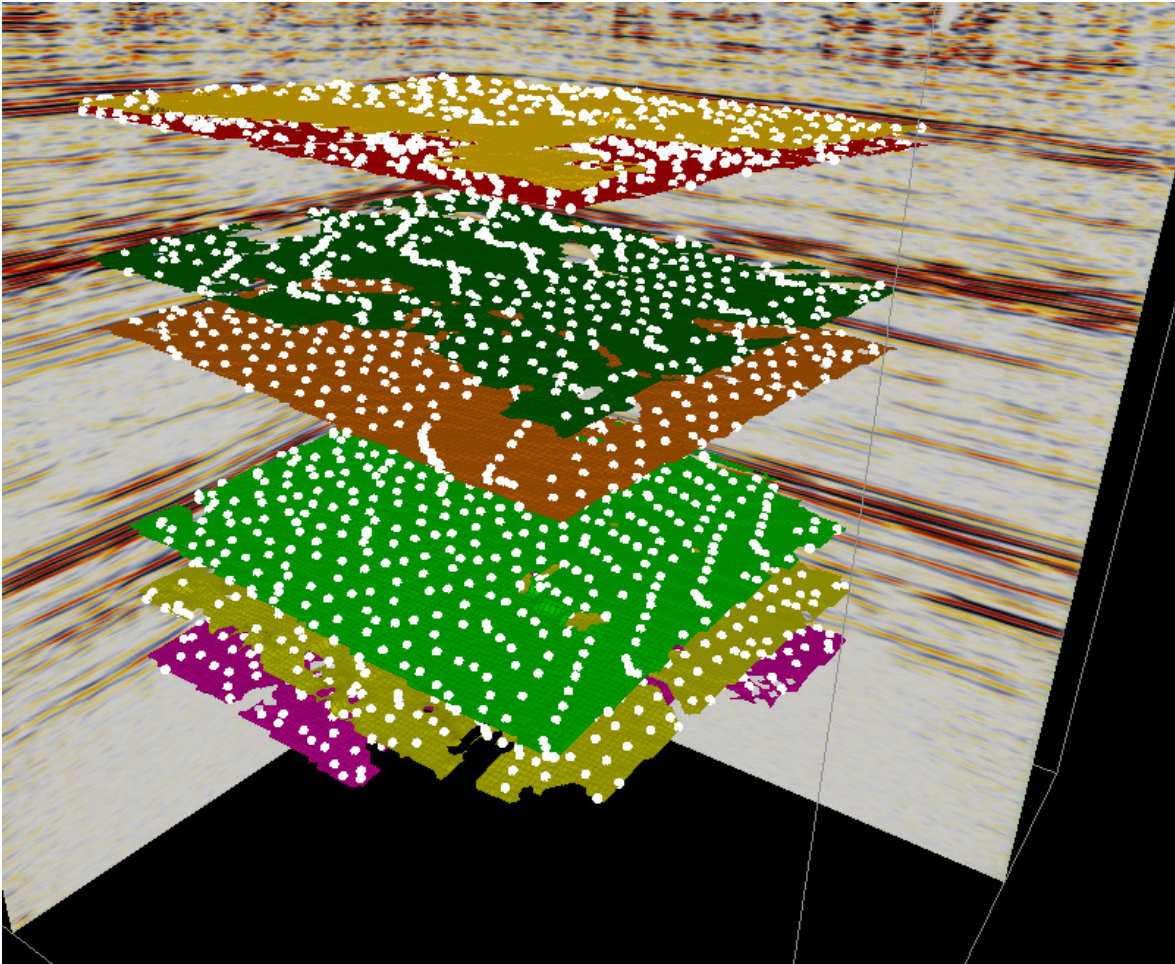


Figure 8.12: The data used in NIP wave tomography (white dots) were obtained by reducing the number of data points of the extracted reflection events by a factor of 20.

Dix-type approach (except for the second interface whose large variations are assumed to be related to the small distance to the first reflector). They also suggest that the velocities below the fifth layer and, thus, also the velocity inversion, may be falsified due to the large scattering in the velocities. Therefore, further quantitative analyses of the results in terms of, e. g., a prestack depth migration are necessary. Unfortunately, corresponding results were not available in the scope of this thesis.

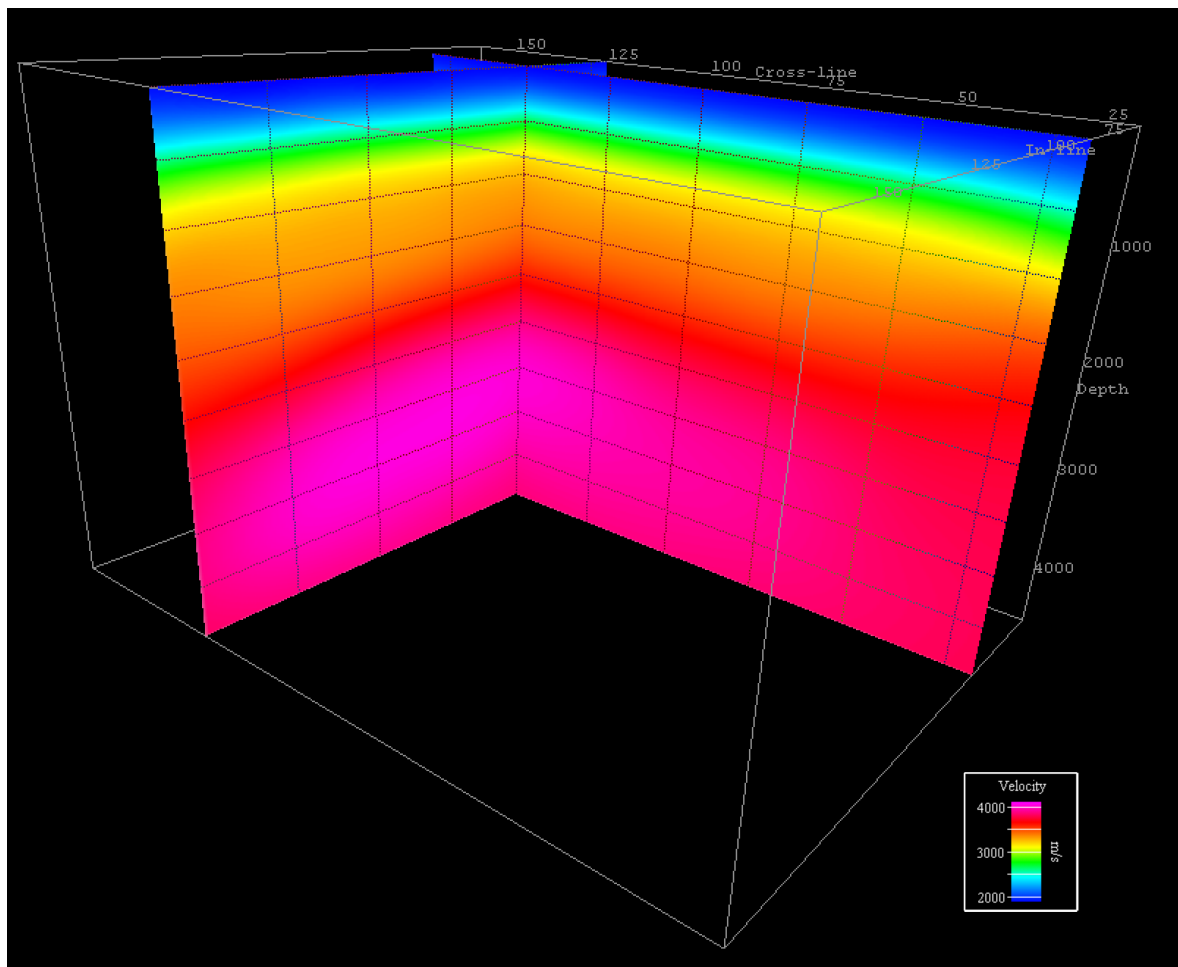


Figure 8.13: Smooth velocity model obtained by NIP wave tomography. Shown are an inline and a crossline section inside the inversion volume.

Interface generation	
Step size used in ray tracing	50 m
Reflector interpolation: grid size (x-, y-direction)	25 m, 25 m
Reflector interpolation: bandwidth (x-, y-direction)	200 m, 200 m
Degree of the B-Spline	4
Velocity determination	
Data discarded by median filter	50%
Utilise M_{12} for velocity estimation	no

Table 8.5: Processing parameters used for the layer stripping.

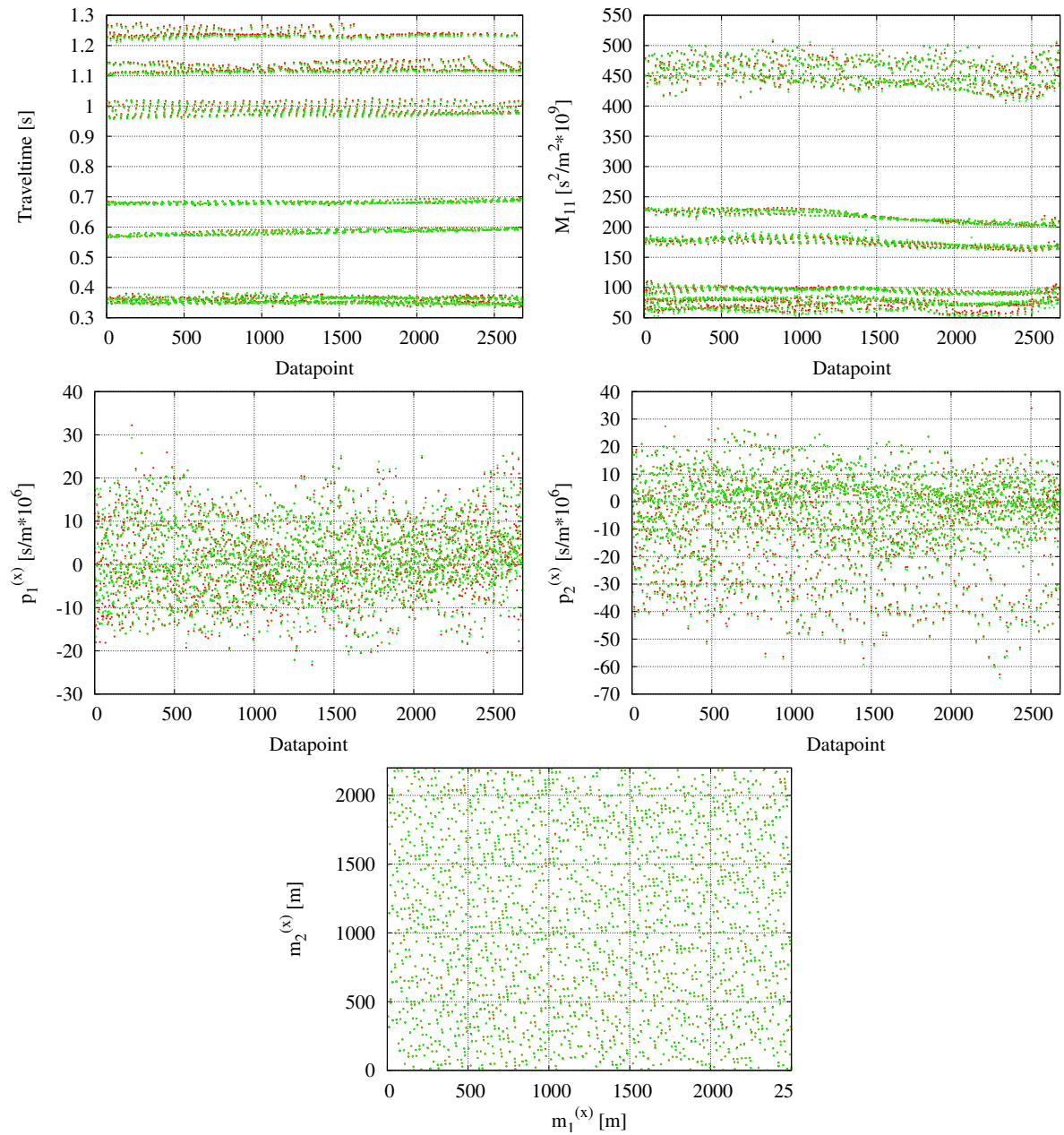


Figure 8.14: Comparison between the forward modelled (green) and data derived (red) quantities used in the NIP wave tomography.

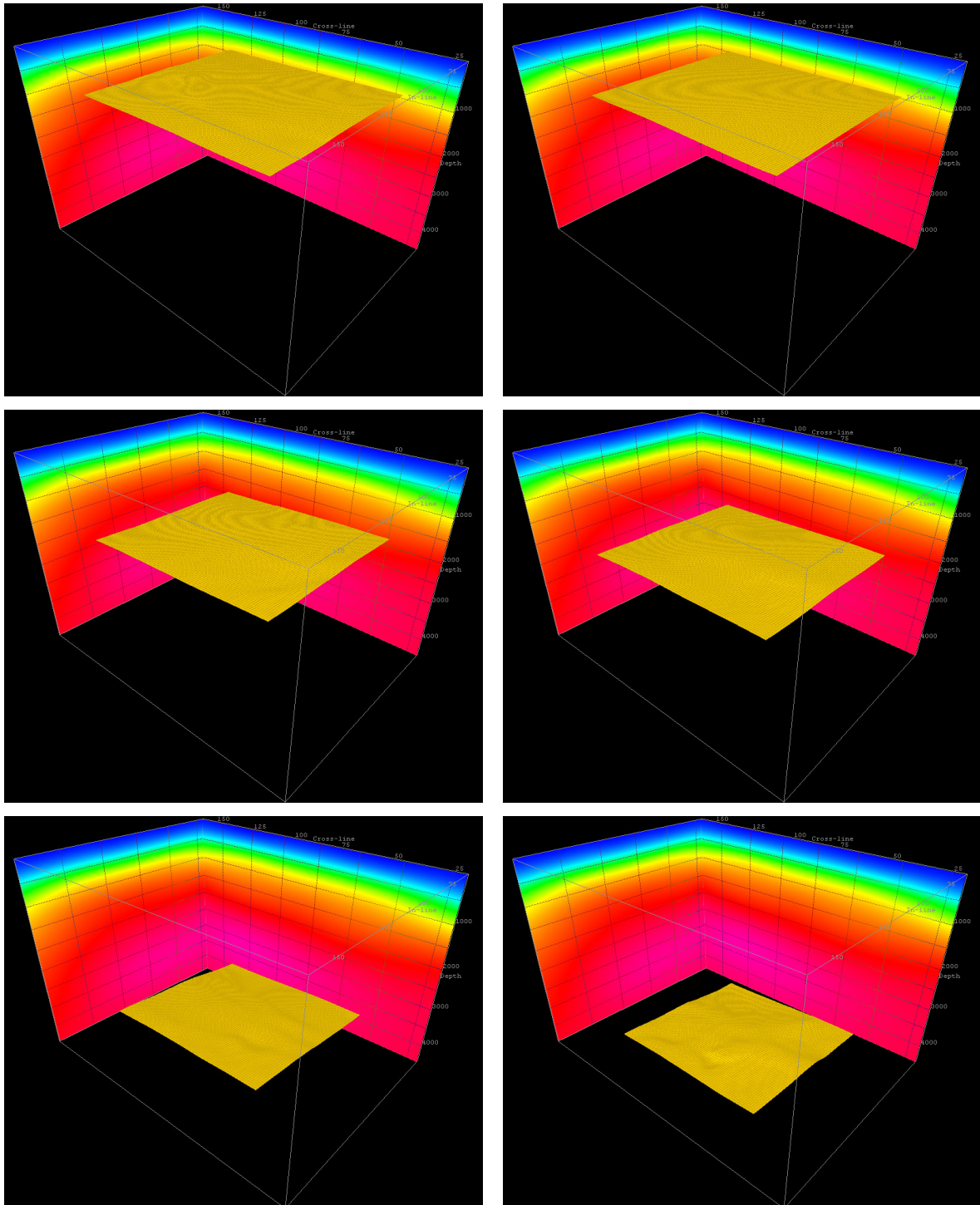


Figure 8.15: The first six reflection events after ray tracing in the smooth velocity model and interpolation to a regular grid. The colours have the same meaning as in Figure 8.13.

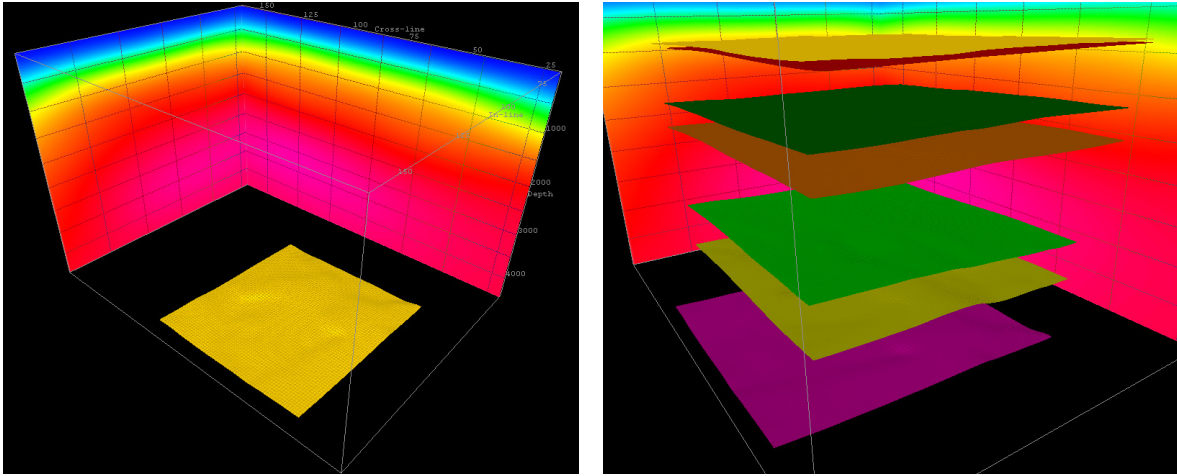


Figure 8.16: Left: the seventh reflection events after ray tracing in the smooth velocity model and interpolation to a regular grid. Right: an overlay of all reflection events. The colours have the same meaning as in Figure 8.13.

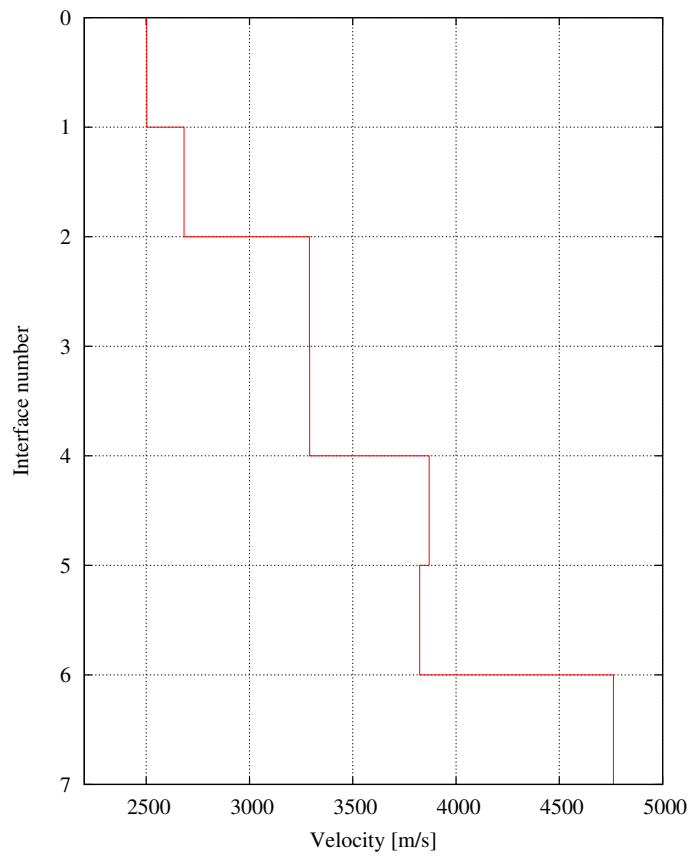


Figure 8.17: Layer velocities obtained by combined Dix-type inversion.

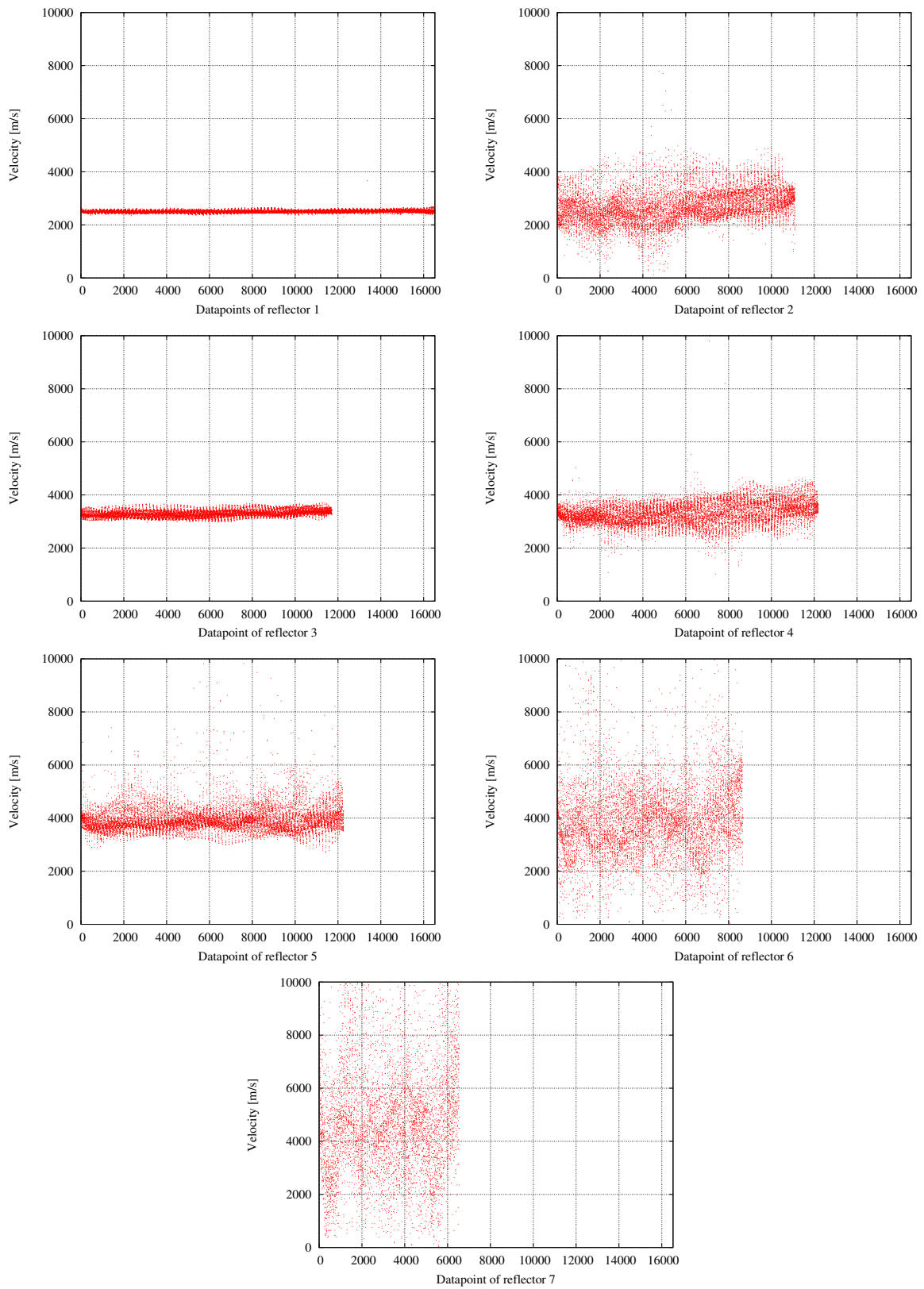


Figure 8.18: Layer velocities from the individual data points. The data are in arbitrary order and show a decreasing number of points for deeper reflectors.

Chapter 9

Summary and outlook

In this thesis, a method for the determination of 3D isotropic velocity models consisting of constant velocity layers has been presented. The method is based on kinematic wavefield attributes that are obtained from the 3D CRS stack.

The CRS stack provides, besides a CRS stacked ZO volume, eight different kinematic wavefield attributes for each imaged output location. These attributes carry information on the distribution of wave propagation velocities in the subsurface and may, thus, be used for structural velocity inversion techniques. However, in order to obtain reliable inversion results it is required that the attributes are determined as accurately as possible. Especially in the case of the 3D CRS stack this is a difficult task as today's computer facilities are not able to perform the required eight-parameter search in a reasonable time-frame. Therefore, the search is usually split into three independent steps carried out in different subsets of the data and for subsets of the attributes. A subsequent constrained optimisation of the complete CRS operator finally provides the required high quality attributes. Another problem inherent in the CRS processing is the spread-length bias which is due to the finite size of the optimisation aperture. This effect induces an aperture dependent bias in the attributes and ZO traveltimes if the corresponding prestack data cannot be described properly by the CRS stacking operator. For the 2D CRS stack this bias can be corrected for by applying a number of optimisations with different apertures. The individual biases can then be used to extrapolate unbiased ZO and attribute sections. Unfortunately, the computational cost of the method is too high to be applied to the 3D CRS stack.

With the knowledge of the kinematic wavefield attributes it is possible to perform the velocity inversion. In this thesis a structural inversion is considered, i. e., the subsurface is described by means of a model that consists of constant velocity layers separated by smoothly curved interfaces. Prior to the inversion it is necessary to structurally extract the required primary reflection events and the corresponding attributes from the CRS stack volume. For this purpose, the normal wave curvatures and emergence angles from the CRS stack are used. As they describe the orientation and curvature of the reflection events in the stacked time domain they can be used in a recursive manner to track the events.

After the structural extraction of the events and the attributes the data is available as required for the inversion. The general idea of the different inversion methods that can be formulated in terms of kinematic wavefield attributes is always the same: the NIP wavefronts, with their curvatures and propagation directions at the measurement surface determined by the CRS stack, stem from hypothetical point sources on the interfaces in the subsurface. Thus, a velocity model is consistent with the

data if the NIP wavefronts collapse to points at zero traveltimes when back-propagated into depth. In structural inversion the collapsed NIP wavefronts additionally define the locations and structural dips of the considered smoothly curved interfaces. Often, structural inversion algorithms are formulated in an iterative manner. They are known as Dix-type or layer-stripping techniques. These methods construct the velocity model beginning at the measurement surface and reach deeper regions step by step. The drawback of this technique is the error accumulation that increases with the number of the layer to be reconstructed. In order to avoid the error accumulation for the layer locations a CRS-based Dix-type inversion has been combined with NIP wave tomography. The smooth velocity models obtained from tomography do not suffer from error accumulation. Therefore, the extracted reflection events can be accurately back-propagated into depth within these velocity models. This provides a structural skeleton of the searched-for layered velocity model that is afterwards filled up with layer velocities by means of Dix-type inversion. The simple synthetic data example in Chapter 7 shows that this combined inversion indeed provides improved results. Furthermore, the feasibility of the complete workflow, i. e., 3D CRS stack, structural extraction, and combined inversion, has been demonstrated on a real 3D land dataset. Unfortunately, the results could not be verified quantitatively as a geological interpretation as well as a 3D prestack depth-migration software were not available.

Future research needs to extend the combined inversion to layers that include laterally varying velocities. This would allow to improve the accuracy as the assumption of constant velocity layers strongly simplifies the Earth's complexity. Furthermore, the inversion process could be carried out on strong key reflectors and, thus, in a target oriented manner.

Appendix A

Coordinate transformations

In the following, two coordinate systems X and Y with basis vectors $\underline{\mathbf{e}}_1^{(x)}, \underline{\mathbf{e}}_2^{(x)}, \underline{\mathbf{e}}_3^{(x)}$, and $\underline{\mathbf{e}}_1^{(y)}, \underline{\mathbf{e}}_2^{(y)}, \underline{\mathbf{e}}_3^{(y)}$, respectively, and the position vector $\underline{\mathbf{r}}$ of an arbitrary point are considered. In the X -system, with coordinates $\underline{\mathbf{x}}$, the position vector is given by

$$\underline{\mathbf{r}} = x_1 \underline{\mathbf{e}}_1^{(x)} + x_2 \underline{\mathbf{e}}_2^{(x)} + x_3 \underline{\mathbf{e}}_3^{(x)}, \quad (\text{A.1})$$

and in the Y -system, with coordinates $\underline{\mathbf{y}}$, by

$$\underline{\mathbf{r}} = y_1 \underline{\mathbf{e}}_1^{(y)} + y_2 \underline{\mathbf{e}}_2^{(y)} + y_3 \underline{\mathbf{e}}_3^{(y)}. \quad (\text{A.2})$$

The origins of the two coordinate systems are assumed to coincide. Otherwise, an additional translation has to be applied before or after the transformations described below.

Coordinate transformation in terms of the Jacobian matrix $\underline{\mathbf{J}}$

In general, the coordinate transformation from the Y -system to the X -system is formulated in terms of the Jacobian or transformation matrix $\underline{\mathbf{J}}$

$$d\underline{\mathbf{x}} = \underline{\mathbf{J}} d\underline{\mathbf{y}}, \quad (\text{A.3})$$

with

$$J_{ij} = \frac{\partial x_i}{\partial y_j}, \quad i, j = 1, 2, 3. \quad (\text{A.4})$$

The backward transformation from the X -system to the Y -system is only possible if the inverse of the Jacobian matrix $\underline{\mathbf{J}}^{-1}$ exists or, equivalently, $\det \underline{\mathbf{J}} \neq 0$. In that case the backward transformation is given by

$$d\underline{\mathbf{y}} = \underline{\mathbf{J}}^{-1} d\underline{\mathbf{x}}. \quad (\text{A.5})$$

Coordinate transformation between Cartesian coordinate systems

The Jacobian matrix (A.4) can be greatly simplified if transformations between Cartesian coordinate systems with orthonormal basis vectors are considered.

In order to obtain the relevant expressions the derivatives of the position vector $\underline{\mathbf{r}}$ with respect to the coordinates are taken. Considering equations (A.1) and (A.2) this yields

$$\frac{\partial \underline{\mathbf{r}}}{\partial x_i} = \mathbf{e}_i^{(x)} \quad , \quad \frac{\partial \underline{\mathbf{r}}}{\partial y_i} = \mathbf{e}_i^{(y)} \quad , \quad i = 1, 2, 3. \quad (\text{A.6})$$

Following these relations, the basis vectors $\mathbf{e}_i^{(y)}$ can be expressed as

$$\mathbf{e}_i^{(y)} = \frac{\partial \underline{\mathbf{r}}}{\partial y_i} = \sum_{j=1}^3 \frac{\partial \underline{\mathbf{r}}}{\partial x_j} \frac{\partial x_j}{\partial y_i} = \sum_{j=1}^3 \frac{\partial x_j}{\partial y_i} \mathbf{e}_j^{(x)} \quad , \quad i = 1, 2, 3. \quad (\text{A.7})$$

Due to the orthonormality of the Cartesian basis vectors the inner product of equation (A.7) with $\mathbf{e}_k^{(x)}$ yields

$$\mathbf{e}_i^{(y)} \cdot \mathbf{e}_k^{(x)} = \sum_{j=1}^3 \frac{\partial x_j}{\partial y_i} \mathbf{e}_j^{(x)} \cdot \mathbf{e}_k^{(x)} = \frac{\partial x_k}{\partial y_i} \quad , \quad i, k = 1, 2, 3. \quad (\text{A.8})$$

Thus, the Jacobian matrix (A.4) reads

$$J_{ij} = \frac{\partial x_i}{\partial y_j} = \mathbf{e}_i^{(x)} \cdot \mathbf{e}_j^{(y)} \quad , \quad i, j = 1, 2, 3. \quad (\text{A.9})$$

In addition, the Jacobian matrix (A.9) is orthonormal, i. e., its inverse and determinant satisfy

$$\underline{\mathbf{J}}^{-1} = \underline{\mathbf{J}}^T \quad , \quad \det \underline{\mathbf{J}} = 1. \quad (\text{A.10})$$

The backward transformation (A.5) from the X -system to the Y -system is therefore given by

$$d\underline{\mathbf{y}} = \underline{\mathbf{J}}^T d\underline{\mathbf{x}}. \quad (\text{A.11})$$

A particularly simple Jacobian matrix is obtained when the X -system coincides with the global Cartesian coordinate system

$$\underline{\mathbf{e}}_1^{(x)} = \begin{pmatrix} 1 \\ 0 \\ 0 \end{pmatrix} \quad , \quad \underline{\mathbf{e}}_2^{(x)} = \begin{pmatrix} 0 \\ 1 \\ 0 \end{pmatrix} \quad , \quad \underline{\mathbf{e}}_3^{(x)} = \begin{pmatrix} 0 \\ 0 \\ 1 \end{pmatrix} \quad , \quad (\text{A.12})$$

The columns of the Jacobian matrix (A.9) are then given by the basis vectors of the Y -system only:

$$\underline{\mathbf{J}} = [\underline{\mathbf{e}}_1^{(y)}, \underline{\mathbf{e}}_2^{(y)}, \underline{\mathbf{e}}_3^{(y)}]. \quad (\text{A.13})$$

Coordinate transformation between Cartesian coordinate systems using rotation matrices

Instead of using the Jacobian matrix (A.9) it is possible to express the transformation between Cartesian coordinate systems by a combination of the matrices

$$\underline{\mathbf{R}}_3^{(y)}(\phi) = \begin{pmatrix} \cos \phi & -\sin \phi & 0 \\ \sin \phi & \cos \phi & 0 \\ 0 & 0 & 1 \end{pmatrix} \quad , \quad \underline{\mathbf{R}}_2^{(y)}(\phi) = \begin{pmatrix} \cos \phi & 0 & \sin \phi \\ 0 & 1 & 0 \\ -\sin \phi & 0 & \cos \phi \end{pmatrix}. \quad (\text{A.14})$$

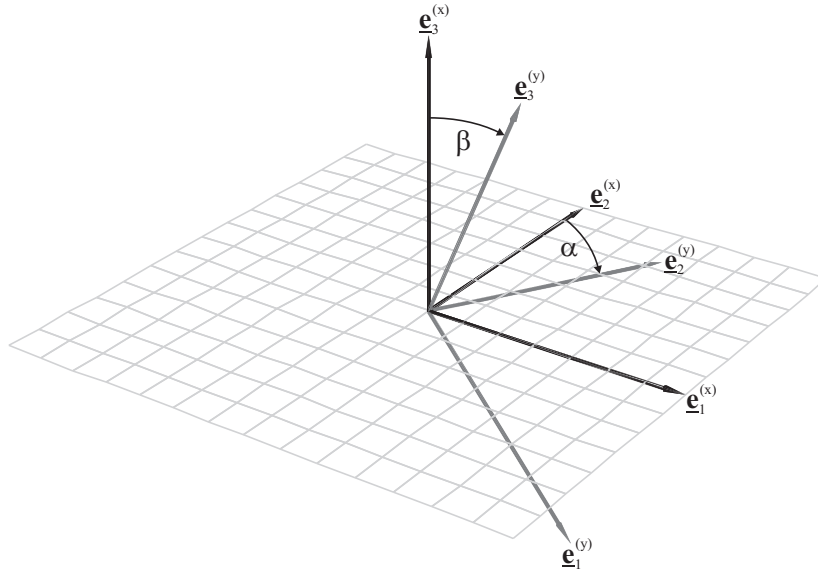


Figure A.1: The transformation between Cartesian coordinate systems with coincident origin can be described by two subsequent rotations around the y_2 - and y_3 -axes with the azimuth angle α and the polar angle β , respectively.

These matrices describe rotations around the y_3 - and y_2 -axes of the Y -system with respect to the angle ϕ .

If the azimuth angle between $\underline{e}_2^{(y)}$ and $\underline{e}_2^{(x)}$ is expressed by α and the polar angle between $\underline{e}_3^{(y)}$ and $\underline{e}_3^{(x)}$ by β (see Figure A.1), then the Jacobian matrix $\underline{\mathbf{J}}$ is given by the two subsequent rotations

$$\underline{\mathbf{J}} = \underline{\mathbf{R}}_3^{(y)}(\alpha)\underline{\mathbf{R}}_2^{(y)}(\beta). \quad (\text{A.15})$$

The complete transformation relation (A.3) in terms of $\underline{\mathbf{R}}_3^{(y)}(\alpha)$ and $\underline{\mathbf{R}}_2^{(y)}(\beta)$ finally reads

$$d\underline{\mathbf{x}} = \underline{\mathbf{R}}_3^{(y)}(\alpha)\underline{\mathbf{R}}_2^{(y)}(\beta) d\underline{\mathbf{y}}. \quad (\text{A.16})$$

Appendix B

Properties of ray propagator matrices

Ray propagator matrices have a number of properties that are required for the formulation of the travel-time approximations. In this appendix a few of these properties are reviewed. Detailed treatments are, for instance, given in [Hubral et al. \(1992\)](#), [Červený \(2001\)](#), or [Schleicher et al. \(2007\)](#)

Simplecticity

In the following an arbitrary ray propagator matrix

$$\underline{\underline{\Pi}} = \begin{pmatrix} \mathbf{Q}_1 & \mathbf{Q}_2 \\ \mathbf{P}_1 & \mathbf{P}_2 \end{pmatrix}, \quad (\text{B.1})$$

and the matrix

$$\underline{\underline{\mathbf{J}}} = \begin{pmatrix} \mathbf{0} & \mathbf{I} \\ -\mathbf{I} & \mathbf{0} \end{pmatrix}, \quad (\text{B.2})$$

are considered.

The ray propagator matrix $\underline{\underline{\Pi}}$ satisfies the simplecticity, that is,

$$\underline{\underline{\Pi}}^T \underline{\underline{\mathbf{J}}} \underline{\underline{\Pi}} = \underline{\underline{\mathbf{J}}}. \quad (\text{B.3})$$

In terms of the submatrices of $\underline{\underline{\Pi}}$ this leads, amongst others, to the relations

$$\mathbf{Q}_1^T \mathbf{P}_1 - \mathbf{P}_1^T \mathbf{Q}_1 = 0 \quad , \quad \mathbf{P}_2^T \mathbf{Q}_1 - \mathbf{Q}_2^T \mathbf{P}_1 = \mathbf{I}, \quad (\text{B.4})$$

$$\mathbf{Q}_2^T \mathbf{P}_2 - \mathbf{P}_2^T \mathbf{Q}_2 = 0 \quad , \quad \mathbf{Q}_1^T \mathbf{P}_2 - \mathbf{P}_1^T \mathbf{Q}_2 = \mathbf{I}. \quad (\text{B.5})$$

Reverse ray

Given a ray $\Omega(R, S)$ from S to R its reverse ray which travels from R to S is obtained by interchanging S and R . As both rays follow the same trajectory their slowness components only differ in their sign. According to the continuation relation (2.50), the propagator matrix $\underline{\underline{\Pi}}^*$ for the reverse ray then reads in terms of the submatrices of $\underline{\underline{\Pi}}$

$$\underline{\underline{\Pi}}^* = \begin{pmatrix} \mathbf{P}_2^T & \mathbf{Q}_2^T \\ \mathbf{P}_1^T & \mathbf{Q}_1^T \end{pmatrix}. \quad (\text{B.6})$$

Chain rule

The chain rule is used to calculate the propagator matrix of a central ray $\Omega(R, S)$ which is decomposed into individual ray segments $\Omega(Q_{i+1}, Q_i)$ with known propagator matrices $\underline{\underline{\Pi}}(Q_{i+1}, Q_i)$:

$$\underline{\underline{\Pi}}(R = Q_n, S = Q_0) = \prod_{i=n}^1 \underline{\underline{\Pi}}(Q_i, Q_{i-1}). \quad (\text{B.7})$$

Chain rule for a normal ray

A normal ray can be decomposed into a down-going and an up-going ray segment, $\Omega(M, S)$ and $\Omega(R, M)$, respectively. As one ray segment is reverse to the other the complete propagator matrix $\underline{\underline{\Pi}}(R, S)$ may be written in terms of the chain rule and the reverse propagator matrix

$$\underline{\underline{\Pi}}(R, S) = \underline{\underline{\Pi}}(S, S) = \underline{\underline{\mathbf{T}}}_0^*(M, S) \underline{\underline{\mathbf{T}}}_0(M, S), \quad (\text{B.8})$$

where $\underline{\underline{\mathbf{T}}}_0(M, S)$ is the one-way propagator matrix

$$\underline{\underline{\mathbf{T}}}_0 = \begin{pmatrix} \mathbf{A}_0 & \mathbf{B}_0 \\ \mathbf{C}_0 & \mathbf{D}_0 \end{pmatrix}. \quad (\text{B.9})$$

The matrix product in equation (B.8) shows that

$$\underline{\underline{\Pi}} = \begin{pmatrix} \mathbf{D}_0^T \mathbf{A}_0 + \mathbf{B}_0^T \mathbf{C}_0 & \mathbf{D}_0^T \mathbf{B}_0 + \mathbf{B}_0^T \mathbf{D}_0 \\ \mathbf{C}_0^T \mathbf{A}_0 + \mathbf{A}_0^T \mathbf{C}_0 & \mathbf{C}_0^T \mathbf{B}_0 + \mathbf{A}_0^T \mathbf{D}_0 \end{pmatrix}. \quad (\text{B.10})$$

Furthermore, the latter equations yield the relationship

$$\mathbf{Q}_2 = \mathbf{D}_0^T \mathbf{B}_0 + \mathbf{B}_0^T \mathbf{D}_0 = 2 \mathbf{D}_0^T \mathbf{B}_0 = \mathbf{Q}_2^T. \quad (\text{B.11})$$

Appendix C

The interface curvature matrix

In order to apply the wavefront transmission/reflection formulas the interface curvature matrix $\mathbf{B}^{(z)}$ in the local Cartesian coordinate system has to be determined. The presented derivation is based on Höcht (2002).

Given an interface point Q , a point Q' in its vicinity may implicitly be described in general Cartesian coordinates by the second-order approximation with expansion point Q

$$F(Q') = \frac{1}{2} \underline{\mathbf{x}}^T(Q', Q) \underline{\mathbf{B}}^{(x)}(Q) \underline{\mathbf{x}}(Q', Q) + \underline{\mathbf{b}}^{(x)T}(Q) \underline{\mathbf{x}}(Q', Q) = 0, \quad (\text{C.1})$$

with

$$\underline{\mathbf{x}}(Q', Q) = \underline{\mathbf{x}}(Q') - \underline{\mathbf{x}}(Q), \quad (\text{C.2})$$

$$\underline{\mathbf{B}}^{(x)}(Q) = \begin{pmatrix} \left. \frac{\partial^2 x_3}{\partial x_1^2} \right|_Q & \left. \frac{\partial^2 x_3}{\partial x_1 \partial x_2} \right|_Q & 0 \\ \left. \frac{\partial^2 x_3}{\partial x_2 \partial x_1} \right|_Q & \left. \frac{\partial^2 x_3}{\partial x_2^2} \right|_Q & 0 \\ 0 & 0 & 0 \end{pmatrix}, \quad (\text{C.3})$$

$$\underline{\mathbf{b}}^{(x)}(Q) = \begin{pmatrix} \left. \frac{\partial x_3}{\partial x_1} \right|_Q \\ \left. \frac{\partial x_3}{\partial x_2} \right|_Q \\ -1 \end{pmatrix}. \quad (\text{C.4})$$

The interface description (C.1), which is given in general Cartesian coordinates, is now transformed to the local Cartesian coordinates as defined in Section 2.5.1. Using transformation matrix $\underline{\mathbf{Z}}(Q)$ (see equation (2.66)) it reads

$$F^{(z)}(Q') = \frac{1}{2} \underline{\mathbf{z}}^T(Q') \underline{\mathbf{Z}}^T(Q) \underline{\mathbf{B}}^{(x)}(Q) \underline{\mathbf{Z}}(Q) \underline{\mathbf{z}}(Q') + \underline{\mathbf{b}}^{(x)T}(Q) \underline{\mathbf{Z}}(Q) \underline{\mathbf{z}}(Q') \quad (\text{C.5})$$

$$= \frac{1}{2} \underline{\mathbf{z}}^T(Q') \underline{\mathbf{C}}^{(z)}(Q) \underline{\mathbf{z}}(Q') + \underline{\mathbf{b}}^{(z)T}(Q) \underline{\mathbf{z}}(Q') = 0. \quad (\text{C.6})$$

Following equation (2.64) it can be stated that

$$\underline{\mathbf{b}}^{(z)}(Q) = \underline{\mathbf{b}}^{(x)T}(Q) \underline{\mathbf{Z}}(Q) = \begin{pmatrix} 0 \\ 0 \\ \mathbf{e}_3^{(z)}(Q) \cdot \underline{\mathbf{b}}^{(x)}(Q) \end{pmatrix}, \quad (\text{C.7})$$

as $\underline{\mathbf{b}}^{(x)}(Q) \cdot \underline{\mathbf{e}}_1^{(z)}(Q) = \underline{\mathbf{b}}^{(x)}(Q) \cdot \underline{\mathbf{e}}_2^{(z)}(Q) = 0$.

So far matrix $\underline{\mathbf{C}}^{(z)}(Q) = \underline{\mathbf{Z}}^T(Q)\underline{\mathbf{B}}^{(x)}(Q)\underline{\mathbf{Z}}(Q)$ is not yet a curvature matrix as the transformation introduces non-zero elements $C_{i3}^{(z)}(Q)$ and $C_{3i}^{(z)}(Q)$, $i = 1, 2, 3$. However, the interface curvature matrix $\mathbf{B}^{(z)}(Q)$ with $B_{ij}^{(z)}(Q) = \partial^2 z_3 / \partial z_i \partial z_j |_Q$ can be obtained from the second derivatives of equation (C.6) with respect to z_1 and z_2 . Considering that $\partial z_3 / \partial z_i = 0$, $i = 1, 2$, the implicit differentiation yields $\mathbf{B}^{(z)}(Q)$ in the local Cartesian coordinate system:

$$\mathbf{B}^{(z)}(Q) = -\frac{1}{\underline{\mathbf{e}}_3^{(z)}(Q) \cdot \underline{\mathbf{b}}^{(x)}(Q)} \mathbf{Z}^T(Q) \mathbf{B}^{(x)}(Q) \mathbf{Z}(Q). \quad (\text{C.8})$$

Here, $\mathbf{Z}(Q)$ is the upper left 2×2 submatrix of $\underline{\mathbf{Z}}(Q)$.

Using equation (C.8) the interface description (C.6) finally reads

$$z_3(Q') = \frac{1}{2} \mathbf{z}^T(Q') \mathbf{B}^{(z)}(Q) \mathbf{z}(Q'). \quad (\text{C.9})$$

List of Figures

Chapter 1 – Introduction	1
1.1 Data geometries	3
1.2 Kinematic wavefield attributes	6
Chapter 2 – Ray theory	9
2.1 Ray-centred coordinate system	13
2.2 Surface-to-surface two-point eikonal	25
Chapter 3 – The common-reflection-surface stack	29
3.1 NIP wave theorem	32
3.2 ZO configuration	33
3.3 Semblance	38
3.4 Sensitivity of the stack with respect to the accuracy of the stacking parameter	40
3.5 Definition and movement of a simplex	41
3.6 Linear search vs. simulated annealing optimisation	42
Chapter 4 – Spread-length bias	47
4.1 Non-hyperbolic reflection event	48
4.2 CMP stacked traces obtained with different search apertures	49
4.3 Stacking parameter M obtained with different search apertures	50
4.4 Traveltime bias over mean-square aperture	51
4.5 Optimum fit stacking parameter M_S over mean-square aperture	51
4.6 Definition of the multi-section volume	52

4.7	Results of the stack time correction	53
4.8	Results of the stacking parameter correction	54
4.9	P-wave velocity model	56
4.10	Forward modelled ZO section	57
4.11	Detailed view at the dome	58
4.12	Differences between stacking parameters M_{corr} and M	59
4.13	Differences between α_{corr} and α	60
4.14	Smooth velocity model	61
4.15	Prestack depth migration	62
Chapter 5 – Automatic picking of reflection events		65
5.1	Determination of the spatial continuation of a reflection event	66
5.2	Navigation in ZO volumes	67
5.3	Delaunay triangulation of the trace locations	69
5.4	Automatically tracked reflection event	70
5.5	Detailed view of a gap in the tracked reflection event	70
Chapter 7 – Dix-type inversion		79
7.1	Representation of interfaces	82
7.2	Ray tracing scheme	83
7.3	Inline section of the model used for the synthetic data example	88
7.4	Inversion results: interfaces	89
7.5	Inversion results: velocities	90
7.6	Smooth velocity model obtained by NIP wave tomography	91
Chapter 8 – Application to real data		93
8.1	Coverage and distribution of traces	94
8.2	Inline CMP stack and stacking velocity sections obtained from the three-parameter simulated annealing optimization.	97
8.3	Crossline CMP stack and stacking velocity sections obtained from the three-parameter simulated annealing optimisation.	98
8.4	Inline dip and azimuth sections obtained from the five-parameter simulated annealing optimisation	99

8.5	Crossline dip and azimuth sections obtained from the five-parameter simulated annealing optimisation	100
8.6	Inline CRS stack and coherence sections obtained after event consistent smoothing and restacking.	101
8.7	Inline stacking velocity and dip sections obtained after event consistent smoothing and restacking	102
8.8	Crossline CRS stack and coherence sections obtained after event consistent smoothing and restacking.	103
8.9	Crossline stacking velocity and dip sections obtained after event consistent smoothing and restacking	104
8.10	The first six reflection events extracted by the automatic tracking technique.	106
8.11	The seventh reflection event extracted by the automatic tracking technique	107
8.12	The data used for NIP wave tomography	108
8.13	Smooth velocity model obtained by NIP wave tomography	109
8.14	Comparison between the forward modelled and data derived quantities	110
8.15	The first six reflection events after ray tracing	111
8.16	The seventh reflection events after ray tracing	112
8.17	Layer velocities obtained by combined Dix-type inversion.	112
8.18	Layer velocities from the individual data points	113
Chapter A – Coordinate transformations		117
A.1	Transformation between Cartesian coordinate systems	119

List of Tables

Chapter 8 – Application to real data	93
8.1 Acquisition geometry and recording parameters	93
8.2 Processing parameters of the CRS stack	95
8.3 Processing parameters used for the tracking of reflection events	105
8.4 Processing parameters used for the NIP wave tomography	105
8.5 Processing parameters used for the layer stripping	109

References

- Aki, K. and Richards, P. G. (1980). *Quantitative Seismology - Theory and Methods, Vol. I and II*. W. H. Freeman.
- Al-Chalabi, M. (1973). Series approximation in velocity and travelttime computations. *Geophys. Prosp.*, 21:783–795.
- Al-Chalabi, M. (1974). An analysis of stacking, RMS, average and interval velocities over a horizontally layered ground. *Geophys. Prosp.*, 22:458–475.
- Al-Yahya, K. (1989). Velocity analysis by iterative profile migration. *Geophysics*, 54(6):718–729.
- Ben-Menachem, I. and Beydoun, W. (1985). Range of validity of seismic ray and beam methods in general inhomogeneous media - general theory. *Geophys. J. Royal Astron. Soc.*, (82):207–234.
- Bergler, S. (2001). The Common-Reflection-Surface Stack for Common Offset – Theory and Application. Master’s thesis, University of Karlsruhe.
- Bergler, S. (2004). *On the determination and use of kinematic wavefield attributes for 3D seismic imaging*. Logos Verlag, Berlin.
- Billette, F. and Lambaré, G. (1998). Velocity macro-model estimation from seismic reflection data by stereotomography. *Geophys. J. Intern.*, 135:671–690.
- Biloti, R., Santos, L. T., and Tygel, M. (2002). Multiparametric travelttime inversion. *Stud. Geophys. Geod.*, 46:177–192.
- Biondi, B. (2003). *3-D Seismic Imaging*. <http://sepwww.stanford.edu/sep/biondi/Lectures>, Stanford University.
- Bishop, T. N., Bube, K. P., Cutler, R. T., Langan, R. T., Love, P. L., Resnick, J. R., Shuey, R. T., Spindler, D. A., and Wyld, H. W. (1985). Tomographic determination of velocity and depth in laterally varying media. *Geophysics*, 50(6):903–923.
- Bleistein, N. (1984). *Mathematical methods for wave phenomena*. Academic Press Inc., Orlando.
- Boelsen, T. (2005). The Common-Reflection-Surface Stack for arbitrary acquisition geometries and multi-component data – Theory and Application. Master’s thesis, University of Karlsruhe.
- Butterfield, K. R. (1976). The Computation of all the Derivatives of a B-Spline Basis. *J. Inst. Maths Applies*, 17:15–25.
- Červený, V. (2001). *Seismic ray theory*. Cambridge University Press.

References

- Chapman, C. H. (2004). *Fundamentals of seismic wave propagation*. Cambridge University Press.
- Chernjak, V. S. and Gritsenko, S. A. (1979). Interpretation of effective common depth point parameters for a spatial system of homogeneous beds with curved interfaces. *Soviet Geology and Geophysics*, 20(12):91–98.
- Claerbout, J. F. (1985). *Imaging the earth's interior*. Blackwell Scientific Publications, Palo Alto.
- de Bazelaire, E. (1988). Normal moveout revisited – inhomogeneous media and curved interfaces. *Geophysics*, 53(2):143–157.
- de Boor, C. (1978). *A practical guide to Splines*. Springer Verlag.
- Delaunay, B. (1934). Sur la sphère vide. *Izvestia Akademii Nauk SSSR, Otdelenie Matematicheskikh i Estestvennykh Nauk*, 7:793–800.
- Dix, C. H. (1955). Seismic velocities from surface measurements. *Geophysics*, 20(1):68–86.
- Dümmong, S. (2005). Alternative Implementation des Common Reflection Surface Stapelverfahrens. Master's thesis, University of Hamburg.
- Duveneck, E. (2004). *Tomographic determination of seismic velocity models with kinematic wavefield attributes*. Logos Verlag, Berlin.
- Everett, J. E. (1974). Obtaining interval velocities from stacking velocities when dipping horizons are included. *Geophys. Prosp.*, 22:122–142.
- Farra, V. and Madariaga, R. (1988). Non-linear reflection tomography. *Geophys. J.*, 95:135–147.
- Gazdag, J. (1978). Wave equation migration with the phase-shift method. *Geophysics*, 43(7):1342–1351.
- Gelchinsky, B. (1989). Homeomorphic imaging in processing and interpretation of seismic data - fundamentals and schemes. In *Expanded Abstracts, 59th Annual Meeting*. Soc. Expl. Geophys.
- Gelchinsky, B., Landa, E., and Shtivelman, V. (1985). Algorithms of phase and group correlation. *Geophysics*, 50(4):596–608.
- Gelchinsky, J., Berkovitch, A., and Keydar, S. (1999). Multifocusing Homeomorphic Imaging: Part I: Basic concepts and formulae. *J. Appl. Geoph.*, 42(3,4):229–242.
- Gjoystdal, H. and Ursin, B. (1981). Inversion of reflection times in three dimensions. *Geophysics*, 46(7):972–983.
- Hale, D. (1984). Dip-moveout by fourier transform. *Geophysics*, 49(6):741–757.
- Heilmann, Z., Mann, J., and Koglin, I. (2006). CRS-stack-based seismic imaging considering top-surface topography. *Geophys. Prosp.*, 54(6):681–695.
- Hertweck, T., Mann, J., and Klüver, T. (2005). Event-consistent smoothing in the context of the CRS stack method. *J. Seis. Expl.*, 14(2-3):197–215.
- Herzberger, M. (1958). *Modern geometrical optics*. Interscience.

- Höcht, G. (2002). *Traveltime approximation for 2D and 3D media and kinematic wavefield attributes*. PhD thesis, Universität Karlsruhe, Germany.
- Höcht, G., Perroud, H., and Hubral, P. (1997). Migrating around on hyperbolas and parabolas. *The Leading Edge*, May:473–476.
- Hormann, K. and Agathos, A. (2001). The point in polygon problem for arbitrary polygons. *Computational Geometry*, 20(3):131–144.
- Hubral, P. (1979). A wave-front curvature approach to computing of ray amplitudes in inhomogeneous media with curved interfaces. *Studia Geoph. et Geod.*, 23:131–137.
- Hubral, P. (1980). Wavefront curvatures in three-dimensional laterally inhomogeneous media with curved interfaces. *Geophysics*, 45(5):905–913.
- Hubral, P. (1983). Computing true amplitude reflections in a laterally inhomogeneous earth. *Geophysics*, 48(8):1051–1062.
- Hubral, P. and Krey, T. (1980). *Interval velocities from seismic reflection traveltime measurements*. Soc. Expl. Geophys., Tulsa.
- Hubral, P., Schleicher, J., and Tygel, M. (1992). Three-dimensional paraxial ray properties, Part II: Applications. *J. of Seismic Exploration*, 1:347–362.
- Jäger, R. (1999). *The Common-Reflection-Surface Stack – Theory and Application*. Master's thesis, University of Karlsruhe.
- Kesmarky, I. (1977). Estimation of reflector parameters by the virtual image technique. *Geophys. Prosp.*, 25(4):621–635.
- Keydar, S., Edry, D., Berkovitch, A., and Gelchinsky, B. (1995). Construction of kinematic seismic model by homeomorphic imaging method. In *Extended abstracts, 57th Conf. Eur. Assn. Geosci. Eng.*
- Kirkpatrick, S., Gelatt, C. D., and Vecchi, M. P. (1983). Optimization by simulated annealing. *Science, Number 4598, 13 May 1983*, 220, 4598:671–680.
- Klüver, T. and Mann, J. (2005). Event-consistent smoothing and automated picking in CRS-based seismic imaging. In *Expanded Abstracts, 75th Annual Meeting*. Soc. Expl. Geophys.
- Koglin, I. (2005). *Estimation of Residual Static Time Shifts by means of the CRS based Residual Static Correction Approach*. Logos Verlag, Berlin.
- Kravtsov, Y. and Orlov, Y. (1990). *Geometrical Optics of Inhomogeneous Media. Series on Wave Phenomena*. Springer Verlag, Berlin.
- Lafond, C. F. and Levander, A. R. (1993). Migration moveout analysis and depth focusing. *Geophysics*, 58(1):91–100.
- Landa, E., Gurevich, B., Keydar, S., and Trachtman, P. (1999). Application of multifocusing method for subsurface imaging. *J. Appl. Geoph.*, 42(3,4):283–300.

References

- Lines, L. R. and Treitel, S. (1984). Tutorial: A review of least-squares inversion and its application to geophysical problems. *Geophys. Prosp.*, 32:159–186.
- Loewenthal, D., Roberson, R., and Sherwood, J. (1976). The wave equation applied to migration. *Geophys. Prosp.*, 24:380–399.
- Mann, J. (2002). *Extensions and applications of the Common-Reflection-Surface stack method*. Logos Verlag, Berlin.
- Mann, J. and Höcht, G. (2003). Pulse stretch effects in the context of data-driven imaging methods. In *Extended abstracts, 65th Conf. Eur. Assn. Geosci. Eng.*
- Mayne, W. H. (1962). Common reflection point horizontal data stacking techniques. *Geophysics*, 27(6):927–938.
- Müller, N.-A. (2003). The 3D Common-Reflection-Surface stack. Theory and application. Master's thesis, University of Karlsruhe.
- Müller, T. (1999). *The Common Reflection Surface Stack Method – Seismic imaging without explicit knowledge of the velocity model*. PhD thesis, Der Andere Verlag, Bad Iburg.
- Neidell, N. and Taner, M. (1971). Semblance and other coherency measures for multichannel data. *Geophysics*, 36:482–497.
- Nelder, J. and Mead, R. (1965). A simplex method for function minimization. *Computer Journal*, 7:308–313.
- Perroud, H., Hubral, P., Höcht, G., and de Bazelaire, E. (1997). Migrating around in circles - part III. *The Leading Edge*, June:875–883.
- Popov, M. M. and Pšenčík, I. (1978). Computation of ray amplitudes in inhomogeneous media with curved interfaces. *Studia Geoph. et Geod.*, 22:248–258.
- Press, W., Teukolsky, S., Vetterling, W., and Flannery, B. (2002). *Numerical Recipes in C++, Second Edition*. Cambridge University Press.
- Schleicher, J., Tygel, M., and Hubral, P. (2007). *Seismic True-Amplitude Imaging*. to be published.
- Schneider, W. A. (1978). Integral formulation for migration in two and three dimensions. *Geophysics*, 43(1):49–76.
- Schneider, W. A. and Backus, M. M. (1968). Dynamic correlation analysis. *Geophysics*, 33(1):105–126.
- Shah, P. M. and Levin, F. K. (1973). Gross properties of time-distance curves. *Geophysics*, 38(4):643–656.
- Sheriff, R. E. and Geldart, L. P. (1982). *Exploration seismology*. Cambridge University Press.
- Stolt, R. H. (1978). Migration by Fourier transform. *Geophysics*, 43(1):23–48.
- Thore, M., de Bazelaire, E., and Ray, M. (1994). Three-parameter equation: An efficient tool to enhance the stack. *Geophysics*, 59(2):297–308.

- Trappe, H., Mann, J., and Buske, S. (2005). High-resolution images of subsurface CO₂ storage sites in time and depth by the CRS methodology (CO₂CRS). *Geotechnologien Science Report No. 6: Investigation, utilization and protection of the underground*. Koordinierungsbüro Geotechnologien.
- Ursin, B. (1982). Quadratic wavefront and travelt ime approximations in inhomogeneous layered media with curved interfaces. *Geophysics*, 47(7):1012–1021.
- Vermeer, G. J. O. (2001). *Fundamentals of 3-D seismic survey design*. PhD thesis, Technische Universiteit Delft.
- Versteeg, R. J. (1993). Sensitivity of prestack depth migration to the velocity model. *Geophysics*, 58(6):873–882.
- von Steht, M. (2004). The Common-Reflection-Surface Stack under Consideration of the Acquisition Surface Topography – Combined Approach and Data Examples. Master’s thesis, University of Karlsruhe.
- von Steht, M. (2006). 2D CO CRS imaging for multicomponent data recorded by the VSP geometry. In *Expanded Abstracts, 76th Annual Meeting*. Soc. Expl. Geophys.
- Williamson, P. (1990). Tomographic inversion in reflection seismology. *Geophys. J. Intern.*, 100:255–274.
- Yilmaz, Ö. (1987). *Seismic data processing*. Soc. Expl. Geophys., Tulsa.
- Zhang, Y. (2003). *Common-Reflection-Surface Stack and the Handling of Top Surface Topography*. Logos Verlag, Berlin.

Danksagung

Prof. Dr. Peter Hubral danke ich für die Betreuung meiner Arbeit und die Übernahme des Referats. Er ließ mir während meiner Doktorandenzeit viel Freiraum für die Verwirklichung eigener Ideen.

Prof. Dr. Dirk Gajewski danke ich für die Übernahme des Korreferats und sein Interesse an dieser Arbeit.

Bei **Miriam Spinner** möchte ich mich nicht nur für die fachliche Zusammenarbeit und das Korrekturlesen dieser Arbeit bedanken, sondern auch für die schönen Stunden abseits der Geophysik.

Ein besonderer Dank geht an **Dr. Jürgen Mann** für die lange und fruchtbare Zusammenarbeit. Darüberhinaus hat er durch zahllose Diskussionen sowie das Korrekturlesen zum Gelingen dieser Arbeit beigetragen.

Die Mittags- und Kaffeepausen mit den Mitgliedern meiner Arbeitsgruppe sowie **Paola Ledermann** waren immer wieder Anlass für Diskussionen über Gott und die Welt. Sie boten eine willkommene Möglichkeit über den eigenen Tellerrand zu blicken und neue Ideen zu entwickeln.

I wish to thank *ENI S.p.A.*, in particular **Paolo Marchetti**, for their cooperation in the scope of this work.

Claudia Payne danke ich für ihre Hilfe bei organisatorischen und bürokratischen Problemen.

Meinen Eltern **Gudrun** und **Rainer Müller** danke ich ganz herzlich für ihre stete Unterstützung in allen Belangen.

Lebenslauf

Persönliche Daten

Name: Nils-Alexander Müller
Geburtsdatum: 14. April 1977
Nationalität: deutsch
Geburtsort: Groß-Gerau

Schulbildung

1983 - 1985 Grundschole Zellerfeld
1985 - 1986 Colegio Ingles Catolico, La Serena, Chile
1986 - 1987 Grundschole Zellerfeld
1987 - 1989 Orientierungsstufe
1989 - 1996 Robert-Koch-Schole Clausthal-Zellerfeld
21.05.1996 Allgemeine Hochschulreife

Zivildienst

1996 - 1997 Studentenwerk Clausthal-Zellerfeld

Hochschulausbildung

1997 - 2000 Studium der Geophysik
an der Christian-Albrechts-Universität, Kiel
2000 - 2003 Studium der Geophysik
an der Universität Karlsruhe (TH)
01.12.2003 Diplom
seit Januar 2004 Doktorand an der Fakultät für Physik
der Universität Karlsruhe (TH)